Dissertation

Microgrid Optimization, Modelling and Control

Submitted by

Yi Han

Department of Electrical and Computer Engineering

In partial fulfillment of the requirements

For the Degree of Doctor of Philosophy

Colorado State University

Fort Collins, Colorado

Fall 2014

Doctoral Committee:

Advisor: Peter M. Young

Edwin K. P. Chong
Ali Pezeshki
Chuck Anderson

Copyright by Yi Han 2014

All Rights Reserved

Abstract

Microgrid Optimization, Modelling and Control

Microgrid has drawn more and more attention because of the enormous benefits it can bring to traditional power system and local communities. Microgrids are essentially modern, small-scale (electrical) power distribution systems. They can afford benefits, such as enhancing system reliability, reducing capital investment and carbon footprint, and diversifying energy sources [1]. Microgrids contain several generators, whose size may range from several tens of kilowatts to a few megawatts [2]. They are different from traditional centralized electricity networks, which transmit vast amounts of electrical energy across long distances at very high voltages. However, microgrid are similar to utility scale power distribution grids, which generate, transmit and regulate electricity to the consumer locally.

To improve the efficiency of microgrids, and to reduce fossil fuel usage and its related pollution, renewable energy sources are integrated with traditional microgrids. Renewable energy sources include photovoltaic power, hydro power, geothermal power and wind power. These are clean and abundantly available energy sources. However, because the output power of renewable energy is strongly correlated with weather conditions, their outputs are not consistent over time. Hence, renewable generation systems significantly impact microgrid stability, and can cause large frequency and voltage deviations in a microgrid [3]. In addition to the load and renewable energy fluctuations, system modelling uncertainties and unmodelled system dynamics can have a large impact when it comes to model based controller design.

Overall, we propose to tackle these issues as follows:

Microgrid Efficiency Improvement Beside increasing renewable energy content within the microgrid, system overall efficiency can be further enhanced by optimally dispatching resources. This means optimally dispatching load to generation units within a microgrid for fuel usage minimization. Further, if a historic load profile as well as generators' fuel consumption curves are known, we are able to find the best generators combination for fuel usage minimization. In this optimization problem, real-world constraints are put into consideration as well.

Natural Gas Engine Modelling and Control Natural gas engines have become more and more popular because of the lower cost of natural gas and their lower environmental impact. However, the applications of natural gas engine based generation units are limited, since the longer transport delay between fuel injection and torque makes the transient repones unsuitable for grid frequency control.

As load is dispatched to generators that have different fuel usage curves, generators are running at dissimilar operation points. They can even be turned on and off depending on the load profile and other circumstances. To handle fast load variations, maximize renewable energy content, allow for rapid adjustment for generators operating points, and keep microgrid frequency deviation within the allowed range in islanded mode, advanced control approaches are needed. Here robust control is implemented and compared with classical control techniques. For controller design and validation purposes, control orientated mathematical models for internal combustion engine, storage system and renewable generation system are developed and validated.

The voltage control of a synchronized generator is realized through the closed-loop current control of the excitor. Within a microgrid, internal combustion engines are used as primary

movers to rotate the alternator. Hence, the internal combustion engine control is mainly focused on grid frequency control by controlling the engine crank shaft speed.

Storage System Modelling and Control for Transient Performance Improvement In the proposed setup, microgrid transient performance is further improved by adding a storage system (e.g., battery). Due to the high cost of storage system, its capacity is limited. It only reacts on high frequency load fluctuation (caused by renewable energy or just big load transients) or load transients with constrained power delivery capability. Its state of charge and output power are monitored and controlled accordingly. The load variations with slower dynamics and bigger amplitude are taken care of by internal combustion engines in the configuration.

From control point of view, we would like to use Multi-Input-Multi-Output (MIMO) control to replace multiple individual Single-Input-Single-Output (SISO) control loops in the system. By doing so, system internal connections between different inputs and outputs are taken care of. In other word, the controller can access more information from various inputs, and at the same time it can maneuver the multiple actuators at the outputs. With tighter emission regulations, multiple SISO loops setup cannot longer provide satisfactory performances, more advanced MIMO control techniques are needed.

Through this research, the methodology of dealing with systems consisting of subsystems that have inherently distinct properties for improving overall system performances are developed. A slower system with bigger capacity is mostly cheaper in terms of per unit deliverables. A faster system with small capacity is more expensive to deliver the same amount of output. In a microgrid, the capital cost of per kW output power of internal combustion engine is much cheaper than per kW output capital cost of a battery. To improve the entire

system performance without significant costs increment, we would like to separate the wheat and chaff of both systems and bring the advantages of both systems together. In microgrids, the battery system and internal combustion engine system work collectively. We maximize the usage of battery and avoid any saturation or drain. At the same time we encourage the internal combustion engines to take the big trend of load fluctuations. The developed methodology can be applied to solve problems in various disciplines.

Acknowledgements

It has been a journey that full of experience, toughening, harvesting and growing in past five years. I have many individuals to thank. First of all, I would like to thank my advisor, Peter Young, for his guidance, understanding, patience and support during my entire study in the United States. This would never happen without him. Dr. Young has the insight of finding the crux of the matter and provides inspiring ideas to overcome it.

I would also like to thank the other members of my committee: Edwin Chong, Ali Pezeshki and Chuck Anderson, for their valuable comments, thoughtful questions and help in many ways at various times. I would like to thank Daniel Zimmerle, who has provided his invaluable industrial experiences and knowledge toward my research.

I would like to thank many friends and colleagues at Colorado State University for their support. I would like to thank the department of electrical and computer engineering, which has provided me teaching assistantships.

I had the opportunity of working at Woodward, Inc. during my study. It has been a joyful and gaining experience. I would like to thank Kamran Shahroudi, Blake Suhre, Suraj Nair, Michael Buehner and Nolan Polley at the Model Based Control Services group. Many thanks also go to other members in the organization, including: Aaron Zimenoff, Chris Defoor and Jason Barta and others.

Last, but certainly not the least, I would like to thank my wife, Mingsui Sun, my parents and all of my family members. Without your love, encouragement and support, many wonderful things in my life would never become true. Finally, I would like to thank my little boy, Elbert, who has brought infinite cheer and happiness to me.

Yi Han

Dedication

To my parents.

To Elaine and Elbert.

Table of Contents

List of Tables

List of Figures

CHAPTER 1

INTRODUCTION

1.1. Introduction and Background

There was a massive blackout in India in 2012. It was the largest power outage in human history. This blackout affected 620 to 700 million people, about half of India's population (or 10% of world population) [6]. In recent years, several blackouts have occurred in different countries, including: 2009 Brazil and Paraguay blackout, 2005 Java-Bali blackout, 2003 U.S. Northeast blackout, 1999 Southern Brazil blackout and so on. Each of them, affected millions people and businesses. These blackouts are caused by various reasons, including: overdraw of power from grid, equipment failures (transmission line, transformer, generator malfunction, etc), human (operator) error, extreme weather conditions and natural disasters. In some countries, the affected area was left in a state of chaos during and after the blackouts periods [7]. These massive blackouts are typically triggered by only a few (one or two) primary events [8]. A single failure in a power system can really put modern society into disorder.

The massive blackouts can be illustrated easily by using an example. If a transmission line is failed, the demanded power from power sources to loads must be carried by other nearby transmission lines. Those nearby transmission lines are then pushed beyond their capacity so they become overloaded and shift their load onto to other elements, prorogating a cascading failure. Referring to the primary failures, the cascading failures are known as the secondary failures. In addition, restoring power after a wide range blackout can be difficult, when power plants need to be brought back on-line [9]. Contrastingly, airports

and major industries were not affected since backup generators were available during the 2012 blackouts in India [10]. Backup generators are typical distributed generation (DG), which have been widely used as emergency and standby generations for hospitals, academic (industrial) campuses and skyscrapers.

1.1.1. *Distributed Generation*

Distributed generation is defined as the generation of electricity by facilities that are sufficiently smaller than central generating plants so as to allow interconnection at nearly any point in a power system according to IEEE [11]. It is also know as 'MicroSources' widely. Technically, they are 'tiny' compare to centralization systems. Frequently, DG is placed near loads to avoid transmission losses. DG is not a replacement of traditional centralized generation (CG), but it provides a reliable, high efficiency and economical way to provide sufficient power to load center. Because of the constraints of land, popular will and environment impact, there is little chance of building new transmission lines or expanding existing ones. Hence, it is difficult to fulfill the power demand at load center during peak hour although there is sufficient power capacity. By building DG at the nearby load center, power demand can be fulfilled locally. DG and CG represent different generation configurations. According to fuel availability, environment pressures, renewable resources, costs and load characteristic, suitable ones should be deployed accordingly.

About two decades ago, centralized generation was indubitable. The principal reason for this was that the economies gained by building larger power plants outweighed the additional costs of transporting the electricity to consumers and DG was almost nonexistent in the 1990s [12]. However, with the deregulation of the power industry and the encouragement of low carbon energy policy aimed at reducing the emissions linked to climate change

by governments, DG is receiving increased attention. With the inherent advantage of low transportation costs and combination of renewable energy, the dependency on fossil fuels and their costs can be minimized. This step will also lead to significant carbon dioxide emissions reduction [13]. In addition, co-generation or combined heat and power (CHP) plants generate electricity and heat in a single process. The waste heat from the generation process can be used beneficially in industrial processes or to provide heat to local communities, rather than rejected to the environment [12]. Such applications can double the system overall efficiency [14].

DG utilizes a wide range of prime movers, including: internal combustion (IC) engines, micro turbine, photovoltaic, wind turbine, fuel cells, etc. Among these prime movers, micro turbine, photovoltaic and fuel cells need inverters to interface with distribution networks [15]. The power electronics based inverters ensure the voltage and frequency of outputs are compatible with the electrical grid. However, alternate current (AC) obtained from inverter will not be a perfect sinusoidal wave. It may generate severe harmonics when converting direct current (DC) output to AC in some circumstances [16]. It is vital that the harmonics distortion level is controlled within limits set by industrial standard [12]. Most importantly, since the output of renewable energy is uncontrollable, the fluctuating power generated by renewable energy sources might downgrade power quality such as voltage and frequency [17]. Individually deployed DG is not suitable for many applications.

1.1.2. *From Distributed Generation to Microgrids*

A fundamental issue for distributed generation is the array of technical difficulties related to control of a significant number of microsources [18]. Utilization of individual distributed generators can cause as many problems as it may solve [15][19]. A better way of realizing

the emerging potential of DG is to take a systems approach that integrates generations and associated loads in a certain area as one subsystem or a "microgrid" [19]. In this way, the power system reliability is enhanced significantly [13]. There are various definitions for microgrids, but essentially it is an aggregation of electrical generation, storage and loads, which is capable of operating in parallel with, or independently from the main grid [20] [21]. From a structural point of view, a microgrid is essentially a modern, small-scaled centralized electricity system. On the one hand, microgrid is different from traditional centralized electricity networks, which transmit vast amounts of electrical energy across long distances at very high voltages [22]. On the other hand, it is similar with the utility scale power grid, which generates, transmits and regulates the the electricity to the consumers, but does so locally. Microgrid has numerous benefits, such as, improving power quality, enhancing system reliability, reducing capital investment and carbon footprint, diversing of energy sources and generation of revenue [1]. It normally involves several generators in the size range of several tens of kilowatts to few megawatts [2].

Although microgrid consists of DGs, these DGs are functioning differently within a microgrid compare to when they are operated as individual power sources. In a microgrid, wind turbine and photovoltaic are considered as variable (nondeterministic) generations. They are largely determined by weather conditions. An internal combustion engine based generator is regarded as a controlled (deterministic) generation. The generators operated in a microgrid are comparatively small, and it is possible to switch them on and off to increase the frequency at which a particular plant is re-called for operation [2][23]. In other words, it is possible to adjust the output of microgrid generator from zero to its rated power. Contrast that with a traditional power plant, where the generators are intended to keep running. Microgrid

may run in islanded or grid-tied mode continuously, as well as in dual mode by changing the grid connection status [13]. Since microgrid has the ability of islanding from the utility, it can continuously provide power to the islanded portion even during unscheduled periods of interruption [24] [7]. Microgrids can be connected and disconnected with utility grid by opening and closing the point-of-common-coupling (PCC) breaker for maximize applicability and functionality [25]. For example, because the voltage at PCC of a grid-connected voltage source converter (VSC) can be controlled by regulating the reactive power injected/absorbed by the VSC to/from the power grid, a grid tied PV system with VSC can be used as a network dynamic voltage regulator at all time to enhance system durability [26]. The interconnection switch ties the microgrid and the rest of the distribution system at the PCC. In North American, the interconnection switches are designed to meet grid interconnection standards, IEEE 1547 and UL 1741 [25]. By connecting microgrid to utility grid, renewable energy in microgrid is utilized without additional frequency regulation effort. In addition, axillary services can be provided to both utilities and microgrid customers. Microgrids located near power demand centers could provide these services much more efficiently than distant generating stations since they would operate close to the loads [27]. In addition, microgrids can serve both electrical and thermal loads. Controlling a microgrid in islanded mode is more interesting and challenging, since frequency is not tied with utility grid. With big load variation or large portion of renewable energy source, microgrid frequency control can be difficult to achieve.

During disturbances, generation and corresponding loads can be disconnected from the distribution network to isolate the microgrid's load from the disturbance without harming the integrity of transmission grid. Intentional islanding of generation and loads has the

potential of providing a higher reliability and power quality than the utility grid to the end customers [15]. Microgrid can also provide additional benefits to the local utility by providing dispatchable power to use during peak hours and alleviating or postponing distribution system upgrades [25]. Microgrid customers can be a university, local communities (a small town) or commercial campuses. Local system reliability is improved through the developed smart technologies that are embedded in the microgrids. Furthermore, microgrids prevent power outages and their related costs. There are several examples of microgrid, such as: U.S. Army Fort Bragg, Beach Cities Microgrid Project and Perfect Power at Illinois Institute of Technology [24].

1.1.3. *Microgrids*

As shown in figure 1.1, starting from electrical generation, a typical microgrid consists of several generators as power sources and other electric elements for transmission, storage and distribution purposes. Above all, there is a microgrid manager, which is a computer based planner and controller. Human operators monitor the system performance without much participation in microgrid operation. The microgrid manager interacts with all the subsystems within a microgrid and implements developed algorithms to achieve desired overall performance. Essentially, it is a supervisory control and data acquisition (SCADA) system that ensures the microgrid is operated safely and efficiently in both grid-connected and islanded modes. It performs two major duties: Microgrids optimization and control. As microgrid manager performs the optimization duty, it optimally dispatches the load to generators for fuel usage minimization; When microgrid manager carries out the control duty, it implements voltage and frequency control to ensure power quality and system stability. Microgrid manager executes these two tasks simultaneously. In addition to optimization and

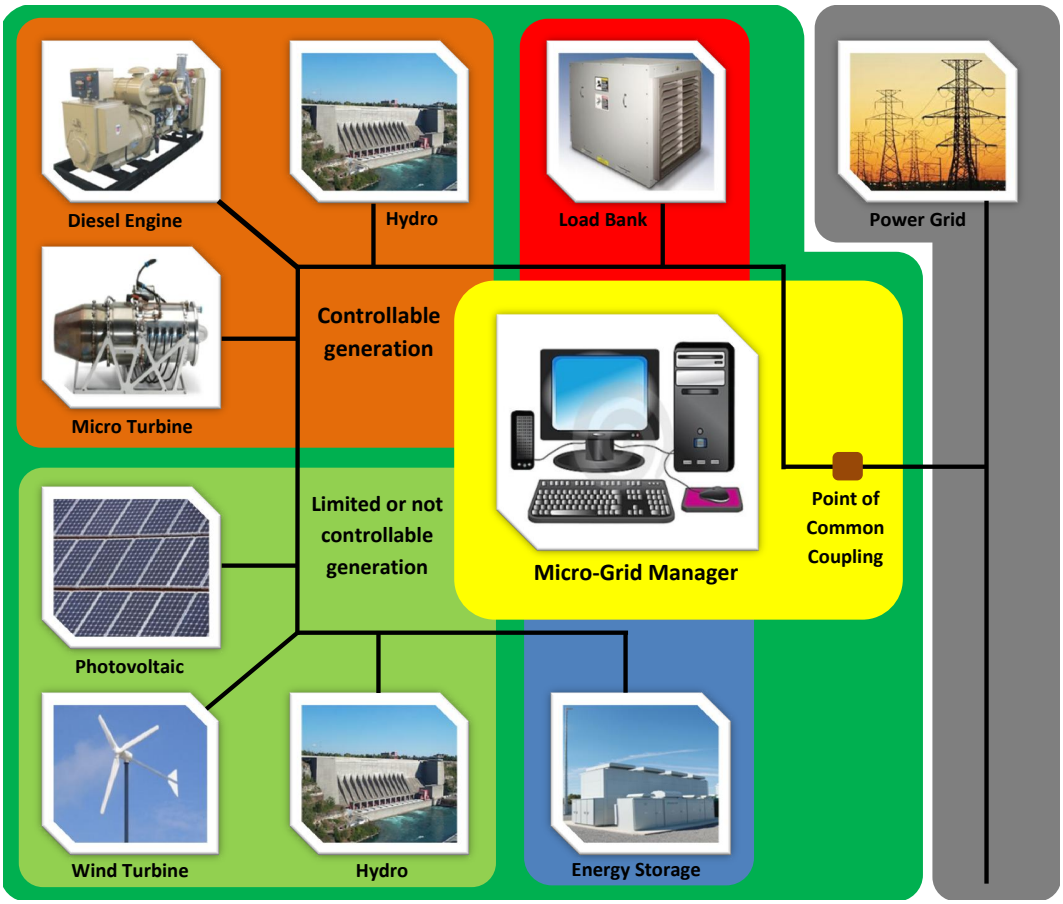

FIGURE 1.1. Microgrid setup with one common point of coupling to the utility grid

control, the microgrid manager also performs other duties, such as: black start after a fault, system efficiency monitoring, carbon dioxide contribution analysis, system health monitoring etc [13]. A ultimate microgrid should have the following features, which are not all available yet [28]:

- Accommodates a wide range of generation.
- Provide power to the consumers
- Plug and play functionality for operating in islanded or grid tied mode.
- Serves variety of loads.

- Deliver high quality power to meet future requirements.
- Anticipates and instantly responds to system malfunctions.
- Mitigates and robust to physical and cyber attacks.
- Competitive in energy markets.
- Optimally utilizes assets within a microgrid.

As the percentage of renewable energy increases, the control and optimization of microgrid becomes a significant challenge [21]. To improve overall grid performance, energy storage system with fast-acting energy absorption and injection capability is used when there is imbalance between generation and loads [29]. Load and generation imbalance is caused by various reasons, such as: load variations, inconsistent renewable energy generation, generation time delays and so on. Energy storage system can be essential for enhanced microgrid performance. However, storage is very expensive, it is not feasible to deploy huge energy density storage system. A good microgrid manager should use least amount of storage to meet the requirements and maximize the performance.

Storage capacity is defined as the time a storage system can supply the load at a rated power. Storage capacity can be classified both in terms of energy density requirements and power density requirements. They are used to fulfil medium or long-term and short or very-short-term needs, respectively [25]. Compare to other generation units, storage system can respond quickly, and therefore add flexibility to the microgrid control. Storage system can also enhance microgrid overall performance. Firstly, when a storage system is operated in power mode, they mitigate the frequent and rapid power output changes of renewable resources. Hence, they can help solve the volatility and intermittency problems associated with renewable resources. Second, they are used as energy mode and contribute to the

economic benefits by storing energy during the periods of low electricity prices and using the stored energy during the high electricity price periods [30]. Third, they stabilize and permit DG units to run at a constant and stable outputs regardless of load fluctuations. In this case, they are used as the combined power and energy mode. Storage system comprising both high power density and high energy density is most desirable [31]. However, when storage system is operated in energy mode, large (huge) batteries are required, it is too expensive and impractical. The profile of renewable output and load demand profile are two critical factors of deciding the capacity and type of energy storage components [31]. Microgrid energy storage system can be composed of battery, ultracapacitor and flywheel since energy storage system with a single type cannot perform all tasks efficiently [32].

In general, because of the high cost of storage system, its size is limited for designing a sustainable microgrid. In other words, a more advanced control scheme is needed to optimally extract the maximum potential of a storage system.

Overall, microgrid provides an advanced power system configuration to satisfy future power demands. It is considered as "A grid where everything is possible" and "an enabling engine for our economy, our environment and our future" [1]. It reveals above mentioned numerous benefits compared to expanding and upgrading existing centralized generation power systems. It can also be a valuable investment opportunity, especially when high value is placed on improving or maintaining reliability or power quality [33]. Microgrid is one of the future energy solutions for both developed and developing countries. It can benefit human beings both socially and economically.

Before microgrids can be implemented comprehensively, a number of associated economic, commercial, technical and security issues need to be solved. Department of Energy has listed five fundamental technologies that will drive the microgrid, which are [1]:

- Integrated communications, connecting components to open architecture for real-time information and control, allowing every part of the grid to both talk and listen.
- Sensing and measurement technologies, to support faster and more accurate response. such as remote monitoring, time-of-use pricing and demand-side management
- Advanced components, to apply the latest research in superconductivity, storage, power electronics and diagnostics.
- Advanced control methods, to monitor essential components, enabling rapid diagnosis and precise solutions appropriate to any event.
- Improved interfaces and decision support, to amplify human decision-making, transforming grid operators and managers quite literally into visionaries when it come to seeing into their systems.

In this research we focus on the the development of advanced control and operational strategies for microgrids, which can be conceptually different than the conventional power system, [24] [34]. Microgrid related research and development has been conducted all over the world. Some of this beneficial research is discussed in the following section.

1.2. Literature Review

A considerable amount of publications have appeared in the area of microgrid research. It is not possible to list all the work conducted in this field. However, some of the creditable

research works are reviewed here. The previous works have given a solid foundation and insight of future direction for continuously carrying on this study.

In [1], [13], [15], [19], [21], [24], [29], [35], [36] and [37], microgrids structure, characteristics, management, control, current status, future development directions, challenges and market segments are analysed, discussed and presented. In [7] and [38], many technical challenges and regulation barriers are mentioned, including: autonomous operation, power and frequency control, power quality, communication and protection issues. Among them, the microgrid control and management is a key part of making a microgrid implementable and profitable.

Within the control management topic, different aspects of control and management have been studied, ranging from market study, load dispatch management, DG units control to prime mover control. Our research emphasis is on microgrid control and management in islanded mode. The control system of a microgrid is designed for safe operation in both islanded and grid-tied modes [25]. The responsibilities of a microgrid controller are given in [39], where the responsibilities are listed as:

- Deal with DG output uncertainty
- Active power control for instantaneous difference between generation and loads
- Smooth transfer between grid-tied and islanded modes
- Uninterrupted power supply for sensitive loads
- Operate through blackout
- Increase system reliability, efficiency and stability
- Microsources output optimization with market participation

Beside these, a microgrid controller should also cope with parametric uncertainties and unmodeled system dynamics. As shown in [34], there are two categories of microgrid control, centralized and decentralized, these two control categories correspond to grid-tied mode and islanded mode control. They are on the level of microgrid supervisory control.

For centralized system, system frequency is nearly constant due the huge amount of rotating masses. The entire system inertia is significantly bigger than the microgrid that is connected. However, as stated in [25] and [40], grid frequency control is a challenging problem in islanded mode. There is very little directly connected rotating masses, like flywheel energy storage. Microgrid frequency is pushed around once there is generation and load imbalances. To maximize the autonomy of the DG units, decentralized microgrid control is implemented with local controllers (LC) attached to each DG and load. Autonomous LCs are intelligent and can communicate with each other to form a larger intelligent system. The main task of each LC is not necessarily to maximize the revenue of the corresponding unit but to improve the overall system performance. For example, the power quality at a integrated circuit manufacturer is crucial. When a microgrid is deployed in such circumstances, maximizing renewable energy content is not as critical as power quality. Hence, each LC is configured to chase the best grid performance. However, there are situations minimizing costs is more critical. Renewable energy content is maximized by using LCs on renewable sources, e.g., the solar unit maximum power point tracking (MPPT) control and wind turbine pitch angle control is utilized to maximized renewable energy source outputs. Some control methods are proposed for renewable source control, such as: in [41], model predictive control (MPC) is proposed and used to control blade pitch angle of wind turbine, it focuses only on one individual DG and lacks system level of consideration. An improved

frequency control method is proposed in [42], however, essentially the proposed method is a PID like control approach. In other words, if multiple DGs are involved, several PID loops have to be used. In such as setup, each controller can only react to one particular output. It does not have the flexibility that a MIMO control approach can provide. Other control techniques used for LC control include: neural network, fuzzy logic control and classical controls. Similarly a Ziegler-Nichols based PID control is shown in [43]. H_∞ control is utilized in [44] which demonstrates that the idea is feasible, but since the system uncertainties are not put into consideration, the designed controller can fail under certain extreme situations. A grid-forming control method is deployed onto "swing source", which can be assigned to regulate the frequency in [45]. For grid-forming control, voltage-droop and frequency control are used for two or more DG units actively participating in grid control. In [46] [47] [48] and [38], conventional droop control is employed. Some improved droop controls are studied in [49] and [50]. More advanced adaptive droop control method is studied in [51] and [52]. In [53] and [54], complete microgrid setups are presented and microgrid control is implemented as well. However, no advanced control algorithms are realized. There is no guarantee for other situations.

Within a microgrid, diesel engines, natural gas engines, micro turbines, hydro turbines etc. have been utilized as prime movers to rotate the generation units. Among them, the diesel and natural gas engine are classified as internal combustion (IC) engines. Compare to micro turbine, IC has wider operation region and it does not need AC-DC-AC back-to-back converters [55]. Hydro turbine is a effective choice but it is only available for limited natural environments. In contrast, IC engines are more controllable in terms of availability and

accessibility. In most microgrids, IC engine are one of the key components, whose output is controllable.

To control an IC engine with model based controller, a control orientated engine model is vital. A variety of IC engine models and control approaches have been developed in [56], [57], [58], [59], [60] and [61]. Most IC engine models are derived for diesel engines. These studies are comprehensive and thorough. Mean-value model and cylinder-by-cylinder model of turbocharged diesel engine have been developed in [62], [63], [64], [65], [66] and [67]. However, limited number of publications are dedicated to modelling and control of spark ignited (SI) engines. Among them, most of SI engine models are dedicated for gasoline engines and specified for automobile applications. Even less work has been done towards modelling and control of natural gas engines [68].

Regarding to SI engine control, some work has been done. In [69], adaptive control method is proposed for air-fuel ratio control and speed control, respectively, but it is not suitable for rapid load variation applications. Neural networks and hybrid radial basis functions were proposed in [70]. The results show that the mean value engine model with hybrid radial basis is more accurate than neural networks in terms of engine power and torque calculation. A direct injection dual fuel diesel natural gas engine simulation model is developed in [71]. Since it is direct injection, there is less fuel transport delay. However, because of the low fuel pressure, fuel is injected before compressor for most of natural gas engine. There is considerable delay between fuel injection and fuel combustion. A limited amount of work has been done for industrial lean burn natural gas engine control. Proportional-Integral-Derivative (PID) control method is deployed in [72] [73], Lyapunov control in [74], fuzzy control method in [75] [76], generalized predictive control in [77] [78] and neural network in

[79]. These studies have shown that these control strategies can be successfully applied for IC engine speed control. However, these results are more focused on reducing steady-state error. The following research is more emphasized on transient performance, which is aligned with our research interests. In [60], a new multi-variable PI tuning approach for lean burn natural gas engine speed control is presented. Nevertheless it is still a PI controller. The constraints of PI controller still apply, which are oscillatory or rolling behavior with high integral gain, also proportional and integral gain interact with each other, this interaction can make tuning the parameters more challenging [80]. With the high standard of emission control, classical control based algorithms can not satisfy the higher requirements anymore.

A H_∞ controller was designed in [81] to control throttle valve and recirculation valve of the engine for speed regulation. Since the system uncertainties are not considered in H_∞ control, system robustness and model uncertainties are not addressed, which means long period of control calibration work still has to be carried out. The uncertainties should also include the parameter variations with engines aging processes. Linear parametric varying (LPV) control is proposed in [82] for lean burn engine AFR control. It is critical to ensure the controller is still valid for entire nonlinear system [83]. In [84], a fuzzy logic and neural networks system for regulating the AFR of a compressed natural gas (CNG) engine is proposed. As the author stated, the method may be difficult to achieve in transient conditions. There are also other issues with fuzzy logic control and neural network control, including manual tuning, tradeoff of performance robustness, long learning curve and so on.

To achieve better microgrid performance in islanded mode, storage system is attached for providing (or absorbing) the instantaneous power difference between generation and loads. There are many generic battery models for dynamic simulations, such as: [85] [86] [87]. The

main parameters are battery voltage, current and State of Charge (SOC). A high accuracy battery model is complicated and requires electrochemistry background. For our application, this level of detail is not necessary. A generic model can accurately represent the battery dynamics with easily extracted parameters from the manufacturer data sheet. It is sufficient for microgrid control applications. The validation results show a generic battery model can capture the general behavior of a battery, which is sufficient for controller analysis and design. Many voltage source inverter (VSI) average models are available in [88] [89] [90] and [91]. From control point of view, [89] and [91] presented a highly accurate single phase inverter average model. It is sufficient for microgrid applications and adopted in our research. Some ongoing microgrid development, testing and evaluation projects are actively conducted around the world as shown in [25], [37] and [34].

1.3. Motivations for the Research

1.3.1. *Primary Motivation*

"With the aging, inefficient, congested power system infrastructure in the United States, it is time to deploy some novel approaches to meet the future energy needs of the *Information Economy* without operational changes and substantial capital investment over the next several decades" [92]. This sentence is cited from "Grid 2030 - A National Vision for Electricity's Second 100 years" by United States Department of Energy. Potentially microgrids can be a novel approach for solving above mentioned energy problems because of their inherent characteristics.

Distributed generation is one of the key components to form a microgrid. DGs that have natural gas or diesel powered prime movers have been widely deployed. In recent years, with worldwide concerns of environment, clean burning natural gas as an alternative fuel to

reduce diesel exhaust emissions are deployed increasingly. However, its applications are still not comprehensive because of some applications need fast responses that natural gas engines cannot provide.

Natural gas is a mixture of different gases. Its main ingredient is methane [93]. People have been using natural gas since 200 B.C [94]. Nowadays, natural gas is widely used in industry, business, home and transportation.

Most importantly, in the United States about one third of the natural gas is consumed for electricity generation. It is the second largest producer of electricity after coal. According to the United States Energy Information Administration Annual Energy Review, 25% of all electricity in the United States was generated by natural gas in 2011 [95]. Natural gas is considered as fossil fuel, but it is the cleanest burning fossil fuel compared to coal and petroleum. Natural gas produces 30% less carbon dioxide emissions compared to diesel when they produce the same amount energy. In addition, natural gas is much cheaper. It is sold one third the price of diesel in terms of the same British thermal unit (BTU) content. It also produces much less sulfur and ash when it is burned [93]. Furthermore, the United States has huge natural gas reserves and an existing pipeline network that extends across the entire country. Hence, increasing the usage of natural gas not only economically benefits modern society but also reduces the environment impact. However, increasing the usage of natural gas for the electricity generation faces a number of theoretical and practical challenges. This is especially true when the natural gas engine is operated in islanded mode in a microgrid, which has considerable renewable energy resources involved. In such a setup, it is difficult to maintain a constant grid frequency with fluctuating load and renewable energy power.

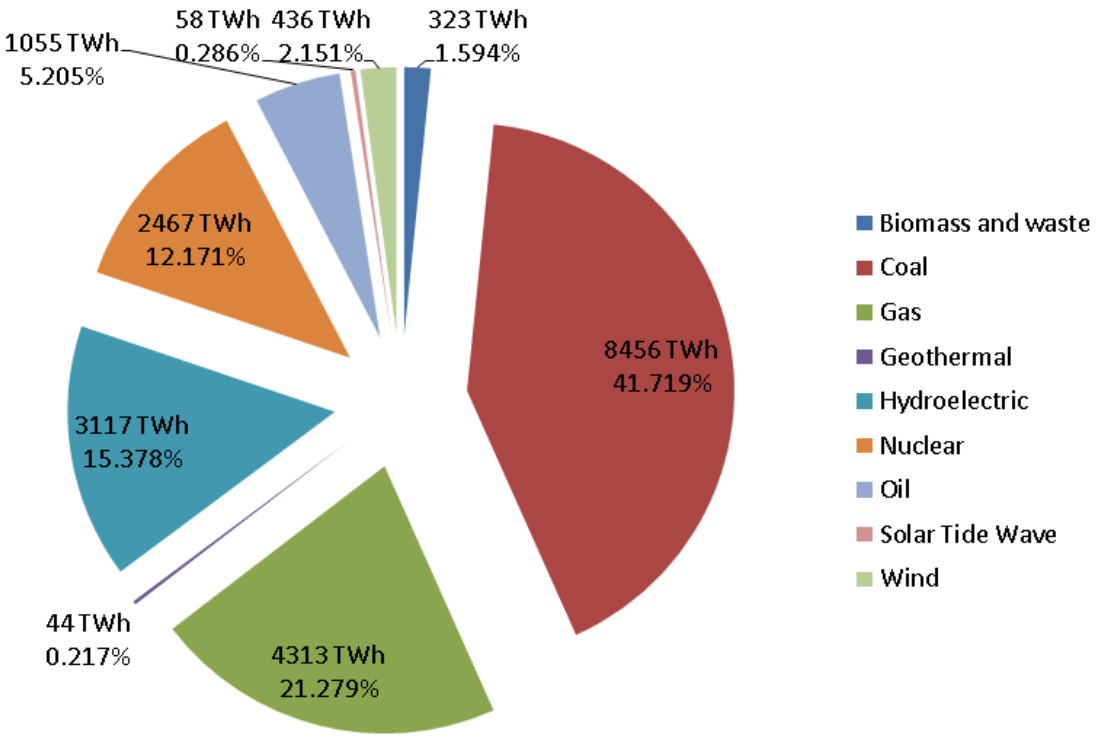

FIGURE 1.2. 2011 breakdown of electricity generation by energy source [5].

In the power industry, 20269TWh electricity was generated in 2011. The breakdown of electricity generation by energy source is shown in Fig. 1.2. It can be seen that 41.72% of world electricity is produced by using coal, about 21.28% is generated by natural gas, hydro contributes 15.38%, nuclear supplies 12.17%, oil provides 5.2% and biomass and waste gives 1.594%. In term of wind, solar and geothermal, they only provide 2.15% , 0.286% and 0.217%, respectively[5]. This pie chart clearly shows that humans mostly rely on coal as the dominant energy source, and we are not taking sufficient advantage of renewable energy sources. There is a huge room to increase the usage of renewable energy if associated difficulties can be resolved accordingly. In addition, the usage of natural gas generation can be further increased, to reduce the usage of coal for power production.

Hence, the primary motivation of the research is to minimize the environment impact caused by power generation while fulfilling the power demand for development and economic growth. From a more technical point of view, we would like to maximize the renewable energy content within a microgrid with a combined natural gas engine and storage system for grid stability compensation. Within this configuration, traditional thermal based generation units are not utilized.

1.3.2. *Technical Motivation*

The technical motivation focuses on how to solve the theoretical and technical challenges that are stated in primary motivation section. One of the essential motivations is natural gas engine control. The main reason that stops the widespread utilization of natural gas engines is the long transport delay, which causes frequency deviations exceeding the allowed tolerance. This long transport delay is inherent with the physical engine hardware configuration.

Compared to a pre-mixed natural gas engine, a diesel engine can be controlled much more easily in islanded mode. A major difference between a turbocharged diesel engine and a premixed turbocharged natural gas engine is the way how the fuel is delivered, and consequently, how the output power is controlled. Lean premixed combustion technology is widely used for reducing emission. In the engines that use this technology, fuel and air are premixed before combustion. For a natural gas engine, gaseous state fuel can be mixed with air even before the compressor. After natural gas and air are mixed, the mixture has to go through compressor, intercooler, throttle valve and intake manifold before it can reach the combustion chamber. Thus, there is significant time delay between fuel injection and torque production. This is different from a modern liquid state fuel engine, which has fuel directly

injected into the combustion chamber. The presences of time delay makes the system much more difficult to analyse and control. Think about a general system without delay. In this case the system should react immediately if the errors are not getting smaller. However, for a system with time delays, the errors will change only after the inherent delays and then often over-react leading to system overshoot or even instability [96].

To compensate for the time delay of natural gas engine and overcome the generation and load imbalance caused by load variation and inconsistent renewable energy output, a storage system with limited size is attached. It is functioning as a buffer to export energy (power) to the load or absorb energy (power) from the generation while it waits for the slower natural gas engine to catch up and take the load gradually.

When power demands fluctuate rapidly, the natural gas engine controller commands the injectors (or fuel valve) to deliver more or less fuel to mix with air. At the same time, the throttle valve decides the amount of mixture which goes into the combustion chamber. However, grid frequency may start to deviate due to the significant time delay between fuel injection and torque generation. A power generation engine has much bigger moment of inertia, which makes the full load acceptance very difficult to achieve. In such a system, we must allow the turbocharger to spool up and achieve high boost pressure. This is generally done by using step loads. In such a case, a storage system can be engaged and supplies power to the load along with the natural gas engine. Once the natural gas engine output power catches up, the load demand is fulfilled only by the natural gas engine. Advanced control strategies manage not only the natural gas engine output but are also used here for optimizing storage usage, resulting in a smaller sized storage system. In practice, the storage system also reacts to the high frequency load variations by itself. Since the attached storage

system only has limited capacity, a storage system management system is needed to extract its maximum potential for maintaining grid stability and reliability.

The delay and nonlinearity caused by turbocharger is another control challenge. Turbocharger dynamics are complicated. It is modelled with not only thermal dynamics, but also with turbine and compressor maps. These maps are obtained experimentally. In addition, engine behaviors are different with the aging of the engine. Even the variations of ambient conditions can impact engine performances. Beside these, the measurement noise and sensor calibration error etc. can also affect the system. In other words, many system uncertainties are associated with this complicated system.

Furthermore, the output of the renewable energy generation units cannot be predicated exactly. Their outputs are sensitive to the weather conditions. For example, there exists a cube relationship between wind turbine output power and wind speed. If the net load is considered as the difference between the total load and output of renewable generators, it can fluctuate very rapidly. The natural gas engine with the attached storage system has to react to this unpredictable and fluctuating load.

In addition, a controller designed based on derived mathematical model of natural gas engine may not be compatible with the physical plant. Robust control strategies are applied to conquer the model uncertainties in the controller design. Our main goal is to use advanced control to achieve stable natural gas generator powered microgrid with limited storage capacity. Additionally, since the model of the plant is always an approximation of the plant, the effect of any discrepancy between the actual plant and the model on the performance of the controller will not be known until the controller is applied to the plant [97]. One important task at this point is the final adjustment or as often called "the tuning".

Overall, we would like to provide our contributions toward design, optimization, modelling, control and simulation of microgrids. Furthermore, we would provide a methodology that can be deployed for studying systems that involves subsystems, that have different costs, behaviours and advantageous, together to improve the overall system performances without significant costs or control effort investment.

One of the technical motivations of the research is to create a high fidelity hybrid electrical and mechanical system that represents a microgrid in system level. This system consists of a number of electrical generation, storage and consumption systems. Another technical motivation is that by deploying advanced control approaches we can achieve good system transient and steady state performances that cannot be achieved by classical control theories. This is despite the presences of many system uncertainties, unmodelled dynamics, large disturbances and so on. The measurements of the system performance include the frequency deviation, the maximum renewable energy content that can be handled without instability, the size of the storage system and the disturbances the system can deal with.

1.4. Awareness of the Problem

The detailed tasks are listed in the following subsections.

1.4.1. *Microgrid Optimization*

A optimization tool need to be developed for solving problems of:

(1) How loads should be dispatched to different generators for minimizing the fuel consumption when a historical load profile is given.

- Purely optimal load dispatch.

- Constrained optimal load dispatch, including: upper and lower operating points of generators, spinning reserve and swing capacity.
- Start-up and cooling down costs associated load dispatch.

(2) How to select generation units to form a microgrid that minimizes the fuel usage when a historical load profiles is given.

1.4.2. *Microgrid Modelling*

Control oriented models are needed for controller design.

(1) Modeling of a turbocharged natural gas engine, including following components:

- Volume elements - mixture, intercooler, intake and exhaust manifold.
- Orifice elements - throttle valve and fuel valve.
- Turbocharger - turbine, compressor and rotor dynamics.
- Engine block - indicated, friction torque and crank shaft dynamic.

(2) Modeling of a storage system:

- Storage system voltage dynamics.
- Storage system SOC variation.

(3) Models integrations:

- Engine system and storage system integration.
- Integrate renewable systems into engine and storage system.

1.4.3. *Control*

More advanced control strategies are needed for dealing with the following issues.

(1) Long time transport delay.

(2) Nonlinearity.

(3) Parameter uncertainties.

(4) Unmodelled dynamics.

(5) Disturbances rejection.

(6) Inherent drawbacks of classical control.

1.5. Microgrid Development Contribution

This research is intended to participate the advancing process of microgrids. The contributions toward microgrid development made by this research include:

(1) Development of Matlab^{TM} based optimization tools for microgrid fuel usage minimization. [23]

- Optimal microgrid net load dispatch for fuel consumption minimization. [98]
- Optimal generation units selection for fuel usage minimization [99] when forming a microgrid.

(2) Development of Simulink^{TM} based modelling platform for microgrid system simulation.

- Control orientated premixed natural gas engine model development and validation.
- Control orientated battery based storage system model development
- Complete high fidelity microgrid system model development.

(3) Development and implementation of advanced control algorithms for microgrid applications.

- Advanced MIMO controller implementation for improved overall microgrid system performances with minimized additional costs (e.g., minimized storage).
- Advanced MIMO controller development for natural gas engine speed and emission control.
- Advanced MIMO controller with storage and natural gas engine combined system expanded the usage of natural gas engines

1.6. Chapter Breakdown

Following the microgrid overview presented in Chapter 1, the rest of this dissertation provides the detailed study of microgrid optimization, modelling and control. This dissertation is divided into the following chapters. In Chapter 2, robust control theories are briefly reviewed. In Chapter 3, generation units optimum dispatch for fuel minimization is studied. How to optimally select generators to form a microgrid for a given or predicted load is presented in 4. Chapter 5 provides the mean value mathematical model of control orientated natural gas engine. Model of the storage system is presented in Chapter 6. Classical controller and robust controller design, simulation with results analysis and discussion are presented in Chapter 7. In Chapter 8, the conclusion is delivered.

1.7. Publications

1.7.1. *Journal*

Y. Han, P. M. Young and D. Zimmerle, "Microgrid Generation Units Optimum Dispatch for Fuel Consumption Minimization" *Journal of Ambient Intelligence & Humanized Computing*, pp.1-17, 2012.

Y. Han, P. M. Young, A. Jain and D. Zimmerle, "Robust Control for Microgrid Frequency Deviation Reduction with Attached Storage System," accepted by IEEE Transactions on Smart Grid.

Y. Han, P. M. Young and D. Zimmerle, "Optimal Generator Selection for Fuel Usage Minimization in Microgrids," submitted to *Elsevier on Electrical Power Systems Research.*

Y. Han, P. M. Young, "Lean Burn Natural Gas Engine Model and Control." Manuscript is ready for submission.

1.7.2. *Conference*

Y. Han, P. M. Young and D. Zimmerle, "Optimum Generation Units Dispatch for Fuel Consumption Minimization" In *50th IEEE Conference on Decision and Control and European Control Conference (CDC-ECC)*, pp. 7206-7211,dec. 2011

Y. Han, P. M. Young and D. Zimmerle, "Optimal Selection of Generators in a Microgrid for Fuel Usage Minimization," In *Power & Energy Society General Meeting (PES), 2013 IEEE*, pp.1-5. IEEE, 2013.

Y. Han, P. M. Young and D. Zimmerle, "Constrained Optimum Generator Dispatch for Fuel Consumption Minimization," In *Power & Energy Society General Meeting (PES), 2013 IEEE*, pp.1-5. IEEE, 2013.

Y. Han, Abhishek Jain, P. M. Young and D. Zimmerle, "Robust Control of Microgrid Frequency with Attached Storage System," In *Decision and Control Conference (CDC), 2013 52nd IEEE Conference on*, pp. 3043-3048. IEEE 2013.

CHAPTER 2

BACKGROUND

Some useful definitions, theorems, lemmas and proofs are reviewed in this chapter. These theoretical tools are used for conducting our research. In this chapter, we are mainly focused on control theory and related studies and we assume readers already have fundamental control system knowledge.

2.1. Norms for Signals and Systems

By examining the size of certain signals of interest, one can conclude the performances of a control system [100]. Hence, norms are briefly reviewed here. The norm of an element of a vector space is a real value function $\|\cdot\|$, which has the following properties:

(1) $\|u\| \geq 0$

(2) $\|u\| = 0 \Leftrightarrow u = 0$

(3) $\|au\| = |a|\|u\|, \qquad \forall a \in \mathbb{R}$

(4) $\|u + v\| \leq \|u\| + \|v\|$

2.1.1. *Signal Norms*

1-Norm: The 1-norm of a signal $u(t)$ is the integral of its absolute value [100]:

$$\|u\|_1 := \int_{-\infty}^{\infty} |u(t)| dt. \tag{2.1}$$

2-Norm: The 2-norm of a signal u(t) is [100]:

$$\|u\|_2 := \left(\int_{-\infty}^{\infty} |u(t)|^2 dt \right)^{1/2}. \tag{2.2}$$

The instantaneous power of a signal $u(t)$ is $|u(t)|^2$ and the square of its 2-norm is its energy.

∞-Norm: The ∞-norm of a signal $u(t)$ is the least upper bound of its absolute value [100]:

$$\|u\|_\infty := \sup_t |u(t)|. \tag{2.3}$$

2.1.2. *System Norms*

For a linear, time-invariant, causal and finite-dimensional system, its time domain input-output model can be written as a convolution equation,

$$y = G * u \tag{2.4}$$

which stands for,

$$y(t) = \int_{-\infty}^{\infty} G(t-\tau)u(\tau)d\tau. \tag{2.5}$$

Let $\hat{G}$ denote the Laplace transform of G. ($\hat{G} = \mathcal{L}\{G\}$.) 2-Norm and ∞-Norm of $\hat{G}$ are:

2-Norm:

$$\|G(s)\|_2 := \left(\frac{1}{2\pi} \int_{-\infty}^{\infty} |G(j\omega)|^2 d\omega \right)^{1/2}. \tag{2.6}$$

∞-Norm:

$$\|G(s)\|_\infty := \sup_\omega |G(j\omega)|. \tag{2.7}$$

Note that if $G(s)$ is stable, then by Parseval's theorem

$$\|G(s)\|_2 = \left(\frac{1}{2\pi}\int_{-\infty}^{\infty}|G(j\omega)|^2 d\omega\right)^{1/2} = \left(\int_{-\infty}^{\infty}|G(t)|^2 dt\right)^{1/2} = \|G(t)\|_2. \tag{2.8}$$

An important property of the ∞-norm is that it is sub-multiplicative:

$$\|G(s)H(s)\|_\infty \leq \|G(s)\|_\infty \|H(s)\|_\infty. \tag{2.9}$$

NOte the 2-norm of $\hat{G}$ is finite if and only if $\hat{G}$ is strictly proper and has no poles on the imaginary axis; the ∞-norm is finite if and only if $\hat{G}$ is proper and has no poles on the imaginary axis.

2.1.3. *Induced Norm of a Matrix*

The matrix $A \in \mathbb{R}^{m\times n}$ maps $\mathbb{R}^m \to \mathbb{R}^n$. The induced p-norm of a matrix is defined as:

$$\|A\|_{ip} \triangleq \sup_x \frac{\|Ax\|_p}{\|x\|_p} = \sup_{\|x\|_p=1} \|Ax\|_p. \tag{2.10}$$

It reveals the maximum amplification of the system A for all possible input directions.

2.1.3.1. *The Induced 1-norm of the matrix A*

The induced 1-norm of matrix A is calculated as:

$$\|A\|_{i1} \triangleq \max_{1\leq j\leq m} \sum_{i=1}^{n} |a_{ij}| \qquad \text{(maximum column sum)}. \tag{2.11}$$

2.1.3.2. *The Induced 2-norm of the matrix A*

The induced 2-norm of matrix A is calculated as:

$$\|A\|_{i2} \triangleq \sqrt{\lambda_{max}(A^T A)} = \bar{\sigma}(A) \qquad \text{(singular value or spectral norm).} \tag{2.12}$$

where $\lambda_{max}(\cdot)$ denotes the maximum eigenvalue.

2.1.3.3. *The Induced ∞-norm of the matrix A*

The induced ∞-norm of matrix A is calculated as:

$$\|A\|_{i\infty} \triangleq \max_{1 \le i \le n} \sum_{j=1}^{m} |a_{ij}| \qquad \text{(maximum row sum).} \tag{2.13}$$

2.2. Nominal Feedback System

In Fig.2.1, a single-input-single-output (SISO) linear time-invariant (LTI) feedback system is shown. In this figure, K is the controller and G is the plant. y is the output of the plant output. r is the reference signal, which the output should follow. $e = r - y$ is the error signal and it equals to 0 if $y = r$ (perfect tracking). u is the control signal, which varies based on e. Nominal stability (NS) is defined as: the system is stable with no model uncertainty. The following theorem can be used for examining if the feedback system in Fig.2.1 is internally stable (NS).

THEOREM 2.1. *[100] The feedback system is internally stable if and only if the following two conditions hold:*

(1) The transfer function $1 + GK$ has no zero in $Re(s) \geq 0$.

(2) There is no pole-zero cancellation in $Re(s) \geq 0$ when the loop gain is formed.

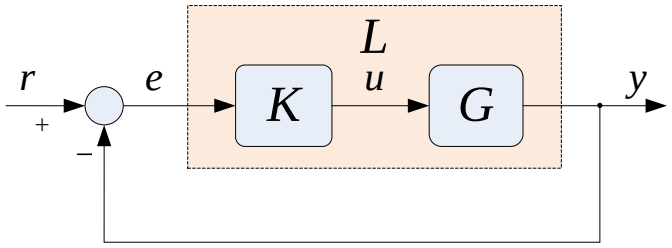

FIGURE 2.1. Unity feedback control system.

Bounded-input-bounded-output (BIBO) stability means if the input r is bounded, then the system output y is bounded too. It shows the input-output relationship, but it does not indicate if the internal signals are bounded. By considering the system internal stability, it can be found if the internal signals are bounded. Thus internal damage to the physical system can be avoided. In this dissertation, by stable we mean internally stable.

2.2.1. *Sensitivity function and complementary sensitivity function*

In our study, the sensitivity function and complementary sensitivity function are used for system analysis. Their definitions are given as below.

DEFINITION 2.2. [100] Let the loop transfer function $L = GK$ in Fig. 2.1, then the sensitivity function S and complementary sensitivity function T are defined as:

$$S = \frac{1}{1+L} \tag{2.14}$$

and

$$T = 1 - S = \frac{L}{1+L}, \tag{2.15}$$

respectively.

Here S denotes the transfer function from r to e. T denotes the transfer function from r to y. S is the sensitivity of the closed-loop transfer function T to an infinitesimal perturbation in G [100].

Intuitively, it is trivial to notice that if y tracks r well at certain frequencies, then e is small, which means S is small and loop gain is big. In other words, S is insensitive in these frequencies. Good performance can be achieved at these frequencies.

2.2.2. *Nominal Performance*

Nominal performance (NP) can be defined as: The system satisfies the performance specifications with no model uncertainty. Mathematically, suppose that good performance is known to be achieved if the plot of $|S(j\omega)|$ lies under some curve. It can be expressed as:

$$|S(j\omega)| < |W_1(j\omega)|^{-1}, \quad \forall\omega, \tag{2.16}$$

which equivalent to,

$$\|W_1 S\|_\infty < 1. \tag{2.17}$$

where W_1 is a frequency-dependent weight function. If $|W_1(j\omega)|$ is small at certain frequencies, it means the error signal amplitude is not controlled tightly at these particular frequencies. (However, the controller should still keep the system stable.) When $|W_1(j\omega)|$ is big, it means S is small and only small error signal is allowed. Better performance is desired.

The system performance requirement can be at low frequency or at somewhat high frequency (but not very high frequency). This really depends on the application. In this dissertation, the engine system and the storage system take care of low frequency and high

frequency loads, respectively. In such a setup, their performance requirements are also different at different frequencies. Note because all physical system are strictly proper, L will roll off eventually. As L goes to 0, T goes to 0. Since $S = 1 - T$, then $S = 1$. In other words, we cannot ask for much performance at very high frequency.

2.3. Robust Control of SISO system

Most mathematical models have lower order than the actual plant. It is impossible to develop a mathematical model that can represent a physical system exactly. Uncertainties are not avoidable, they are always there. This means even when the input is known, the output still cannot be predicted perfectly. There are two types of uncertainties, the first type comes from unknown or unpredictable inputs (disturbances, noise, etc.) and the other type are unpredictable dynamics. Based on the studies of system nominal stability (NS) and nominal performance (NP), SISO system robust stability (RS) and robust performance (RP) are reviewed in this section. we also review basic notions of multiplicative and additive uncertainty.

2.3.1. *Multiplicative Uncertainties*

Suppose the transfer function of the nominal plant is G, the perturbed plant with multiplicative uncertainty has the following form:

$$G_p = (1 + \Delta W_2)G \tag{2.18}$$

Here W_2 is a fixed stable transfer function, which is known as the weight. Commonly, $\|W_2(j\omega)\|$ is a high pass filter like function, because the models are more accurate at low frequencies, and so not much robustness is required. At high frequencies, there are a lot of

model uncertainties and more robustness is desired. Δ is a variable stable transfer function that satisfies $\|\Delta\|_\infty \leq 1$.

A feedback system with multiplicative uncertainties is shown in Fig.2.2.

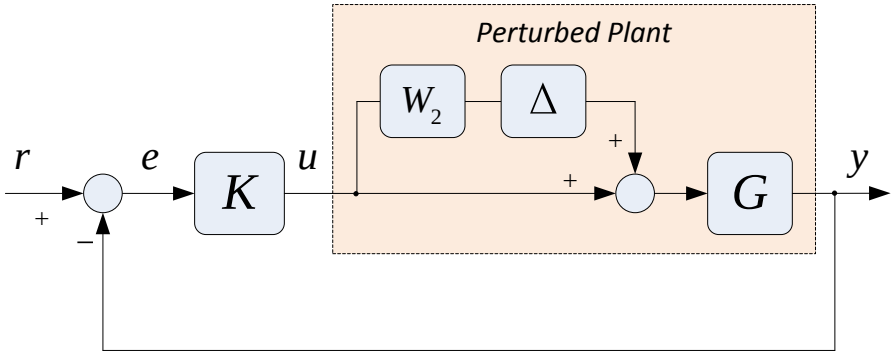

FIGURE 2.2. Feedback system with multiplicative uncertainty.

The following two theorems indicate the criteria of RS and RP for systems with multiplicative uncertainty.

THEOREM 2.3. *[100]* ***Multiplicative uncertainties model*** *K provides robust stability if and only if*

$$\|W_2 T\|_\infty < 1. \tag{2.19}$$

The complete proof can be found in [100].

THEOREM 2.4. *[100]* ***Multiplicative uncertainties model*** *A necessary and sufficient condition for robust performance is:*

$$\||W_1 S| + |W_2 T|\|_\infty < 1. \tag{2.20}$$

The complete proof can be found in [100], too.

2.3.2. *Additive Uncertainties*

If the nominal plant model of a system is G, then its perturbed system with additive uncertainty can be expressed as:

$$G_p = G + \Delta W_2 \tag{2.21}$$

Similarly, W_2 is a fixed stable transfer function. Δ is variable stable transfer function satisfying $\|\Delta\|_\infty \leq 1$. A feedback system with additive uncertainty is shown in Fig.2.3.

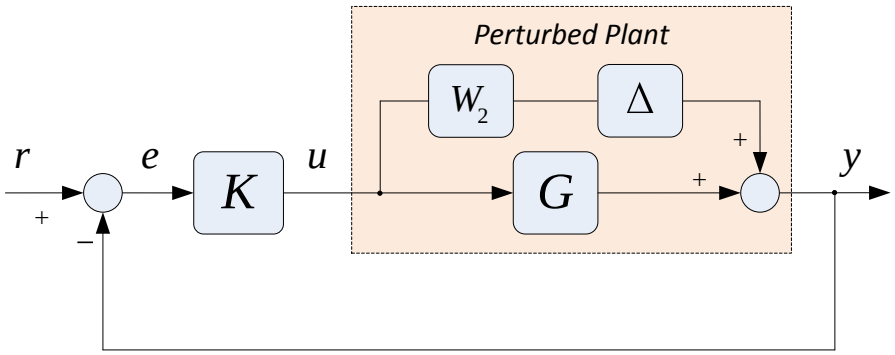

FIGURE 2.3. Feedback system with additive uncertainty.

The following two theorems indicate the criteria of RS and RP for systems with additive uncertainty.

THEOREM 2.5. *[100]* ***Additive uncertainties model*** *K provides robust stability if and only if*

$$\|W_2 KS\|_\infty < 1. \tag{2.22}$$

The complete proof can be found in [100].

THEOREM 2.6. *[100]* ***Additive uncertainties model*** *A necessary and sufficient condition for robust performance is:*

$$\||W_1S|+|W_2KS|\|_\infty < 1. \tag{2.23}$$

The complete proof can be found in [100], as well as a graphical interpretation in terms of the classical Nyquist plot.

2.4. Robust Control of MIMO System

In the previous section, RS and RP of a perturbed SISO system were studied. For MIMO systems, more general robust control theory is reviewed in this section. Since no mathematical model can exactly describe a physical system, this modeling error can dramatically affect the performance of a control system. The difference between the actual system and its mathematical model (used to develop controller designs) is known as model uncertainty. The uncertainties and perturbations are usually lumped together in a structured uncertainty description Δ, where

$$\Delta = diag\{\Delta_i\} = \begin{bmatrix} \Delta_1 & & & \\ & \ddots & & \\ & & \Delta_i & \\ & & & \ddots \end{bmatrix} \tag{2.24}$$

Δ is generally normalized in such a way that $\|\Delta\|_\infty \leq 1$.

As shown in Fig.2.4, the shaded area represents a general feedback control configuration for the case with no model uncertainties. It is the equivalent representation of Fig.2.1. When Fig.2.4 is considered as a whole, it represents the general control configuration with model uncertainties.

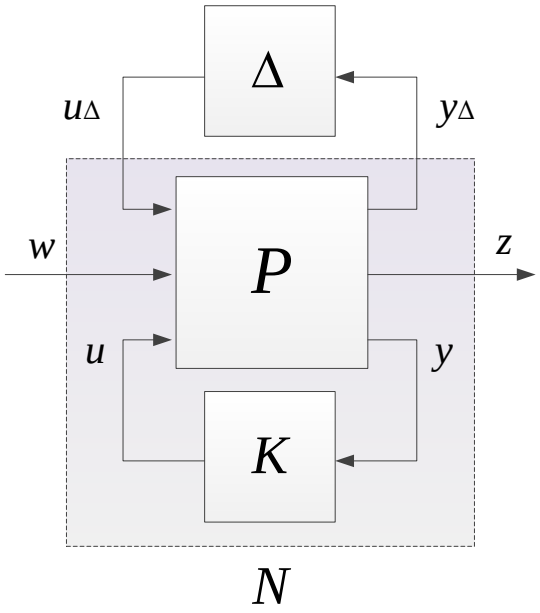

FIGURE 2.4. General control configuration for the case with model uncertainties.

2.4.1. *Robust Control Configuration*

By using linear fractional transformation, the block diagram in Fig.2.4 in terms of P is transformed into the block diagram in Fig.2.5 in terms of N by using controller K to close a lower loop around P.

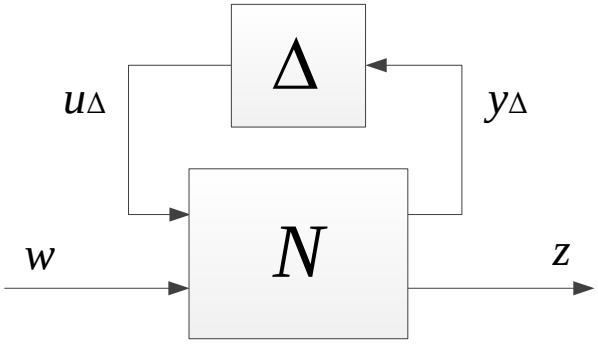

FIGURE 2.5. General control configuration for analysis uncertainties included.

If P is partitioned to be compatible with K and take lower LFT, the following expression is obtained:

$$N = F_l(P, K) = P_{11} + P_{12}K(I - P_{22}K)^{-1}P_{21} \tag{2.25}$$

In order to obtain the input-output transfer function from external inputs w to external outputs z, Δ is used to close the upper loop around M. Take upper LFT, we will have:

$$z = F_u(N, \Delta)w \tag{2.26}$$

where

$$F_u(N, \Delta) \triangleq N_{22} + N_{21}\Delta(I - N_{11}\Delta)^{-1}N_{12} \tag{2.27}$$

where F_l and F_u represent lower and upper LFT, respectively. In addition, P and N are partitioned as:

$$P = \begin{bmatrix} P_{11} & P_{12} \\ P_{21} & P_{22} \end{bmatrix} \tag{2.28}$$

$$N = \begin{bmatrix} N_{11} & N_{12} \\ N_{21} & N_{22} \end{bmatrix} \tag{2.29}$$

The system in Fig.2.5 can be rearranged into the $M\Delta$-structure as shown in Fig.2.6, where $M = N_{11}$ is the transfer function from the output to the input of the perturbations [101].

This $M\Delta$-structure is particularly useful when it comes to robust stability analysis. It will be revisited later in this chapter.

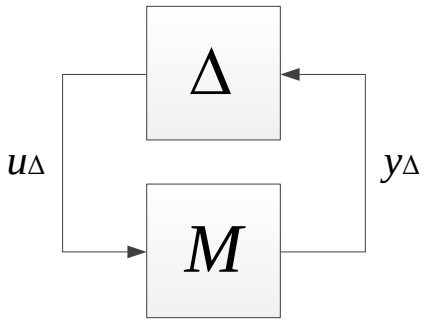

FIGURE 2.6. $M\Delta$-structure for robust control.

2.4.2. *The Structured Singular Value*

Given the setup in Fig.2.4, the system robustness can be quantified via the smallest structured Δ which makes the matrix $I - M\Delta$ singular at any given frequency. Computing this quantity over all frequency enables one to find the smallest destabilizing perturbation, and hence the system robustness. This metric is termed the structured singular value (denoted Mu, mu, SSV or μ), which stated mathematically is defined for a matrix M as (see [101]):

DEFINITION 2.7. [101] **Structured Singular Value.** Let M be a given complex matrix and let $\Delta = diag\{\Delta_i\}$ denote a set of complex matrices with $\bar{\sigma} \leq 1$ and with a given block-diagonal structure (in which some of the blocks may be repeated and some may be restricted to be real). The real non-negative function $\mu(M)$, called the structured singular value, is defined by

$$\mu(M) \triangleq \frac{1}{\min\{k_m | det(I - k_m M\Delta) = 0 \text{ for structured } \Delta, \bar{\sigma}(\Delta) \leq 1\}} \tag{2.30}$$

If no such structured Δ exists then $\mu(M) = 0$. Again, M is the lower LFT of P and K, and Δ=diag$\{\Delta_i\}$. In addition, $\mu(M)$ depends on both M and Δ.

A simple statement is: Find the smallest structured Δ (measured in terms of $\bar{\sigma}(\Delta)$) which makes the matrix $I - M\Delta$ singular; then $\mu(M) = 1/\bar{\sigma}(\Delta)$. Note a small value of μ is good as it means a bigger perturbation is required to make $I - M\Delta$ singular. However, a big value of μ means smaller perturbation can destabilize the system [101].

2.4.3. *Robust Stability with structured uncertainty*

From the definition of μ, it can be seen the uncertainty Δ is scaled by k_m. The smallest k_m that makes the system 'borderline unstable' is that satisfying

$$det(I - k_m M\Delta) = 0 \tag{2.31}$$

From the definition of μ in 2.4.2, $k_m = \mu(M)^{-1}$. Hence, the necessary and sufficient condition for robust stability is obtained as follow.

THEOREM 2.8. *[101]* ***RS for block-diagonal perturbation (real or complex).*** *Assume that the nominal system M and the perturbations Δ are stable. Then the $M\Delta$-system in Fig.2.6 is stable for all allowed perturbations with $\bar{\sigma} \leq 1$, $\forall\omega$, if and only if*

$$\mu(M(j\omega)) < 1, \quad \forall\omega \tag{2.32}$$

The complete proof of this theorem can be found in [101].

Equation.2.32 can be rewritten as:

$$RS \quad \Leftrightarrow \quad \mu(M(j\omega))\bar{\sigma}(\Delta(j\omega)) < 1, \quad \forall\omega \tag{2.33}$$

By interpreting this with "small gain theorem", it is equivalent to saying that as long as the loop gain is smaller than 1, the perturbed feedback system is stable.

2.4.4. *Robust performance*

The RP-requirement is the $\mathcal{H}_\infty$ norm of the transfer function

$$F = F_u(N, \Delta) = N_{22} + N_{21}\Delta(I - N_{11}\Delta)^{-1}N_{12} \tag{2.34}$$

remains less than 1 for all allowed perturbations. It can be tested exactly by computing $\mu(N)$ as stated in the following theorem.

THEOREM 2.9. *[101]* ***Robust performance.*** *Rearrange the uncertain system in to the $N\Delta$-structure. Assume nominal stability that N is (internally) stable. Then we have*

$$RP \quad \overset{def}{\Longleftrightarrow} \quad \|F\|_\infty = \|F_u(N, \Delta)\|_\infty < 1, \quad \forall \|\Delta\|_\infty \leq 1 \tag{2.35}$$

$$\Leftrightarrow \quad \mu_{\hat{\Delta}}(N(j\omega)) < 1, \quad \forall\omega \tag{2.36}$$

where μ is computed with respect to the structure

$$\hat{\Delta} = \begin{bmatrix} \Delta & 0 \\ 0 & \Delta_p \end{bmatrix} \tag{2.37}$$

and Δ_p is a full complex perturbation with the same dimensions as F^T.

Again, the complete proof of this theorem can be found in [101].

2.4.5. *Design of Robust Controller*

μ-synthesis controllers are designed so as to deliver both robust stability and robust performance. It can be considered as an extension of H_∞ to the case with uncertainty Δ.

Of course μ-synthesis sacrifices some nominal performance (as compared to optimal control methods like H_∞) but provides robustness to model uncertainties.

2.4.5.1. *DK-Iteration*

The issue of finding a controller that minimizes a given μ condition is known as the μ-synthesis problem. In practice, there is no direct method to synthesize a μ-optimal controller. A method known as 'DK-iteration' can be used for solving problems with complex perturbations. The method combines H_∞ synthesis and μ-analysis. Practical experience shows that this method works well in most cases. Here D is known as the block-diagonal scaling matrix,

$$D = diag\{d_i I_i\} \tag{2.38}$$

where d_i is a scalar and I_i is an identity matrix which has the same dimension as the i'th perturbation block, Δ_i. $D \in \mathcal{D}$, where $\mathcal{D}$ is the set of block-diagonal matrices whose structure is compatible to that of Δ, i.e. $\Delta D = D\Delta$.

The DK-iteration method iterates between μ upper bound analysis and H_∞ optimal control design synthesis. These iterations approximate μ-synthesis. The upper bound on μ in terms of the scaled singular value is:

$$\mu(N) \leq \inf_{D\in\mathcal{D}} \bar{\sigma}(DND^{-1}) \tag{2.39}$$

We would like to find the controller that minimizes the peak value over frequency of this upper bound, which is:

$$\min_K(\min_{D\in\mathcal{D}}\|DN(K)D^{-1}\|_\infty) \tag{2.40}$$

The DK-iteration alternates between minimizing $\|DN(K)D^{-1}\|_\infty$ with respect to either K or D. Identity matrix is often used as initial guess for stable rotational transfer matrix $D(s)$. The DK-iteration works as follows [101]:

(1) K-step. Synthesis an H_∞ controller for the scaled problem, $\min_K \|DN(K)D^{-1}\|_\infty$ with fixed $D(s)$.

(2) D-Step. Find $D(j\omega)$ to minimize at each frequency $\bar{\sigma}(DND^{-1}(j\omega))$ with fixed N.

(3) Fit the magnitude of each element of $D(j\omega)$ to a stable and minimum-phase transfer function $D(s)$ and go back to step (1).

In this dissertation, the DK-iteration method is adopted for finding the robust controllers in the microgrid system. These controllers are used for controlling natural gas engine, storage system and both of them at the same time.

2.4.6. *Summary of μ-conditions for NP, RS and RP*

In this section, μ-conditions for NP, RS and RP are summarized as follow.

$$NS \quad \Leftrightarrow \quad \text{N (internally) stable} \tag{2.41}$$

$$NP \quad \Leftrightarrow \quad \bar{\sigma}(N_{22}) = \mu_{\Delta_{N_{22}}} < 1, \forall\omega, \text{and NS} \tag{2.42}$$

$$RS \quad \Leftrightarrow \quad \mu_\Delta(N_{11}) < 1, \forall\omega, \text{and NS} \tag{2.43}$$

$$RP \quad \Leftrightarrow \quad \mu_{\hat{\Delta}}(N) < 1, \forall\omega, \hat{\Delta} = \begin{bmatrix} \Delta & 0 \\ 0 & \Delta_p \end{bmatrix}, \text{and NS} \tag{2.44}$$

2.5. Conclusion

H_2, H_∞ and μ-synthesis controllers are all designed based on optimal/robust control theory. Among them, only μ-synthesis control is specifically designed to cope with system uncertainties. Note that this robust control approach yields a powerful tool for synthesizing multivariable controllers with high levels of robustness (to uncertainty) and performance (tracking, disturbance and noise rejection) [102]. The uncertainties considered in this robust control approach are described via norms bounds [103], but these mathematical descriptions can be related back to classical measures (e.g., gain and phase margins) [101, 100].

By reviewing the mathematical tools that are used in this dissertation, one should have some fundamental understanding of robust control. The reviewed robust control theory has been well implemented in software packages. In our research, the controller design processes are implemented by using available software, such as: Matlab$^{\text{TM}}$ Robust Control Toolbox$^{\text{TM}}$ and Simulink$^{\text{TM}}$.

CHAPTER 3

OPTIMAL LOAD DISPATCH

3.1. Introduction

In this chapter, we address the problem of how to dispatch load to generation units within a microgrid for fuel usage minimization, based on a known load profile.

Let us start by using an illustrative problem, namely the United States Marine Corps (USMC) applications. The USMC utilizes generators covering a broad range, from: 2 kW to over 200 kW. These generation units can have very different fuel consumption curves. The highest efficiency normally occurs when the generators are loaded at near rated capacity, with larger generators typically being more efficient than smaller units. Considering fuel consumption as the primary cost, each generation unit has a different cost function.

Properly designed and equipped microgirds with economic load dispatch can minimize the fuel consumption and improve power stability. There are several existing methods for dispatching load to generators, which are currently implemented in commercial systems, including: All Uniformly Dispatch (AUD), Descend Uniformly Dispatch (DUD) and Maximum Load Uniformly Dispatch (MLUD). These existing approaches, which are explained in the beginning of section 3.7, are easily applied and widely used [104][105], but they have not been shown to be optimal. Note that the load dispatch planning problem has also been tackled by linear, quadratic programming and differential evolution based tools [106] [107], which have been deployed for small and/or isolated power systems.

Note further that little work has been done on dispatching small generation units, or for the case where a broad range of generation units is present in one dispatch stack. In this case a more sophisticated dispatch approach is required. Certain configurations of the nascent "smart grid" present similar scenarios, as do island power implementations. In all such cases, it is necessary to dispatch the generation units in an economical way, whilst maintaining grid stability and reliability [108].

In this chapter, a classic two-tier power generation configuration is assumed. The studies are done separately for idling and shut-off cases. For the unconstrained problem, since no extra constraint is applied, the global optimum dispatch solution is deployed for dispatching the load to generators. For the constrained optimization dispatch problem, one generation unit is reserved as the "swing machine" to maintain system frequency (and voltage) stability by servicing fast load transients. The Karush-Kuhn-Tucker (KKT) conditions are then used to optimally dispatch the remaining load to the remaining generation units, so as to minimize fuel consumption. These generators are termed "base load" units [109]. The generation units that supply the base load may be restricted by upper and lower operating limits for reliability considerations, and to extend their life. "Overloading" for a generation unit means overheating due to high current, which can cause generator electrical and mechanical failures. Finally, spinning reserve is required, so as to be able to cope with unanticipated rapid load variations [110].

For the constrained optimum generator dispatch problem, load limits and spinning reserve are considered as extra constraints on the KKT conditions. This is distinct from constraints that are inherent to the KKT conditions themselves, which are denoted here as internal constraints. By applying the KKT conditions, all feasible solutions are found. The

optimum solution, or suboptimum solution which does not violate any of the internal or extra constraints, is utilized to dispatch the load. As a contrast, the unconstrained problem uses the true optimum solution to dispatch the load, where only the internal constraints are taken into consideration.

From world circumstances, the start-up and cooling down costs are also considered. For a general dispatching problem, the load is varying, and each generator has its own fuel consumption curve and impacts from the extra constraints, so it is inescapable to start-up and shut-off generators. For an internal combustion engine generator to provide power to a "microgrid", it needs to start-up and synchronize first. This process is managed by automatic control devices nowadays [111]. During this period, it consumes fuel but does not provide power to the grid. Once a generator is disconnected from a grid, internal combustion engine continuously consumes fuel for cooling down itself. By adding the start-up and cooling down costs to the cost function, the decision making of the generators dispatch problem can be influenced.

Following the introduction in section 3.1, the rest of the chapter is organized as follows. In section 3.2, the general load dispatch problem is setup, and the KKT conditions are briefly reviewed. The general KKT conditions of a generator dispatch problem are established in section 3.3. In section 3.4, the KKT conditions based algorithm for solving unconstrained problem is developed. The constrained optimization dispatch problem is introduced and resolved in section 3.5. In section 3.6, the start up and cooling down costs are considered. Based on the algorithms and methodologies developed in previous sections, several simulation tools are developed in Matlab$^{\text{TM}}$, and some examples with simulation results are presented and discussed in section 3.7 individually for the unconstrained problem, constrained problem

and constrained problem with start-up and cooling down costs, along with comparisons to existing methods. Finally, some concluding remarks are presented in section 3.8.

3.2. Problem Setup and Review of Karush-Kuhn-Tucker Conditions

In this section, the problem is set up. We wish to find an optimal approach, in the sense of minimizing fuel consumption, for dispatching generation units. This is an extremum problem with equality and inequality constraints, and hence the KKT optimality conditions are briefly presented as well.

3.2.1. *Generator Dispatch Problem Setup*

Suppose there are n generators ($i = 1, 2, 3, \ldots, n$), with each generation unit having its own input-output characteristic curve. Further suppose this curve can be expressed by a quadratic function [106] as:

$$\Phi_i = \alpha_2^i \beta_i^2 + \alpha_1^i \beta_i + \alpha_0^i \tag{3.1}$$

where α_2^i, α_1^i, and α_0^i are given parameters of the generation unit (typically obtained via identification experiments or manufacturer specifications). A typical 60 kW gas generator unit input-output characteristic curve as shown in Fig. 3.1. Note it is very well approximated by a quadratic function.

Let P_i be the output power of generation unit i, ranging from a minimum P_{min}^i to a maximum P_{max}^i [108]. We define β_i as: $\beta_i = P_i / P_{max}^i$ (i.e., output power as a fraction of maximum rated power). Suppose F_i is the fuel consumption of generation unit i (whilst producing corresponding output power P_i), and it varies from a minimum F_{min}^i to a maximum F_{max}^i. We define Φ_i as: $\Phi_i = F_i / F_{max}^i$ (i.e., fuel usage as a fraction of maximum fuel usage). Note of course that P_i and F_i are both physical quantities, which only assume non-negative

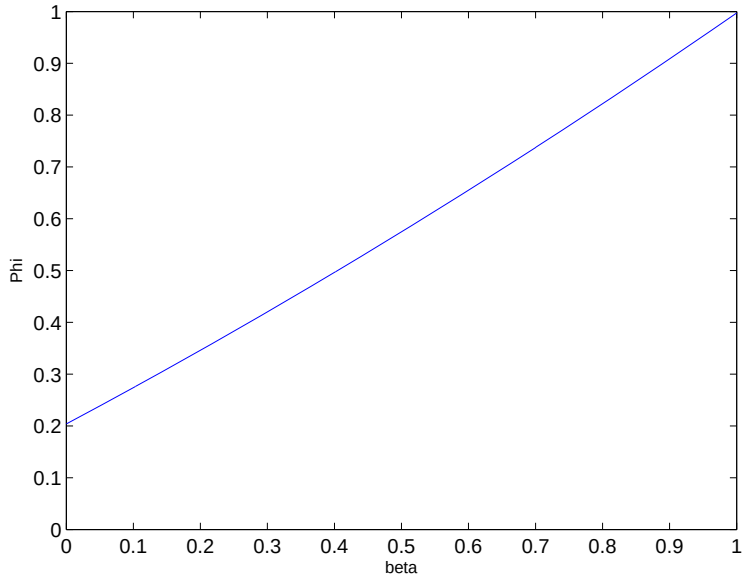

FIGURE 3.1. A typical generation unit input-output characteristic curve

values. Note further that β_i varies between 0 and 1 (i.e., zero power to maximum power), but when the generation unit is idling at zero output power, it still consumes some fuel. Hence, Φ_i varies from a small offset α_0^i to its upper limit of 1 (i.e., idling to maximum fuel usage). With these definitions, the total output power can be expressed as: $\sum_{i=1}^{n} P_{max}^i \beta_i$ and the total fuel consumption can be expressed as: $\sum_{i=1}^{n} F_{max}^i \Phi_i$. If storage of electrical energy is not considered, the generators' total output power always equals the total power demand, with power produced at essentially the same time as it is consumed [112]. In this case, the demanded power P_T, and the total fuel consumption F_T, of n generation units are given respectively as follows:

$$P_T = \sum_{i=1}^{n} P_{max}^i \beta_i \tag{3.2}$$

$$F_T = \sum_{i=1}^{n} F_{max}^i \Phi_i \tag{3.3}$$

The economic generator dispatch problem is to minimize the fuel usage, while at the same time ensuring the total generator output power meets the total power demand. In addition, the generators are operated within their upper and lower limits. This problem can now be formulated as [113]:

$$\begin{aligned} \text{minimize} \quad & F_T = \sum_{i=1}^{n} F_{max}^i \Phi_i \\ \text{subject to} \quad & P_T = \sum_{i=1}^{n} P_{max}^i \beta_i \\ & 0 \leq \beta_i \leq 1 \end{aligned}$$

Observing that the above inequality constraint $0 \leq \beta_i \leq 1$ is trivially equivalent to $-\beta_i \leq 0$ and $\beta_i - 1 \leq 0$, the optimization problem can be reposed as a set of equality/inequality constraints. This kind of extremum problem can be solved by utilizing the KKT optimality conditions. It is important to note that the equality/inequality constraints on β_i indicated here are the extreme upper and lower limits of operation. For the unconstrained problem, these upper and lower limits are utilized on the base load generators. However, for the constrained problem (and in practice), base load generation units would typically be constrained to tighter limits to enhance reliability and unit life. This kind of extremum problem can be solved by utilizing the KKT optimality conditions, and hence before proceeding further we briefly review the general KKT optimality conditions.

3.2.2. *Karush-Kuhn-Tucker Optimality Conditions*

Considering the following optimization problem:

$$\begin{aligned} \text{minimize} \quad & f(\boldsymbol{x}) \\ \text{subject to} \quad & \boldsymbol{h}(\boldsymbol{x}) = \boldsymbol{0} \end{aligned}$$

$$\boldsymbol{g}(\boldsymbol{x}) \leq \mathbf{0}$$

where $\boldsymbol{h}$: $\mathbb{R}^n \rightarrow \mathbb{R}^m$ and $\boldsymbol{g} : \mathbb{R}^n \rightarrow \mathbb{R}^p$ [114]. The five parts of the KKT conditions can be written as:

(1) $\boldsymbol{\mu}^* \geq \mathbf{0}$.

(2) $Df(\boldsymbol{x}^*)+\boldsymbol{\lambda}^{*T} D\boldsymbol{h}(\boldsymbol{x}^*)+\boldsymbol{\mu}^{*T} D\boldsymbol{g}(\boldsymbol{x}^*) =\mathbf{0}^T$.

(3) $\boldsymbol{\mu}^{*T}\ \boldsymbol{g}(\boldsymbol{x}^*) = 0$.

(4) $\boldsymbol{h}(\boldsymbol{x}^*) = \mathbf{0}$.

(5) $\boldsymbol{g}(\boldsymbol{x}^*) \leq \mathbf{0}$.

where $\boldsymbol{x}^*$ is the feasible solution, and also a local minimum. $\boldsymbol{\lambda}^* \in \mathbb{R}^m$ is regarded as the Lagrange multiplier vector, and $\boldsymbol{\mu}^* \in \mathbb{R}^p$ is taken as the Karush-Kuhn-Tucker (KKT) multiplier vector. Their components are referred to as the Lagrange multipliers and Karush-Kuhn-Tucker (KKT) multipliers, respectively. Df is defined as: $Df \equiv \left[\frac{\partial f}{\partial x_1}, \frac{\partial f}{\partial x_2}, \ldots, \frac{\partial f}{\partial x_n}\right]$, with $D\boldsymbol{h}$ and $D\boldsymbol{g}$ defined similarly [114].

To have the problem formulated in a general manner, the base load generation unit's extreme limits 1 and 0 are replaced by general upper and lower limits, denoted as: U_i and L_i, respectively; where $i = 1, 2, 3, \ldots, n$ and $0 \leq L_i < U_i \leq 1$. $L_i \leq \beta_i \leq U_i$ is simply equivalent to $-\beta_i + L_i \leq 0$ and $\beta_i - U_i \leq 0$. Accordingly, the original optimal generators dispatch problem in subsection 3.2.2 is mapped into the following problem, in a form suitable for applying the KKT conditions.

$$\begin{aligned} \text{minimize} \quad & f(\beta_i) = F_T = \sum_{i=1}^{n} F_{max}^i \Phi_i \\ \text{subject to} \quad & \boldsymbol{h}(\beta_i) = \sum_{i=1}^{n} P_{max}^i \beta_i - P_T = \mathbf{0} \end{aligned}$$

$$\boldsymbol{g}(\beta_i) = \begin{cases} -\beta_1 + L_1 & \leq 0 \\ \beta_1 - U_1 & \leq 0 \\ \vdots & \\ -\beta_n + L_n & \leq 0 \\ \beta_n - U_n & \leq 0 \end{cases}$$

To this point we have set up the general generator dispatch problem. This unconstrained pure KKT optimization problem is further developed in section 3.3 and solved in section 3.4 (see also [98] for details). The constrained problem (applying extra constraints) is then solved in section 3.5 and startup and cooling down costs are added in section 3.6.

3.3. Karush-Kuhn-Tucker Conditions for Dispatch

In the general case, we assume that n generation units are interconnected to serve the load. Then the KKT conditions are given as:

(1) $\boldsymbol{\mu} = [\mu_1^1 \quad \mu_2^1 \quad \mu_1^2 \quad \mu_2^2 \quad \dots \quad \mu_1^n \quad \mu_2^n]^T \geq \mathbf{0}$

(2) $F_{max}^1(2\alpha_2^1\beta_1 + \alpha_1^1) + \lambda P_{max}^1 - \mu_1^1 + \mu_2^1 = 0$

$F_{max}^2(2\alpha_2^2\beta_2 + \alpha_1^2) + \lambda P_{max}^2 - \mu_1^2 + \mu_2^2 = 0$

$\vdots$

$F_{max}^n(2\alpha_2^n\beta_n + \alpha_1^n) + \lambda P_{max}^n - \mu_1^n + \mu_2^n = 0$

(3) $\mu_1^1(-\beta_1 + L_1) + \mu_2^1(\beta_1 - U_1) + \mu_1^2(-\beta_2 + L_2) + \mu_2^2(\beta_2 - U_2) + \dots + \mu_1^n(-\beta_n + L_n) +$

$\mu_2^n(\beta_n - U_n) = 0$

(4) $h(\beta_i) = \sum_{i=1}^{n} P_{max}^i \beta_n - P_T = 0$

$$(5)\ \boldsymbol{g}(\beta_i) = \begin{bmatrix} -\beta_1 + L_1 \\ \beta_1 - U_1 \\ -\beta_2 + L_2 \\ \beta_2 - U_2 \\ \vdots \\ -\beta_n + L_n \\ \beta_n - U_n \end{bmatrix} \leq \mathbf{0}$$

where the superscript i in μ_j^i denotes (that it is a KKT multiplier for) generation unit i. Note that each generation unit has two KKT multipliers, μ_1^i and μ_2^i, which correspond to the lower and upper limits of each β_i. Note two states may exist when a generator is producing no power: The generator may be 'idling' or 'shut-off'. In the idling case, as discussed earlier, even generation units producing no power still consume fuel to remain idling (Note that $\Phi_i \neq 0$ for $\beta_i = 0$). In the shut-off case, it is assumed that generators not contributing to the load are turned off and hence do not consume any fuel. Note further that this involves a modified (KKT) solution, since the generator input-output curve is essentially discontinuous at $\beta_i = 0$. Hence, the 'idling' and 'shut-off' cases are considered separately for each problem.

3.4. Karush-Kuhn-Tucker Based Solutions

For the unconstrained generator dispatch problem, the KKT conditions presented in the previous section are utilized directly to find the problem solution. Note that when the KKT conditions are deployed to solve the unconstrained shut-off case, KKT condition 1) is not enforced because the effective generator input-output curve is discontinuous at $\beta_i = 0$. Otherwise, the 'idling' and 'shut-off' cases utilize the KKT conditions identically. Furthermore, since no extra constraints are considered, only the (inherent) internal KKT

condition constraints are applied, and in particular the upper and lower operating point limits of all generators are 1 and 0, respectively. Hence, replacing all U_i with 1 and L_i with 0 in the KKT conditions, condition 3) is now equivalent to:

$$\begin{aligned} -\mu_1^1\beta_1 + \mu_2^1(\beta_1 - 1) - \mu_1^2\beta_2 + \mu_2^2(\beta_2 - 1) + \ldots \\ -\mu_1^n\beta_n + \mu_2^n(\beta_n - 1) = 0 \end{aligned} \tag{3.4}$$

Note from condition 1), all μ_j^i's are nonnegative, and from condition 5), all elements of $g(\beta_i)$ are nonpositive. Equation (4) implies that all elements of $h(\beta_i)$ equal 0. Taking this into account, and for ease of presentation considering only the first generation unit, the first two terms of equation (4) are:

$$-\mu_1^1\beta_1 = 0 \tag{3.5}$$

and

$$\mu_2^1(\beta_1 - 1) = 0 \tag{3.6}$$

There are three possibilities for β_i, namely $\beta_i = 0$, $\beta_i = 1$, and $0 < \beta_i < 1$. Note that when $\beta_1 = 0$, from equation (6) immediately it can be observed that $\mu_2^1 = 0$, so that theonly unknown is μ_1^1; When $\beta_1 = 1$, from equation (5), it is easy to see that $\mu_1^1 = 0$, and μ_2^1 is the only unknown. Similarly, when $0 < \beta_1 < 1$, from equation (5), it can be seen that $\mu_1^1 = 0$, and from equation (6) it follows that $\mu_2^1 = 0$, so that β_1 is the only unknown.

These three situations cover all the possible combinations. Notice that among the variables β_1, μ_1^1, and μ_2^1, two variables are always known, leaving us with only one unknown variable. The other generation units may be solved by the same approach. For the entire system, there is one more unknown, the Lagrange multiplier λ associated with the equality constraint in condition 2). It has been ignored in the discussion till now, since it does not

$$\boldsymbol{A} = \begin{bmatrix} 2F^1_{max}\alpha^1_2 & 0 & \cdots & 0 & P^1_{max} & -1 & 1 & 0 & 0 & \cdots & 0 & 0 \\ 0 & 2F^2_{max}\alpha^2_2 & \cdots & 0 & P^2_{max} & 0 & 0 & -1 & 1 & \cdots & 0 & 0 \\ \vdots & \vdots & \ddots & \vdots & \vdots & \vdots & & & & \ddots & & \vdots \\ 0 & 0 & \cdots & 2F^n_{max}\alpha^n_2 & P^n_{max} & 0 & 0 & 0 & 0 & \cdots & -1 & 1 \\ P^1_{max} & P^2_{max} & \cdots & P^n_{max} & 0 & 0 & 0 & 0 & 0 & \cdots & 0 & 0 \end{bmatrix}$$

appear in condition 3). Thus, for n generation units interconnected as a system, there are 3^n possible combinations, and for each combination we always have $2n$ variables known, with $n+1$ variables unknown, to be solved for from the resulting $n+1$ remaining equations [104].

Referring to the five components of the KKT conditions, note that conditions 1), 3), and 5) are constraints, with conditions 2) and 4) used to compute the unknown variables. By putting conditions 2) and 4) into matrix form, equation 3.7 is obtained as:

$$\boldsymbol{Ax} = \boldsymbol{b} \tag{3.7}$$

where $\boldsymbol{A} \in \mathbb{R}^{(n+1)\times(3n+1)}$, $\boldsymbol{x} \in \mathbb{R}^{3n+1}$ and $\boldsymbol{b} \in \mathbb{R}^{n+1}$

$$\boldsymbol{x} = \begin{bmatrix} \beta_1 & \beta_2 & \cdots & \beta_n & \lambda & \mu^1_1 & \mu^1_2 & \cdots & \mu^n_1 & \mu^n_2 \end{bmatrix}^T$$

$$\boldsymbol{b} = \begin{bmatrix} -F^1_{max}\alpha^1_1 & -F^2_{max}\alpha^2_1 & \cdots & -F^n_{max}\alpha^n_1 & P_T \end{bmatrix}^T$$

Note that of the $3n+1$ elements in x, only $n+1$ of them are unknown. In order to find all potential solutions, the 3^n possible combinations need to be solved via:

$$\boldsymbol{x_{ukn}} = \boldsymbol{A_{ukn}}^{-1}\boldsymbol{b} \tag{3.8}$$

where $\boldsymbol{x_{ukn}} \in \mathbb{R}^{n+1}$ represents the unknown elements in $\boldsymbol{x}$. $\boldsymbol{A_{ukn}} \in \mathbb{R}^{(n+1)\times(n+1)}$ only consists of the column elements of $\boldsymbol{A}$ that correspond to unknown (row) elements in $\boldsymbol{x}$. Equation

(8) computes all the unknown variables. By substituting the solution in $\boldsymbol{x_{ukn}}$ back into $\boldsymbol{x}$, all the elements of $\boldsymbol{x}$ are now known. Thus, by using the objective function $f(\beta_i)$, the fuel consumptions of all the potential solutions may be computed. The minimum fuel consumption is now readily found, and the corresponding β_i's constitute the (global) optimal generator dispatch solution.

Note that the solution of $\boldsymbol{x}$ is valid for both 'idling' and 'shut-off' cases. However, when the fuel consumption at β_i equals to 0 is calculated, because of the offset Φ_i in the fuel consumption curve of 'idling' case, the cost function for 'idling' and 'shut-off' cases are slightly different. The difference of the two cost functions can impact the decision making of how the generators are dispatched (i.e., change which of the feasible solutions is the optimal one).

3.5. Real World Constraints of Generators

In this section, the constrained KKT-optimality based generators dispatch approach is developed, by adding constraints to the general generators optimal dispatch problem in section 3.2. There are three types of extra constraints that must be considered, namely: reservation of generation swing capacity, limitation of base load generation units to operate within specified upper and lower limits, and reservation of spinning reserve capacity. Note that now the difference between the 'idling' and 'shut-off' cases impacts the lower operating points of base load generation units and the decision of how the spinning reserve is maintained.

Swing generation units are normally configured with high governor gain, and are reserved to respond to fast load transients, in either direction. Typically, these generators are set to operate around a "preferred operating point" (POP), commonly at 50% of the generator

rated output power. This is straightforward to account for in the optimization problem, namely the total output power of the swing generators at their POP is first subtracted from total power demand P_T. Then, the KKT conditions with tighter upper and lower limits are derived. Finally, the spinning reserve is checked at the end of the computation stage. In the shut-off case, the algorithm manipulates the base load generation units' status (on, off or idling) to meet the spinning reserve requirement.

3.5.1. *The Swing Capacity*

For the general case, suppose there are n generation units interconnected to serve the total load demand P_T. Among them, m generators (where $m < n$) serve the base load. The remaining $n-m$ generators are used as the swing generation units with their POP set to β_l, where $l = m+1, m+2, \ldots, n$. Typically, a single unit is allocated to swing operation, but for the purposes of this chapter, the more general formulation will be retained. Since the operating points of the swing generators are pre-set, the total swing generation units output power P_{T_s} at their pre-set operating points can be expressed as:

$$P_{T_s} = \sum_{l=m+1}^{n} P_{max}^{l} \beta_l \tag{3.9}$$

Let P_{T_b} denote the base load that needs to be supplied by the m base load generators, then we have $P_{T_b} = P_T - P_{T_s}$. The load P_{T_b} is dispatched using the KKT-based method.

3.5.2. *Operating Limits*

In this section the KKT optimality conditions for dispatching the demanded power P_{T_b} to the m base load generators is considered. Note that for the constrained problem, the KKT conditions for the idling and shut-off cases are slightly different. For the idling case, the upper

and lower operating point limits can be defined freely between 0 and 1. For the shut-off case, however, the lower limit is pre-set at 0 to allow the generators to be completely shut-off. With these modifications it is straightforward to extend the KKT conditions developed in section 3.3 to the more general case allowing any upper/lower operating limits and we leave the details to the interested reader, or see [115].

3.5.3. *Spinning Reserve*

Spinning reserve is defined as the unused capacity which can be called on by the system operator, and which is provided by devices that are already running and synchronized to the grid and ready to deliver power [116]. In this chapter the spinning reserve is denoted as P_{sp}. Spinning reserve is used to supply incremental load when there is insufficient time to start another generator from a shutoff condition [117]. The planning load is defined as the summation of hourly load and spinning reserve. The rated power summation of the running and idling generators must be greater than or equal to the planning load to keep the system functioning properly. In other words, the spinning reserve is the difference between the spinning generation units' total capacity and the hourly load. For the idling case, since no generation units can be turned off, this is trivially satisfied provided the total capacity of all generators is greater than or equal to the planning load. For the shut-off case, in order to meet the planning load, some generation units may be required to serve the load or to idle. These decisions are made by the algorithm based on fuel consumption. Thus, the planning load in the shut-off case equals the rated power summation of both idling (zero power) and running (serving load) generation units.

Overall, any potential solution that violates an internal or extra constraint is eliminated. Among potential solutions which meet all constraints, the optimal solution is selected based

on the objective function $f(\beta_i)$, i.e., minimum fuel consumption. In the next section we start from the constrained problem presented here and add start-up and cooling down costs, to formulate the problem in a more realistic manner for real-time operation.

3.6. Startup and Cooling Down Costs

In practice, as generators may be started or shut down throughout some running period (rpd), it is important to include the generator start-up and cooling-down costs in the overall optimization problem. Since the idling case always keeps all of the generators running, only the shut-off case is considered here.

As a simple example, suppose five generators, labelled G_1 through G_5, are used to supply loads. During one particular time interval t_1, the load demand is L_1, and we use G_1, G_2 and G_5 to supply the load. Within the next time interval t_2, the load is L_2, and our algorithm deploys G_2 and G_3 to furnish that load. As is shown in Table 3.1, a cooling-down cost is incurred when a generator changes status from on to off, and similarly, when a generator changes its status from off to on, there is a start-up cost involved. If a generator maintains its status, no start-up or cooling down costs are incurred. In Table 3.1, +s, +c and +0 denote the plus start-up cost, cooling-down cost and no-cost, respectively.

Note that in order to start up a new generator and connect it to the microgrid a process of synchronization is needed (sometimes also referred to as paralleling the generator to the

TABLE 3.1. Generator star-up and cooling down map

	Generators Status				
Generator	$G1$	$G2$	$G3$	$G4$	$G5$
t_1	on	on	off	off	on
costs	$\downarrow +c$	$\downarrow +0$	$\downarrow +s$	$\downarrow +0$	$\downarrow +c$
t_2	off	on	on	off	off

microgrid). This synchronization process consists of matching voltage amplitude, frequency, and phase angle before connecting the generator to the grid. Once this match is accomplished, the generator connection to the bus is established by closing a circuit breaker [118], after which the generator can start to service load. Note that before a generator is synchronized it does not provide power to the grid, but consumes fuel, and hence the start-up costs.

Note also that when a generator is disconnected from the system, the engine is not turned off immediately but rather left on to allow itself and the generator to cool down. During this period it again consumes fuel without delivering electrical power and hence the cooling-down costs.

In this chapter, the start-up and cooling-down costs are measured by the amount of fuel that was used. In order to study how often the generators should be re-dispatched for minimizing the total costs the start-up and cooling-down costs need to be accounted for. To this end we introduce a new variable Δt, which specifies the time interval for how often the re-dispatch is implemented. The start-up cost and cooling-down costs of generators are different. Based on practical experience, we assume them (for our examples) to be equal to the fuel usage of keeping the generator idling for 1.5 and 5 minutes, respectively.

3.7. Results and Discussion

In this section we perform some detailed simulation studies of various dispatch approaches. Several existing standard dispatch approaches are used to compare with the KKT-based Optimal Dispatch (KOD) methods developed in this chapter. The KOD method is considered with extra constraints (KwC) and with no extra constraints (KnC). The existing approaches used for comparison include: All Uniformly Dispatch (AUD), Descend Uniformly

Dispatch (DUD) and Maximum Load Uniformly Dispatch (MLUD). These existing methods are briefly introduced in the following paragraphs. All approaches are deployed for 'idling' and 'shut-off' cases separately.

The AUD method specifies that all n generation units are running, and they are all loaded to the same power ratio, i.e., $\frac{P_T}{P_R}$, where P_T is the total power demand, and P_R is the total rated output power of the (running) generation units. This explains the term 'uniformly' dispatch. The other standard approaches described below pre-select a group of generators, and then uniformly dispatch from within that group.

In the DUD method, the available generation units are arranged in descending order, in the sense of their rated output power. For one particular time period, so long as the total output rated power of the first g ($g < n$) generation units is greater than or equal to the total power demand, only the first g generation units are running. The remaining $n-g$ generation units are either shut-off or idling. If spinning reserve is considered, the total power demand is equivalent to the planning load. After selecting generators, a power ratio is calculated using the running and idling units, as in the AUD case, and utilized to set the commanded load on all operating units. If the total power demand is greater than the total generation capability of the first $n-1$ generation units, all generation units need to be running. At this point, the DUD method utilizes the same power ratio as the AUD method.

The MLUD method first finds all possible combinations of the given n generation units, and computes the rated power of each combination P_C. If n generation units are used, there are $N_{comb} = \sum_{l=1}^{n} \frac{n!}{l!(n-l)!}$ combinations. Each combination has total rated power of $P_C^r = \sum_{s=1}^{t} P_{max}^s$, where $r = 1, 2, ..., N_{comb}$, and t is the number of generation units in the r^{th} combination. Then, the algorithm selects the particular combination P_C, which gives

the minimum non-negative value of $P_C - P_T$. Generation units which form the particular combination P_C are running, with the remaining generation units either idling or shut-off. Similarly, if all n generation units are utilized, it becomes the same as the AUD approach.

The KOD methods developed in this chapter first use the KKT conditions to find all feasible solutions. KnC then utilizes a pure KOD approach and simply picks out the optimum from all the feasible solutions. KwC deploys the KOD approach first, then eliminates any feasible solutions that violate any of the extra constraints. The optimum is selected from the remaining feasible solutions. Note that there may exist conditions where no optimum or suboptimum solution exists that does not violate one or more constraints (in which case the problem is ill posed).

Several simulation tools are developed in Matlab™ to compare the KKT-based dispatch methods to existing methods. This section is divided into three subsections which corresponds to the content in sections 3.4, 3.5 and 3.6.

3.7.1. *Unconstrained Problems*

Suppose there is a microgrid with three generation units. For the KKT-based dispatch method, the solution algorithm is implemented in Matlab™, with the corresponding flowchart shown in Fig. 3.2 for one iteration. In this section, the simulation results of the unconstrained KKT-based dispatch method and the above mentioned existing standard dispatch methods are compared.

In all simulations, the total demand power P_T sweeps from 1 kW to the total rated output power P_R. Five different generation units are used, and their parameters are shown in Table 3.2. Note the difference between the idling and shut-off cases as discussed in section 3.3,

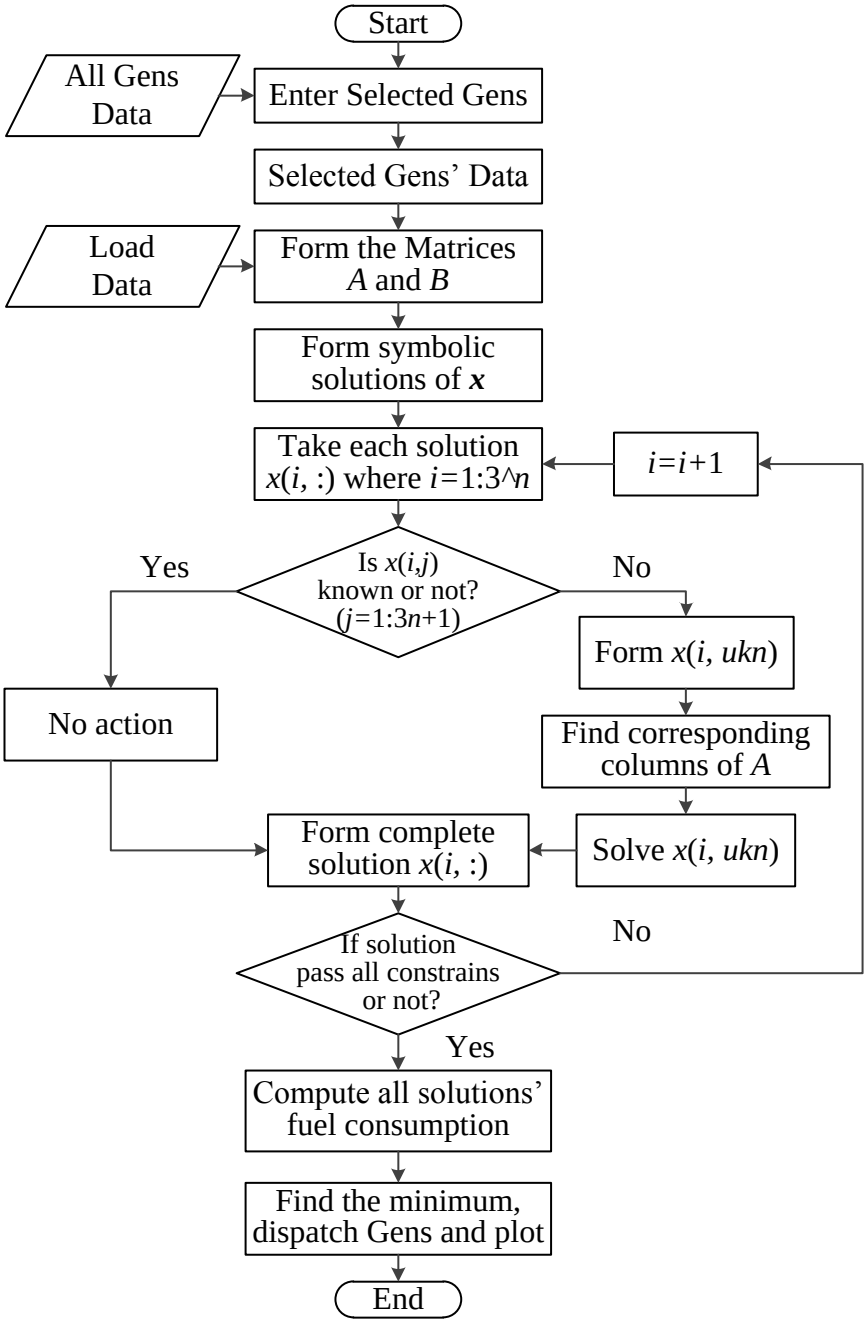

FIGURE 3.2. Flowchart of the Matlab^{TM} script file

namely in the idling case, generators consume fuel to remain idling (at zero power), but in the shut-off case, it is assumed that once a generator is turned off, it does not consume fuel.

TABLE 3.2. Generation Units Parameters

No.	P_{max} (kW)	α_2	α_1	α_0	F_{max} (gal/hr)
1	20	0.071428571	0.753571429	0.183928571	1.6
2	30	0.064285714	0.748214286	0.193035714	2.9
3	40	0.057142857	0.742857143	0.202142857	4.0
4	60	0.103512881	0.689929742	0.203881733	4.8
5	150	0.167758847	0.676277851	0.160419397	10.9

Although this difference does not impact solving for the unknown variables in the KKT-based approach, it does affect the cost functions, and hence the decision making of how the generators are dispatched. Hence, we consider the 'idling' and 'shut-off' cases separately.

Three different configurations are compared. We first consider generation units 1, 2, and 3, which represents a microgrid that consists of similar (but not the same) small rated output power generators. The second microgrid is constructed using three of the No. 4 generators, hence representing a microgrid with identical generators. The third microgrid consists of generators 1, 3, and 5, representing a microgrid containing very different generators. Simulation results for the shut-off case are shown in Figures 3.3, 3.4, 3.5, and 3.6, and for the idling case in Figures 3.7, 3.8, 3.9, and 3.10.

Fig. 3.3 illustrates the fuel consumption curves for each method tested on configuration 1 in the shut-off case. Clearly, it can be seen that the KKT-based approach consumes the least fuel. The AUD method, which keeps all generators on, consumes the most fuel. The DUD method initially has the 40 kW generator turned on. This is the one of the most inefficient generators at low loads. For the MLUD method, with total power demand between 30 kW and 40 kW, the 40 kW generator is turned on. By contrast, the KKT-based method combines more efficient 20kW and 30 kW generators to supply the load.

Fig. 3.4 shows how the generators are actually dispatched for the above test using the KKT-based method. At the beginning, the most efficient generator, namely 20 kW, is turned on. Once the total load demand exceeds 20 kW, the method turns off the 20 kW generator and starts the 30 kW generator, because it is more efficient than having two generators running. However, the combined 20 kW and 30 kW generators are more efficient than the 40 kW one. Hence, once the load exceeds 30 kW, the combined 20 kW and 30 kW generation units are used. When load exceeds 50 kW, the 20 kW and 40 kW generators are used, up to $P_T = 60$ kW, at which point all three generators are required serve the load.

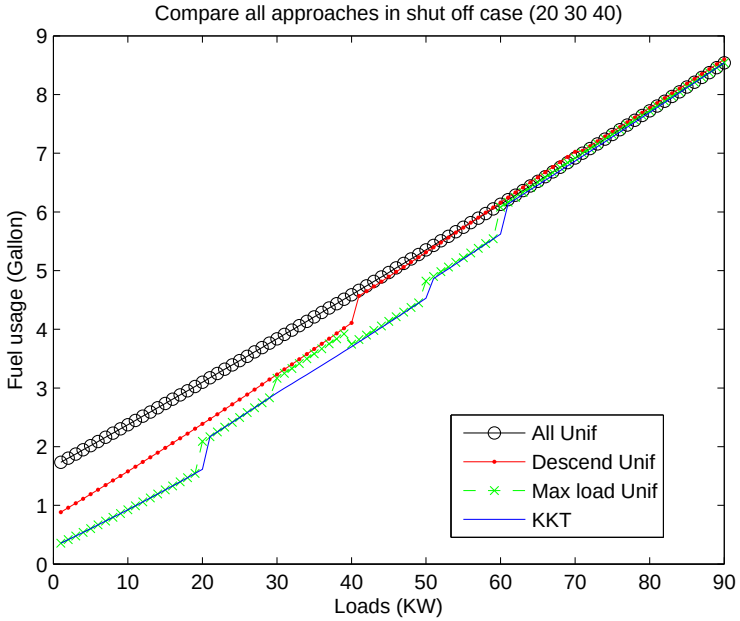

FIGURE 3.3. Fuel consumption of 1st configuration in shut-off case

Three identical generators form configuration 2, whose fuel consumption curves are shown Fig. 3.5. As one would expect, there is no preference in how to dispatch between them, so that the DUD method, MLUD method, and KKT-based method all consume the same amount of fuel, indicating that uniform dispatch is the optimal solution for this case. Note,

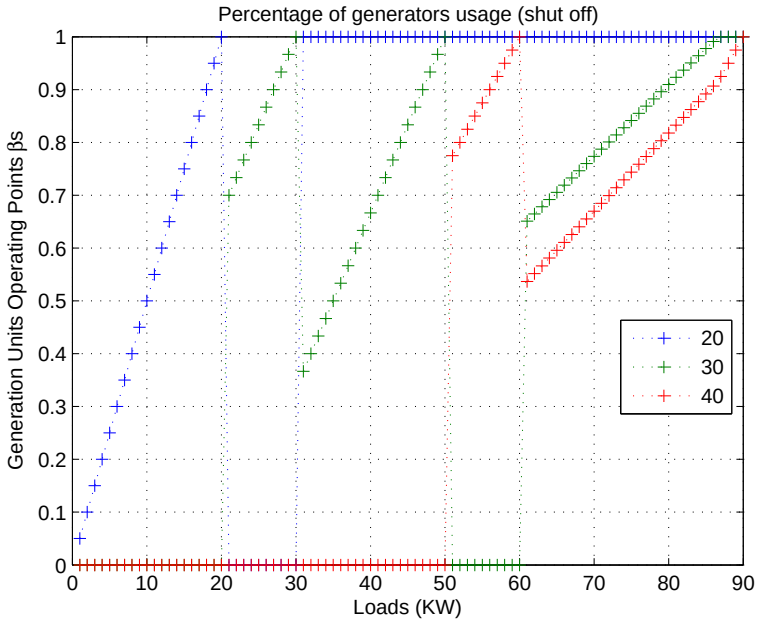

FIGURE 3.4. 1st configuration generators dispatch in shut-off case

however, that the above approaches utilize a sub-group of generators (big enough to serve the load). The AUD method has all generators running all the time, and so it consumes more fuel than the other methods.

In the shut-off case, when there are huge differences between the generators in the system, the AUD and DUD methods perform poorly. This is because both of these methods always have the biggest generators on, but big generators are inefficient when the load is too low. The MLUD method is considerably more efficient, since it is more flexible compared to the previous two methods. However, note that the objective function is to min $P_C - P_T$, subject to: $P_C - P_T \geq 0$, which is not directly minimizing fuel consumption. Hence, it is still slightly out-performed by the KKT-based method, which finds the true optimal dispatch for least fuel consumption, as can be seen in Fig. 3.6, which shows the fuel consumption curves for configuration 3.

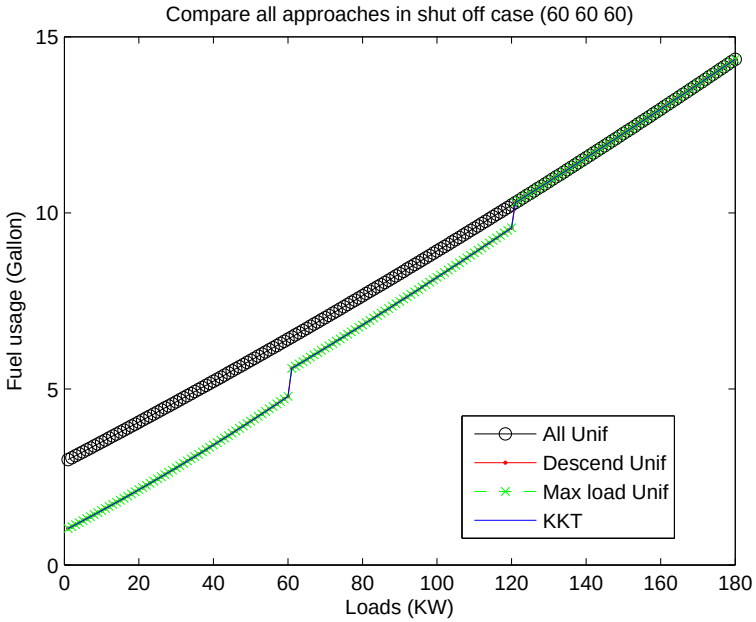

FIGURE 3.5. Fuel consumption of 2nd configuration in shut-off case

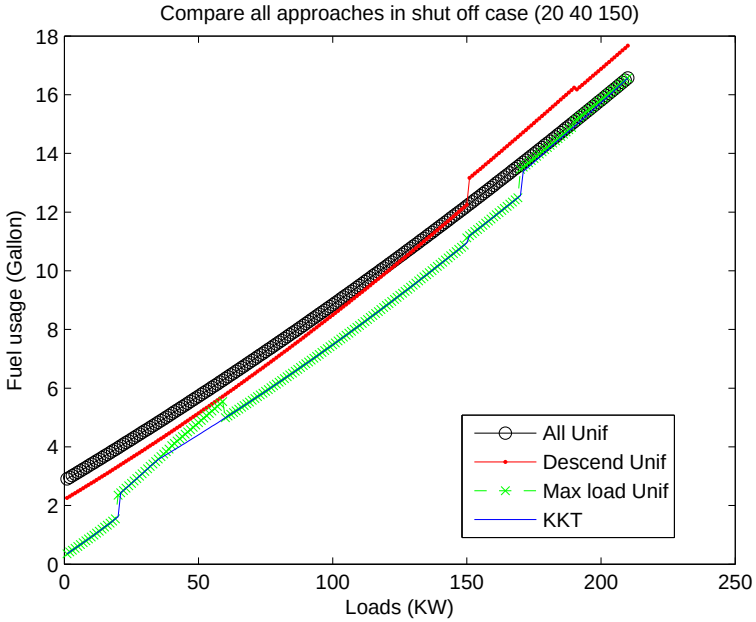

FIGURE 3.6. Fuel consumption of 3rd configuration in shut-off case

We now consider the idling case, and the fuel consumption curves for the 1st configuration are shown in Fig. 3.7. Although the KKT-based method still consumes least fuel, its superiority over the other approaches is now less apparent. In the idling case all the generators are on all the time for all the methods. Hence, the space of fuel performance curves is compressed, with small differences between the approaches.

Fig. 3.8 shows how the KKT-based method dispatches the generation units for the above test. Note that this is much smoother than the dispatch schedule shown earlier in Fig. 3.4 for the shut-off case, because there is no longer any advantage to switching machines in and out. There are some similarities between Fig. 3.4 and Fig. 3.8, since we can see that both of them utilize the 20 kW generator first. However, note that in Fig. 3.8, once the load exceeds 25 kW, all three generators supply the load (versus the shut-off case in Fig. 3.4). This happens since all the generators are idling anyway, so it is better to have them contribute to the load, rather than just idling and wasting fuel.

For the second configuration, shown in Fig. 3.9, there is little difference between the approaches. In fact the AUD and KKT-based methods consume identical amounts of fuel, as do the DUD and MLUD methods. This makes perfect sense, since all the generators are identical, and all are kept idling, there is little room for optimal dispatch to make a big difference.

The third system is operated in the idling case to generate the curves in Fig. 3.10. It can be seen that the KKT-based method shows great advantages over the MLUD and DUD methods. The reasons are similar to the earlier discussion regarding Fig. 3.6, where uneconomical generators are turned on at low load. Conversely, the AUD method shows more economical behavior, and is largely similar to the KKT-based method, but is less efficient for

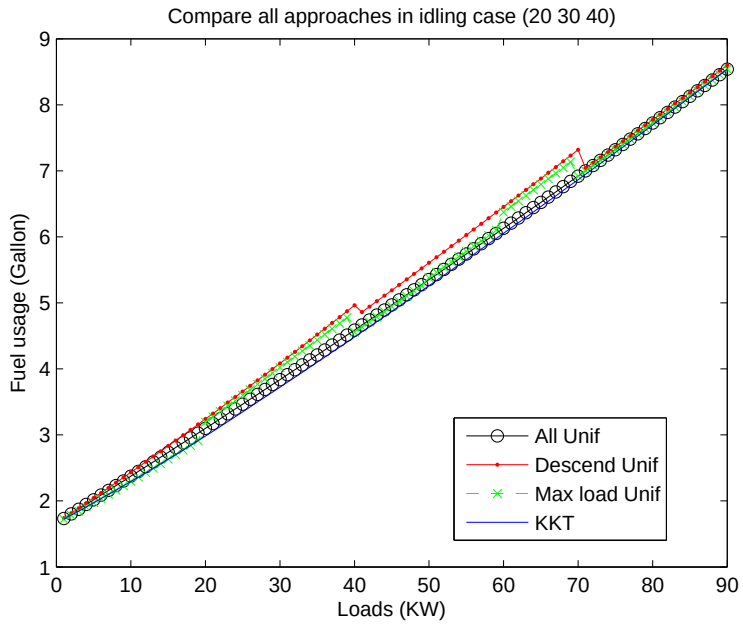

FIGURE 3.7. Fuel consumption of 1st configuration in idling case

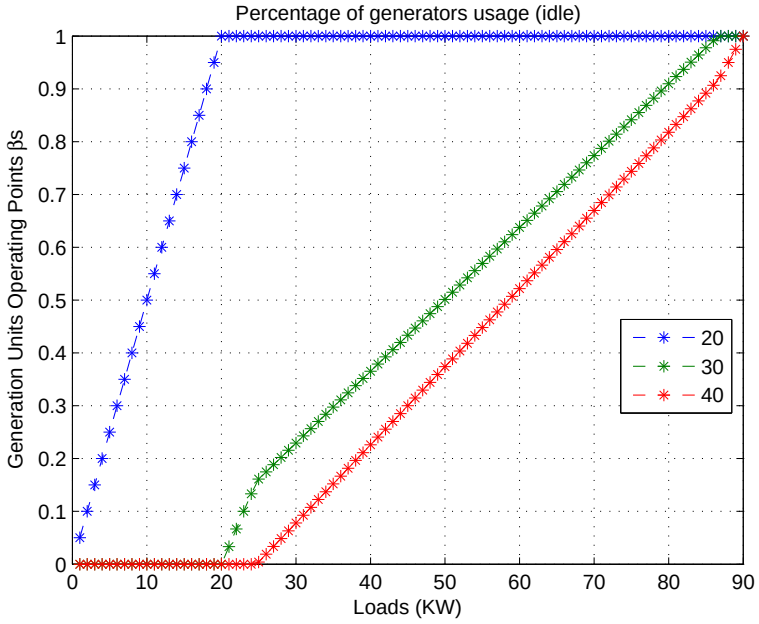

FIGURE 3.8. 1st configuration generators dispatch in idling case

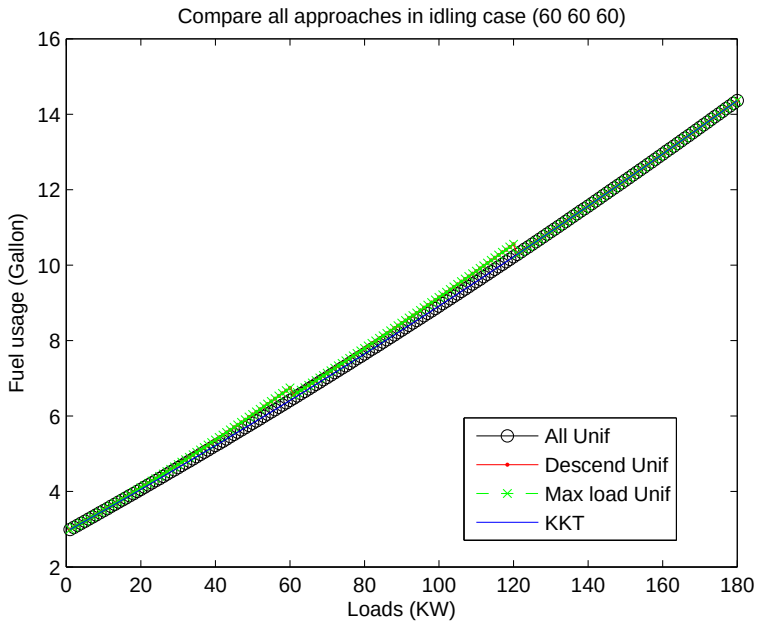

FIGURE 3.9. Fuel consumption of 2nd configuration in idling case

mid-range total loads. This is because the AUD method dispatches all generators identically, but the individual generators themselves are inefficient at low and high loads. Hence, we see once again that the KKT-based dispatch method is the best in terms of fuel economy.

3.7.2. *Constrained Problems*

In this subsection an example that corresponds to the constrained problem is presented. A hypothetical hourly load profile (for 24 hours) is given in Table 3.3. For this example, five generation units (i.e., $n = 5$) are used to supply the load. These generation units' parameters are given in Table 3.4. Among them, the first generator is used as the swing machine and the other four generators are used as the base load machines. The KKT-based dispatch method is applied separately for the 'idling' and 'shut-off' cases.

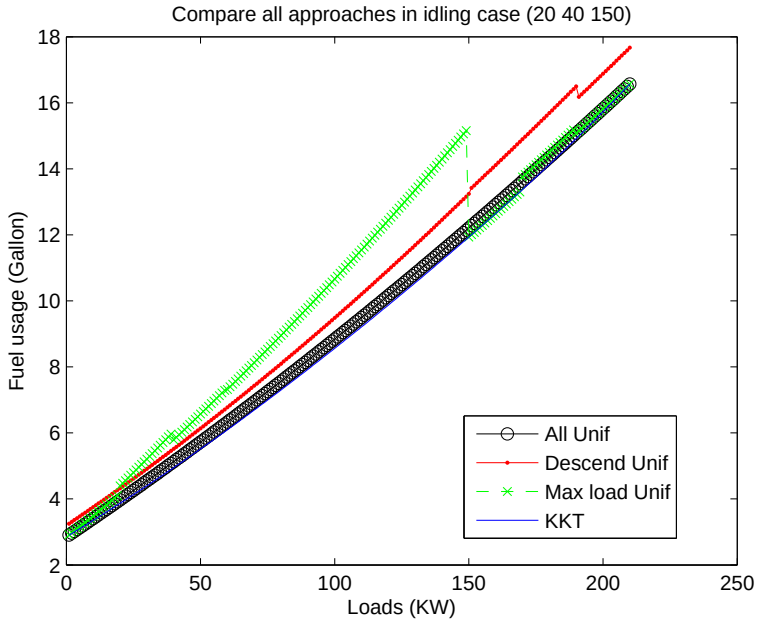

FIGURE 3.10. Fuel consumption of 3rd system in idling case

TABLE 3.3. hourly load profile

hours	1	2	3	4	5	6	7	8	9	10	11	12
load (kW)	160	150	145	140	150	165	180	190	200	190	190	190
hours	13	14	15	16	17	18	19	20	21	22	23	24
load (kW)	185	190	185	190	205	215	215	210	200	195	185	170

TABLE 3.4. Generation Units Parameters

No. Type	P_{max} (kW)	α_2	α_1	α_0	F_{max} (gal/hr)
1(S)	100	0.123552124	0.708880309	0.172200772	7.4
2(B)	30	0.064285714	0.748214286	0.193035714	2.9
3(B)	60	0.103512881	0.689929742	0.203881733	4.8
4(B)	75	0.149882904	0.637002342	0.205620609	6.1
5(B)	125	0.138147567	0.701412873	0.165620094	9.1

All five dispatch approaches are simulated and compared based on the same scenario, whereby one generation unit is used as the swing machine, and all others serve the base load. In the remainder of this subsection we present these simulation results.

For the simulation results in figures 3.11 through 3.15, the swing generator is set at 50%, and there are no (extra) limits on the upper or lower operating points. Figure 3.11 shows how the generation units are dispatched in the idling case. Since all the generators are running in the idling cause, and the bigger generators are more efficient, the load is supplied by the biggest three generators. Furthermore, since this is the idling case, spinning reserve is calculated by subtracting the hourly load from the total capacity of all generation units. The figure legend contains the following information: The first column shows the generation units' rated output power, the second and fourth columns show the upper and lower limits of each base load generation unit, respectively, and the third column shows the swing set point. Unused parameters are shown as "NaN" (from Matlab^{TM}). The first row shows the swing machine, operating at 50% of its rated output power, and the other rows show the base load machines.

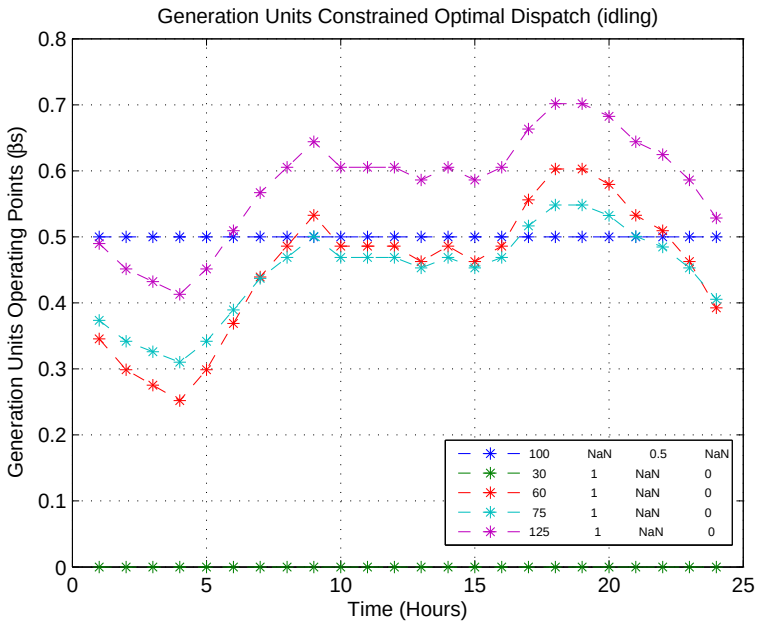

FIGURE 3.11. KKT-based dispatch in idling case

Figures 3.12, 3.13, 3.14 and 3.15 show how the generation units are dispatched in the shut-off case with spinning reserves of 0 kW, 30 kW, 60 kW and 125 kW, respectively. When no spinning reserve is required (i.e., 0 kW), the planning load and the hourly load are identical, and the algorithm is allowed to identify the true minimum possible fuel consumption, albeit at an increased risk to stable and reliable operation. As can be seen in figure 3.12, in order to achieve this optimum, the selection of the generation units becomes very sensitive to load level. Selected units and their operating points change dramatically with relatively small changes in load. As long as the biggest generator can supply the load sufficiently, no other generator is turned on to minimize fuel usage. Otherwise, the most economical combination is selected. As shown in figure 3.12, the combination only consists of the biggest two generators. It avoids using more generators to maintain the minimum fuel usage, but we note that frequent switching of the generators on and off would not be practical in the real world.

Once we impose a spinning reserve constraint, the planning load differs from the hourly load. In order to maintain the required planning load, additional generators must be operating (either idling or running). The fuel usage of an idling generator is determined by the product of its F^i_{max} and α^i_0. It is easy to see that the 30 kW generator is the most efficient one for idling. As long as the required idling power is less than or equal to 30 kW, the 30 kW generator is the primary option. On the other hand, since idling generators just consume fuel without contributing to the load, the optimum solution may also dispatch load to more units to avoid idling generators. As shown in figure 3.13, the first hourly load is 160 kW, with 50 kW being provided by the swing machine, which means that the 125 kW generator is sufficient to supply the remaining 110 kW load. Once spinning reserve is considered, the

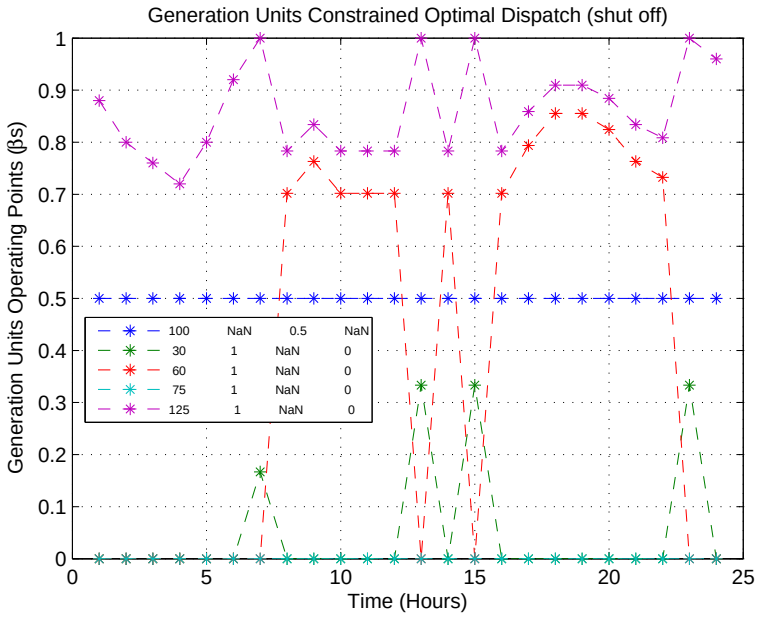

FIGURE 3.12. KKT-based dispatch in shut-off case with no spinning reserve

30 kW generator must be kept at idling to meet the required planning load of 140 kW. In table 3.5, the idling generators output power for maintaining the spinning reserve are listed for different figures in the shut-off case. The peak load hours happen at the 18th and 19th hour. For 30kW spinning reserve, the biggest two generators can sufficiently provide the load and meet the spinning reserve. No additional generators are turned on.

TABLE 3.5. Idling generators output power for the planning load

hours	1	2	3	4	5	6	7	8	9	10	11	12
Fig. 3.13	30	30	0	0	30	30	0	0	0	0	0	0
Fig. 3.14	0	0	30	30	0	0	0	0	30	0	0	0
Fig. 3.15	0	30	30	30	30	0	0	30	30	30	30	30
Fig. 3.16	0	30	30	30	30	0	0	30	30	30	30	30

hours	13	14	15	16	17	18	19	20	21	22	23	24
Fig. 3.13	0	0	0	0	0	0	0	0	0	0	0	30
Fig. 3.14	0	0	0	0	30	30	30	30	30	30	0	0
Fig. 3.15	0	30	0	30	30	30	30	30	30	30	0	0
Fig. 3.16	0	30	0	30	30	30	30	30	30	30	0	0

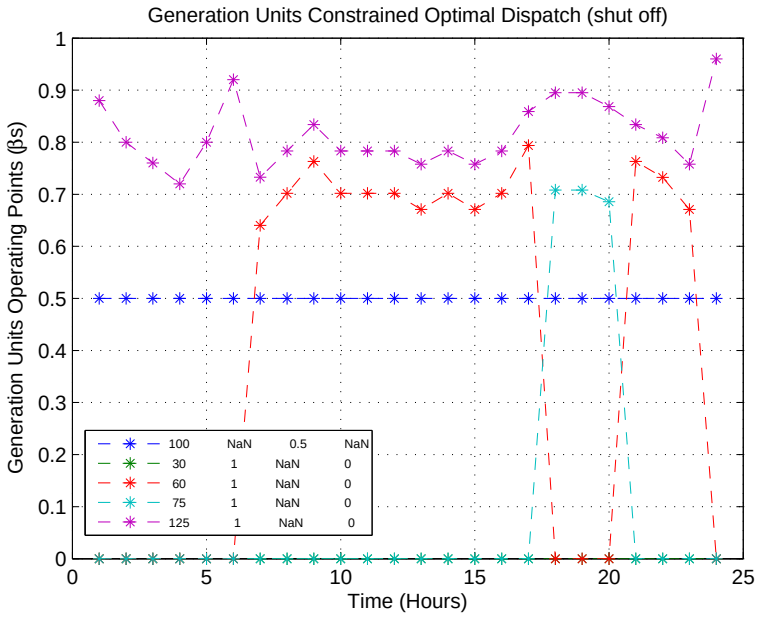

FIGURE 3.13. KKT-based dispatch in shut-off case with spinning reserve at 30 kW

As required spinning reserve increases, the planning load increases. In order to meet the required planning load, bigger generators are deployed more often. Furthermore, some generators can be kept idling more frequently. As shown in figure 3.14, the 75 kW generator is deployed in 13 (hourly) time slots, and the idling generator is used for 9 hours. Both generators are used much more frequently compared to the 30 kW spinning reserve case shown in figure 3.13.

When spinning reserve requirements increase to 125 kW (see figure 3.15), theoretically only if the hourly load is greater than 185 kW, all generators must be either running or idling to meet the planning load. In practise, since the 30 kW generator is very inefficient compared to the others, the algorithm typically forces it to idle (zero load) while using other generators to supply the load. Hence, once the load exceeds 155 kW, all generators are turned on. Additionally, it can be seen that when the hourly load is greater than 155 kW,

figures 3.11 and 3.15 are identical, since all generators are kept running or idling in both scenarios.

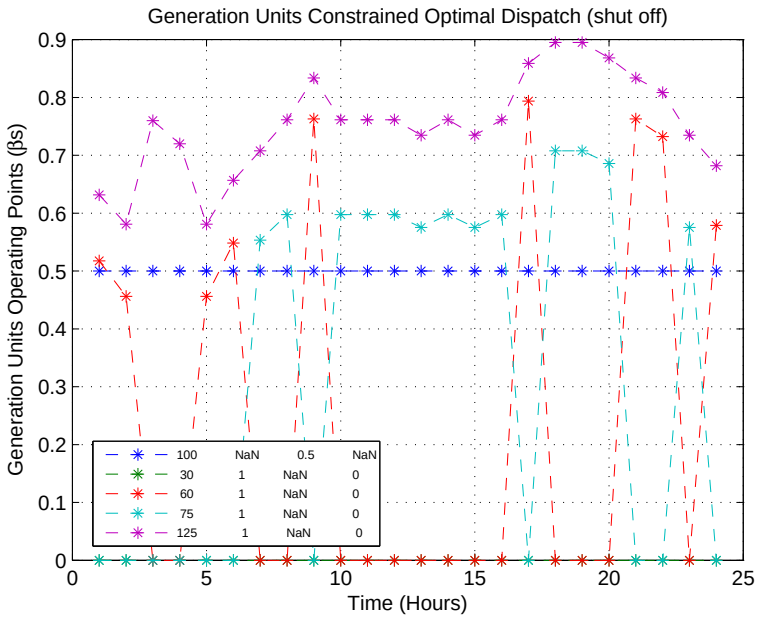

FIGURE 3.14. KKT-based dispatch in shut-off case with spinning reserve at 60 kW

To this point the upper and lower operating points have simply been set to 1 and 0, respectively (no extra constraints). We now consider cases where these limits may take other values (as shown in the figure legend).

Figure 3.16 shows results from a scenario where upper limit constraints are applied to the shut-off case with spinning reserve set at 125 kW. It can be seen that the 125 kW generator, which is the most efficient generator, is kept mostly at its upper operating limit. The 75 kW and 60 kW generators are used to supply the rest of the load. Since figures 3.15 and 3.16 have the same spinning reserve, the same idling generators are applied for same hours as shown in Table III. Since the upper limit of the 125 kW generator is restricted to 60%,

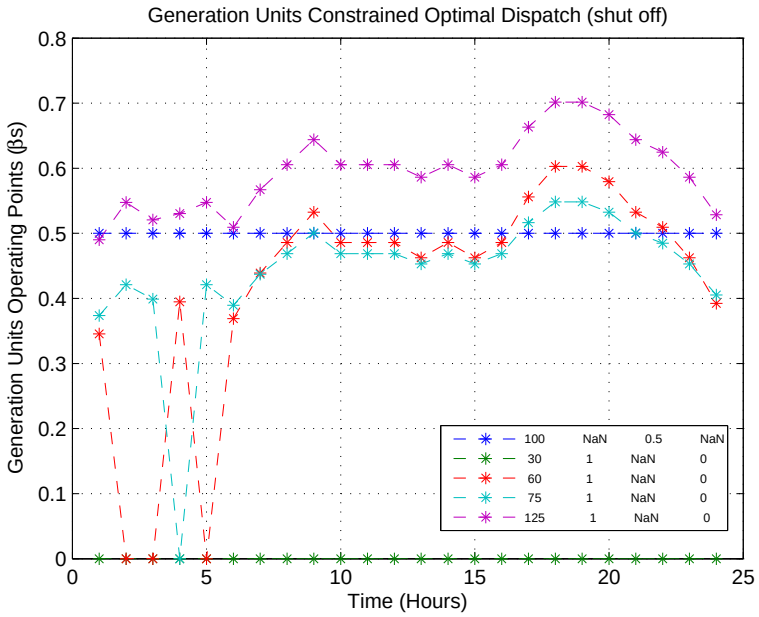

FIGURE 3.15. KKT-based dispatch in shut-off case with spinning reserve at 125 kW

at the peak load hours, the 60 kW and 75 kW generators increase their output to meet the load demand.

Figure 3.17 shows results from a scenario where both upper and lower operating limits are applied to the idling case. It can be seen that some of these constraints are active. For example, the 60 kW generator lower limit was triggered between the 2^{nd} and the 5^{th} hour. Also, the 125 kW generator upper limit was activated during the 17^{th} to the 22^{nd} hour. As before, the 30 kW generator is kept at its lower limit (0.2), due to its inefficient operation.

Figure 3.18 shows the fuel usage comparison in the idling case across four methods, which are indicated in the figure legend. It clearly shows that the KnC method consumes the least fuel, since it is the true optimum.

When extra constraints are required (for reliable operation), it is readily seen from figures 3.19, 3.20, and 3.21 that the KnC approach delivers the most economical dispatch. Figure

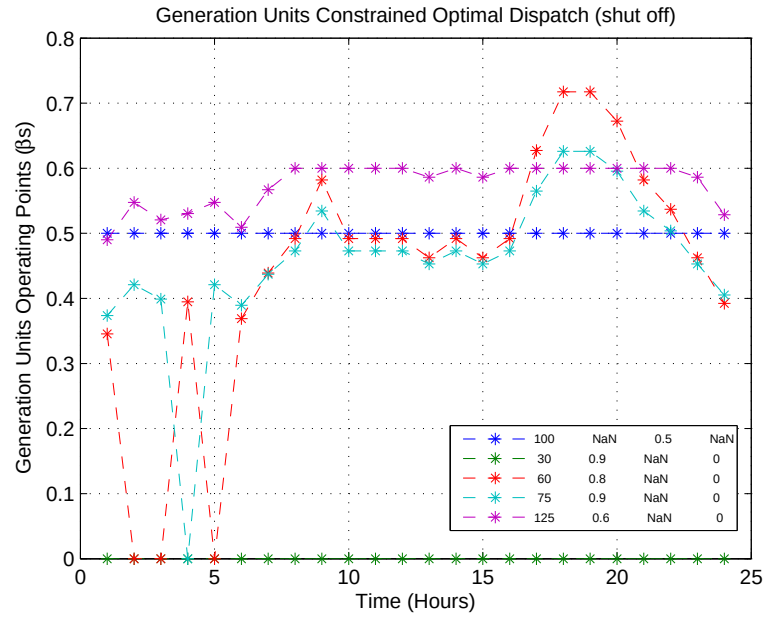

FIGURE 3.16. KKT-based dispatch in shut-off case with spinning reserve at 125 kW and (extra) upper limit constraints

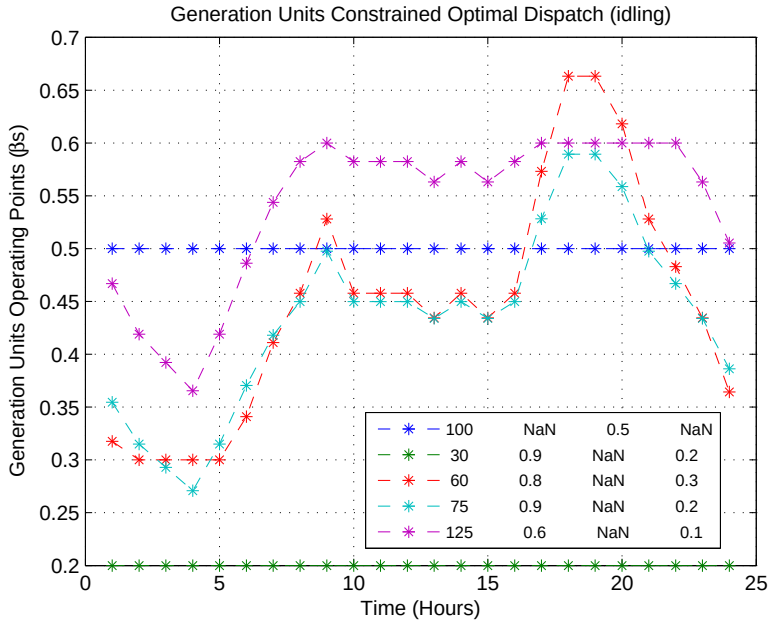

FIGURE 3.17. KKT-based dispatch in idling case

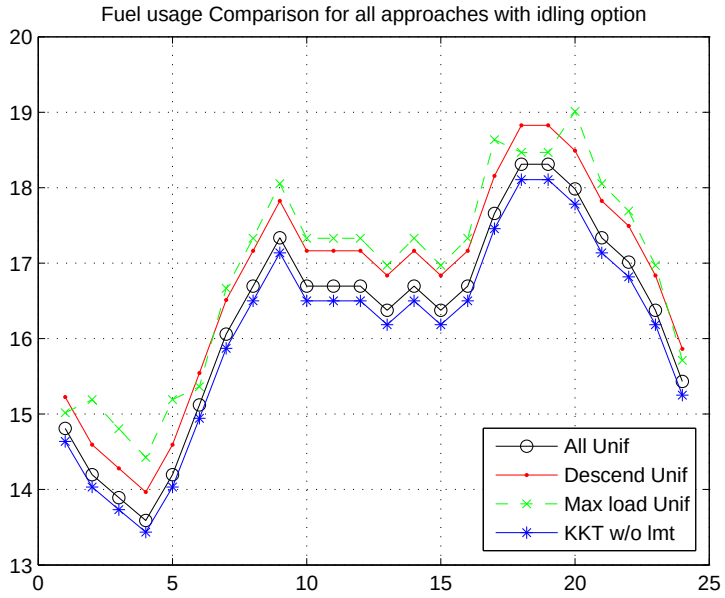

FIGURE 3.18. Fuel usage comparison for four methods in idling case

3.19 shows the fuel usage when there is no spinning reserve. Since the AUD approach has all generators turned on, it consumes more fuel than all the other methods. The DUD approach does not have the flexibility to find a suitable combination to share the load, and also consumes considerably more fuel than the optimum. MULD can find better combinations to dispatch the load, which leads it to use less fuel than DUD, but it is still not a true optimum. Finally, KnC consumes the least fuel, since it tracks the true optimum. Figure 3.20 shows that when the spinning reserve requirement increases, the DUD, MULD and KnC methods all consume more fuel than with smaller spinning reserve. They all trend so as to be closer to the AUD curve. The increased spinning reserve requirement forces more generators to be running, leaving less room for these algorithms to manipulate their solutions. These operational limit constraints improve system reliability and extend unit life, but they also reduce the overall system efficiency and increase fuel consumption. Figure 3.21 shows that

with limitations on the operating points, the KwC approach consumes more fuel on the peak hours (which is the cost of enhancing the system reliability and robustness).

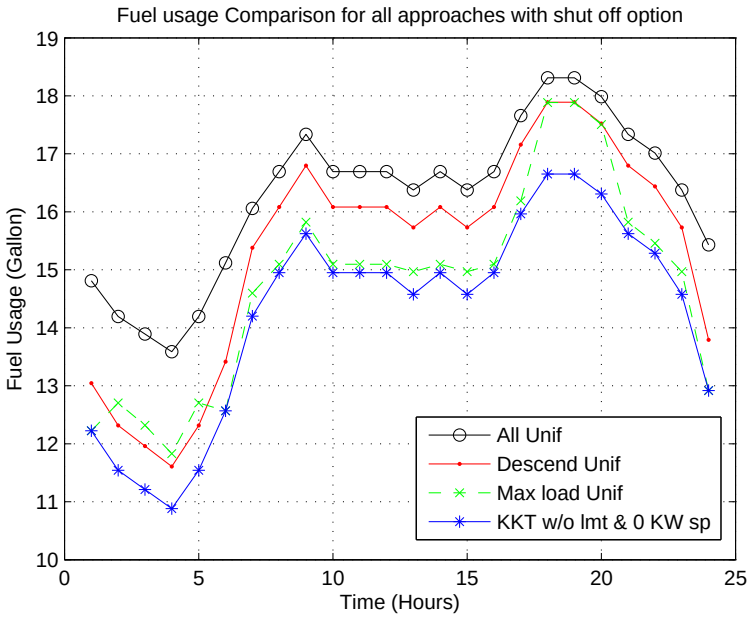

FIGURE 3.19. Fuel usage comparison for four methods in shut-off case without spinning reserve

3.7.3. *Adding Startup and Shutdown Costs*

In this section, we add start-up and cooling down costs into the optimization problem. The 30 kW, 40 kW, 60 kW 100 kW and 125 kW generators are used, with the 100 kW generator as the swing machine with POP at 50% (all others are baseload machines), and a 50 kW spinning reserve. Generator parameters may be found in Table 3.2 and 3.4. A real 24 hours load data trace is obtained from Central Electric Power Cooperative (CEPC), and slightly modified to provide one minute resolution data.

The algorithm developed for incorporating start-up and cooling-down costs is described here. For a particular Δt, the load profile used is extracted from the one minute resolution

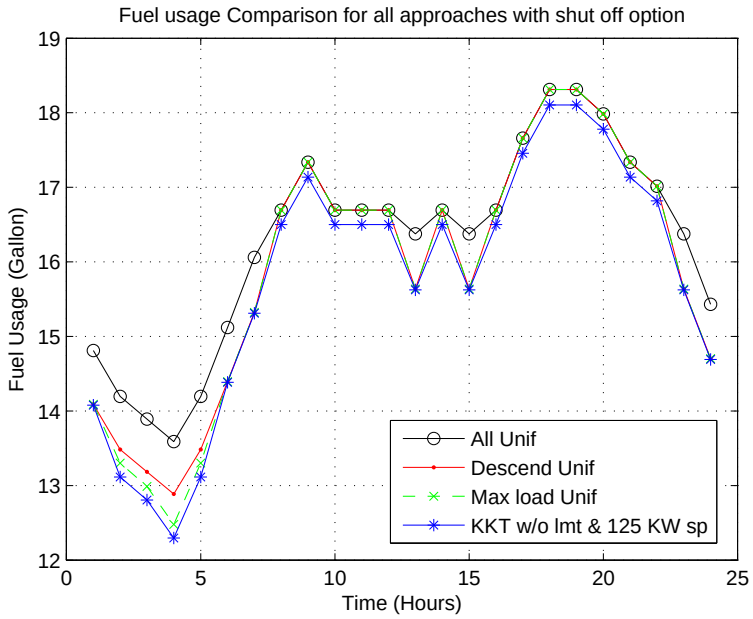

FIGURE 3.20. Fuel usage comparison for four methods in shut-off case with spinning reserve of 125 kW

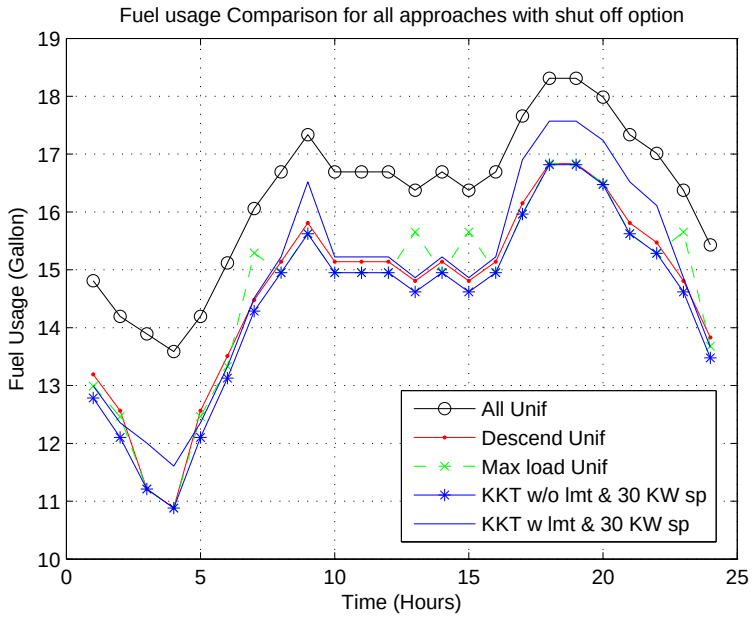

FIGURE 3.21. Fuel usage comparison for all methods in shut-off case with spinning reserve of 30 kW

load profile at minutes 1, Δt+1, 2Δt+1, ..., $u\Delta t$+1, where $u = 0, 1, 2, \ldots, v$ and $v = rpd/\Delta t$ (rpd denotes the running period). We assume that all generators are turned off initially. For the very first time interval, all 3^n combinations of fuel usage for the constrained problem are obtained. Since all generators are off, only start-up costs are considered and computed for each combination. We select the combination with minimum overall cost, and dispatch accordingly. For the second time interval, the fuel usage without considering start-up and cooling down costs is first calculated. Referring to Table I, assume that the generators status at t_1 is the optimal solution for the first time interval. Start-up and cooling-down costs for all combinations in the second time interval are now computed according to the generation status at t_1. The total fuel consumption of each combination is calculated and the optimal solution found. Note that the time interval Δt plays a crucial role in this process, since in order to add startup and shutdown costs into the mix we now have to compare on the basis of energy (not power as earlier), which means that the time interval of interest can greatly impact the decision process.

In the following figures (specifically figures 3.22, 3.24 and 3.25) we consider the fuel consumption using three metrics. First the KKT approach with start-up and cooling down costs (denoted 'KKT w s/s'), utilizes the algorithm described above. Second pure KKT (denoted 'pure KKT') utilizes our earlier algorithm that ignores startup and shutdown costs. Finally pure KKT with its own start-up and cooling down costs (denoted 'pkkt w cost') takes the decision made by 'pure KKT' and adds the startup and shutdown costs after the fact (in other words startup and shutdown are not factored into the decision here but they do show up in the final cost).

Note from figure 3.22 that, as we would expect, 'pure KKT' consumes the least fuel. This is because it simply does not account for startup and shutdown costs. However, once those costs are added in, to get a more realistic estimate of the true cost, as in 'pkkt w cost', then in fact it uses more fuel that the 'KKT w s/s' algorithm developed here which properly accounts for startup and shutdown costs in the decision process.

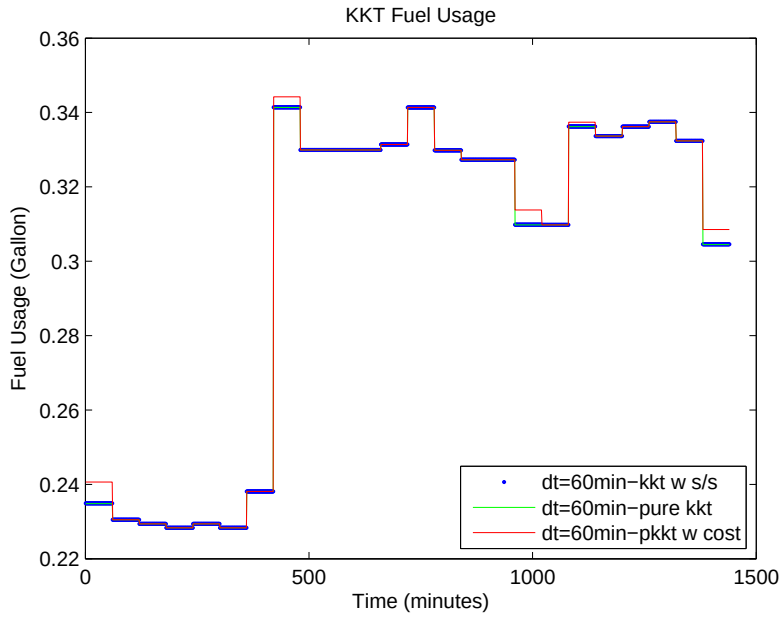

FIGURE 3.22. Fuel usage comparison when Δt is 60 mins

Figure 3.23 shows how the generators are dispatched by the 'KKT w s/s' algorithm. It appears almost identical to how the 'pure KKT' algorithm would dispatch the generators. The reason is because of the big time interval (Δt=60 mins) considered here. With a large Δt, compared to the fuel costs of generating power to supply the load over that time interval, the start-up and cooling-down costs are negligible. Hence, it minimally affects how the generators are re-dispatched at the next time interval, which also explains why the fuel consumption curves in figure 3.22 are close to each other.

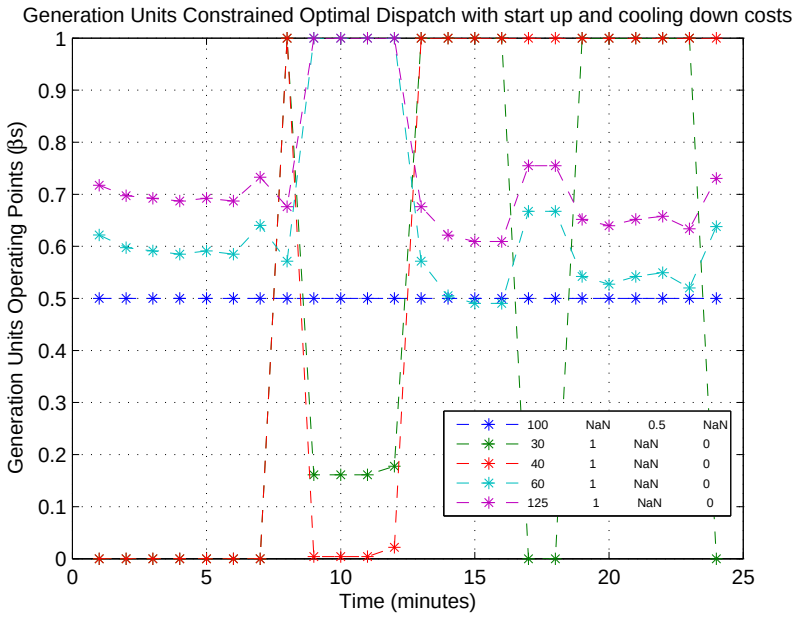

FIGURE 3.23. KKT-based dispatch with start-up/cooling down costs added when Δt is 60 mins

Consider now the fuel consumption curves in figure 3.24, where Δt=1 minute. It is readily apparent that there is a large difference between the different dispatch schemes. In this case, with such a short time interval (Δt=1 min), the startup and shutdown costs play a big role, and ignoring them in the decision process yields a much higher overall fuel usage. Note how superior the 'KKT w s/s' algorithm performs as compared to 'pkkt w cost' (of course the 'pure KKT' algorithm appears best here but that is not realistic as the startup and shutdown costs have not been added in yet).

In table 3.6, all baseload generators' fuel consumptions for 24 hours, with a wide range of different Δt, are listed. It can be seen that very small Δt allows for fast dispatching, but over emphasizes the impact of startup and shutdown costs (discouraging switching generators). Conversely very large Δt tends to underestimate the importance of startup and shutdown costs, and also only allows for infrequent re-dispatching. It appears that Δt between 4 and

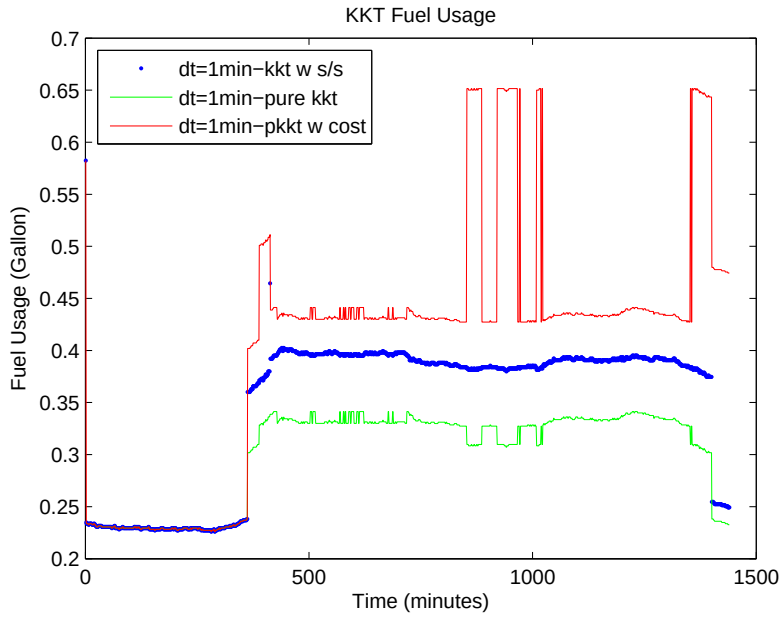

FIGURE 3.24. Fuel usage comparison when Δt is 1 min

30 minutes affords a good compromise, allowing the system the flexibility to re-dispatch to cope with a varying load, without dramatically increasing the fuel usage, and this leads to the overall true minimum fuel usage. The fuel consumption profile with Δt=4 mins is shown in figure 3.25, where the advantage of considering startup and shutdown costs in the algorithm (as in 'KKT w s/s') is readily apparent.

3.8. Conclusion

This chapter presents a KKT-based approach for optimal generator dispatch in a micro-grid, with the primary objective of minimizing fuel consumption. Three different but related problems are addressed. First of all, a pure KKT optimum dispatch problem is presented.

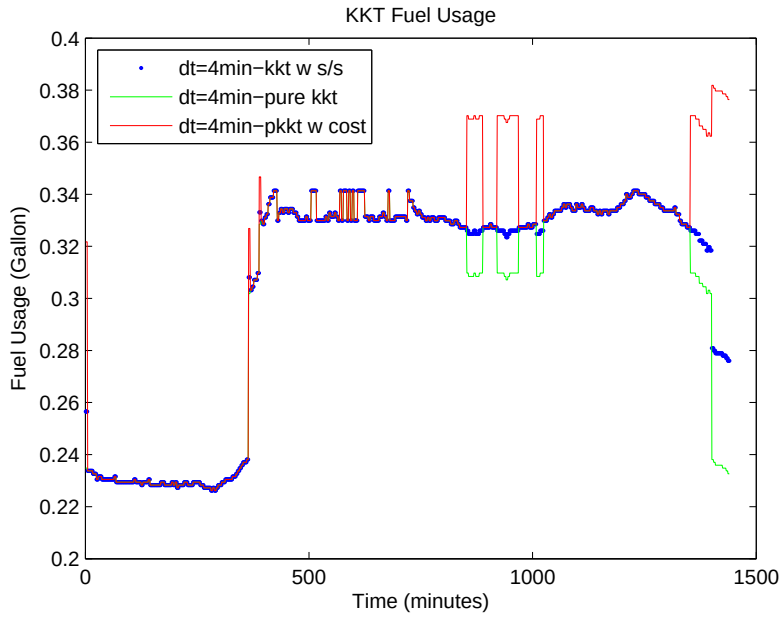

FIGURE 3.25. Fuel usage comparison when Δt is 4 mins

TABLE 3.6. Fuel consumption comparison for different Δt

No. units	KKT w s/s (gallon)	pure KKT (gallon)	pkkt w cost (gallon)	Δt (mins)	rpd (mins)
1	398.9776	334.9535	484.4135	1	1440
2	339.2211	334.9535	363.8902	2	1440
3	338.9944	334.7270	349.9387	4	1440
4	338.6854	334.4947	346.6230	5	1440
5	338.9639	334.9764	344.7464	6	1440
6	338.3018	334.0827	340.5277	10	1440
7	338.3498	334.2136	339.6003	12	1440
8	334.7284	334.5926	336.6301	15	1440
9	333.3417	333.2398	335.2773	20	1440
10	333.8449	333.7770	335.8145	30	1440
11	333.4176	333.3997	334.4755	60	1440

Then some real world considerations, such as spinning reserve, are added to form a constrained problem. Finally, startup and cooling-down costs are considered for dispatch over an extended operating period.

Simulation testing demonstrates that the KKT-based dispatch methods are the most economical, regardless of the system structure and operation situation. Standard existing dispatch methods can have similar performance in the right circumstances, but they all also exhibited poor performance under other circumstances, and the KKT-based approach was the only one that always dispatched the generators in the most economical manner.

Additional real world constraints, such as baseload operating limits and spinning reserve, can be added to the pure KKT dispatch problem. There is a moderate increase in fuel consumption versus a pure (unconstrained) KKT approach, but in practice these constraints could significantly improve unit life and system stability. In any case once again the KKT approach outperforms traditional dispatch schemes.

Once startup and shutdown costs are considered, the problem needs to be considered over a time interval (i.e., comparing energy not power). It is seen that the problem is sensitive to this time interval, but with a smartly chosen time interval the flexibility to re-dispatch generators to cope with varying load can be achieved without excessively increasing fuel costs.

CHAPTER 4

GENERATOR CONFIGURATION

4.1. Introduction

In this chapter, we solve the problem of how to select generation units from a range of available generators to form a optimal microgrid, which minimizes the fuel consumption when there is a given load profile.

For a given load profile, a variety of generators (in term of their rated output power) should be selected to form a microgrid which copes well with the load transient, as well as peak and off-peak power demand. Also, generators with different fuel consumption curve characteristics should be selected optimally for reducing fuel usage at different load demand levels. Hence, it is critical to optimally select the generators when a microgrid is formed. Optimally selected generation units can significantly enhance microgrid stability by keeping a certain amount of spinning reserve, bounding the generators' "preferred operating point" (POP) and adding swing capacity. Optimally dispatching the load to a set of optimally selected generators, should significantly reduce the running costs compared to traditional load dispatching methods, such as: maximum load uniform, descend load uniform etc. [23].

To form a sophisticated microgrid, tailored for a particular customer, their historical load profile is needed. By adding renewable power sources, microgrid economical efficiency can be improved even further. Note also that if there are renewable power sources, their historical and/or predicted output power is combined with the customer historical load profile to yield a profile for the required generator power.

In this chapter, two approaches for optimally selecting microgrid generators are developed, based on the associated Karush-Kuhn-Tucker (KKT) conditions. The approaches are designed for constant and varying load applications separately. There are other considerations about how the generators are selected, such as capital cost, familiarity of operators and maintainers, and the popularity of the market of a generation unit [119]. This chapter mainly focus on fuel usage minimization by optimally selecting generators. It is the first crucial step to build an efficient microgrid.

The studies in this chapter leverage our previous work in Chapter 3. Part of the implementation utilizes our optimum generation units dispatch tools. The analyses are done based on the 'shut off' cases (see [115]), since the 'idling' case consumes more fuel to keep all generators running and it is not applicable in practice. Following the introduction in section 4.1, the rest of the chapter is organized as follows. In section 4.2, the problem is set up. The KKT conditions based optimum generator selection approach with real world extra constraints is presented in section 4.3. Some applications are presented in section 4.4. Finally, some concluding remarks are presented in section 4.5.

4.2. Problem Setup

Suppose there are n generation units ($r = 1, 2, 3, \cdots, n$), each with its own unique rated output power and input-output characteristic curve. Theoretically, there are $k = \sum_{l=1}^{n} \frac{n!}{l!(n-l)!}$ combinations in total, each with its distinguished name: $C_1, C_2, \cdots, C_k$. For these combinations, each has its own unique configuration of generators. In practice we may also wish to consider cases where only a few ($m < n$) types of generators are considered. In that case we can have combinations where the same generator (type) appears more than once. This can have significant meaning in practice, since such combinations are more friendly for operators

and they simplify the maintenance and reduce its related costs. In this kind of combinations, the same generators are operated at the same operating points. Because of the similarity of the fuel consumption curves, it limits the flexibility of tracking the minimum fuel usage. In this chapter, only combinations with distinct generators are considered (though the tools developed here are capable of handling the more general case). In this kind of setup, the problems are more challenging and interesting. At the same time, we can demonstrate the maximum potential of our developed tool.

For the real-world microgrid generator selection problem, only combinations whose total output power exceeds (or is equal to) the peak power demand of the historical load profile are considered. This is the minimum requirement for a combination to be feasible. $P_{C_v} \geq P_{Load_{peak}}$, where C_v contains all the valid combinations, $v = 1, 2, \cdots, p$, and $p \leq k$; P_{C_v} is the total power of each C_v and $P_{Load_{peak}}$ is the peak load demand. As mentioned earlier, if renewable power sources are to be considered, their output power should already be subtracted from the historical load (since they consume no fuel). To enhance the system safety margin, a safety ratio factor "SR" is introduced, so as to ensure that the generators have sufficient output power to cope with sudden load transients. As shown in Eq. (4.1), only the combinations that have total output power greater than or equal to the product of "SR" and the peak load are considered as "safe combinations".

$$P_{C_s} \geq P_{Load_{peak}} \times SR \tag{4.1}$$

where C_s contains all the safe combinations, $s = 1, 2, \cdots, q$, $q \leq p$ and $SR > 1$; P_{C_s} is the total power of each C_s. By adjusting "SR" to a larger value, the system stability and

reliability can be improved, although at the expense of sacrificing the number of available safe combinations.

Now the problem reduces to how can we identify which one (or more) of the combinations among all q safe combinations consumes the least amount of fuel for a particular application.

4.3. Optimum Combination Selection

The historical load at each time interval (t_j, where $j = 1, 2, \cdots, u$; $u = rpd/\Delta t$; rpd denotes the running period and Δt is the time length of each time interval) is optimally dispatched to all or some of generators of every safe combination. The dispatching procedures are studied separately by deploying the pure KKT conditions based approach and the constrained KKT conditions based approach. These two approaches correspond to two different engine applications. When the engines are used as short period of emergency power backup, pure KKT conditions based approach can be deployed. For instants, the backup engines in a hospital. However, we should implement the constrained KKT conditions based approach to enhance the life-time of the engines, if the engines are running continuously as they are the only power sources. For examples, the engines deployed in a remote area to supply power for a military base.

4.3.1. *Pure KKT Conditions Based Combination Selection*

Here the load is optimally dispatched by using the pure KKT conditions-based approach. Within a particular time interval t_j, suppose there are g generators in a given safe combination C_q.

Since the pure KKT conditions-based generator dispatch approach finds the true optimum for each combination during every time interval, the special combination that meets power

demand and consumes the least amount of fuel during the full running period is the optimum combination. $C_{opt} = C_s(\min_q(F_T(t_j, C_q))$, where $C_{opt} \in C_q$ and $F_T(t_j, C_q) = \sum_{j=1}^{u} F_T(t_j) = \sum_{j=1}^{u} \sum_{i=1}^{g} F_{max}^{i} \Phi_i(t_j)$. The generators in combination C_{opt} are selected to form a microgrid that handles minimal (or no) load profile variation. Generators that are selected using the pure KKT conditions-based approach are so-called "continuous rated generators", which are used for co-generation and base load applications with (near) constant load. These generators are operated without running time limit and their typical load factor is between 70% to 100% [120].

4.3.2. *Constrained KKT Conditions Based Combination Selection*

Here the constrained KKT conditions-based generator combination selection approach is developed.

Taking into account the above constraints on generator dispatch as preconditions, the load is dispatched (in simulation) to each generator in every safe combination. Among all the safe combinations, only those that correspond to feasible solutions are considered. These are the so-called "feasible combinations". Hence, similarly the total fuel consumptions of a particular load profile for every feasible combination are calculated individually. Among them, the corresponding combination(s) that consumes the minimum amount of fuel is selected. The generators within this combination are used to form a microgrid that can handle a varying load profile. By interconnecting these selected generators, they are deployed as the sole power source for a (islanded) microgrid. There is no operating time limit on them, and their maximum outputs are typically limited at 70% of their rated power.

4.4. Results and Discussion

A (varying) load profile extracted from the operational profile of a medium-sized military base is used (note that the data has been appropriately scrambled for security reasons). We will demonstrate how the constrained KKT conditions-based generator selection approach is implemented to optimally select generators and form a microgrid for fuel usage minimization, and also life cycle economic considerations, given this varying load profile. The original data are taken every 15 minutes for four weeks. The maximum load is 1661.2KW and the minimum load is 774.2KW.

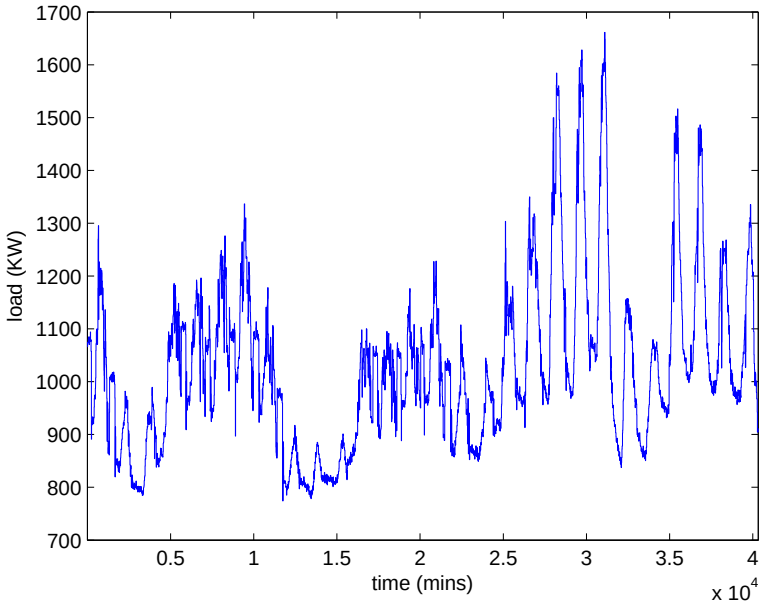

FIGURE 4.1. Scrambled medium-sized military base load profile

Suppose six different generators with rated output powers of 200KW, 500KW, 600KW, 750KW, 1000KW and 1250KW are deployed. These units' parameters, along with their unit prices, are given in table 4.1. Among them, the 400KW unit is used as a swing machine, and the others all serving base load.

TABLE 4.1. Generation Units Parameters

No.	P_{max} (kW)	α_2	α_1	α_0	F_{max} (gal/hr)	Price (USD)
16	400	0.2438	0.6052	0.1525	28.6	85k
11	200	0.1905	0.6540	0.1592	14.4	40k
17	500	0.2561	0.5932	0.1513	35.7	110k
18	600	0.2697	0.5780	0.1524	42.8	140k
19	750	0.2718	0.5784	0.1503	53.4	165k
20	1000	0.2781	0.5720	0.1498	71.1	225k
21	1250	0.2831	0.5673	0.1495	88.8	320k

We specify 'SR' equal to 1.15, which implies that the total rated output power of a combination must exceed 1910.28KW to be qualified as a safe combination, when there are no upper limits on generator operating points. We limit the maximum number of generators in each combination to four, which yields the first five columns of Table 4.2, which lists all the safe combinations that satisfy the required specifications. All simulations are conducted under the same conditions, which set the 400KW generator as the swing machine (with POP at 50%), and the spinning reserve capacity at 200KW. In Table 4.2, there are three separate columns under 'Fuel Usage'. The first column lists the fuel usage of each combination that would be obtained without considering the generators' upper operating point limits. In the second and the third columns, the fuel usages corresponding to upper operating points of 85% and 70% are shown respectively.

Note that applying the upper operating point limits further reduces the number of safe combinations, since the maximum output power of every generator is limited at: 85%(or 70%) $\times P^i_{max}$. Considering upper limits of 85% and 70% means that only combinations that have total output power of equal to or greater than 2247.5KW or 2729KW are counted (note that 'N/A' indicates a combination does not satisfy the total output power requirement with the relevant upper operating limits). We re-dispatch the load every fifteen minutes,

and any startup/cooling down costs are considered as the fuel usage of that generator idling for 22.5/75 seconds (these values are estimates based on typical relevant generators).

TABLE 4.2. Available Safe Combinations

No.	Generators				Power Sum	Fuel Usage		
	Gen1 (KW)	Gen2 (KW)	Gen3 (KW)	Gen4 (KW)	(KW)	no lmt (gal)	lmt 85% (gal)	lmt 70% (gal)
C1	750	1250			2000	49049	N/A	N/A
C2	1000	1250			2250	49107	49107	N/A
C3	750	1000	1250		3000	49049	49049	49425
C4	600	1000	1250		2850	49028	49028	49315
C5	600	750	1250		2600	49028	49028	N/A
C6	600	750	1000		2350	49544	49550	N/A
C7	500	1000	1250		2750	49012	49012	49272
C8	500	750	1250		2500	49012	49012	N/A
C9	500	750	1000		2250	49295	49286	N/A
C10	500	600	1250		2350	49012	49012	N/A
C11	500	600	1000		2100	49285	N/A	N/A
C12	200	1000	1250		2450	49026	49027	N/A
C13	200	750	1250		2200	48999	N/A	N/A
C14	200	750	1000		1950	49158	N/A	N/A
C15	200	600	1250		2050	48987	N/A	N/A
C16	200	500	1250		1950	48989	N/A	N/A
C17	600	750	1000	1250	3600	49082	49028	49294
C18	500	750	1000	1250	3500	49012	49012	49234
C19	500	600	1000	1250	3350	49012	49012	49229
C20	500	600	750	1250	3100	49012	49012	49229
C21	500	600	750	1000	2850	49157	49157	49285
C22	200	750	1000	1250	3200	48999	48999	49214
C23	200	600	1000	1250	3050	48987	48987	49157
C24	200	600	750	1250	2800	48987	48987	49154
C25	200	600	750	1000	2550	49142	49143	N/A
C26	200	500	1000	1250	2950	48989	48988	49152
C27	200	500	750	1250	2700	48989	48988	N/A
C28	200	500	750	1000	2450	49118	49121	N/A
C29	200	500	600	1250	2550	48989	48988	N/A
C30	200	500	600	1000	2300	49186	49190	N/A
C31	200	500	600	750	2050	49474	N/A	N/A

As shown in table 4.2, with no upper operating point limits, C15, C23 and C24 consume the least amount of fuel, with C16, C26 and C27 delivering almost the same performance

(burning just two more gallons of fuel); with an upper operating limit of 85%, C23 and C24 consume the least amount of fuel at 48987 gallons, with C26, C27 and C29 almost the same (just one more gallon of fuel); with an upper operating limit of 70%, C26 uses the least amount of fuel at 49152 gallons, with almost equivalent performance from C24 (using just two more gallons of fuel). All other combinations are either invalid with regard to the operating specifications, or utilize significantly more fuel. In the following sections, we make some observations based on analyzing the data shown in Table 4.2.

4.4.1. *Prime Rated Generators for Microgrid Application*

Decreasing units upper limits from 100% to 70%, more fuel is consumed. By further constraining the allowed operating region, we force the generators to run in a operating region that excludes their most economical operating points. Since we know the generator's input-output characteristic curve can be expressed approximately as a quadratic convex function that starts from α_0 at 0 and gradually rising to 1 at 1, which means the larger generators are typically more efficient and the highest efficiency normally occurs when the generators are loaded at near rated capacity[115]. However, on the other hand, we know that if several generators are interconnected as the only power source to supply a variable load and they are running 24 hours per day, 365 days per year, then they are functioning as prime-rated generation units[121]. When generators are used as prime-rate units, they should be sized as 60% to 70% of their rated power. This military base application has exactly the same scenario. These interconnected generators are the only power source and they are used to power a variable load for a long period of time (several years or even longer).

As shown in the last column of Table 4.2, C26 consumes the least amount of fuel when the upper limits are preset at 70%. Fig.4.2 shows how the scrambled military base variable load

is dispatched to these generation units. There are a lot of switching actions taking place in order to find the best combinations within the four assigned units that can provide sufficient capacity, minimum the fuel usage and put startup and cooling down cost into consideration at the same time. The fuel consumption curve associated with the dispatch curve is shown in red in Fig.4.4.

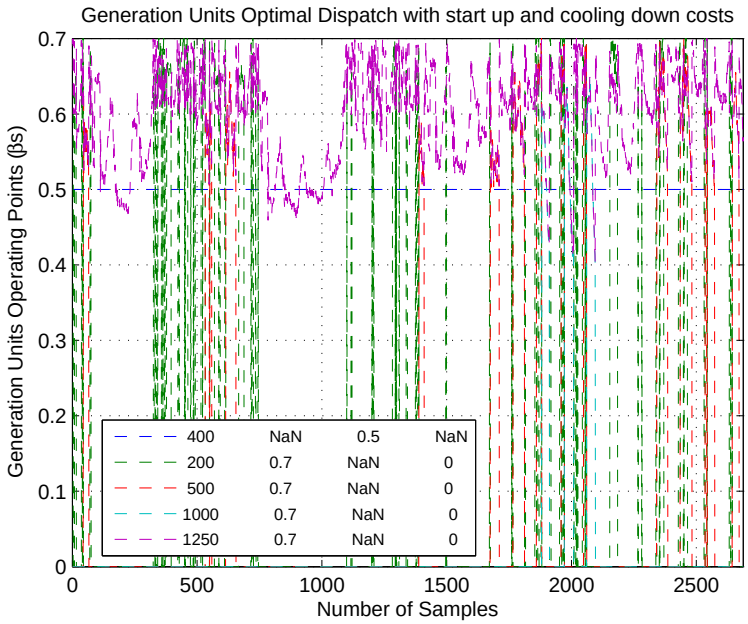

FIGURE 4.2. Generators Dispatch Scheme with 70% upper limits

4.4.2. *Continuous Rated Generators for Baseload Application*

For the application of baseload and co-generation, generators are selected based on continuous rating. Continuous rated units are operated at 70% to 100% of maximum load and work parallel with utility baseload units. They are used to provide power to constant or near constant load and has no hour-use limit[121][122]. In our case, if baseload generators need to be selected to work with utility grid for co-generation purpose, then C23 is the best choice for this kind of application because of its lowest fuel consumption rate and higher power

capacity compare to other combination across different units output ratings. Although the lower limits of the continuous rated units should be set at 70% in theory to enhance system efficiency, we did not pre-set the lower limits to allow the algorithm to find the possible global minimum.

Regardless of generation units application, the effects of altitude and ambient temperature can significantly affect the prime mover (IC engine) performance. With altitude increases, the ambient pressure decreases. It becomes more difficult to force air into engine combustion chamber because of the bigger pressure difference between ambient and intake manifold. With higher environment temperature, air and/or fuel density become lower, an IC engine has to breath harder to increase the air and/or fuel volume flow into the engine, in order to maintain the same output power. To obtain desired generator power at high altitude and high temperature environment, oversized generation unit should be chosen accordingly to ensure the load-supply balance [120].

4.4.3. *Relevancy of Number of Units in Combinations*

Combinations with three or four units may consume same amount of fuel, since one of the generator within the combinations with four units is too expensive to use and it is not participating load dispatch, in other words, it is simply turned off during the entire operating period. However, the combinations with four generators consume less fuel compare to combinations that are composed with three or two generators in general, since there are more flexibility of how the combinations are formed with in the four units in a certain combination or shall we say the combinations with less units are just subsets of possible combinations of four units. Fig.4.3 shows how the generators in C24 are dispatched when there is no upper limits, C15 and C23 has almost the same dispatch mapping, expect that

units 19 is not considered and unit 20 is completely shut down, correspondingly. The fuel usage that correlate with Fig.4.3 is shown in Fig.4.4 with color of blue. Till this point, only the running costs are considered. For complete analysis, life cycle cost, which includes capital cost, running cost and maintenance cost, is studied as well.

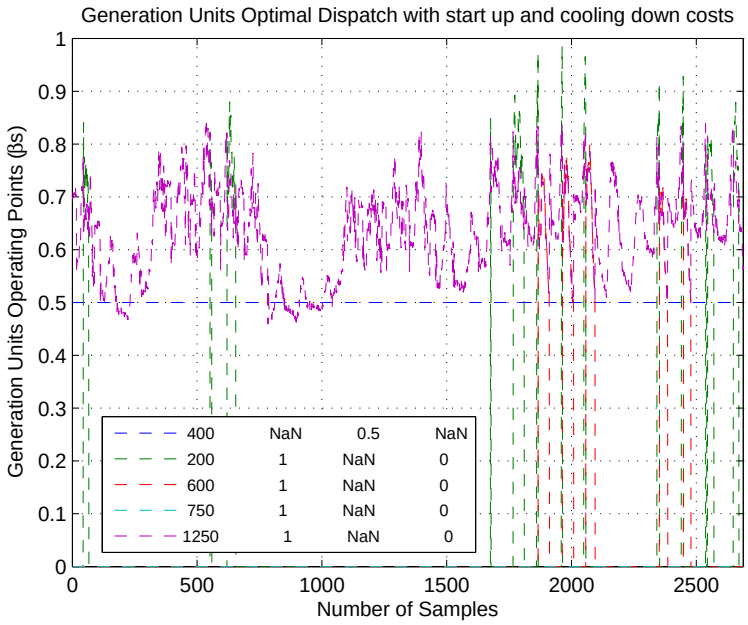

FIGURE 4.3. Generator Dispatch Scheme without limits

4.4.4. *Economical Analysis*

For this military base microgrid application, the life cycle cost analysis is implemented. The life cycle cost analysis helps us to choose the combination that minimum the total investment during the entire operating period. From the last column of Table 4.2, it can be seen that C7 and C26 consumes least amount of fuel in three units and four units combinations, respectively. The life cycle cost analysis is conducted by using future equivalent evaluation, which defines a future equivalent amount [123].

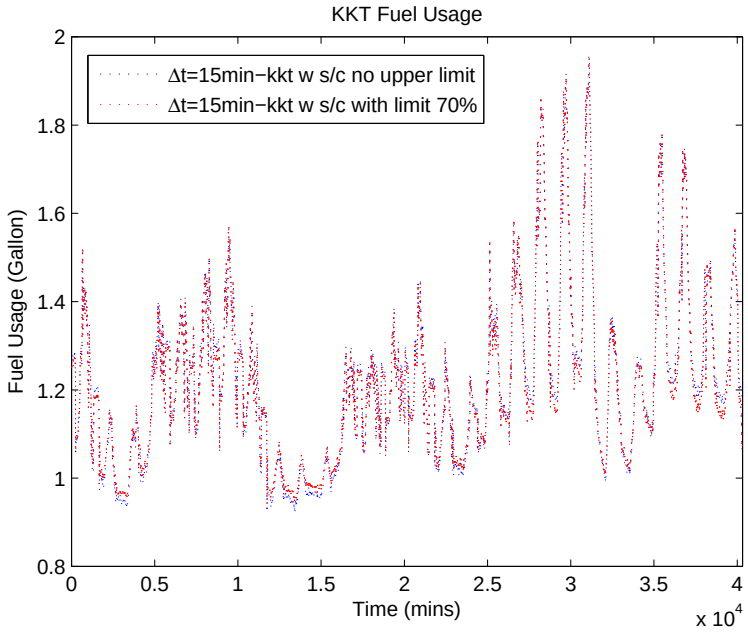

FIGURE 4.4. Fuel usage Scheme

The fuel usage listed in Table 4.2 shows the fuel consumptions to provide the load profile in Fig.4.1, which last for four weeks. Assuming that the load during this period is typical and we know there are 52 weeks a year, then a year total fuel usage volume can be obtained by multiplying 13 with the listed amounts. Suppose the price of diesel is four dollars per gallon, the total fuel cost can be calculated. Further suppose that there is a nominal annual rate of interest $\gamma\%$ and planned maintenance period is δ. For C7, the generators' maintenance is scheduled every two years and the maintenance for generators in C26 is implemented every three years. During the ten years operating period, generators in C7 need four periods of scheduled maintenance on the 2^{nd}, 4^{th}, 6^{th} and 8^{th} year. Similarly, however generators in C26 need only three maintenance periods on the 3^{rd}, 6^{th} and 9^{th} years. In addition, the maintenance cost is assumed to be equivalent to 20% of their purchasing price. In general, these units are operated for y years (where $y \leq 10$). Hence, we have the general expressions

of:

$$\text{capital cost} : C_{cap} = \left[\sum_{r=1}^{n} C_{g_r} \right] \cdot (1 + \gamma\%)^{y} \tag{4.2}$$

$$\text{fuel cost} : C_{fuel} = \sum_{r=1}^{n} \left[C_{f_r}(1 + \gamma\%)^{y} + C_{f_r}(1 + \gamma\%)^{y-1} + \cdots + C_{f_r}(1 + \gamma\%)^{0} \right] \tag{4.3}$$

$$\text{maintenance cost} : C_{maint} = 20\% \left[\sum_{r=1}^{n} \left(C_{g_r}(1 + \gamma\%)^{\delta} \right) + \sum_{r=1}^{n} \left(C_{g_r}(1 + \gamma\%)^{2\delta} \right) + \cdots \right] \tag{4.4}$$

where C_{g_r} is the capital cost and C_{f_r} is the fuel cost of unit r, noting that we also need to add the capital, fuel and maintenance costs of swing generators in to the total costs.

By assigning $\gamma = 4\%$, the total investments of providing power to this military base (scrambled) load for the last ten years for all the feasible combinations are listed in Table 4.3. It can be seen that the combinations that contain four generators normally require less investment in total during the entire operating period and C21 requires the lowest capital investment. In other words, combinations with more generators can have lower life cycle cost. Although C26 consumes least amount of fuel, C24 is the best combination for overall life cycle cost. This shows the best fuel economical combination is not necessarily the best option. However, by implementing life cycle cost analysis, the best combination for investing can be readily identified. In addition, C24 has lowest total power among all four units combinations, which means each generator are loaded with higher operating points than other combinations when all generators are kept running. Put differently, the generators are operated in more efficient regions than other generators in other combinations during the peak load periods.

TABLE 4.3. Available Safe Combinations

No.	Generators				Power Sum (KW)	Fuel lmt 70% (gal)	Capital Costs (USD)	Total Costs (USD)
	Gen1 (KW)	Gen2 (KW)	Gen3 (KW)	Gen4 (KW)				
C_3	750	1000	1250		3000	49425	710k	36669k
C_4	600	1000	1250		2850	49315	685k	36506k
C_7	500	1000	1250		2750	49272	655k	36371k
C_{17}	600	750	1000	1250	3600	49294	850k	36724k
C_{18}	500	750	1000	1250	3500	49234	820k	36589k
C_{19}	500	600	1000	1250	3350	49229	795k	36507k
C_{20}	500	600	750	1250	3100	49229	735k	36318k
C_{21}	500	600	750	1000	2850	49285	640k	36058k
C_{22}	200	750	1000	1250	3200	49214	750k	36355k
C_{23}	200	600	1000	1250	3050	49157	725k	36237k
C_{24}	200	600	750	1250	2800	49154	665k	36047k
C_{26}	200	500	1000	1250	2950	49152	695k	36140k

4.5. Conclusion

In this chapter, we have presented the use of a KKT conditions-based optimal dispatch method to select generation units so as to form a microgrid. The approach minimizes the total fuel usage during the entire operating period, with constraints for either prime-rated or continuous-rated generation applications, as well as practical operating constraints (e.g., spinning reserve and safety margin for load transients) and costs (e.g., startup and cool-down). Note that the KKT approach guarantees to find the global optimum (for a given load profile), so that the configuration selection decision is systematic. Note further that the approach utilizes optimization-based analysis (i.e., the method selects from among all points satisfying the KKT optimality conditions). As such it not only guarantees to find the true optimum (versus heuristic search approaches), but is also readily capable of being extended with further realistic constraints/costs (versus purely analytic approaches).

This approach is taken further with economic life cycle analysis tools. These augment the above (optimal) fuel-usage/running-costs with other costs (e.g., capital costs and maintenance costs), incurred over the full life cycle. Performing future equivalent economic analysis (correcting for the time value of money) allows for a direct comparison of various combinations/scenarios. It is seen in the examples that the optimum selection with regard to overall life cycle cost does not necessarily coincide with the configuration with minimum running costs.

By introducing safe ratio, system reliability is enhanced before the load is dispatched. During load dispatch process, the spinning reserve ensures there are enough power reserve to cope with load transients for the military base application. Results shows that although C26 consumes the least amount of fuel, C24 has better economical performance. For constant load applications, C23 is the best option, which consumes less fuel in different ratings and with bigger power reservation capacity. KKT conditions base optimal generators selection approaches do provide the true optimum.

CHAPTER 5

MODELING I: NATURAL GAS ENGINE

5.1. Introduction

From both environmental and economic points of view, natural gas is widely used for electricity generation and transportation. In the United States, more than 30% of electricity is generated by natural gas. In recent years, with the modern technology in hydraulic fracturing, shale gas as a kind of natural gas is expected to be significantly expand worldwide energy supply.

Natural gas internal combustion (IC) engines are mostly used as emergency power units or independent power supply stations [81]. A natural gas engine is different from a diesel engine in terms of how the fuel is delivered. For a natural gas engine, fuel is injected at various locations, such as: before the compressor, before (or after) the throttle, or right at the manifold ports. Each type of engine has their own configurations. For a pre-mixed lean burn natural gas engine, which is modelled in this chapter, fuel is injected before a turbocharger because of the low fuel pressure (normally just quarter Psi higher than the ambient pressure). In contrast, for a diesel engine, diesel fuel is mostly injected directly into the combustion chamber by using high pressure common rail with injectors. As a result, for natural gas engines, there is a considerable fuel transport delay. In other words, natural gas engines cannot react promptly to produce desired power to meet rapid load variations. Furthermore, air-fuel ratio is not controlled in a diesel engine. Diesel engines suck as much air as necessary since the fuel status is liquid. There is no problem of lighting the fuel. However,

for a lean burn natural gas engine, air-fuel ratio (AFR) should be controlled tightly. The relative air/fuel ratio (λp) is in the range of 1.5 to 1.7. The excess air is used to reduce the peak in cylinder temperature. If the mixture is too rich, the in cylinder peak temperature of combustion is increased and more NO_x is formed. If it is too lean, the combustion may not even start (misfire). Typically the excess oxygen is measured by a universal exhaust gas oxygen (UEGO) sensor, which is mostly located at the downstream of the exhaust system. This implies there is a significant time-varying delay for the combusted gas to reach the UEGO sensor. To resolve such long time delay problems, more sophisticated control techniques are needed. Another commonly used method for reducing emissions is to add the exhaust gas recirculation (EGR) flow from the exhaust manifold. The benefit of using EGR is that three-way catalyst can be utilized. The "three-way catalyst" (TWC) has three main duties, which include the oxidation of CO, the oxidation of unburnt hydrocarbons (HC's) and the reduction of NO_x to N_2 [124]. In order to have the TWC work properly, more complex structure and control are needed to ensure the engine is running at stoichiometric conditions [124].

Many different control methods have been applied for engine control. Most of them are focused on controlling gasoline and diesel engines (automotive engines). Not much work has been done for industrial lean burn natural gas engine control. There are some exceptions. With the high standard of emission control, classical control based algorithms may not satisfy the requirements anymore. A H_∞ controller was designed in [81] to control throttle valve and recirculation valve of the engine for speed control. To have engine control units (ECU) control engines stably, robustly and efficiently, lots of calibration work has to be done. This process consumes a lot of power, time and other resources. Since the system uncertainties are

not considered in H_∞ control, system robustness and model uncertainties are not addressed, which means long period of calibration still has to be carried out. The uncertainties also include the parameter variations with engines aging processes. Gain-scheduled control is proposed in [125] for diesel engine AFR control. Gain-scheduled control only provides local stability and performance guarantees near equilibrium point models. It is critical to ensure the controller is still valid for entire nonlinear system operating range [83]. In [84], a fuzzy logic and neural networks system for regulating the AFR of a compressed natural gas (CNG) engine is proposed. As the author stated, the method may be difficult to achieve in transient conditions. There are also other issues with fuzzy logic control and neural network control, including manual tuning, tradeoff of performance and robustness, long learning curve and so on.

Furthermore, above mentioned work is either focused on AFR control or engine speed control, although many of them have used multi-variable control methods. None of them are really controlling AFR and engine speed at the same time. In this chapter, we would like to propose a μ-synthesis based robust control technique for both AFR and engine speed control with a single MIMO controller.

Fundamentally, there are two criteria to meet for controlling a pre-mixed lean burn natural gas engine. Firstly, maintaining a constant engine speed, while producing varying power to meeting load demands in order to maintain a solid grid frequency in islanded mode. Secondly, reducing exhaust diluent to meet the required emission regulations. In order to reduce the emission for a natural gas lean burn engine, we need to maintain a constant AFR. However, AFR is very sensitive to small fluctuations of the engine parameters. This task is

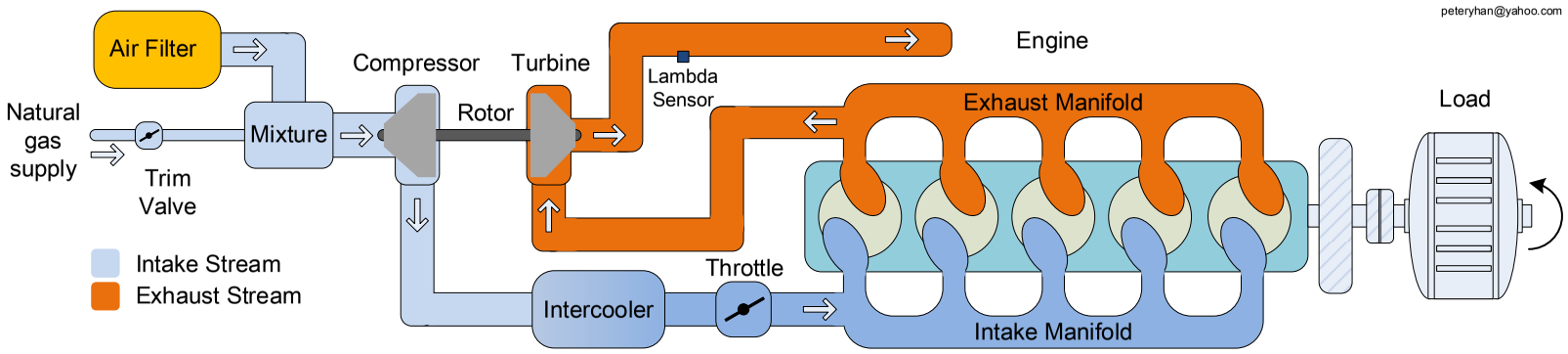

FIGURE 5.1. Pre-mixed Natural Gas Engine Model. (If it is a lean-burn engine, then there is no catalyst.)

very complex [126]. In addition, for a pre-mixed natural gas engine, the long fuel transport delay makes both speed and emission control more difficult.

In this dissertation, we would like to propose a robust control approach for controlling both the engine speed and AFR for natural gas engine systems as well as microgrid systems. The essential idea is to develop a controller that is not too sensitive to engine parameter variations, in order to reduce the calibration time and increase the flexibility of the controller. In addition, the controller should provide robust performance under extreme conditions and operating points. In order to study the engine control, we develop a control orientated pre-mixed natural gas engine model in this chapter. The chapter is divided into the following sections. In section 5.2, the overall configuration of the modelled engine is described. Following it, all the components that form a natural gas engine are modelled in detail in section 5.3 to section 5.11. The major components include: manifolds, engine block, turbocharger and various orifice elements. The conclusion forms the last section of the chapter. For our research, the natural gas engine is modelled in Simulink^{TM} environment.

5.2. Overall Configuration of the Modelled Natural Gas Engine

The configuration of the developed natural gas engine model is shown in Fig.5.1. This particular natural gas engine model presented here includes the following parts: air filter, fuel valve, mixture volume (mixer), turbocharger, intercooler, intake manifold, engine block and exhaust manifold. Because of the lower pressure at the mixer caused by compressor and/or engine intake stroke, air and fuel flow are mixed at the mixer and sucked further down to the compressor. When a good controller is deployed, trim value should regulate the fuel flow to ensure near constant AFR to reduce emissions. The compressor of the turbocharger compresses the mixture to increase its density. The intercooler cools the compressed mixture

to further increase its density. The reason for increasing the mixture density is to raise the amount of mixture in the cylinders. With the same engine displacement, if more mixture can be pushed into the combustion chamber, more power can be produced. It is a way to increase the engine power to weight ratio and decrease the engine physical size. The throttle regulates the flow rate of mixture to control the engine output power. The intake manifold is a reservoir that stores the mixture. Once the inlet valves are open, the mixture rushes into the combustion chamber. Combustion happens inside of the cylinders and is ignited by spark plugs. During the exhaust stroke, the exhaust gas goes into the exhaust manifold. The turbine of the turbocharger is blown by the hot high pressure exhaust gas. With the mechanical linkage of turbocharger rotor, the mechanical power generated by the turbine is passed to the compressor with some friction losses. Compressor uses the torque generated by the turbine to increase the upstream flow rate. After the exhaust gas passes through turbine, its temperature and pressure drop. Before exhaust gas reaches atmosphere, the last component it goes through is the muffler.

These parts can be catalogued into orifice elements, volume elements and combustion elements. An abbreviation for each component is given in brackets in Table.5.1. For this particular model, ambient conditions are used for all the pressure and temperature initial conditions. It is a control oriented mean value model (MVM), which uses lumped parameters to describe a physical system. A control oriented model represents input-output behavior of a system with reasonable accuracy and inexpensive computational effort. In this kind of model, the system dynamics are characterized by using differential equations [127]. The differential equations used are physics based representations of the components of a natural

TABLE 5.1. Engine parts classification

Class	Orifice	Volume	Combustion
Parts	Air Filter (AF) Trim Valve (TR) Compressor (CP) Turbine (TB) Throttle Valve (TV)	Mixture (Mix) Intercooler (Int) Intake Manifold (IMF) Exhaust Manifold (EMF)	Engine Blocks (Eng)

gas engine. The essential idea of this model is to capture most (if not all) of the system dynamics (especially transient responses) with rapid simulation speed.

There is a complementary relationship between orifice elements and volume elements. On one hand, the upper and lower orifice elements of a volume element provide the mass flow rate in and out of the volume with their associated properties. The mass variation determines the volume states. On the other hand, the volume elements next to an orifice element supplies the states for an orifice element to compute the mass flow. This relationship applies throughout the entire system.

5.3. Air Filter

Physically, an air filter is the first device on the air inlet path. It purifies the air going into the combustion chamber to prevent unnecessary engine wear. In many engine models, the air filter is simply ignored. In fact, it is important to include an air filter model, since it produces a pressure drop which propagates through the inlet system and affects the entire engine flow [128]. In this chapter, the air filter is considered as a giant orifice. Therefore the air flow rate can be calculated by using standard compressible fluid flow equations [129]. It consists of two parts: sub-sonic flow and sonic flow. These two equations are switched based on a critical value κ. The compressible flow equation can be expressed as:

$$\dot{m} = \begin{cases} \frac{C_d A_{af} P_{up}}{\sqrt{RT_{up}}} \left(\frac{2\gamma}{\gamma - 1} \left[\left(\frac{P_{dw}}{P_{up}} \right)^{\frac{2}{\gamma}} - \left(\frac{P_{dw}}{P_{up}} \right)^{\frac{\gamma+1}{\gamma}} \right] \right)^{\frac{1}{2}} & if \ \frac{P_{dw}}{P_{up}} > \kappa \\ \frac{C_d A_{af} P_{up}}{\sqrt{RT_{up}}} \gamma^{\frac{1}{2}} \left(\frac{2}{\gamma+1} \right)^{\frac{\gamma+1}{2(\gamma-1)}} & if \ \frac{P_{dw}}{P_{up}} < \kappa \end{cases}$$

where the critical value is defined as: $\kappa = (\frac{2}{\gamma+1})^{\frac{\gamma}{\gamma-1}}$. It is calculated by using gas specific heat ratio γ; P_{up} and T_{up} are the upstream pressure and temperature; P_{dw} is the downstream pressure; C_d is the discharge coefficient, which can be determined experimentally; A_{af} is the air filter cross section area; R is the gas constant; γ is the specific heat ratio. For an air filter, the upstream pressure and temperature are the ambient pressure P_{amb} and temperature T_{amb}. The downstream pressure is obtained by the very next volume element - the mixture volume P_{mix}.

The compressible flow equation is used not only for modeling the air filter, but also when the fuel valve and throttle valve are modeled. The critical values and gas properties are different at each orifice element. Note that since an air and fuel mixture goes through the throttle valve, the critical value and gas constant are computed based on AFR.

5.4. Fuel Valve

A fuel valve controls natural gas flow rate, in order to maintain a constant AFR. A fuel valve is also modeled by using compressible fluid flow equation. The effective area of an air filter is its cross section area. Here a fuel valve is modeled as a butterfly valve, the effective area is adjusted by varying the butterfly valve plate angle. A butterfly valve open area A_b can be ascertained by:

$$A_b = \frac{\pi \cdot {D_f}^2}{4} \left(1 - \frac{\cos(\psi_f)}{\cos(\psi_{f_0})} \right) \tag{5.1}$$

where ψ_f is the fuel valve plate angle; ψ_{f_0} is the minimum fuel valve plate angle (angle between the bore and the plate when the valve is closed); D_f is the fuel pipe diameter. By using A_b to replace A_{af} in the compressible fluid flow equation in air filter model, the fuel valve model is obtained. Here the upstream conditions are commonly the regulated natural gas pressure P_f and temperature T_f. The gas constant (R_{ng}) and specific heat ratio(γ_{ng}) of natural gas are used in the equation. Fuel and air are mixed in the mixture volume, and the downstream states are obtained from it.

5.5. Mixture Volume

In general, there are some assumptions for modeling of volume elements. Here we adopt some of them from [130], such as:

(1) all the thermodynamic states including pressure, temperature, composition, gas constant and specific heat ratio are the same over the entire volume.

(2) All the volume elements have fixed size.

(3) All of volume elements are modeled by using the filling and emptying method.

(4) Only the input and output mass flows are considered. Leakages are ignored.

(5) The reservoirs store mass and thermal energy.

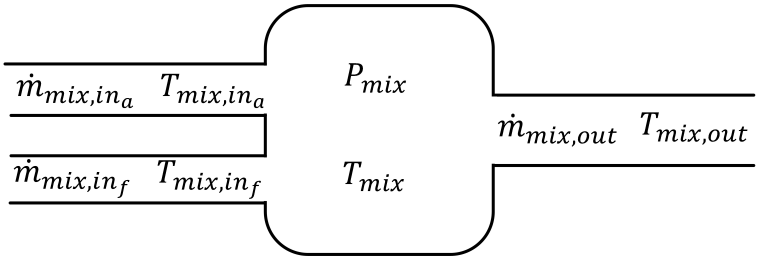

FIGURE 5.2. Mixture volume

The schematic of a mixture volume is shown in Fig.5.2. As the first volume element on the inlet path, the mixture volume is the chamber where natural gas and air are mixed. We assume they are mixed homogeneously and there is no heat or mass transfer through the walls. By using the ideal gas law, we know the mass inside of the mixture m_{mix} is:

$$m_{mix} = \frac{P_{mix} V_{mix}}{R_{mix} T_{mix}} \tag{5.2}$$

where V_{mix} is the mixture volume size; R_{mix} is the gas constant of the mixture gases inside of the mixture. It is calculated based on the flow rate of air and fuel; T_{mix} is the temperature of the mixed gases, which equivalent to the outlet temperature of the gases $T_{mix,out}$. For a running engine, the mass flow through the engine is continuous, then the mass flow rate variation of a mixture volume is expressed as [131]:

$$\dot{m}_{mix} = \dot{m}_{mix,in_f} + \dot{m}_{mix,in_a} - \dot{m}_{mix,out} \tag{5.3}$$

where $\dot{m}_{mix,in_f}$ and $\dot{m}_{mix,in_a}$ are the mixture inlet fuel and air flow rate correspondingly; Here mixture volume is different from other volumes, since it has two inlet flows that have different temperature and properties. $\dot{m}_{mix,out}$ is the flow rate that leaves the mixture volume; T_{mix,in_f} and T_{mix,in_a} are the fuel and air inlet flow temperatures, respectively.

By substituting Equation. 5.3 into Equation. 5.2 and considering the properties of the inlet flows individually, we can easily obtain the mixture volume pressure dynamics model, which can be expressed by the following first order differential equation:

$$\begin{aligned}\dot{P}_{mix}(t) = &\frac{\gamma_f R_f}{V_{mix}}\dot{m}_{mix,in_f}(t)T_{mix,in_f}(t) \\ &+\frac{\gamma_a R_a}{V_{mix}}\dot{m}_{mix,in_a}(t)T_{mix,in_a}(t) \\ &-\frac{\gamma_{mix} R_{mix}}{V_{mix}}\dot{m}_{mix,out}(t)T_{mix,out}(t)\end{aligned} \tag{5.4}$$

where γ_f, γ_a and γ_{mix} are the specific heat ratio of fuel, air and mixture. γ_{mix} is computed by finding the mixture c_p and c_v based on masses of air and fuel inside of the volume.

By integrating $\dot{P}$, volume pressure state is resolved. Based on the mass conservation law, the difference of the inlet flow and outlet flow represents the change of mass in the volume [132]. By using ideal gas law and Equation. 5.4, volume temperature dynamic can be expressed as:

$$\dot{T}_{mix,out}(t) = \frac{\dot{P}_{mix}(t)V_{mix}}{R_{mix}\int \Delta\dot{m}_{mix}dt} \tag{5.5}$$

where $\Delta\dot{m}_{mix} = \dot{m}_{mix,in_f} + \dot{m}_{mix,in_a} - \dot{m}_{mix,out}$. The initial condition of $\int \Delta\dot{m}_{mix}dt$ is found by using ideal gas law with ambient temperature, pressure and air gas constant.

In the developed engine model, there is a properties computation block in each volume element. The properties block is used to find the mixed gases properties inside the volume, including: AFR, c_p, c_v, γ, R, x_{air} and x_{fuel}, where x_{air} and x_{fuel} denote the friction of air and fuel inside the volume. All the computations are done based on masses. Here by integrating the mass flow rate differences for fuel and air separately, the actual masses of air and fuel within the volume can be found as:

$$m_{vol,f} = \int \Delta\dot{m}_{vol,f}dt + IC_f \tag{5.6}$$

and

$$m_{vol,a} = \int \Delta \dot{m}_{vol,a} dt + IC_a \tag{5.7}$$

where $\Delta \dot{m}_{vol,f} = \dot{m}_{vol,in_f} - \dot{m}_{vol,out_f}$; $\Delta \dot{m}_{vol,a} = \dot{m}_{vol,in_a} - \dot{m}_{vol,out_a}$; IC_f and IC_a are the initial conditions. Here $\dot{m}_{vol,in_f}$ and $\dot{m}_{vol,in_a}$ are obtained from the upstream orifice element; $\dot{m}_{vol,out_f}$ and $\dot{m}_{vol,out_a}$ are acquired from the downstream orifice element. The calculated properties are also used by the downstream orifice element.

5.6. Turbocharger

A turbocharger consists of a turbine, compressor and rotor. It uses the available energy in the engine exhaust to increase the inlet flow [129]. By increasing inlet flow, more power can be produced with the same size of engine displacement. Since turbochargers can increase engines output power and reduce emissions at the same time with three-way catalyst, they have been well adopted on modern engines that run at stoichiometry [128]. For a lean burn engine, exhaust emission is regulated by controlling AFR tightly.

It is not trivial to describe the behavior of a turbocharger at different engine running conditions. This is especially true when there is no waste gate, compressor bypass or variable geometry turbine (VGT) associated for regulating the turbine back pressure. All the inlet flow must go through all the components between the compressor and turbine path. If the compressor and the turbine are not well matched, the turbocharger model would not behave properly, where choke and surge may occur. In other words, the model is not representing a well established engine system. For example, if a compressor is operated in the surge region, flow instability is expected. For a real turbocharger, continued operation within the surge region can cause premature turbo failure due to heavy thrust loading [133]. High thrust

loading is created by the difference in air pressures across the turbine and compressor wheels [134]. If a compressor is operated in the choke region, a bigger compressor should be adopted, since it cannot provide sufficient flow. In other words, there is a matching problem between the adopted turbocharger and the engine. Both algebraic equations and differential equations are used to model a turbocharger. The former describe the 'instantaneous' performance and the latter characterize the 'time developing' variables [57]. Through this model, the initial conditions for each state is pre-calculated and embedded into the model to ensure the model simulation starts smoothly. In addition, the initial conditions can also be defined in the software package. The embedded initial conditions at each components have lower priority compare to those defined in 'model configuration parameters' in Matlab$^{\mathrm{TM}}$. In other words, if initial condition is defined at 'model configuration parameters', it will overwrite the initial conditions defined at the components level.

5.6.1. *Turbine*

The power generated by a real turbine can be expressed as [132]:

$$P_{tb} = \dot{m}_{tb} c_{p_{tb}} \left(T_{tb_{in}} - T_{tb_{out}}\right) \tag{5.8}$$

where $\dot{m}_{tb}$ is the turbine mass flow rate; $T_{tb_{in}}$ is the inlet temperature of a real turbine, it is assumed to be the same as the exhaust temperature T_{emf}; Here 'real' is relative to 'ideal'; For a ideal turbine, there is no heat loss at all. $T_{tb_{out}}$ is the temperature at the outlet of a real turbine. From the table of isentropic relations for an ideal gas, it is known that:

$$\left(\frac{T_{tb_{out}}}{T_{emf}}\right) = \left(\frac{P_{tb_{out}}}{P_{emf}}\right)^{\frac{\gamma_e - 1}{\gamma_e}} \tag{5.9}$$

where $P_{tb_{out}}$ is the pressure at the turbine outlet, γ_e is the turbine inlet mixture gas specific heat ratio.

Suppose the turbine generates power P_{tb}, denote $P_{tb,isen}$ and $T_{tb_{out},isen}$ as the power and temperature at the outlet of an isentropic turbine, then the turbine isentropic efficiency can be expressed as [61]:

$$\eta_{tb} = \frac{P_{tb}}{P_{tb,isen}} = \frac{T_{emf} - T_{tb_{out}}}{T_{emf} - T_{tb_{out},isen}} \tag{5.10}$$

From Equation. 5.10, we get $\eta_{tb}\left(T_{emf} - T_{tb_{out},isen}\right) = T_{emf} - T_{tb_{out}}$, by substituting it into Equation. 5.8, we obtain $P_{tb} = \dot{m}_{tb} c_{p_{tb}} \eta_{tb}\left(T_{emf} - T_{tb_{out},isen}\right)$. Since $T_{tb_{out},isen} = T_{emf}\left(\frac{P_{tb_{out}}}{P_e mf}\right)^{\frac{\gamma_e - 1}{\gamma_e}}$, then:

$$P_{tb} = \dot{m}_{tb} c_{p_{tb}} \eta_{tb} T_{emf} \left\{1 - \left(\frac{P_{tb_{out}}}{P_{emf}}\right)^{\frac{\gamma_e - 1}{\gamma_e}}\right\} \tag{5.11}$$

or put into torque form:

$$T_{tb} = \frac{\dot{m}_{tb} c_{p_{tb}} \eta_{tb} T_{emf}}{\omega_t c} \left\{1 - \left(\frac{P_{tb_{out}}}{P_{emf}}\right)^{\frac{\gamma_e - 1}{\gamma_e}}\right\} \tag{5.12}$$

Also by using Equation. 5.10, we can find the turbine outlet temperature as:

$$T_{tb_{out}} = \eta_{tb}\left(T_{emf} - T_{tb_{out},isen}\right) - T_{emf} \tag{5.13}$$

After some simple algebraic manipulation, we obtain:

$$T_{tb_{out}} = T_{emf}\left\{1 - \eta_{tb}\left[1 - \left(\frac{P_{tb_{out}}}{P_{emf}}\right)^{\frac{\gamma_e - 1}{\gamma_e}}\right]\right\} \tag{5.14}$$

For a real turbocharger, the turbine steady state data is usually provided by the manufacturer in either map or tabular form. The data in the map or table is put into lookup

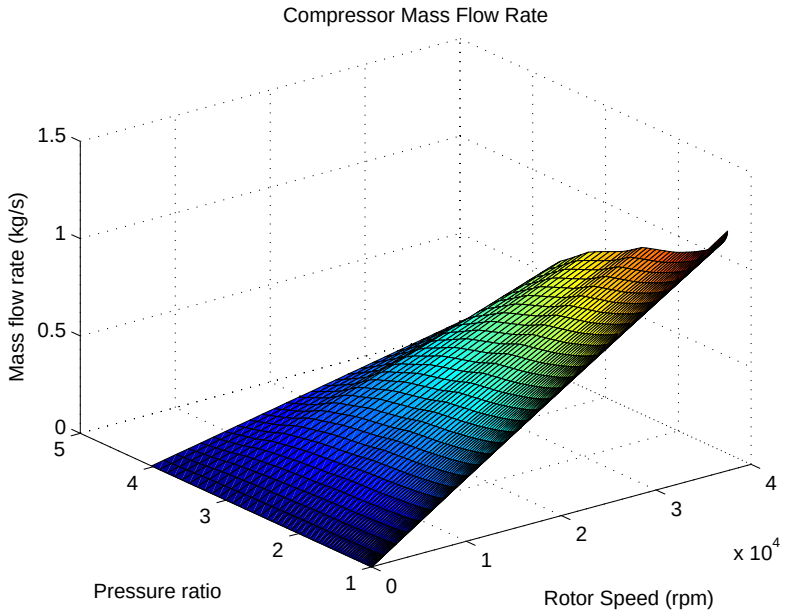

FIGURE 5.3. Compressor mass flow rate map

tables to represent its behavior. The intermediacy data are found by using linear or other interpolation and extrapolation methods [135].

$$\dot{m}_{tb_{corr}} = f_{\dot{m}_{tb}}\left(N_{corr}, \frac{P_{emf}}{P_{tb_{out}}}\right) \tag{5.15}$$

$$\eta_{tb} = f_{\eta_{tb}}\left(N_{corr}, \frac{P_{emf}}{P_{tb_{out}}}\right) \tag{5.16}$$

The provided turbine and compressor maps have mass flow rate as the x-axis and pressure ratio ($\Pi = \frac{P_{dw}}{P_{up}}$) across the devices as y-axis. At a particular pressure ratio (Π), if the turbocharger rotor speed is known, then the mass flow rate and efficiency of the devices are specified (can be read from maps). The actual values, which form the performance maps, can be calibrated by:

$$N_{tc} = N_{corr} \cdot \sqrt{\frac{T_{emf}}{T_{std}}} \tag{5.17}$$

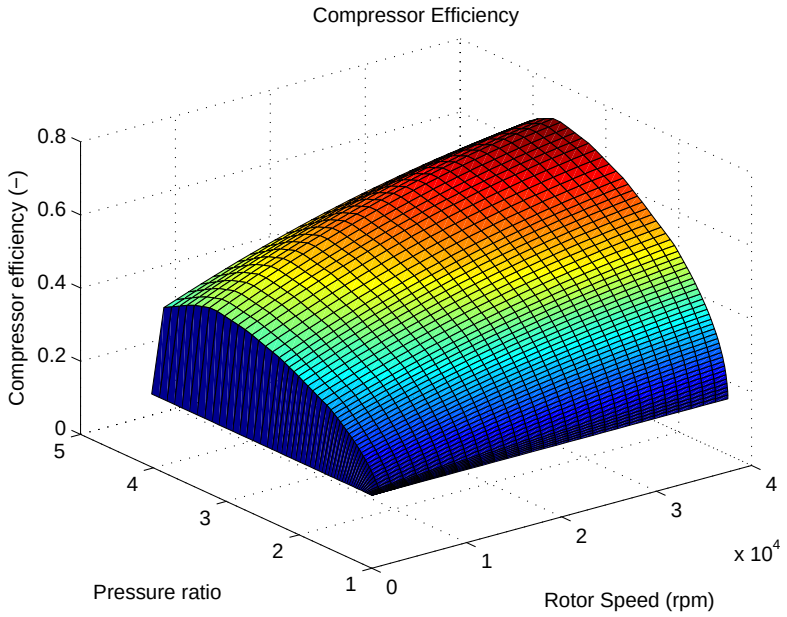

FIGURE 5.4. Compressor efficiency map

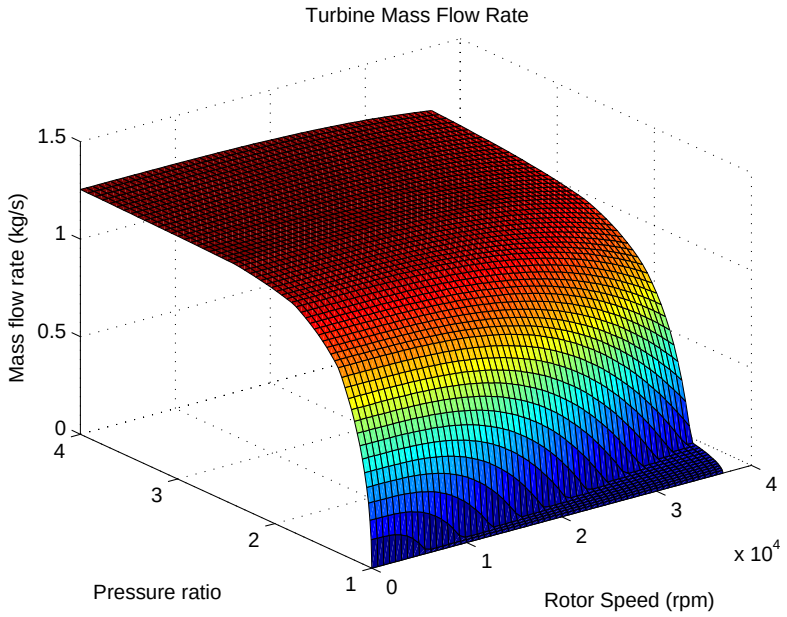

FIGURE 5.5. Turbine mass flow rate map

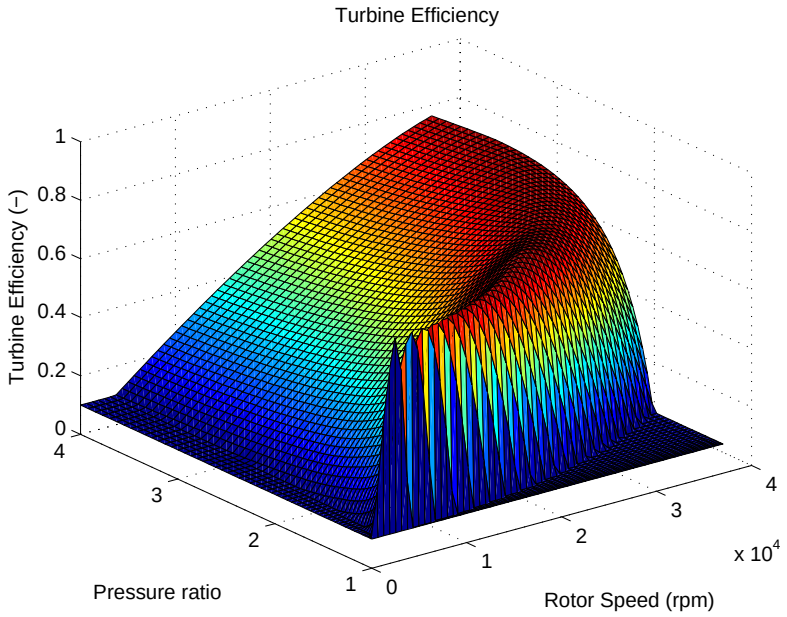

FIGURE 5.6. Turbine efficiency map

$$\dot{m}_{tb} = \frac{\dot{m}_{tb_{corr}} \frac{P_{emf}}{P_{std}}}{\sqrt{\frac{T_{emf}}{T_{std}}}} \tag{5.18}$$

A set of compressor and turbine mass flow rate and efficiency maps used in the model are presented in Fig.5.3 to Fig.5.6. Our maps are created by manipulating existing turbocharger maps.

5.6.2. *Compressor*

Similarly, by using the enthalpy efficiency relationship, the torque absorbed for driving the compressor and the compressor outlet temperature is expressed as:

$$T_{cp} = \frac{\dot{m}_{cp} c_{p_{cp}} T_{int}}{\eta_{cp} \omega_{tc}} \left\{ \left(\frac{P_{int}}{P_{mix}} \right)^{\frac{\gamma_i - 1}{\gamma_i}} - 1 \right\} \tag{5.19}$$

$$T_{cp_{out}} = T_{mix}\left\{1 + \frac{1}{\eta_{cp}}\left[\left(\frac{P_{int}}{P_{mix}}\right)^{\frac{\gamma_i - 1}{\gamma_i}} - 1\right]\right\} \tag{5.20}$$

where γ_i is the specific heat ratio of the compressor inlet mixture gases. Here it is the mixture of natural gas and air. By using the same method, the compressor flow rate and efficiency can be specified and calibrated as follow.

$$\dot{m}_{cp_{corr}} = f_{\dot{m}_{cp}}\left(N_{corr}, \frac{P_{int}}{P_{mix}}\right) \tag{5.21}$$

$$\eta_{cp} = f_{\eta_{cp}}\left(N_{corr}, \frac{P_{mix}}{P_{int}}\right) \tag{5.22}$$

$$N_{tc} = N_{corr} \cdot \sqrt{\frac{T_{mix}}{T_{std}}} \tag{5.23}$$

$$\dot{m}_{cp} = \frac{\dot{m}_{cp_{corr}} \frac{P_{mix}}{P_{std}}}{\sqrt{\frac{T_{mix}}{T_{std}}}} \tag{5.24}$$

5.6.3. *Turbocharger Rotor*

The rotor is a mechanical coupling between turbine and compressor [136]. The turbocharger speed state is derived from Newton's second law. Exhaust gas blows the turbine blades and generates rotational torque, and the generated torque is passed down to the compressor by the rotor. The spinning compressor uses its blades to compress inlet flow into the intercooler and downstream. During this process, torque generated by the turbine is consumed. This gives rise to:

$$T_t - T_c - T_{f_{tc}} = J_{tc} \cdot \dot{\omega}_{tc} \tag{5.25}$$

where T_t, T_c and $T_{f_{tc}}$ are the turbine, compressor and rotor bearing friction torque; J_{tc} is the total moment of inertia of turbine, compressor and rotor. T_f is often negligible. [131]

5.7. Intercooler

An intercooler or aftercooler structurally sits after a compressor. It reduces the temperature of compressed flow, which increases the flow density. By increasing the flow density, more air and fuel can be used for combustion process and more power is produced with the same size of engine displacement. A lower inlet flow temperature is also helping the engine to avoid knock (unwanted auto ignited combustion). It is a harmful phenomenon to the engine. With lower mixture temperature, it is more difficult for auto ignition to start. For most of the industrial engines, the compressed inlet flow is cooled by liquid.

Physically, a intercooler consists of series of tubes to allow mixture gas flows through. These tubes are surrounded by cooling medium. In order to maximize the cooling efficiency, the tubes are made very thin. Theoretically, one would think intercooler is a orifice element because it is constructed by tubes. However, it is modeled as a volume element in this chapter because of its noticeable volume relative to the engine displacement. The differential equations that model the intercooler are given below. They are derived from Equation. 5.4 and Equation. 5.5. There is an additional term (the first term) in Equation. 5.26, which is used to represent the heat losses through the intercooler.

$$\begin{aligned}\dot{P}_{int}(t) = \frac{\gamma_{int} R_{int} \dot{Q}_{int}}{c_{p_{int}} V_{int}} + \frac{\gamma_{int} R_{int}}{V_{int}} \dot{m}_{int,in}(t) T_{int,in}(t) \\ - \frac{\gamma_{int} R_{int}}{V_{int}} \dot{m}_{int,out}(t) T_{int,out}(t)\end{aligned} \tag{5.26}$$

$$\dot{T}_{int,out}(t) = \frac{\dot{P}_{int}(t) V_{int}}{R_{int} \int \Delta \dot{m}_{int} dt} \tag{5.27}$$

where $\dot{Q}_{int} = ht \cdot A \cdot (T_{cp_{out}} - T_{cool})$ is the heat loss rate (kW); ht is a heat transfer coefficient (kW/Km^2); A is heat transfer area (m^2); T_{cool} is the EGR coolant temperature

(K). In [128] and [135], the pressure drop across the intercooler is modeled by using the mass flow rate. The temperature drop is described with an efficiency coefficient, which is also a function of the mass flow rate. In other words, these models are just functions of the mass flow rate of the compressor. In addition, since this kind of model involves experimentally determined parameters, they need more experimental data for data fitting and parameter calibration. In our proposed model, volume states are described by physics laws, where more accurate system dynamics are captured with less requirement of experimental data. In addition, the gas properties are calculated in real time in our model.

5.8. Throttle Valve

The throttle valve is modeled with the same set of equations in 5.3 and 5.4. Since the mixture properties are different from fuel, and also the throttle valve has different geometry setup with the fuel valve, the parameters used in above mentioned equations must be changed accordingly.

5.9. Intake Manifold

In our setup, the intake manifold gathers the mixed air and fuel charge and distributes it into the different cylinders [137]. Intake manifold is one of the very important components on an engine, it provides mixture uniformly to all the cylinders [131]. By using the principle of energy conservation and the ideal gas law, the differential equations of the intake manifold are found as:

$$\begin{aligned}\dot{P}_{imf}(t) = &\frac{\gamma_{imf} R_{imf}}{V_{imf}} \dot{m}_{imf,in}(t) T_{imf,in}(t) \\ &- \frac{\gamma_{imf} R_{imf}}{V_{imf}} \dot{m}_{imf,out}(t) T_{imf,out}(t)\end{aligned} \tag{5.28}$$

The intake manifold volume temperature is found by using the pressure state and mass inside of the volume.

$$\dot{T}_{imf,out}(t) = \frac{\dot{P}_{imf}(t)V_{imf}}{R_{imf}\int \Delta\dot{m}_{imf}dt} \tag{5.29}$$

where $\Delta\dot{m}_{imf} = \dot{m}_{imf,in} - \dot{m}_{imf,out}$; $\int \Delta\dot{m}_{imf}dt = m_{imf}$ is the mass of air and fuel mixture within the intake manifold at any time t; V_{imf} is the intake manifold size and R_{imf} is the gas constant of the mixed gases within the volume.

5.10. Engine Block

The engine block can be considered the most important element in a engine model. This is the place where the combustion events take place and torque is generated. In this natural gas engine MVM, the mixture flow rate goes into the combustion chamber is computed by using speed density equation. Based on the fuel lower heating value and engine thermal efficiency, the indicated torque of the engine can be found. In this section, a experiment based engine frication model is presented as well. By using Newton's second law with these torque models and the load, the engine crankshaft dynamic model is obtained. In the following sections, engine block model is derived step by step.

5.10.1. *Speed Density*

The mixture flow into the cylinders of the engine is modelled with the standard model based on the volumetric efficiency [58],

$$\dot{m} = \frac{\eta_v \cdot P_{imf} \cdot V_d \cdot N}{120 \cdot R \cdot T} \tag{5.30}$$

where $\dot{m}$ is the total mass flow rate that goes into the engine cylinders (kg/s); η_v is the volumetric efficiency, it indicates how efficiently the engine can breathe during the intake

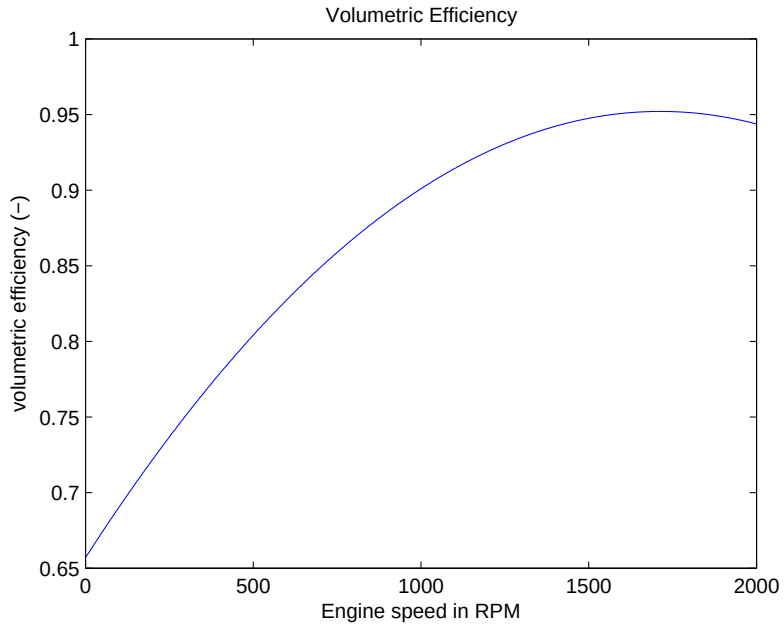

FIGURE 5.7. Engine speed influence on volumetric efficiency for a SI engine

strokes; ρ is the density of the mixture (kg/m^3); V_d is the engine displacement (m^3); N is the engine speed (rpm). The volumetric efficiency is the measure of the breathing ability of an engine. As indicated in [135], $\eta_v = f(N, P_{imf})$ is a function of engine speed and intake manifold pressure. Alternatively, a quadratic function with engine speed as the variable may be used as well [131][136].

$$\eta_v = a_0 {\omega_e}^2 + a_1 \omega_e + a_2 \tag{5.31}$$

where a_0, a_1 and a_2 are constants that are identified from experimental data; ω_e is the engine angular velocity (rad/s). A set of proposed constants are given in [131], and the plot is shown in Fig.5.7. It can be seen that the power generation engine is designed to have its highest efficiency at its rated speed. In addition, the volumetric efficiency of a large engine does not vary significantly around its rated speed.

5.10.2. *Indicated Torque*

Since air and fuel fraction are tracked through the model by the properties calculation blocks, we can find the amount of air and fuel charge that goes into the cylinders. The product of the fuel mass in the cylinders, the fuel lower heating value (LHV) and indicated efficiency is the mean indicated torque.

$$T_i = m_f \cdot Q_{LHV} \cdot \eta_{ind} \tag{5.32}$$

where m_f is calculated by using the speed density equation and fuel fraction. In both [135] and [131], a curve-fitted experimental based expression of η_{ind} is given as: $\eta_{ind} = (b_0 N^2 + b_1 N + b_2)(1 - b_3 \lambda^{b_4})$. η_{ind} is known as the engine indicated thermal efficiency and it has a parabolic form. It is a function of engine speed and the relative AFR (λ). Heat losses through the wall are relatively large at very low speeds, which reduces the engine efficiency. While at very high engine speeds, the combustion time is relatively larger than the available time interval in the expansion stroke [130]. In Fig.5.8, a set of indicated efficiency curves are shown for different λ.

As shown in Fig.5.9, besides the indicated torque, the rest of energy that comes from burning fossil fuel can be computed by $Q_{loss} = m_f \cdot Q_{LHV} \cdot (1 - \eta_{ind})$, which is identical to the sum of $Q_{coolant}$ and $Q_{exhaust}$. It is the heat loss through the engine coolant and the energy leaves the combustion chamber with exhaust gases. In this chapter, Q_{loss} is equivalently divided to form $Q_{coolant}$ and $Q_{exhaust}$.

5.10.3. *Friction and Pumping Losses*

Engine friction model is usually estimated experimentally. For example, motoring tests, measure brake torque from a dynamometer and subtract brake torque from the indicated

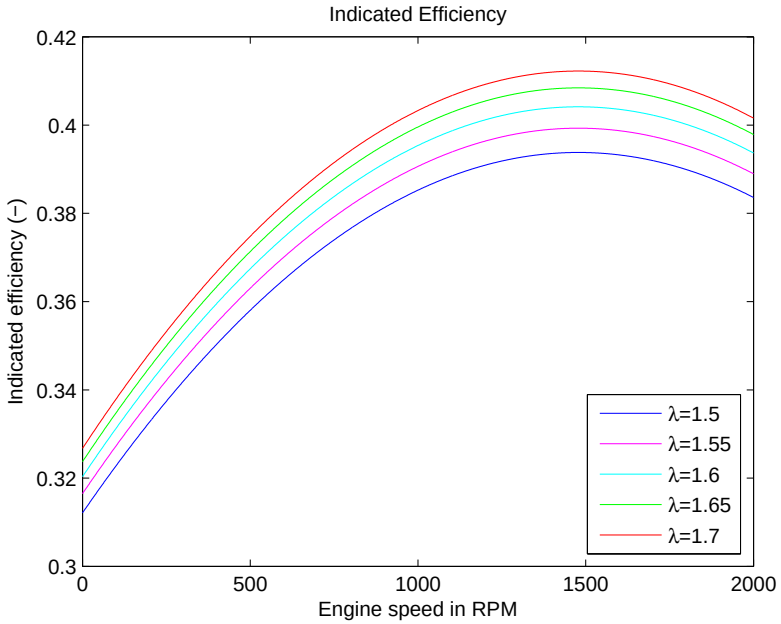

FIGURE 5.8. Engine speed and relative AFR influence on indicated efficiency for a SI engine

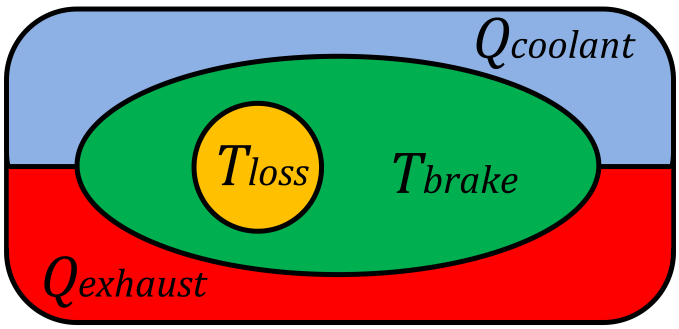

FIGURE 5.9. Energy split

torque acquired from cylinder pressure map [135]. In [138], a detailed spark ignited engine friction model is presented and an improved model of [138] is given in [139]. In the developed

model, we have limited the complexity of the friction model. The proposed friction losses and pumping losses model in [140] is adopted. The friction losses and pumping losses are expressed in Equation. 5.33 and Equation. 5.34.

$$F_{loss}(t) = c_0\omega_e^2 + c_1\omega_e + c_2 \tag{5.33}$$

$$P_{loss}(t) = d_0\omega_e P_{imf} + d_1 P_{imf} \tag{5.34}$$

By summing them together, we get the total engine friction and pumping losses in Equation. 5.35.

$$T_{loss}(t) = c_0\omega_e^2 + c_1\omega_e + c_2 + d_0\omega_e P_{imf} + d_1 P_{imf} \tag{5.35}$$

where c_i and d_i are constants that are determined experimentally.

5.10.4. *Crankshaft Dynamics*

By subtracting T_l from indicated torque, the brake torque is obtained. The brake torque is used to drive our load. Newton's second law is used again here to find the crankshaft speed (engine speed).

$$T_i(t - \tau_i) - T_{loss}(t) - T_{load}(t) = I_{eng} \cdot \dot{\omega}(t) \tag{5.36}$$

where I_{eng} is the engine crankshaft and flywheel inertia. A time delay term τ_i is added to indicated torque. The time delay is due to engine cycle delays, such as ignition delay, cylinder pressure force propagating, fuel-air mixing and so on [135].

5.11. Exhaust Manifold

The hot exhaust gas rushes from each cylinder exhaust port into the exhaust manifold and this is combined together to form the exhaust flow. Similar approach for modelling intake manifold is deployed here to model the exhaust manifold. The outlet of the exhaust manifold transports the exhaust gas to the turbine, where some of the exhaust energy is extracted for increasing the inlet flow.

$$\begin{aligned}\dot{P}_{emf}(t) = &\frac{\gamma_{emf} R_{emf}}{V_{emf}} \dot{m}_{emf,in}(t) T_{emf,in}(t) \\ &- \frac{\gamma_{emf} R_{emf}}{V_{emf}} \dot{m}_{emf,out}(t) T_{emf,out}(t)\end{aligned} \tag{5.37}$$

$$\dot{T}_{emf,out} = \frac{\dot{P}_{emf}(t) V_{emf}}{R_{emf} \int \Delta \dot{m}_{emf} dt} \tag{5.38}$$

where $\Delta \dot{m}_{emf} = \dot{m}_{emf,in} - \dot{m}_{emf,out}$; γ_{emf} and R_{emf} are the properties of the mixture gases inside of the exhaust manifold. Since we are modeling a lean burn engine, there is excess air in the mixture. Volume properties are computed by its attached properties block.

5.12. Conclusion

In this chapter, a mean-value-model for a pre-mixed turbocharged natural gas engine is developed. In this developed model, each component of the physical engine is modelled by using physics laws and experimental data. A simulink^{TM} based engine model is realized by using the proposed equations in this chapter. The purpose of developing this control-orientated model is for engine and microgrid control research. In addition, this model is also a useful contribution in its own right.

Through this natural gas engine model development, many objects are accomplished. We would like to make the following comments toward engine modelling studies:

(1) Various elements of an engine can be modelled as volume elements or orifice elements.

(2) Turbocharger dynamics are very important for a turbocharged engine dynamic studies.

(3) Compressor and turbine must be well matched.

(4) States including pressure, temperature and mass flow are essential for dynamic studies.

(5) Mass and energy conservation must be obeyed in the model all the time.

(6) Initial conditions need to be defined properly for the model to run smoothly.

(7) For a gas engine, gas properties have to be calculated in real-time.

Because of manufacturers' sensitivity with regard to the engine experimental data, it is hard to obtain any engine transient data and hence it is difficult to validate the engine transients performance. However, the engine states at steady-state are validated. Part of our further work includes the model transient validation to enhance the model's accuracy. Other engine features can also be added, such as: EGR feedback, waste gate, compressor bypass and so on.

CHAPTER 6

MODELING II: Storage System

6.1. Introduction

In practice, other than pumped hydro energy storage system, energy storage has very little application in utility or large-scale industrial applications [141]. This is because of the high cost of storage system, it is not feasible to utilize it as an energy source but rather a power source.

In the setup of our microgrid, a storage system plays a very important role. For such a battery based storage system, it is used here to improve the power quality, mainly used as a rapidly fluctuating power source performing frequency deviation reduction [141]. When load demands is higher than what is produced by other generations, the storage system discharges and provides additional power to the microgrid. When there is excess power within the microgrid, the storage system absorbs power and charges itself. If there is no limitation about storage size, it would be easy to maintain grid frequency. However, in reality because of the high cost of storage, it is deployed as a power source.

The batteries used in power system storage applications are deep cycle batteries [142], which are similar to those used in electrical vehicles [143]. Existing battery technologies include: lead-acid, Nickel Cadmium (NiCd), Lithium ion, metal air and so on. Among these technologies, Lithium ion has some unique advantages, such as: small size and low weight. At the same time, it has the highest energy density and close to 100% storage efficiency [143]. The major disadvantage of Lithium ion battery is its high cost, which limits

its utilization expansion. Because of its superiority. In this section, a Lithium ion battery model is developed.

Most significant issue of operating a battery is to maintain its state-of-charge (SOC) within a proper range [144]. For the purpose of this dissertation, SOC is one of the key parameters that need to be carefully controlled in order to enhance the overall microgrid performance. In other words, only when the SOC is well handled, can battery size be minimized and can it provide the greatest contribution towards enhancing grid stability and reliability. Dynamic models of batteries during charging and discharging are essential for estimating the SOC of a battery. The model is used to estimate the power that the battery has delivered or absorbed from the microgrid.

A well known analytical battery model with empirical data fitting is proposed in [145], this model is known as the "initial model of Shepherd". It has been well referenced in the field of battery study. Additional work has been performed based on the original work, including: [146], [147], [148], [149], [150], [151] and [152]. In [153], a non-experimental based battery voltage dynamic model is presented. In the above work, the battery discharge curve voltage model still cannot be very well fitted to the real experimental data. Part of the reason is the relationship between SOC and battery voltage is not well understood.

In this section, a modified lithium ion battery model is presented. The proposed model introduces a parameter, which is known as 'H' factor, to correlate the relationship between battery SOC and one of its voltage decline terms. This model uses the parameters that can be obtained from a battery datasheet [147] [154]. Following the introduction section, the rest of the section is organized in the following way. In section 6.2, a generic lithium ion battery model is presented. The parameter identification for the model from a given datasheet is

given in section 6.3. Finally, the battery model is validated against a real lithium ion battery in section 6.4. In this chapter, we intend to model a storage system, which is formed with individual batteries. By interconnecting individual batteries in series and/or parallel, the overall storage system voltage and/or current are enhanced, respectively. Hence, a storage system model is essentially created based on a good battery model.

6.2. Battery Model Development

6.2.1. *Assumptions*

Before we start the battery model development, some assumptions that have been used for modelling the battery are presented here [145][147]:

(1) The battery parameters are the same during discharging and charging processes.

(2) Temperature effect on battery is ignored.

(3) The battery self-discharging is ignored.

(4) The battery internal resistance remains constant while it is discharging and charging.

(5) The battery capacity does not change with the current amplitude.

(6) The polarization has linear relationship with active material current.

6.2.2. *Battery Discharge Model*

Fig. 6.1 shows a typical battery discharge curve. Its x-axis is discharge time, which indicates at certain current how long it takes to drain the battery. This time is directly related with battery capacity when a constant drain current is applied. Therefore, another kind of battery discharge curves use battery capacity (Ah) as its x-axis. Nevertheless, the x-axis is directly or indirectly related to the capacity of the battery.

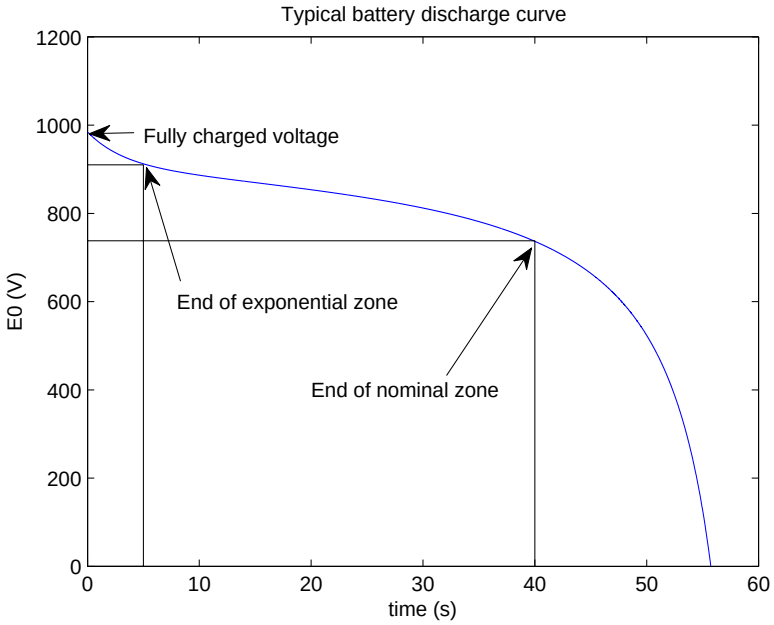

FIGURE 6.1. Typical battery discharge curve

From [145], the original battery model is derived based on the understanding of a voltage characteristic on the battery cathode E_c during discharge. Let us define:

$$E_c = E_{sc} - K_c i_{am} \tag{6.1}$$

where E_{sc} is a potential constant (V); K_c is the cathode coefficient of polarization; i_{am} is the active material current (A), which can be defined as:

$$i_{am} = \left(\frac{Q_c}{Q_c - it} \right) \cdot i \tag{6.2}$$

where Q_c is the available cathode active charge (Ah); i is a filtered current, which is used to represent the slow voltage dynamic; t is the time at any point during the discharge. If i is a constant, then the actual battery charge $Q_{batt} = it$. Otherwise, $Q_{batt} = \int_0^t i dt$. When

a battery is almost fully charged, $it = 0$. It can be seen 'it' is a measure of the current charge the battery carries that differs from its fully charged capacity. In other words, it can be considered as the charge that has delivered its power. When 'it' approaches battery charge Q_{cap} indicates the battery is almost completely drained. Q_{cap} is the battery nominal capacity.

By combining Eq. 6.1 and 6.2, we get:

$$E_c = E_{sc} - K_c \cdot \left(\frac{Q_c}{Q_c - Q_{batt}} \right) \cdot i \tag{6.3}$$

If the anode and cathode voltage potential are modelled similarly with the same parameters, then:

$$E = E_0 - K \cdot \left(\frac{Q}{Q - Q_{batt}} \right) \cdot i \tag{6.4}$$

where $E = E_a + E_c = 2E_c$ is the battery potential across the terminals. $E_0 = E_{sa} + E_{sc} = 2E_{sc}$ is the battery's constant potential. Similarly, polarisation constant $K = 2K_c = 2K_a$. In Shepherd's original model, $Q = Q_c = Q_a$. In this dissertation, we denote that $Q = Q_{cap}$. In other words, the voltage potential is modeled by the available amount of active material in coulombs when the battery is fully charged.

Suppose the battery has constant internal resistance of R, then Eq. 6.4 becomes:

$$E = E_0 - K \cdot \left(\frac{Q}{Q - Q_{batt}} \right) \cdot i - Ri \tag{6.5}$$

An additional term for modelling the initial voltage exponential drop is added to Eq. 6.5, this exponential term can be expressed as:

$$E_{exp} = Ae^{-B \cdot Q_{batt}} \tag{6.6}$$

where A and B are constants that can be determined experimentally or can be calculated from battery manufacturer discharge curve (this is discussed in section 6.3). A and B are known as the exponential zone amplitude (V) and exponential zone time constant inverse (Ah^{-1}), respectively.

By substituting Eq. 6.6 into Eq. 6.5, a generic battery discharger model is obtained as shown in [145]:

$$E = E_0 - K \cdot \left(\frac{Q}{Q - Q_{batt}} \right) \cdot i - R \cdot i + Ae^{-B \cdot Q_{batt}} \tag{6.7}$$

In [147], an additional term called "Polarisation Voltage" is introduced. This additional term is intended to represent the open circuit voltage (OCV) behaviour as a function SOC.

$$E_{pol} = K \cdot \left(\frac{Q}{Q - Q_{batt}} \right) \cdot Q_{batt} \tag{6.8}$$

However, the voltage drop across a battery is also correlated with the drain current of the battery. Here we introduce an coefficient 'H' to replace the polarization constant K. This newly introduced coefficient is defined as:

$$H = 4 - \frac{i}{Q_{batt}} \tag{6.9}$$

As one can see, this 'H' fit coefficient directly interacts with both battery drain current and its charge. It makes the model more responsive to the variation of both signals. Since it is a function of a current, there is no need for additional parameter identification.

Now the modified battery discharge model is obtained as:

$$E = E_0 - K \cdot \left(\frac{Q}{Q - Q_{batt}} \right) \cdot i - R \cdot i - H \cdot \left(\frac{Q}{Q - Q_{batt}} \right) \cdot Q_{batt} + Ae^{-B \cdot Q_{batt}} \tag{6.10}$$

In Eq.6.10, our contribution towards battery voltage dynamic is the introduction of 'H' factor. The general model structure is adopted from existing tools in the literature.

6.2.3. *Battery Charge Model*

In contrast to the discharge model, the polarization resistance during charge increases abruptly [147] and is modelled as:

$$R_{pol} = K \cdot \frac{Q}{Q_{batt}} \tag{6.11}$$

Since $it = 0$ when the battery is fully charged, it is easy to see that theoretically $R_{pol} = \infty$. However, in practice the polarization resistance is shifted by around 10% of the battery capacity. Therefore, the following expression is obtain for polarization resistance,

$$R_{pol} = K \cdot \left(\frac{Q}{Q_{batt} - 10\%Q} \right) \tag{6.12}$$

The other terms are the same as the discharge model. Hence, a generic battery charging model can be presented as:

$$E = E_0 - K \cdot \left(\frac{Q}{Q_{batt} - 10\% \cdot Q} \right) \cdot i^* - R \cdot i - K \cdot \left(\frac{Q}{Q - Q_{batt}} \right) \cdot Q_{batt} + Ae^{-B \cdot Q_{batt}} \tag{6.13}$$

Please note that when the battery is being discharged, $i > 0$; and when the battery is being charged, $i < 0$.

6.2.4. *SOC calculation*

In order to have the battery well utilized, it is essential to have the SOC of the batteries estimated. In this dissertation, SOC is estimated by using the charge left within the battery

and it is expressed as:

$$SOC = \left(1 - \left(\int_0^t i(t)dt\right)/Q\right) \times 100 \tag{6.14}$$

6.3. Battery Parameter Identification

Least square method has been successfully deployed for determining the numerical values of the battery parameters. However, this method is particularly time consuming [145]. By using two different discharging curves that are experimentally constructed at different current, one can solve a quadratic equation to obtain battery discharge parameter. Then other parameters can be found by using battery charging and discharging equations [145]. However, this kind of method requires data obtained from physical experiments.

In [146], parameters are identified by using the datasheet of the battery. This method is adopted in our work. Essentially, this method studies three particular points on the battery discharge curve. These three points are: fully charged voltage (V_{max}), the end of the exponential zone (V_{exp}, Q_{exp}) and end of nominal zone (V_{nom}, Q_{nom}). These three points are indicated in Fig. 6.1. By using these three points, three equations, which contain unknown parameters A, B and K, can be formed by using discharge equation in Eq. 6.10. By solving these three equations, the numerical values of the unknown parameters are obtained. The only unknown parameter is the time constant of the current filter. It can be obtained from experimental data.

The battery voltage dynamic model given in Eq. 6.10 and Eq. 6.13 is validated based on the datasheet of GP18650CH from GP^{TM} Batteries. Because of the introduced coefficient 'H', the proposed battery model is so called '$H-model$'. The parameters that are used for its model development are listed in Table. 6.1.

TABLE 6.1. GP18650 Lithium-Ion Battery Parameters. [4]

Type	Rechargeable Lithium Ion Cylindrical Cell
Nominal Voltage	3.6 V
Maximum Voltage	4.2 V
Capacity	Typical: 2200 mAh Minimum: 2150 mAh
Internal Resistance	50 mΩ
Recommended discharge current	440 mA t0 6600 mA
Recommended charge current	440 mA to 2200 mA

By using the parameters given in Table. 6.1 and deploying the method proposed by [146], the coefficients that are adopted in the battery model are presented in Table. 6.2.

TABLE 6.2. Parameters Adopted in GP18650 Lithium-Ion Battery Model.

Name of the Parameters	Adopted Numerical Values
Battery Voltage ($E0$)	3.6 V
Battery Internal Resistance (R)	50 mΩ
Battery Capacity (Q)	2200 mAh
Polarization Resistance (K)	0.012 Ω
Exponential Zone Amplitude (A)	0.468 V
Exponential Zone Time Constant (B)	3.529 $(Ah)^{-1}$
Voltage Time Constant (T_c)	30 sec

6.4. Battery Model Validation

In this section, our proposed battery model is validated. In modern battery industry, 'C'-rate is used to describe the charge and discharge current of a battery. '$1C$' means a 1000mAh battery discharged at '$1C$' rate should under ideal conditions provide a current of 1000mA for an hour [155].

For microgrid applications, the storage is used for coping with fast transient power imbalance. Therefore, power density is more important here. Because of the application requirements, the battery should be operated around its allowed maximum charge and discharge current, which are '$1C$' and '$3C$', respectively. The current flow rate is limited within

the battery model. Hence, the battery model is validated for higher 'C'-rates, particularly at '$3C$', '$2C$' and '$1C$'. '$4C$' is also validated for demonstrating our model accuracy.

In this section, the $H-model$ is validated against the discharge curve that is provided in the battery datasheet for GP18650CH. In Fig. 6.2, the battery discharge curves at different 'C'-rate are shown. This figure is directly taken from its datasheet and it can be found in [4].

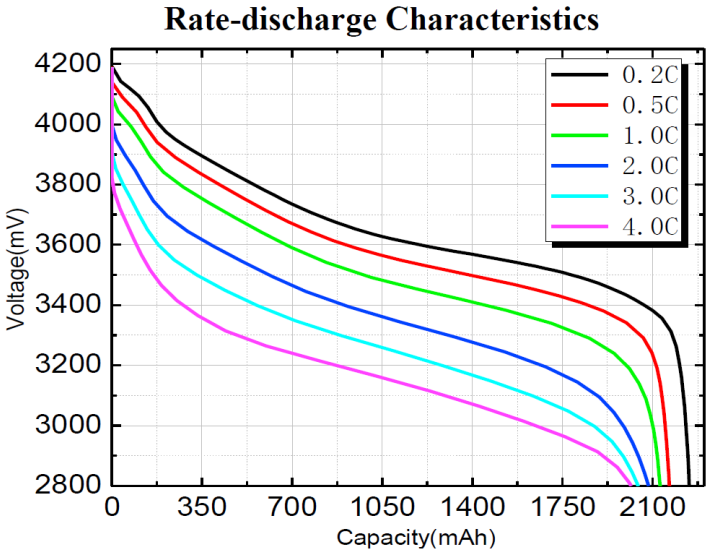

FIGURE 6.2. GP18650CH discharge curve at different 'C'-rate

In Fig. 6.3, the discharge characteristic curve at '$3C$' is shown. It can be seen that before 1000mAh, the voltage dynamic of the $H-model$ matches the experimental data very well. Our model has trouble matching the data between 1000mAh and 1500mAh, and so does the original model. This mismatch exists because of the low fidelity of the model. However, compared to the original model that is proposed in [146], the $H-model$ in this section captures model dynamic of the real battery and reduces the offsets during the initial

and the very end discharge stages. Overall, the proposed $H-model$ has better relation to the experimental data than the original model at '3C'. For a control orientated model, the accuracy of the model at '3C' is acceptable.

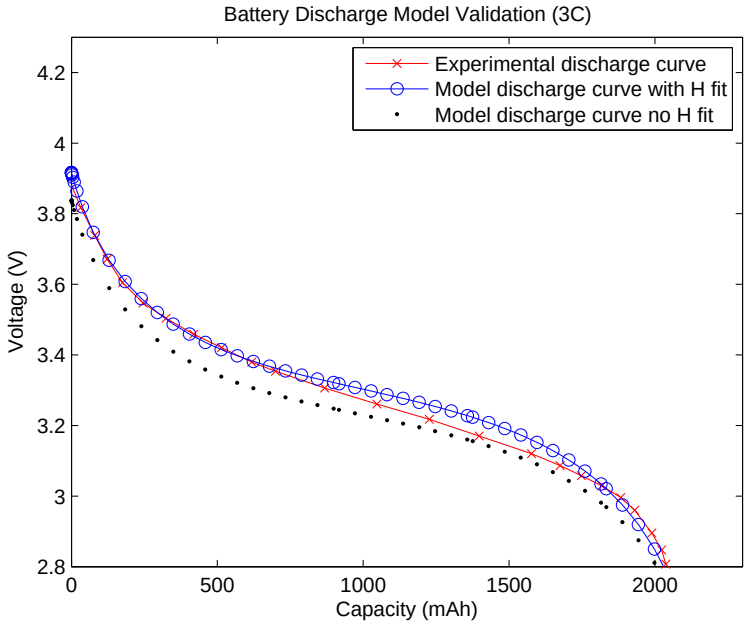

FIGURE 6.3. Typical battery discharge curve

As shown in Fig. 6.4, the proposed model voltage is almost on top of the experimental data. This shows the proposed model can represent the real battery very well. In contrast to the $H-model$, the original model cannot follow neither the initial discharge nor the post nominal discharge sections of the discharge curve.

It can be seen from Fig. 6.5 that the original model losses track of the experimental data from about 800mAh on. After that, it diverges more and more from the real discharge curve. Although our proposed $H-model$ is not a perfect match of the data, it still captures most of the dynamics. Since the storage system is not intended to be operated in this low 'C'-rate, the performance of the $H-model$ is acceptable.

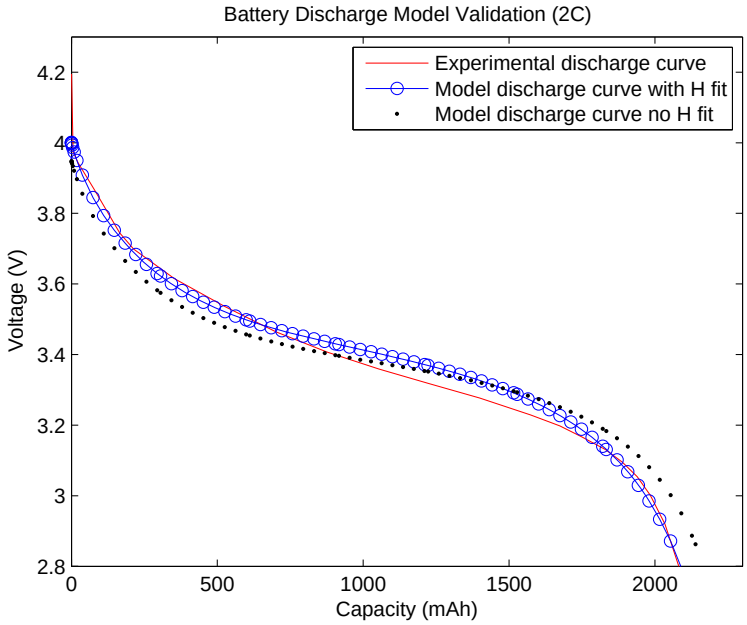

FIGURE 6.4. Typical battery discharge curve

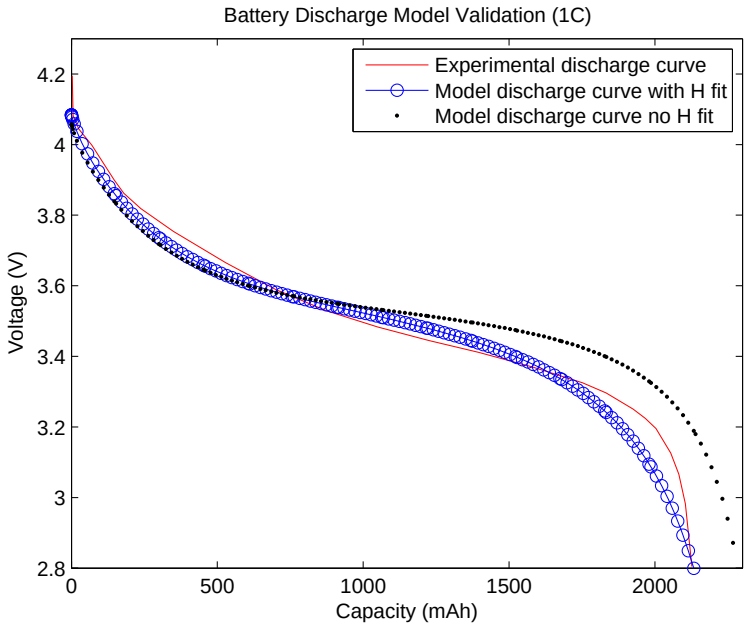

FIGURE 6.5. Typical battery discharge curve

Here, the discharge voltage dynamic curve at‘$4C$’ is also validated to show our proposed model can handle a broad range of ‘C’-rate test. As one can see in Fig. 6.6, the original model cannot follow the experimental data since the very beginning of the discharge. Our proposed model can track the data without any major problem.

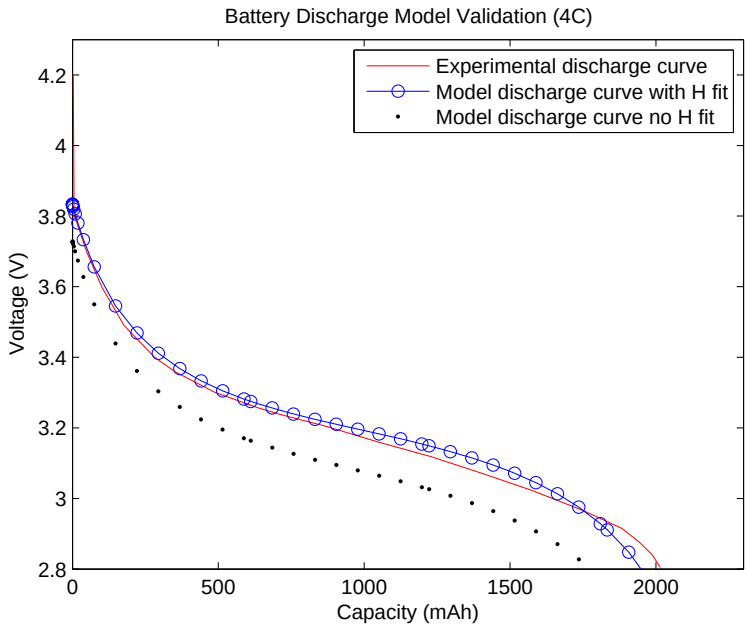

FIGURE 6.6. Typical battery discharge curve

6.5. Storage System Model

After a well validated battery model is obtained. It is time to form the storage system. One way of forming a storage system model is to use the individual battery model. In this case, the batteries are interconnected to each other either in parallel or in series. By increasing the number of batteries connected in parallel, the current of the storage system increases. If the number of batteries in series increases, the voltage of the storage system

increases. By increasing the number of the batteries, the output power of the storage system increases.

Another way of forming a storage system model using individual battery models is to modify the parameters of a single battery model. For example, increase the battery nominal voltage and current to increase its output power. In this dissertation, this method is adopted because of its low computation costs and simplicity of implementation.

For the storage system developed here, the current of the storage system is the control signal, which is used to control the output power that is delivered or absorbed to or from the microgrid. It is also used to control the SOC of the storage system. Furthermore, the size of the storage system is related to the load. In this dissertation, we would like to show that with the same storage system attached in the microgrid, better performance can be achieved if more advanced MIMO control is deployed. This also indicates that to achieve the same performance, smaller storage system is required when advanced control is utilized.

6.6. Conclusion

In this chapter, an analytical battery model with parameters computed from a given manufacturer datasheet is derived and validated. The proposed 'H' factor is a function of current and battery charge. It can enhance the original model performance without additional parameter identification. The validation results show that the proposed '$H-model$' can represent the experimental discharge curve better than the original model at different $C-rate$. This is especially true when the higher $C-rates$ are applied. This has significant meaning for our microgrid application since the storage system is intended to be operated at higher $C-rates$. In this chapter, a battery based storage system is modelled. Because of the structure of such storage systems, a good battery model is important. To form

a storage system model by using individual battery models, the used parameters are changed accordingly according to basic physics. By using the individual battery model, eventually a storage system model is obtained without losing the general dynamics of a single battery cell.

CHAPTER 7

Microgrid Control

7.1. Introduction

In this chapter, microgrid control is presented. The controller within a microgrid is essentially a power management system and it should keep the balance between power generation and consumption in order to minimize the frequency deviation that results from load fluctuation and variability in renewable energy sources. As we know, when there is excess power in a grid, the grid frequency tends to increase. This applies to both utility grid and microgrid. On the other hand, the grid frequency decreases if the generated power within a grid cannot fulfill the load demands. As one knows, if the utility grid frequency deviation exceeds the allowed limits, breakers will open and cause blackouts. The same principle applies to microgrids. Hence, it is critical to maintain a constant engine speed regardless of system disturbances, variations and uncertainties.

This power balancing or frequency control is achieved via engine speed control and storage system current control. A diesel engine speed control is realized by controlling the fuel injection rate. If a natural gas engine is used as prime mover, beside engine speed control, AFR control is also vital, since it correlates with engine emission. In such a setup, the throttle valve controls the amount of mixture flows into the combustion chamber and fuel valve tries to maintain a constant AFR. By adjusting the throttle valve, the internal combustion engine output power is controlled. By controlling the storage system charge and discharge current, it delivers power to or absorbs power from the microgrid. Storage system state of charge

(SOC) is also regulated by this control current. For a battery based storage system, SOC control is essential. It ensures the storage system capacity is utilized optimally, thus there is enough energy capacity for charging and discharging. Furthermore, SOC is also directly related with the life-time of a battery.

Renewable generation is the power generated by solar panels and wind farms or other renewable sources. In order to maximize the efficiency of the microgrid, all the power generated by renewable sources are utilized in our system. The renewable energy is considered as passive power for our purposes here, because we treat it as uncontrollable. In contrast with that the power generated by fossil fuel based system is regarded as the active power. (This active power is not corresponding to the term of 'reactive power' in power industry.) For passive power generation, its output mostly relies on weather conditions. For active power generation systems, by controlling fuel flow rate or charging and discharging current, their output power can be controlled accurately. In the setup of this dissertation, the concept of 'net load' is used. Net load really is the power difference between the total load and the renewable generation at a particular point of time. In other words, it is the load that has to be supplied by fossil fuel generation and(or) storage system. Because of the uncontrollability of the passive renewable generation power and load, the net load can fluctuate significantly, which makes microgrid frequency control one of the hottest research topics in microgrid research. In this chapter, the robust control approach is developed. For comparison purposes, some classical control approaches are also demonstrated.

By controlling the engine and storage system intelligently, we have achieved the following goals, including:

(1) Microgrid frequency deviation minimization.

(2) Storage system capacity minimization.

(3) Fossil fuel usage minimization.

(4) Renewable energy usage maximization.

(5) Emission minimization.

(6) Microgrid stability and reliability enhancement.

To illustrate the work that has been done, different configurations for engine control and microgrid control are presented in the following sections. The system simulation model is presented for each section along with simulation results, analysis and discussion. If robust control technique is applied in the section, the controller design model is presented as well. By showing the controller design model, one should have better understanding of how the weights that were mentioned in Chapter 2 are chosen and why they are critical. All the simulation work that is accomplished in this chapter is done by using Matlab™ and Simulink™. Before we go into the detailed studies, the overall general setups of the systems are shown in the next section.

7.2. General system configurations

The general system configuration is shown in Fig. 7.1.

As shown in this figure, there are two subsystems: natural gas engine control system and storage control system. Overall, it represents a microgrid control system. Here, the natural gas engine control can be realized by using the classical controls or the modern MIMO controls. The classical controls and modern MIMO controls can be applied for storage system. Two configurations can be used for microgrid control. In the first configuration, the microgrid control can be implemented by using two separate controllers that are used individually for engine system and storage system. These two controllers can be designed by

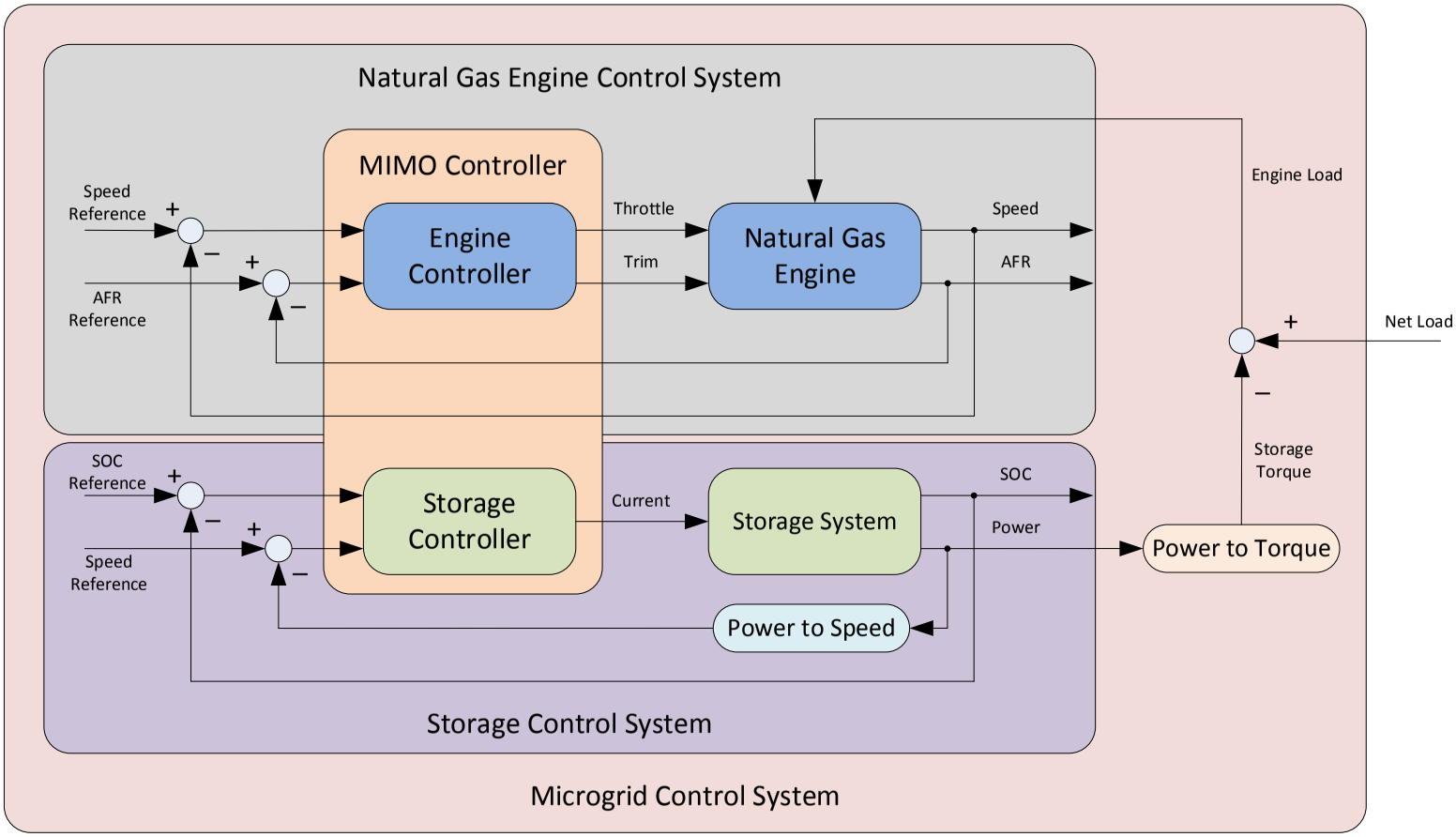

FIGURE 7.1. Overall system configuration.

using classical control techniques or modern control approaches. The other configuration uses a single MIMO controller to control both engine system and storage system for improving the overall system performance. Note for the full MIMO system, it does not repeat the speed error measurement. Now let us visit each configuration on an individual basis. The configurations are discussed separately for system with or without storage system attached. More explicitly, the natural engine system and the natural gas engine system with storage system associated are studied individually.

7.3. Classical Natural Gas Engine Control

PID control has been well utilized in industry for various applications due to its simplicity and reasonable performance to a certain extent. In theory, it simply reacts on the error signals based on given gains for proportional, integral and differential terms of the controller. More information about PID control can be found in many classical control system text books. Even nowadays, PID control is still being widely deployed in large engine power generation applications. However, PID control has some fundamental drawbacks, such as:

- Constant gains are unsuitable for highly nonlinear systems.
- PID controller is designed without knowing process.
- Noise on derivative term of PID controller can dramatically affect the control signal. (Potentially destabilize the system.)
- When PID control is used, additional tools such as gain scheduling and adaptive gain modification often have to be added.

For microgrid applications, PID based control techniques can no longer provide satisfactory performance with highly fluctuating renewable power source and load as well as tighter emission requirements. In addition, there are many related PID tuning issues. Furthermore,

since PID control is inherently a SISO approach, multiple SISO control loops for a MIMO system can be fighting to each other to ensure its own interests. However, the fight has unpreferable influences and side affects on the overall system performance. This fight can be seen in experimental data and it can cause the system to go unstable.

A typical configuration of natural gas engine control is shown in this section in Fig.7.2. This typical setup consists of natural gas engine and two PID feedback control loops for engine crank shaft speed control and engine AFR control, respectively. The engine model represents a pre-mixed lean burn natural gas power generation engine. In the particular setup we have proposed for this dissertation, the desired engine speed is 1500rpm and the desired AFR is 27.4, which is equivalent to λ of 1.7. In current practice, the AFR of an engine is not controlled during transients. This is because the emission is not regulated during transients. If there is a step load, the trim valve will allow the engine to run rich to ensure the engine speed does not deviate too far from its reference. During the speed recovering process, the AFR is allowed to deviate from its reference. After the engine speed is recovered, the AFR control loop is reconnected. In other words, AFR control is only active during steady-state operating conditions. This practice has been adopted in industry because PID control simply could not deliver AFR and speed control during transients.

Since a typical PID controller can only form a SISO system, there has to be two individual control loops for controlling a natural gas engine. For all of our system configurations, the engine controller(s) takes speed error signal and AFR error signal as its input signals. Its outputs are the desired throttle valve angle and the trim valve angle. This is slightly different from the real setup, where the outputs of the engine controller(s) are used to control throttle valve and trim valve actuators. The purpose of including the PID natural gas engine control

is to setup a benchmark for comparison purposes. In addition, the PID controllers have been well used in the large engine control area. However, because of the inherent drawbacks of PID control, it cannot achieve as good performance as modern control approaches. PID control simulation is conducted by using the simulation model shown in Fig.7.2. In this simulation model, the PID controller is designed by using classical Ziegler-Nichols method.

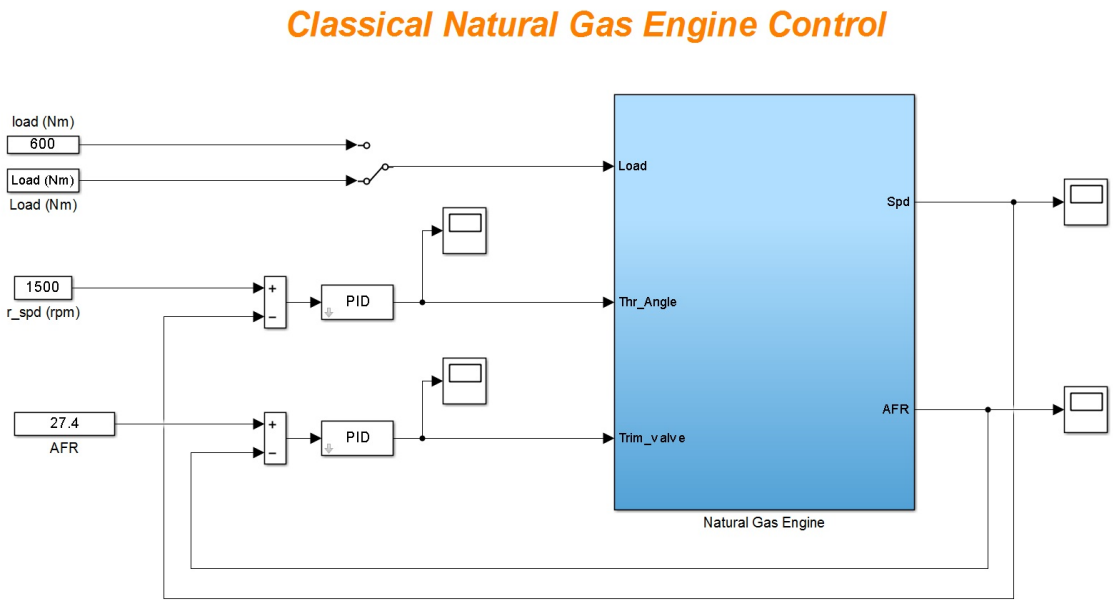

FIGURE 7.2. Simulink Model for Natural gas engine PID control.

A step load is used for controller design and examination purposes. If we mention a step load in this chapter, we refer to this particular step load profile. This particular step load is derived from a real engine test configuration. As shown in Fig.7.3, the step load profile steps up to its rated torque of 6000Nm and steps down to 400Nm. Each torque step is positive or negative 400Nm and each step takes place every 20 seconds.

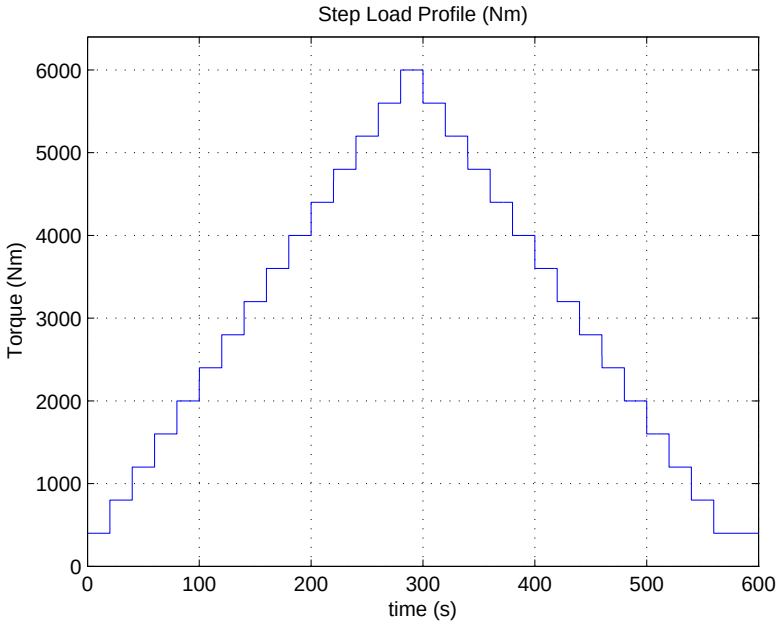

FIGURE 7.3. Step load profile.

The natural gas engine crankshaft speed responses of the step load is illustrated in Fig.7.4. As one can see, engine speed responses are reasonable from 0 seconds to 180 seconds during the load acceptance process. Correspondingly, the load rejection process engine speed responses behave similarly between 400 seconds to 600 seconds. However, within the high load region (simulation time between 200 seconds to 400 seconds, load between 3000Nm to 6000Nm), much bigger overshoots and undershoots take place. This is mainly caused by butterfly valves and turbocharger dynamics. The similar speed responses can be found in real engine test data when PID controllers are deployed. In addition, it can be seen that the speed deviation is getting larger and they tend to be more oscillatory when the engine is operated at higher load regions. The biggest speed deviation in rpm is just over 40rpm. In practice, the excitor voltage loop also helps the engine speed recovery. In our configuration,

the voltage loop is neglected. Furthermore, even within the lower load responses, they are not uniform. At different load levels, the responses have different speed deviations.

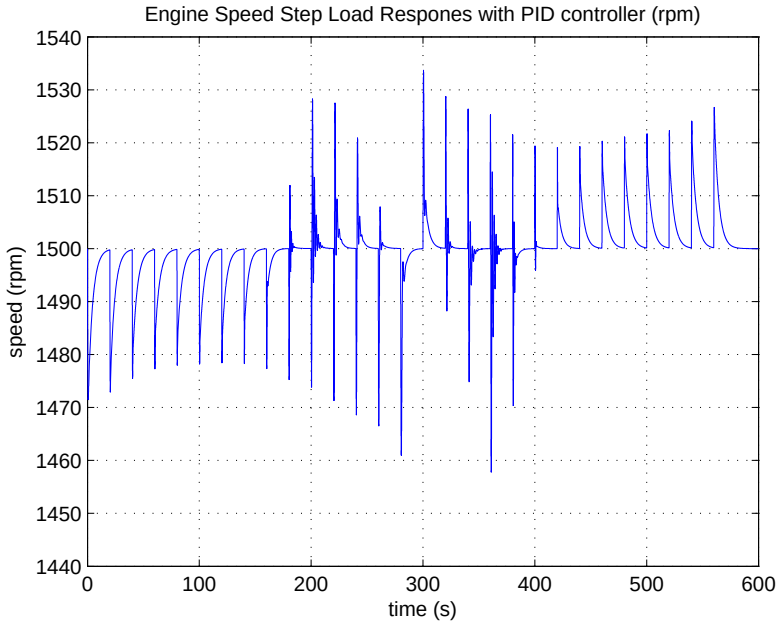

FIGURE 7.4. Engine speed step load responses when PID controller is used.

As shown in Fig.7.5, two noise signals are added to speed and AFR feedback signals. These two particular noises signals are used through all of our simulations. Similarly, if we mention noise signals in this chapter, we are referring to these two special measurement noise signals.

When these two measurement noises are added to the feedback pathes. The engine speed responses become even worse. As shown in Fig. 7.6, the worst speed deviation almost reaches 60rpm. In general, the oscillations last much longer with bigger amplitudes during the load range of 3000Nm to 5600Nm.

Beside speed control, the simulation results also indicate that the AFR control at steady-state is not difficult by using a well tuned PID controller as shown in Fig.7.7. However, it is

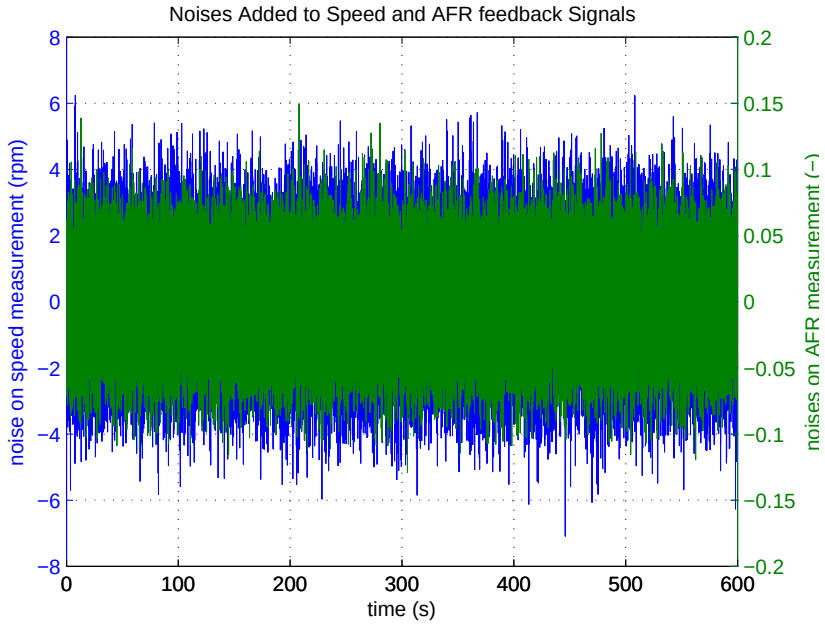

FIGURE 7.5. Engine speed and AFR measurement noises.

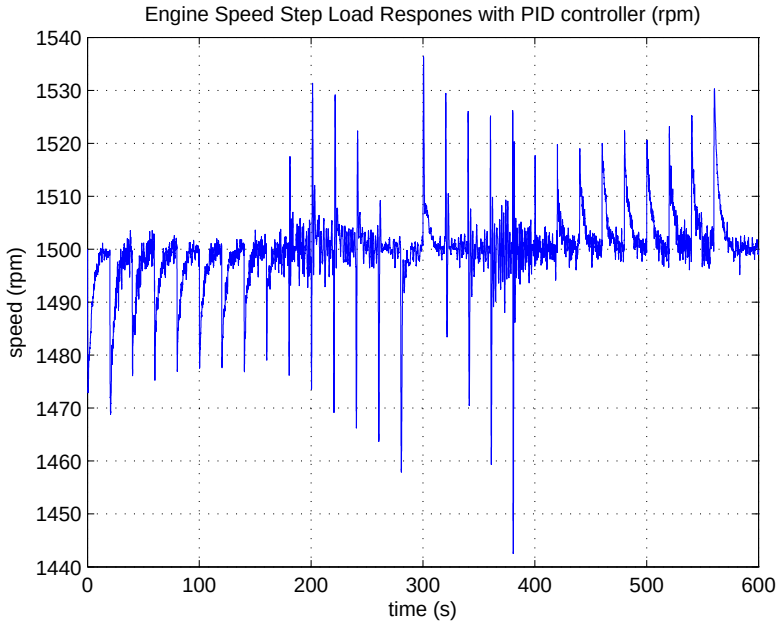

FIGURE 7.6. Engine speed step load responses when PID controller is used and measurement noises are added.

not trivial to maintain the AFR during transients. One of the major issues is the feedback delay. The AFR is normally measured after combustion. There is a significant transport delay between fuel injection and its equivalent feedback signal. This long delay degrades overall system performance and can even lead the system to go unstable. As experience from our simulation suggests, PID cannot satisfy AFR transient control while maintaining a decent speed control.

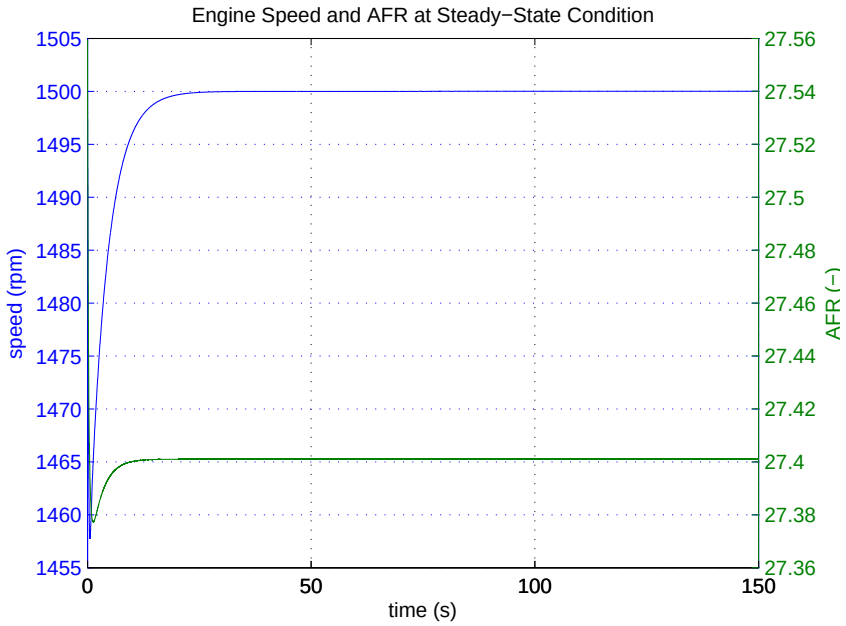

FIGURE 7.7. Engine speed step load responses when PID controller is used.

7.4. Robust Control of Natural Gas Engine

Considering the PID control as our baseline, let us now take a look at robust natural gas engine control. The robust control theory has been reviewed in the second chapter. In this chapter, we focus on controller design and system simulation. Just as for the classical PID controller, the robust engine controller intends to maintain a constant crank speed while

limiting the engine environmental impact and at the same time meeting the fluctuating load demand. For a robust controller, it is designated as a MIMO control system. In contrast to the two single PID loops, the MIMO controller can take multiple input signals and command multiple actuators at the same time. As shown in Fig.7.9, the design model is presented with properly chosen weight functions. As discussed in chapter 2, the design model is structured in the same way as the general control configuration for the system with model uncertainties, as shown in Fig.7.8.

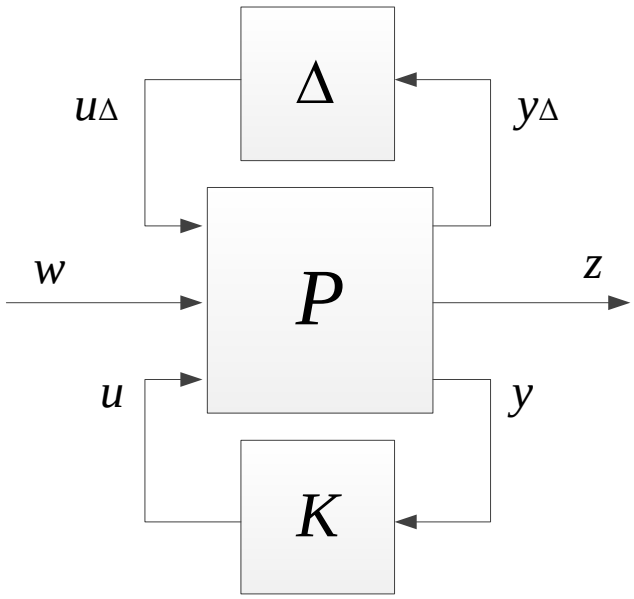

FIGURE 7.8. Control configuration for μ-synthesis.

In the setup of Fig.7.8, one wants to penalize the signal(s) 'z', as it normally represents the signal(s) to be manipulated or punished. The most common ones are the error signals, but there can be other signals too. 'y' is the measured system output(s), the controller 'K' reacts on it or the error signals (that originated by using output and reference signal) to generate the control signal(s) u. In addition, model uncertainties are included in 'Δ'. It

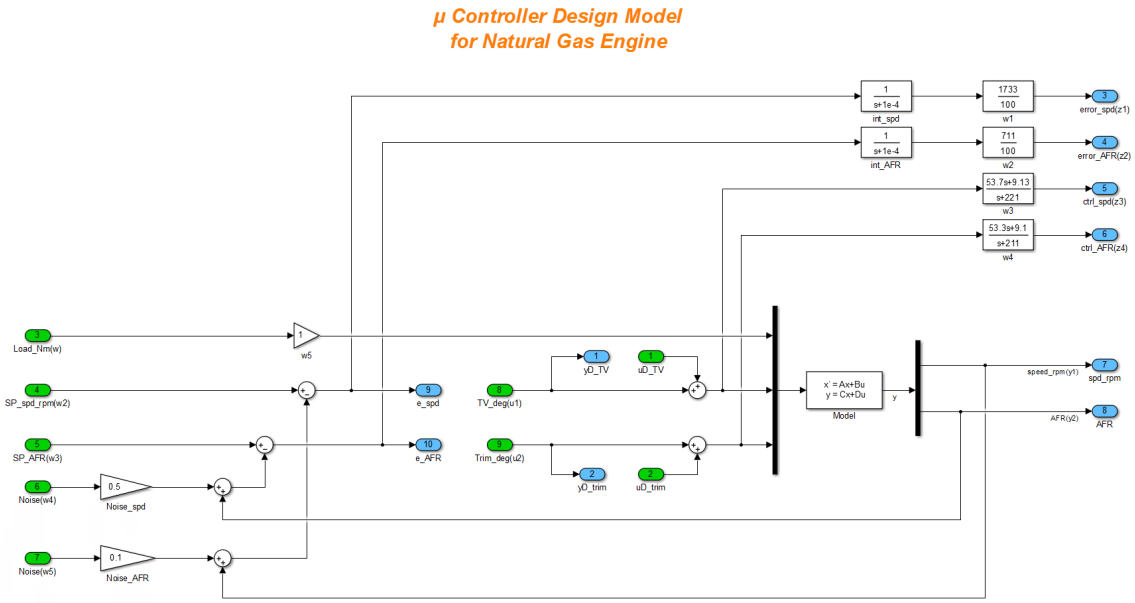

FIGURE 7.9. Design model for natural gas engine robust control.

includes all the possible uncertainties in block diagonal form and is normalized so its infinity norm is less than 1. As indicated in Fig.7.9, the robust controller design model is built in Simulink^{TM} environment. The output ports of the model should be labelled in the order of system uncertainties, penalized signals and controller input signals. Similarly, the same order should be adopted by the input signal ports. This particular order corresponds to Fig. 7.8. This defines the system design interconnection P (see Fig.7.8). In this chapter, all the robust controllers are designed by using Matlab^{TM} Robust Control Toolbox^{TM}.

Let us look at Fig.7.8 and Fig. 7.9 correspondingly to illustrate how the transformation between these two figures are realized. In Fig.7.9, the system uncertainties Δ sit between input and output ports 1 and 2. The output ports 3 to 6 indicate the signals we want to penalize. The controller has access to the error measurements at these ports (9 and 10). The penalty signals on the plant inputs labeled as output port 5 and 6 are used to ensure the

actuators are operated within their working bandwidth. The controller 'K' should be located between input ports 8, 9 and output ports 9, 10. The input signals of the controller are the engine speed error and engine AFR error signals. The other input signals include load, engine speed reference, engine AFR reference and noises. By using this robust controller design model and Robust Control Toolbox^{TM}, a corresponding μ controller can be designed.

Before we start simulation, let us take a closer look at the selected weight functions. The weight functions which have been used for penalizing the error signals are:

$$W_{e_{speed}} = 1.73 \cdot \frac{1}{s + 10^{-4}} \tag{7.1}$$

and

$$W_{e_{AFR}} = 0.71 \cdot \frac{1}{s + 10^{-4}} \tag{7.2}$$

If these two error signals are punished over the entire frequency range, constant weight functions could be selected. The corresponding weight functions can also be chosen as low pass filter like functions, which allow the error signals to be bigger at the higher frequencies. Theoretically, to keep the order of the controller low, constant weight functions should be deployed. However, because the lack of integral action of constant penalty functions, steady-state errors always exist. Hence, the deployed weights are the combinations of modified integrators and constant weights. The bode plots of the penalty functions applied on the error signals are shown in Fig.7.10. It does place most of the emphasis at low frequency. As one can see, the integrals that have been utilized are not pure integrators (they are approximate integrators above $10^{-4} rad/s$). A minor constant 10^{-4} is added to make these weight functions stable. Furthermore, these integrators also help to avoid marginal instability when the full model P is formed.

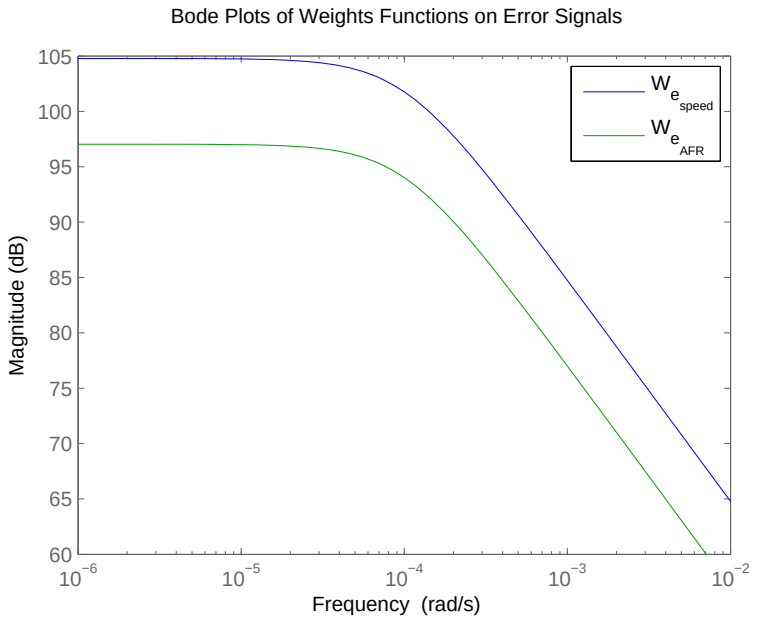

FIGURE 7.10. Bode plots of the weight functions on error signals.

The weight functions that are used for constraining the control outputs to the actuators are shown as below:

$$W_{in_{throttle}} = \frac{0.1s + 1}{s + 221} \tag{7.3}$$

and

$$W_{in_{trim}} = \frac{0.11s + 1}{s + 211} \tag{7.4}$$

The bode plots of the weight functions in equation 7.3 and 7.4 are shown in Fig.7.11. As one can see, they are high pass filter like functions. Because the butterfly valves used for engine control have natural frequencies under 100 rad/s, the control signals are penalized when the control signal is higher than 100 rad/s. In other words, the control signals are constrained for the frequency that the valves cannot actually react to. In addition, the bode plots of these two functions are similar but not the same. Since the valves are modeled by

using the same mathematical models with their own distinct parameters, the responses of these two valves are similar. Consequently, alike weight functions are chosen. To avoid pole and zero overlap at the same location, we purposely modified the pole and zero locations of the weight functions slightly.

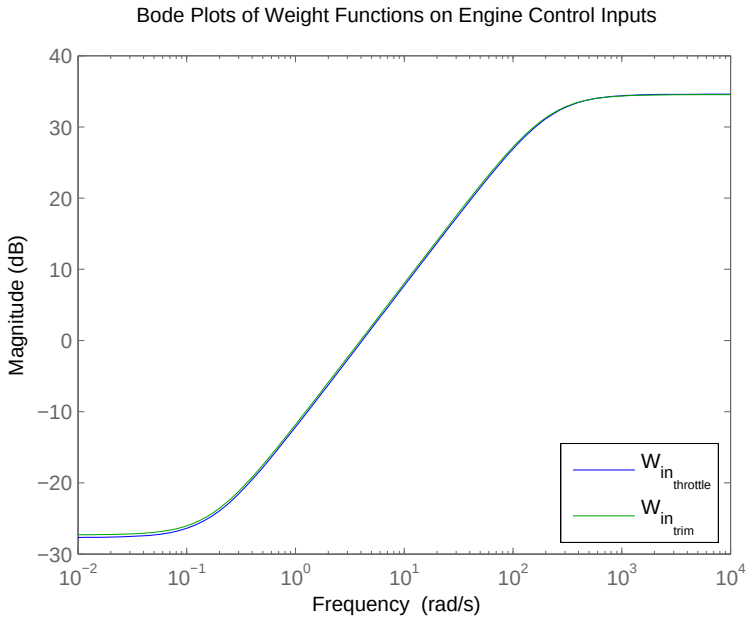

FIGURE 7.11. Bode plots of the weight functions on model inputs.

After the design model is constructed with appropriately selected weight functions, one can take the advantage of the Matlab ™ Robust Control Toolbox ™ for controller design. Once the controller is designed, the system performance can be examined through the simulation results by using the simulation model. The simulation model used for robust engine control performance study is shown in Fig.7.12. As one can see, the simulation model does not only contain the nonlinear engine model and MIMO state-space robust controller, but also the noise signals and model uncertainties. This setup has been used in classical engine control beside the modern MIMO control is adopted here.

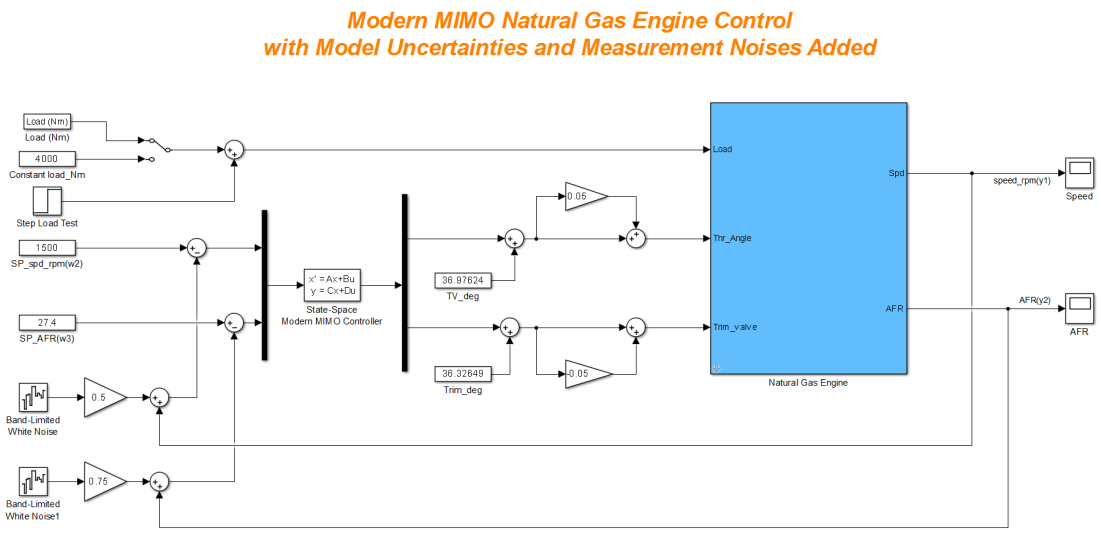

FIGURE 7.12. Simulink model for natural gas engine modern MIMO control.

We now study the simulation results. The speed and AFR responses of the step load are shown in Fig. 7.13 and Fig.7.14, respectively. As one can see, over the entire step load responses, the engine speed deviation has always been limited within 15rpm and the AFR deviation is kept less than 2.18, which is less than 8%. In fact, most time the AFR is kept within the envelope of 26.4 and 28.4, which are only +/- 1 from the desired AFR reference. This corresponds to a variation of less than 3.7%. Contrast that to PID control, which can hardly provide transient AFR control while maintaining system stability.

In Fig.7.15, the speed responses for the systems with PID controller and μ controller are compared over the whole step load test. As the figure indicates, the robust control has much better performance. It has much smaller undershoot and hardly any overshoot. The maximum engine speed deviation across the entire step load is less than 15rpm when a robust controller is deployed. Compare that to the PID controlled system, which has almost 60rpm speed deviation. That is almost 4 times worse. The figure also shows the robust controller

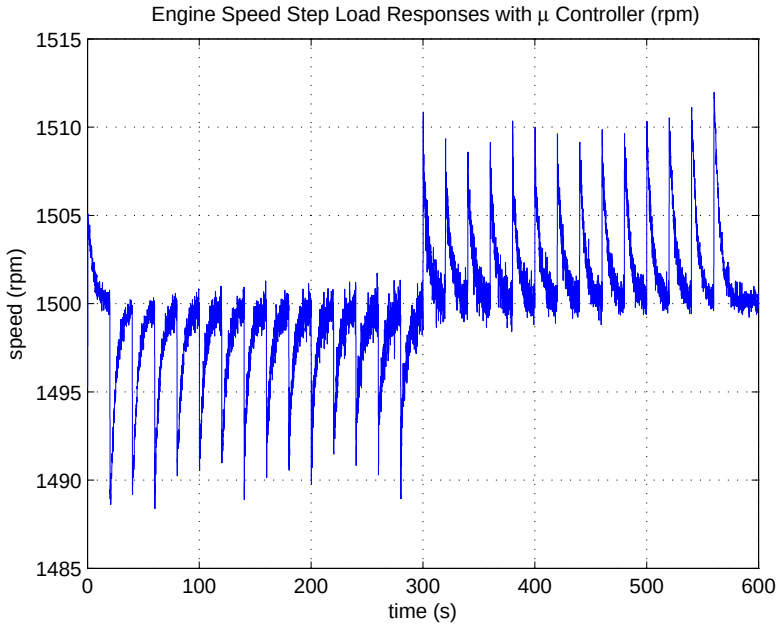

FIGURE 7.13. Engine speed step load responses when robust control is used.

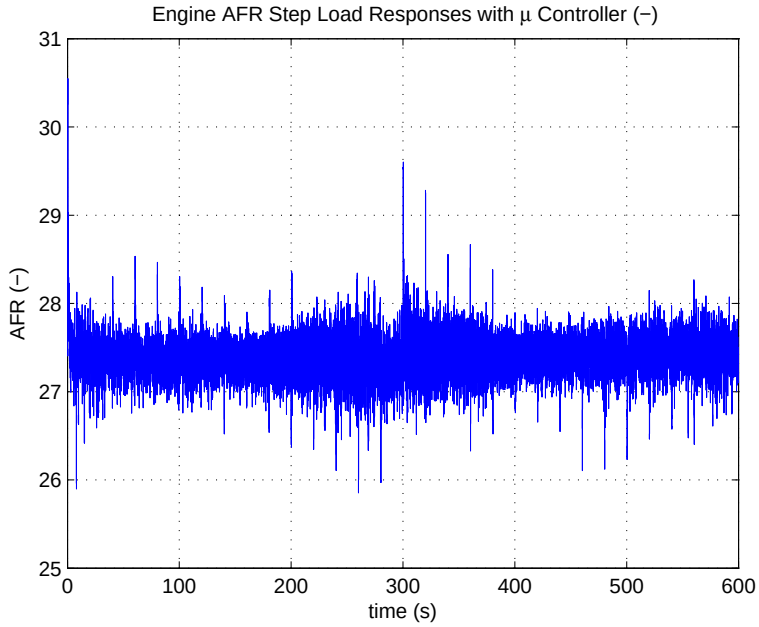

FIGURE 7.14. Engine AFR step load responses when robust control is used.

system tends to be more uniform. Oppositely, the speed variations of the PID controlled system vary significantly.

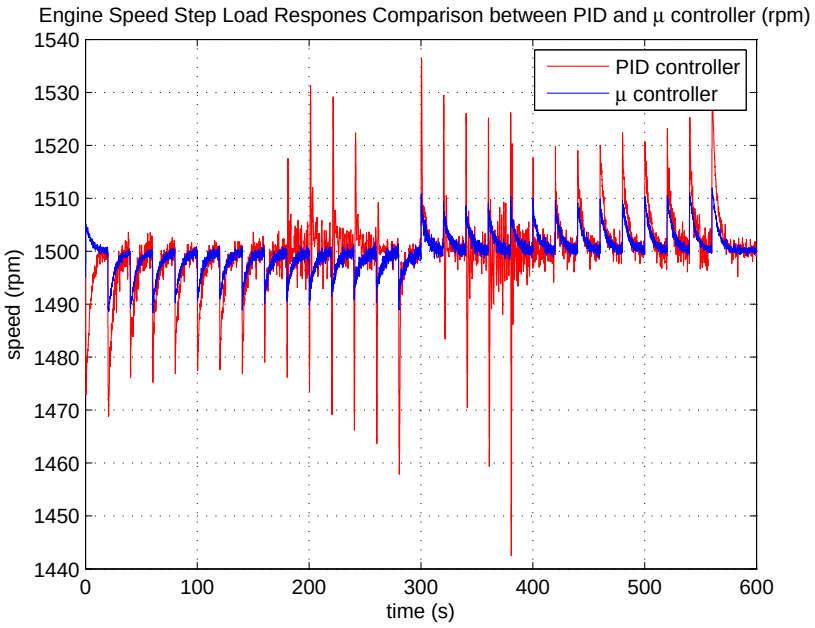

FIGURE 7.15. Engine speed step load responses comparison between PID controller and μ controller.

The speed responses between the 280th second and the 320th seconds are zoomed in and shown in Fig.7.16. During this special period, the engine first reacts on load acceptance to its rated torque, and then an immediate load rejected from its rated torque. One can easily notice that within 5 seconds, the frequency reduces to an envelop of $\pm$3rpm regardless of whether it is load acceptance or load rejection.

.

By comparing the robust system responses to the PID system responses, it is obvious that the robust control system presents a much better performance as shown in Fig.7.17 and Fig.7.18. As shown in these two figures, the step responses of the robust control system behaves like a first order system without any oscillation and overshoot. The speed signal

FIGURE 7.16. Engine speed step load responses when robust control is used.

settles and locks to the reference smoothly. The noise signal is essentially superposed on the original signal and does not affect the overall system performance. However, as shown in Fig. 7.17 in red, the PID control has much bigger overshoots. In addition, as shown in Fig.7.18 in red, between the 200th second and the 240th second, the PID controlled system tends to be very oscillatory and the oscillation amplitude is not reducing when the same feedback measurement noise signals are added. The system exhibits a speed hunting kind of behavior (shown in the real engine data as well). The speed hunting behavior means the engine speed does not settle down to the reference but oscillates around it. Such sort of engine behavior is unpleasant.

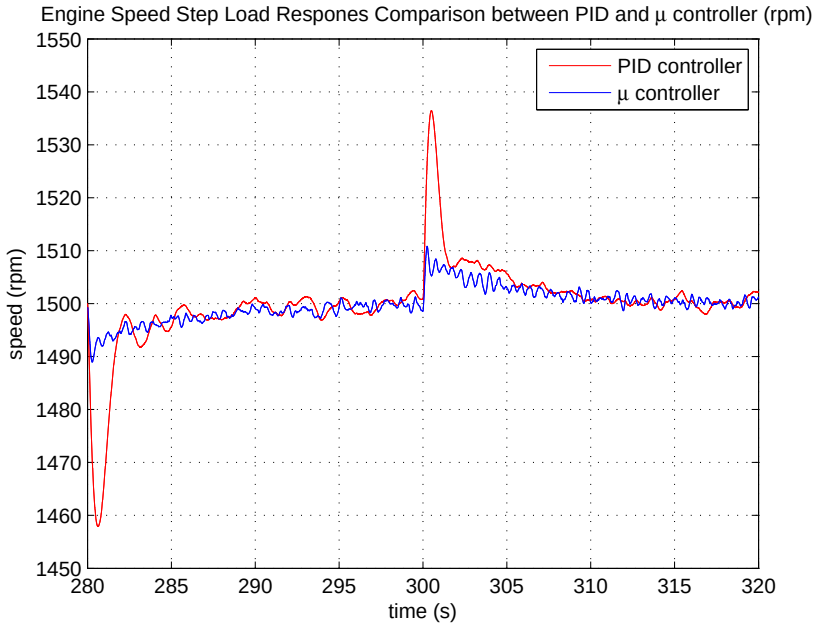

FIGURE 7.17. Engine speed step load responses comparison between PID controller and μ controller with no storage attached.

7.5. Classical Control of Microgrid System

In this setup, microgrid is controlled by using four SISO PID control loops. The purpose of including the classical microgrid control is mainly for comparison purposes. In this chapter, the PID system simulation results represent the baseline control performance, the MIMO robust control presented in the later sections illustrates much better performance with the similar system configuration.

In Fig. 7.19, the microgrid simulation model with PID controllers are presented. It can be seen, there are four individual PID control loops. The classical engine system control has been studied in previous sections in this chapter. For the storage system, two PID controllers are used for SOC control and engine speed compensation, respectively. The combined current command signal is used to control the power and regulate the SOC of the storage system.

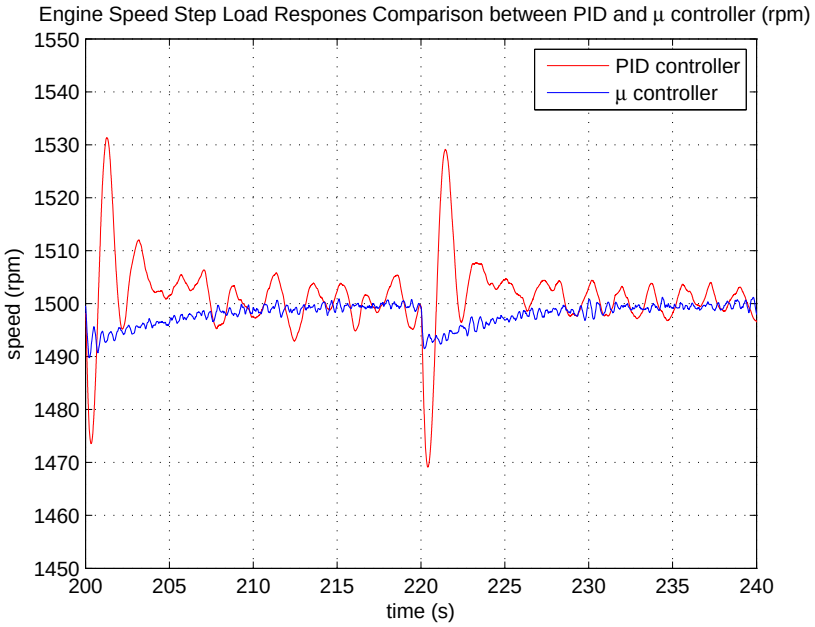

FIGURE 7.18. Engine speed step load responses comparison between PID controller and μ controller with no storage attached.

These two PID control loops are critical for overall microgrid performance. They ensure the storage system takes care of the high frequency net load fluctuation as well as the sudden load transients. But it should not react on large or slow load trends. In this microgrid system, we assume the storage power can be used directly for load supporting. In other words, if there is power delivered from storage system, it is subtracted from the net load with power to speed conversion. The load that needs to be provided by the engine is really the difference between net load and the storage torque. This is a reasonable assumption because the electrical dynamics are very fast.

By using the simulation model and carefully tuned PID controllers, the microgrid classical control simulation results are presented in the following figures. Fig.7.20 shows the speed deviations, it can be seen the maximum speed deviation is just over 20rpm. There is significant overshoot and undershoot around the 360th second and 380th second. The

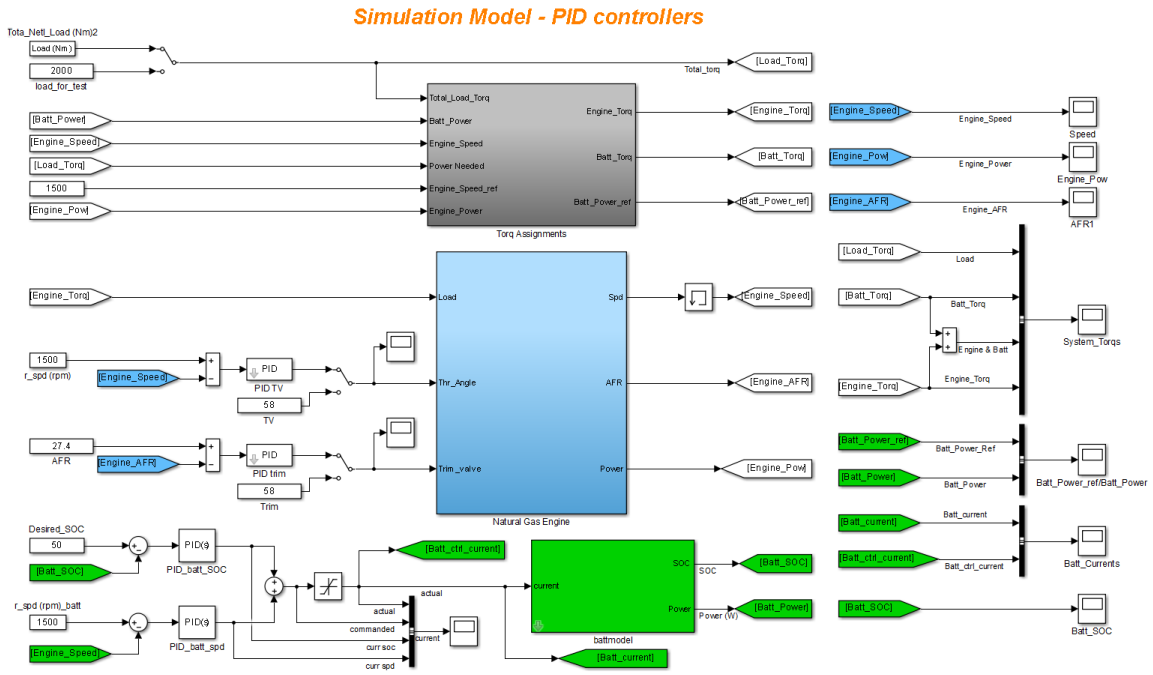

FIGURE 7.19. Microgrid simulation model with PID controller.

settling time is about 10 seconds for each step load. During the high loads periods, the nonlinearities of the microgrid system are shown from the speed step responses.

A zoom in view of the speed deviation between the 275th second and the 320th second is shown in Fig.7.21. As one can see, with the help of storage system, the biggest engine speed deviation has been reduced from over 40rpm to about 20rpm. However this engine speed deviation still degrades the microgrid power quality. In practice, small speed overshoot is desired when PID controllers are used. This small overshoot can accelerate the system recovery process (reduce the settling time).

With the help of the storage system, engine AFR is controllable during transients. However, there are still obtrusive AFR deviations. The biggest AFR deviation is about 12.4% as one can see from Fig.7.22. In other words, the AFR control is achieved but not with excellent

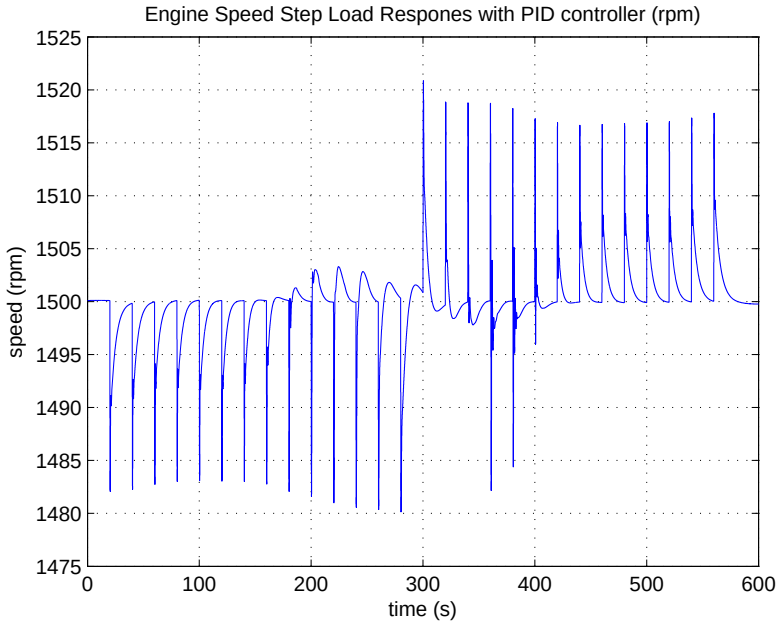

FIGURE 7.20. Engine speed step response with PID controllers and storage attached.

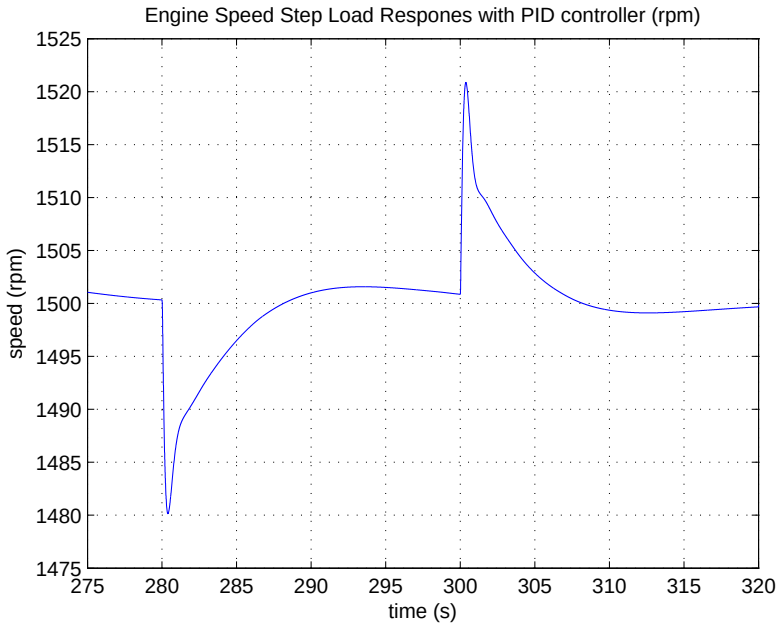

FIGURE 7.21. Engine speed step response with PID controllers and storage attached.

performance. Hence, emission reduction is not fully accomplished. Additional work can be done for further improvements.

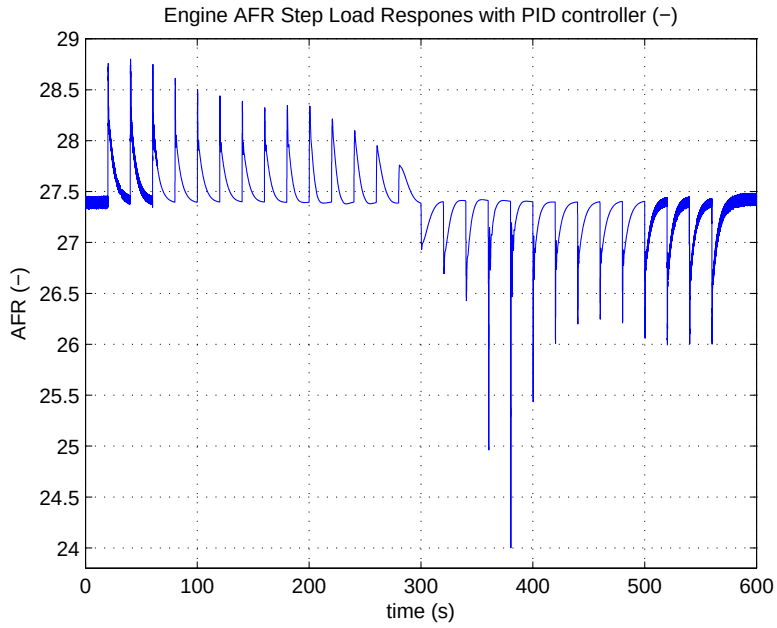

FIGURE 7.22. Engine AFR step response with PID controllers and storage attached.

The storage system power is shown in Fig.7.23. If the PID controlled storage system had delivered the required power in blue, there would have been no speed deviation at all. Of course the feedback controller does not get a load measurement, so it cannot just deliver the power in blue. Before we go into more detailed investigation, let us take a look at an example. For instance, if there is a load step up, the storage delivers power to the load during the very first couple of seconds. During this discharge period, the SOC of the storage system drops. The PID controller that acts on SOC deviation tries to reduce the discharge current. However, if there is still positive speed error, the speed compensation PID controller wants to deliver more power for load supporting, so the engine load can be reduced for helping with engine speed recovery. It can be readily seen, one PID controller tries to reduce discharge

current and the other one does exactly the opposite. They are literally fighting each other. Because of this fight, the actual storage power does not mach the desired power. In addition, the command current should avoid the current limitations on the storage system.

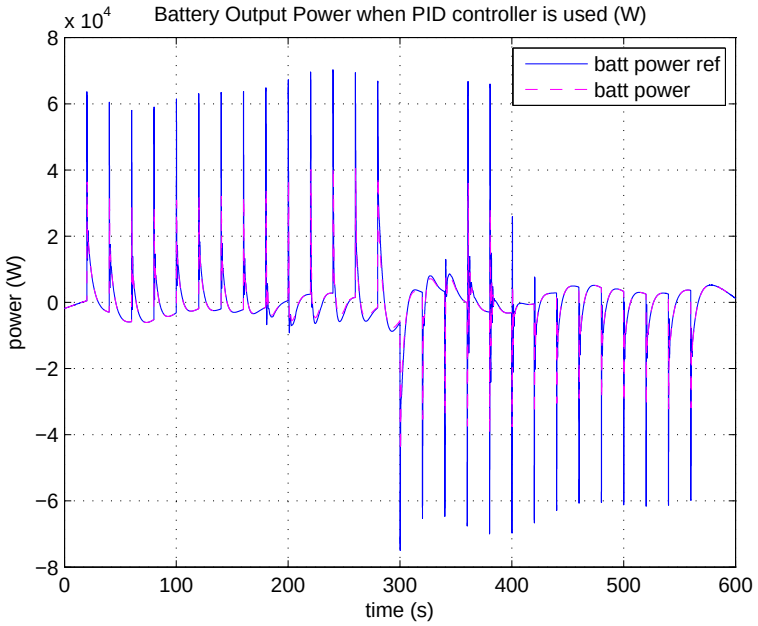

FIGURE 7.23. Battery power step response with PID controllers.

The torque balances are shown in Fig.7.24. The load at steady-state is fulfilled by the engine system as it should be. It can be seen, the storage system only reacts to the load steps at the very beginning, then its output returns to 0W. During transients, the engine system and the storage system work together to supply the load. In such a system, the engine system only supports the slow and large load variations, the rest of the load is provided by the storage system. These are the desired behaviors of both systems for improving the overall microgrid system performance.

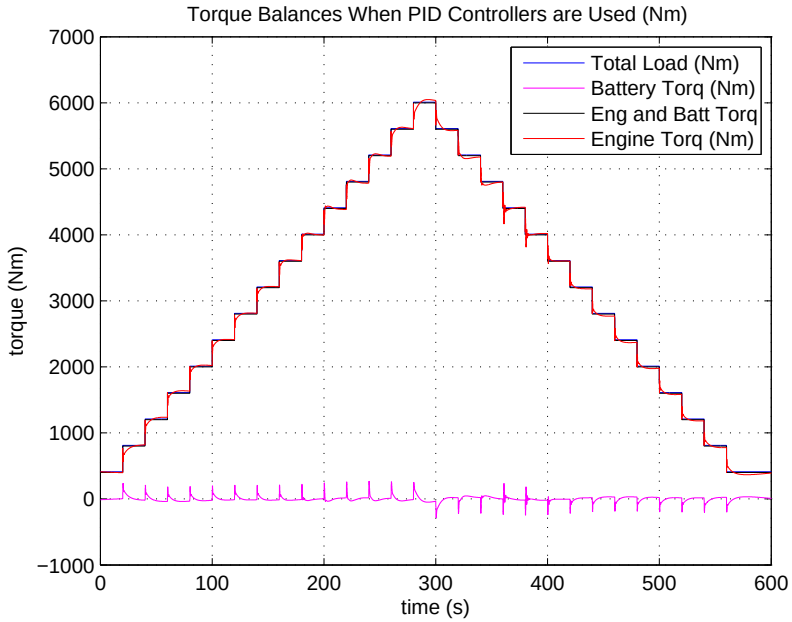

FIGURE 7.24. System torques balance step response with PID controllers.

The last figure of the classical microgrid control shows the storage SOC variations. As shown in Fig.7.25, the SOC of the storage system does not deviate from its desired value significantly. This means in a microgrid system, the storage system is used as a load supporting power source. It is not required to continuously charge or discharge. In such case, it is not required to have huge energy storage capacity. This has large practical significance. With much smaller energy storage capacity, it means the whole system is more implementable in practice, the additional cost to make the system functional is minor and not much space is required to accommodate the storage system.

7.6. Robust Control of Microgrid System

Robust control implementation for a microgrid system is accomplished in this section. Two different robust control configurations are implemented in this section for microgrid

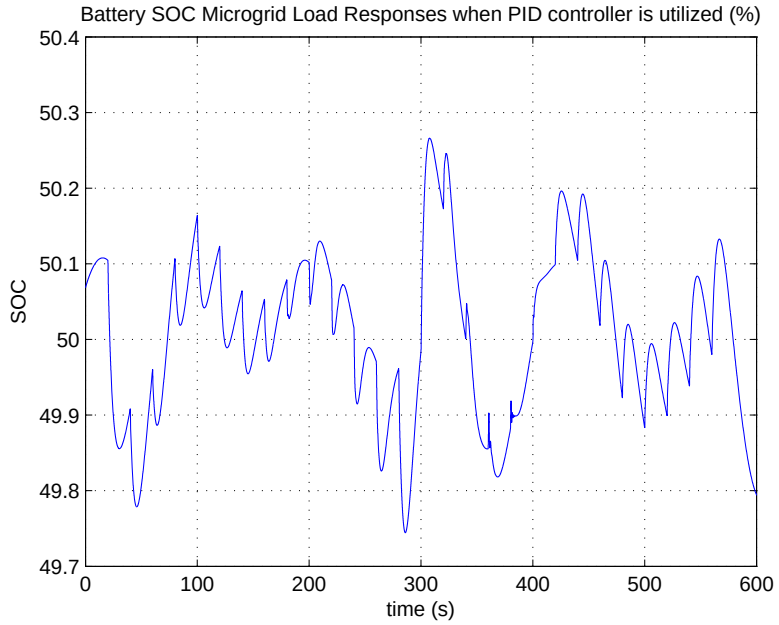

FIGURE 7.25. Battery SOC step response with PID controllers.

system control. In the first configuration, two robust controllers are designed individually and integrated to the microgrid system separately. However, there is only one MIMO robust controller designed and deployed for the second configuration. These two different configurations are studied extensively in the following subsections.

7.6.1. *Separate Robust Controllers for Storage System and Natural Gas Engine*

In this setup, two robust controllers are needed. One is dedicated for controlling the natural gas engine system and the other one is used to address the storage system control. In this setup, there is no communication or understanding between these two controllers. They operate independently and they just react on the error signals that are sent to their input. In such a case, they are concentrated to do their own job without considering the possible potential of affecting each other negatively. As good engine performance has already been achieved by using the robust controller designed in section.7.4, the same engine control

system is adapted here for the microgrid engine system control. In this subsection we focus on storage system robust controller design.

The design model for the storage system is shown in Fig. 7.26. As one can see, the input signals to the storage system controller are the SOC error signal and the engine speed error signal. The output signal of the controller is the commanded current signal. If this signal is positive, that means the storage system is discharging. Oppositely, the storage system is absorbing power if the current is negative. Otherwise, the storage is neither charging nor discharging, its output is 0W. By controlling the storage system current, its output power and SOC are controlled. The power output of the storage system can be directly used to provide power to the load with necessary inverters in practice. The point that needs to be emphasised is that compared to engine dynamics, storage system can react to the load fluctuations much faster. By directly injecting or absorbing power (torque) to and from a microgrid system, the engine speed tends to increase or decrease. The power (torque) injection and absorption are almost equivalent to removal or addition of a certain amount of load to the engine system. Because of this property, by cleverly deploying the engine and storage system resources, better overall microgrid performance has been achieved and our arguments are supported by the simulation results presented in this subsection.

Load allocation is implemented based on the load and the systems' characteristics, such as response time, power density and energy capacity. Most of the fast (high frequency) load fluctuation (for which the engine does not have the bandwidth to react) should be provided by the storage system. The slow load variations, which storage does not have the energy capacity to provide, are supported by engine system. These two systems should work cooperatively to ensure good overall system performance. In addition, storage system SOC

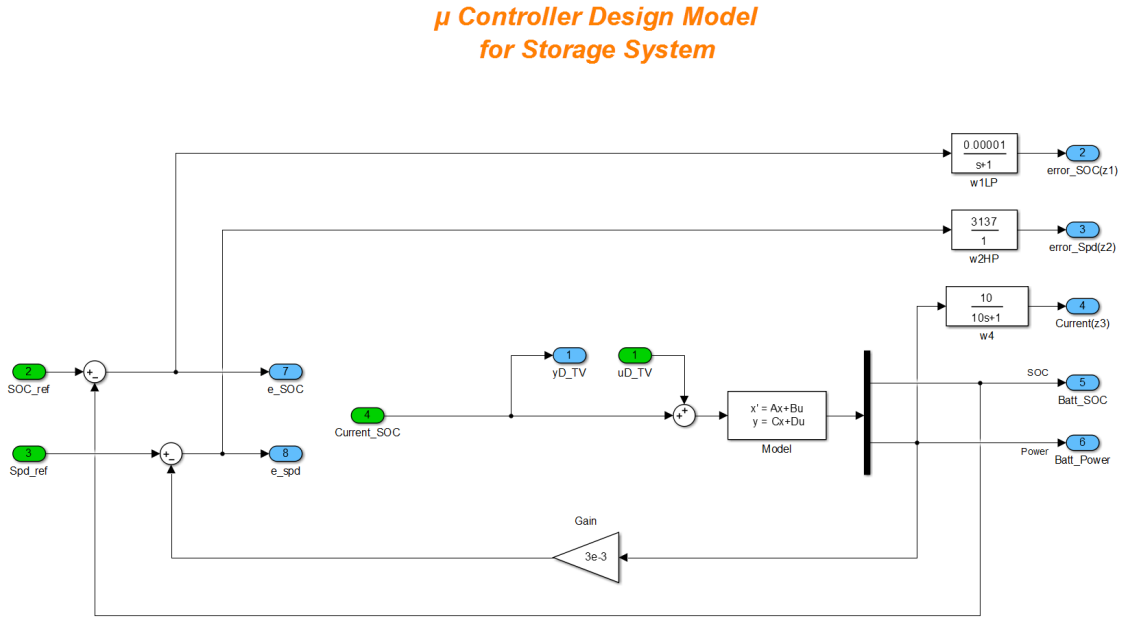

FIGURE 7.26. Design model for storage system robust control.

is always part of the equation, although battery system can provide load as long as there is charge available. However, the battery system in this system is used wisely to minimize the storage system capacity (size). The storage system only deviates around 0W and only reacts to high frequency load perturbations. It should neither continuously supply positive power to the load nor continuously absorb power from the grid. To clarify this statement, let us take a look at an example. If a step load is applied, most of the load is provided by the storage system at the very beginning. With the engine ramping up, storage system hands over the load to the engine gradually and eventually pushes itself to back out to 0W output. In fact, before it backs off to 0W, normally there is a charge action. In other words, the storage system absorbs power to recover its SOC. This topic will be revisited with more detailed simulation results in this subsection.

As shown in Fig. 7.26, there is a power to speed feedback gain. This gain is used to convert the storage system output power to a Δrpm signal. Theoretically, storage output power contribution towards the load can be converted to engine speed by using a load torque signal. However, the load is not directly measurable and it varies a lot. To simplify this problem, a constant gain (50% of engine rated torque) value is used for this conversion. Note, this conversion is only used for controller design process because of the missing speed signal from an engine system. For the simulation model or a real microgrid system, this signal can be obtained directly from the engine system since it is readily available and measurable.

In the storage design model, we attempt to ensure the system behaves as we wish by choosing the weight functions wisely. As shown in Fig.7.26, there are three weight functions that correspond to battery SOC error signal, engine speed error signal and battery output power signal. The first two weights ensure the storage SOC and engine speed is well controlled by minimizing the error signals. The third weight function is used to penalize or enhance the storage output power in certain frequency ranges. By doing so, we would like to enforce the contribution and availability of the storage system. By enhancing its contribution, we mean improve the overall system performance by allowing the storage system charge and discharge when load variations are in certain frequency ranges and do not act on other frequency regions. By well maintaining its SOC around 50%, the storage system availability is enlarged, because when the SOC of a storage system is at 50%, it has the the maximized charging and discharging capacities. Performance penalty weights were chosen as:

$$W_{e_{soc}} = \frac{10^{-4}}{s+1},$$

$$W_{e_{speed}} = \frac{3137}{1}$$

and

$$W_{out_{power}} = \frac{1}{10s+1}$$

As one can see from Fig.7.27, beside the constant weight function on the speed error signal. The other two weights functions have low pass filter like feature. The reason is that the storage system should only contribute towards the high frequency load fluctuations and leave the slow load trends to the engine system. Therefore, there are more penalties at low frequencies and less penalties at high frequencies. In addition, the selected weights have slow roll off rate, which are used to ensure the storage system hands over the load smoothly to engine system. In other words, avoid sudden shape load transfer between two systems.

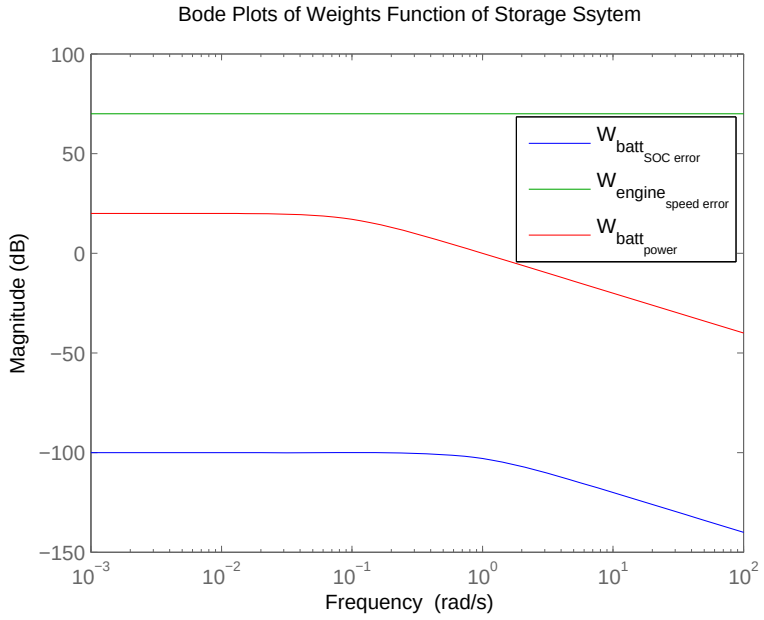

FIGURE 7.27. Bode plots of the storage system weight functions.

The simulation model for two separate μ controller is shown in Fig. 7.28. As one can see, there are two state-space MIMO controllers, which are dedicated to the storage system

and the engine system, respectively. It can be seen that the speed error signal going into storage system controller in this simulation model is formed by using real engine speed and speed reference. This setup is different from the design model which does not have speed measurement, but it agrees with the real system configuration. The controller output is current command signal, which regulates the power and SOC of the storage system. The power output of the storage system is then converted to torque signal by using real-time engine speed signal. The torque provided by the storage system is subtracted from the total load and sent to the engine system. In this simulation model, model uncertainties and noises signals are added as well to mimic model error and real world disturbances.

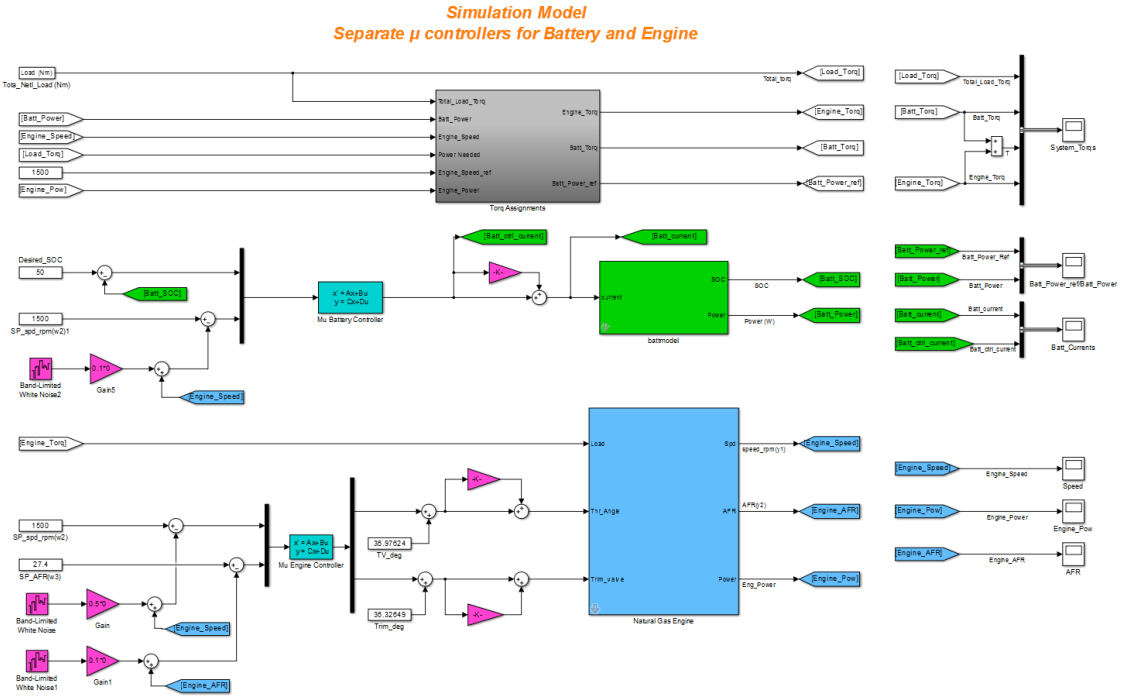

FIGURE 7.28. Simulation model for modern MIMO control.

In the rest of the section, the simulation results are presented with analysis and discussion. In this section, the simulations are conducted in two setups, one includes noises and

uncertainties and the other one does not. The simulation results for these two setups are plotted in the same figure for comparison purposes. Let us start with speed responses.

The engine speed responses for the step load is presented in Fig.7.29. As one can see, the maximum speed deviation is smaller than 8rpm. In addition, even after the model uncertainties and noise signals are added, the performance of the perturbed system is only slightly degraded compare to the unperturbed system. This indicates the designed controller is robust.

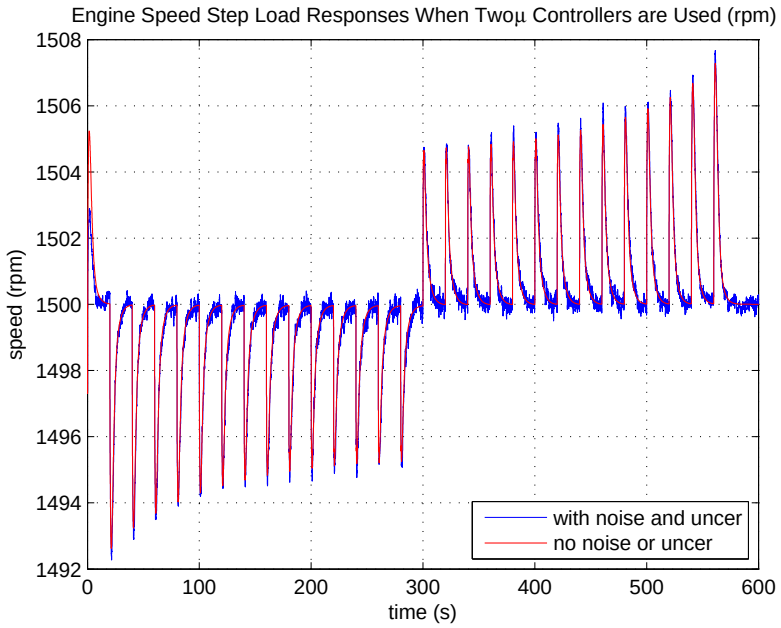

FIGURE 7.29. Engine speed step load responses with two μ controllers.

In Fig.7.30, we zoom in the speed responses signal between the 275th and the 320th seconds, where the system reacts to both load acceptance and load rejection. It can be seen that these two signals are almost overlapping each other besides the add on high frequency noises. There is no additional overshoots or undershoots. In addition, the engine speed deviation reduces to less than 3rpm in 2.5 seconds.

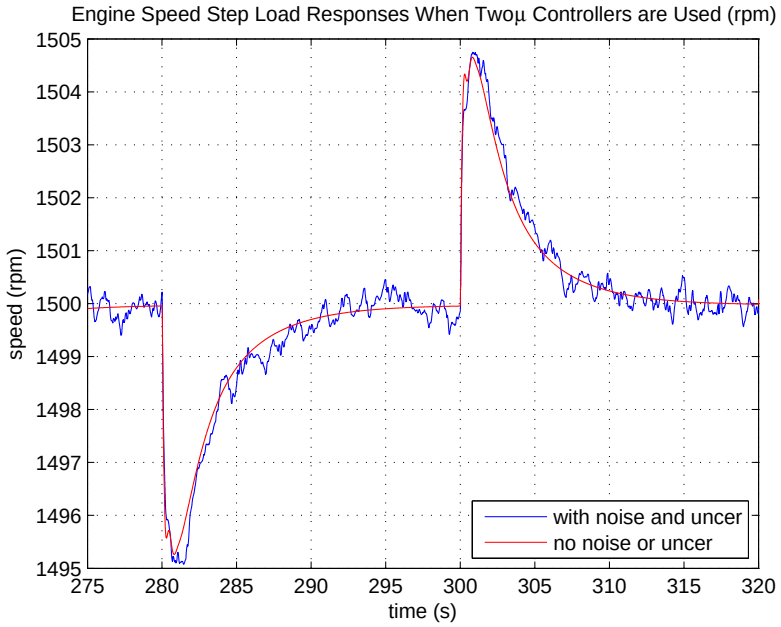

FIGURE 7.30. Engine speed step load responses with two μ controllers.

The engine AFR step load responses is plotted in Fig.7.31. One can easily see that the AFR is kept within a narrow band during steady-state conditions. During transients, the maximum overshoot is less than 5%. Part of its zoom in view is shown in Fig.7.32. In this figure, some of the worst cases are presented. It can be seen the AFR is controlled in the same fashion regardless whether noises or model uncertainties were applied. Similarly, just high frequency noises are superposed. One point we would like to emphasis is the noise signals and uncertainties do not make the peak overshoot worse.

The storage system output power is shown in Fig.7.33. It can be seen the transient responses is less than 70kW. The rated output power of the engine system is 1MW. Hence, the required storage system output power is less than 7% of the engine rated power for this particular step load. One can also readily observe that the output power of the storage system

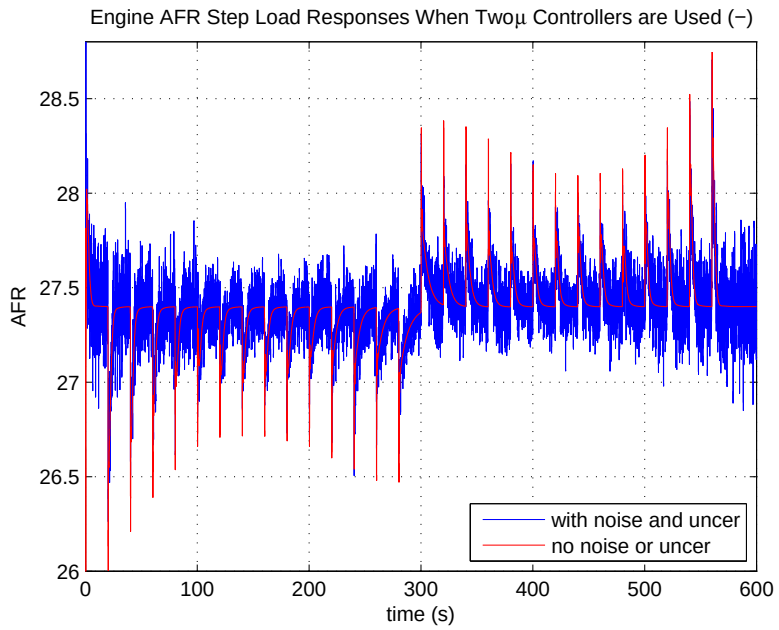

FIGURE 7.31. Engine AFR step load responses with two μ controllers.

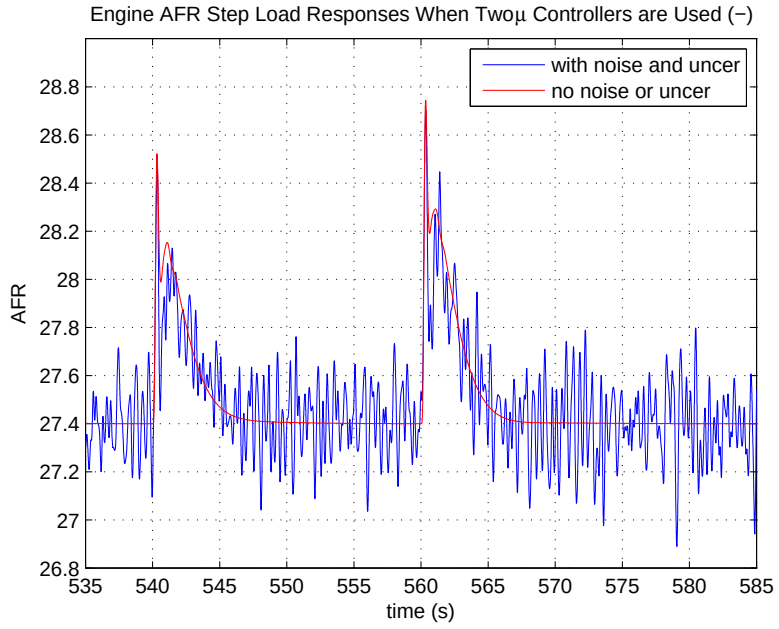

FIGURE 7.32. Engine AFR step load responses with two μ controllers.

at different load levels is mostly uniform. The affects of noises and model uncertainties on storage output are mainly appearing at steady-state conditions.

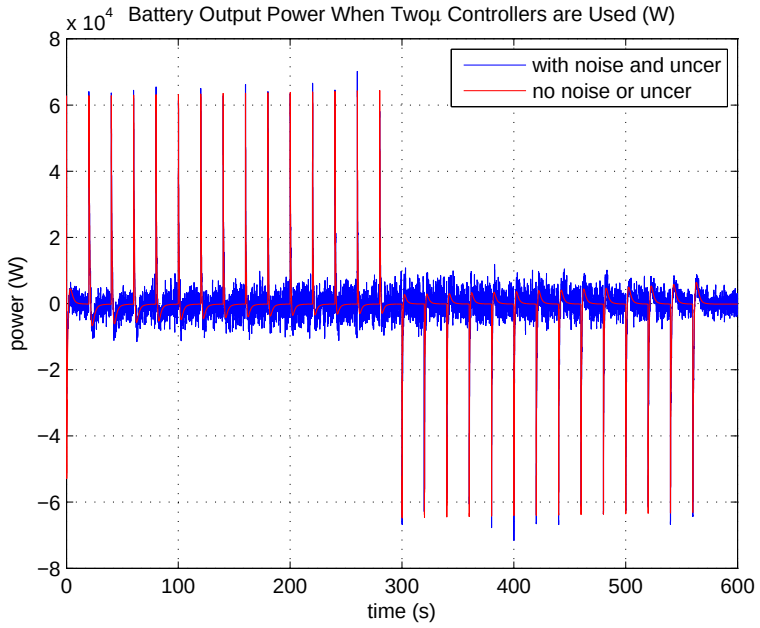

FIGURE 7.33. Battery power step load responses with two μ controllers.

A zoom in view of Fig.7.33 is shown in Fig.7.34. The load step up takes place at the 280th second, it can be seen the battery output power spikes to just over 60kW. Each step load here is 400Nm, which is equivalent to $400 \cdot (1500\pi/30) = 62.832$kW if the engine is kept at 1500rpm. This value is very well matched with the peak power for both step up and step down. This shows that at the very beginning of the step load, the entire load step is supported by the storage system.

Within the first two seconds after a load step, the storage system output power backs off from its peak output to negative for charging (SOC recovery). During these two seconds, the engine system ramps up and provides power to the load as shown in Fig.7.35. Clearly, the storage system power rolls down and engine system power ramps up between the 280th

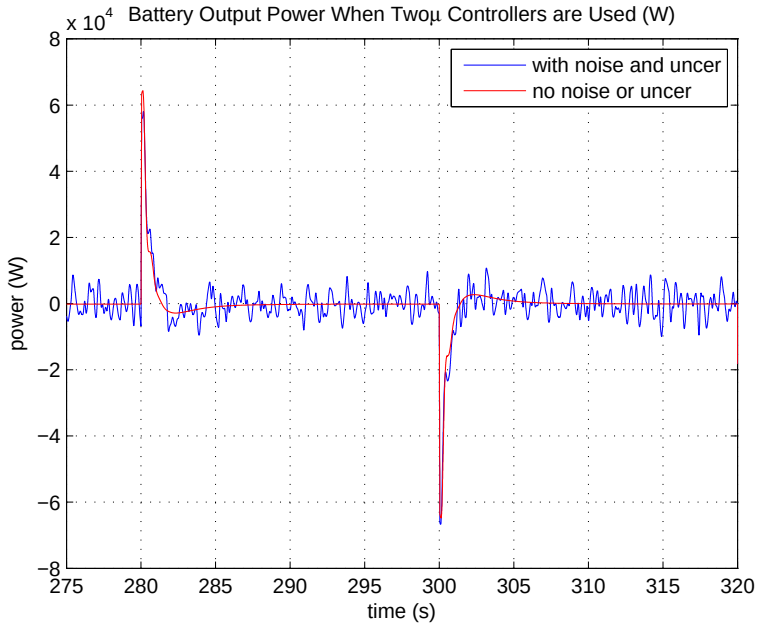

FIGURE 7.34. Battery power step load responses with two μ controllers.

second and the 283rd seconds. This load transfer action illustrates the power handover between these two systems. This is a remarkable behavior for both systems. They work together to maximize their own specialities and improve the overall system performance. In our setup, the engine has slow responses, but its speciality is larger capacity. Oppositely, the storage system can react much faster, but its energy capacity is limited.

Between the 283rd second and the 300th second, all the increased load is supplied by the engine system and at the same time the storage system only reacts to small load fluctuations around 0W. These are exactly the system behaviors we desired.

This figure also demonstrates the storage system in our setup is only used as a power source. The output of the system does not hold at a continuous positive or negative value. In addition, it can be seen that the storage system power and engine power reflect each other around the 0W y-axis. This is also desired behavior, since it shows the storage system

charges when there is excess power generated by the engine and discharges when engine cannot fulfill the load demand.

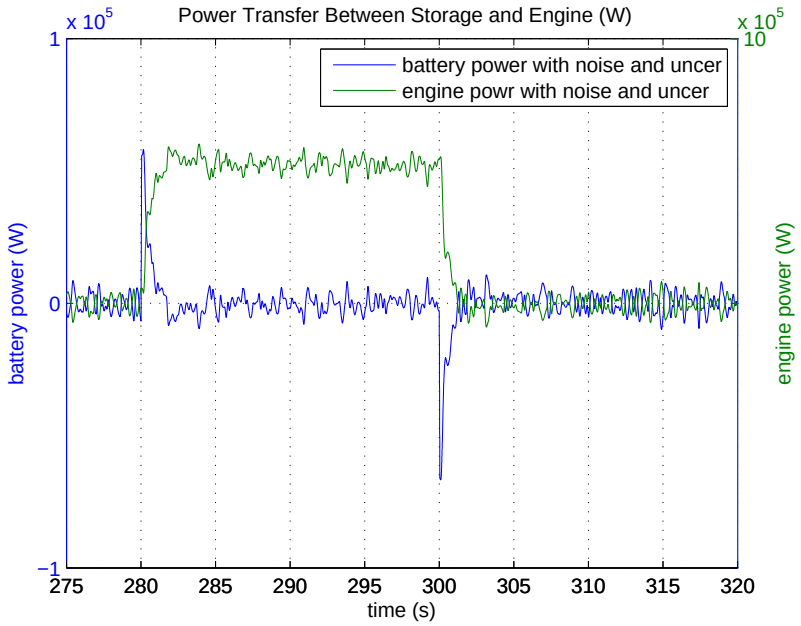

FIGURE 7.35. Step load power handover between storage system and engine system with two μ controllers.

The SOC of the storage system is shown in Fig.7.36. As one can see the SOC moves only minimally from its reference value. This is because the storage system is not used as energy source. It also indicates that in our setup, we care more about power density of the storage system. In this case, the traditional lead-acid battery based storage system can satisfy the system requirements. As we all know, the lead-acid batteries are much cheaper and readily obtained.

In Fig.7.37, the torque balances are shown. As we expected, the torque provided by the storage system is around 0Nm. At the same time, the engine system also behaves as we wanted. It steps up and steps down concordantly with the load variations. This shows

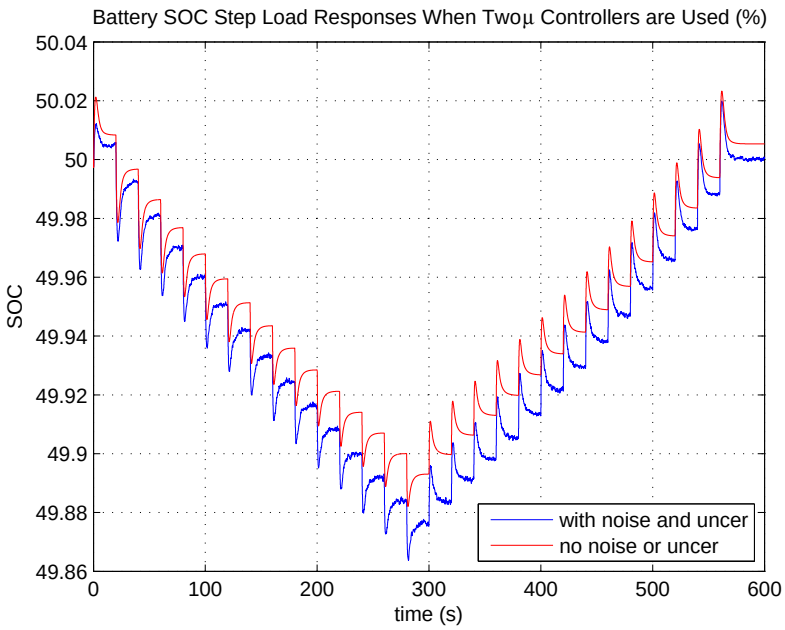

FIGURE 7.36. Battery current step load responses with two μ controllers.

that these two systems work together harmoniously. It further confirms our controllers are designed properly.

A zoom in view of the torque balance is shown in Fig.7.38. In this figure, the top two signals are the required total torque demand (load) and the provided torque summation of engine system and storage system. It can be seen that they are on top of each other, which means the microgrid system can support the load requirements. The battery torque is shown at the bottom of the figure in magenta. These three signals use the left y-axis. In the middle, the engine torque is presented in green. It uses the right y-axis. This figure indicates at the maximum load 6000Nm, the engine is really providing the load. It is clear that storage system only charges and discharges around 0W to fight with high frequency disturbances.

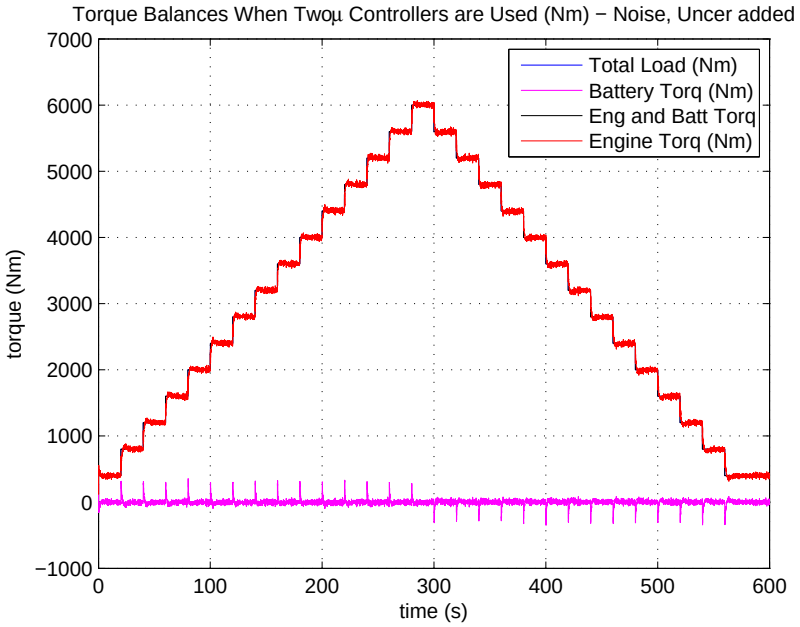

FIGURE 7.37. Torque balances with two μ controllers.

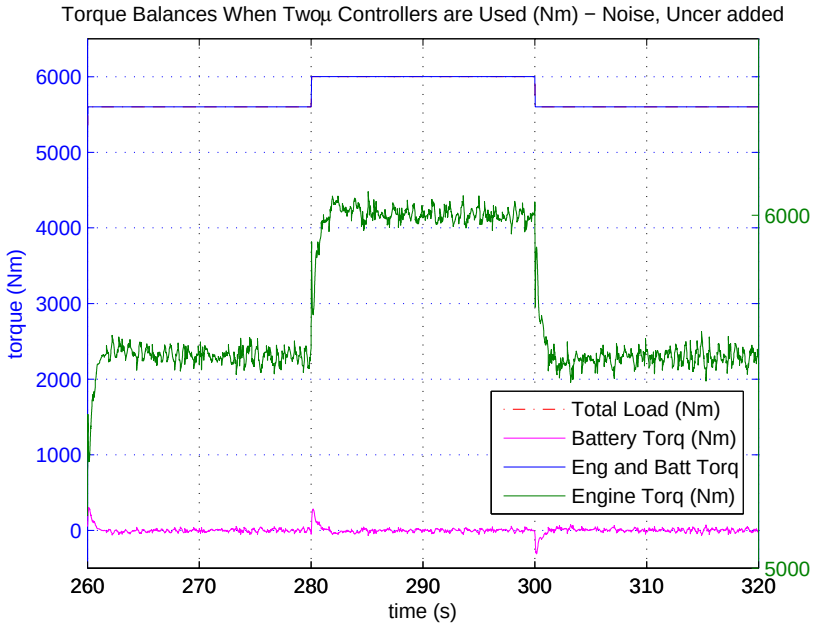

FIGURE 7.38. Torque balances with two μ controllers.

7.6.2. *Single Robust Controller for Storage System and Natural Gas Engine*

In this section, the single robust controller configuration is presented. In this configuration, there is only one MIMO controller, which controls natural gas engine and storage system at the same time. In this setup, the MIMO controller has the access to all the system inputs and outputs. This implies that the MIMO controller has more flexibility over the system being controlled and hence the potential to deliver better overall system performance. In such setup, the controller understands the internal dynamics between interconnected systems and could compute more suitable control signals for maximizing the overall system interests rather than just certain subsystems. In this section, the design model and weight functions are discussed first. Then the simulation results are presented with discussions and remarks. In addition, a case study is accomplished by using processed real microgrid load data. The purposes of this case study is to demonstrate the overall system is feasible under real world circumstances.

7.6.2.1. *Robust Control Design Model*

The design model for the single MIMO controller configuration is shown in Fig.7.39. In this design model, the engine system and storage system are interconnected through the dynamic torque balance. The storage power output is converted to torque by using real-time engine speed signal. Because only part of the load is provided by the battery, the rest of the load still has to be supplied by the engine system. The inputs of the controller are engine speed error, engine AFR error and storage SOC error. The controller's outputs are throttle valve angle, trim valve angle and storage commanded current. This MIMO controller is located between output ports 11, 12 and 13 and input ports 10, 11 and 12 as shown in Fig.7.39. The uncertainties and unmodelled dynamics are wrapped into Δ and

placed between output and input ports 1, 2 and 3. The other input ports are for references and disturbances. The rest of the output ports are associated with the signals needing to be penalized for achieving the desired performance. In addition, the linearized engine system model and storage system is included in this design model.

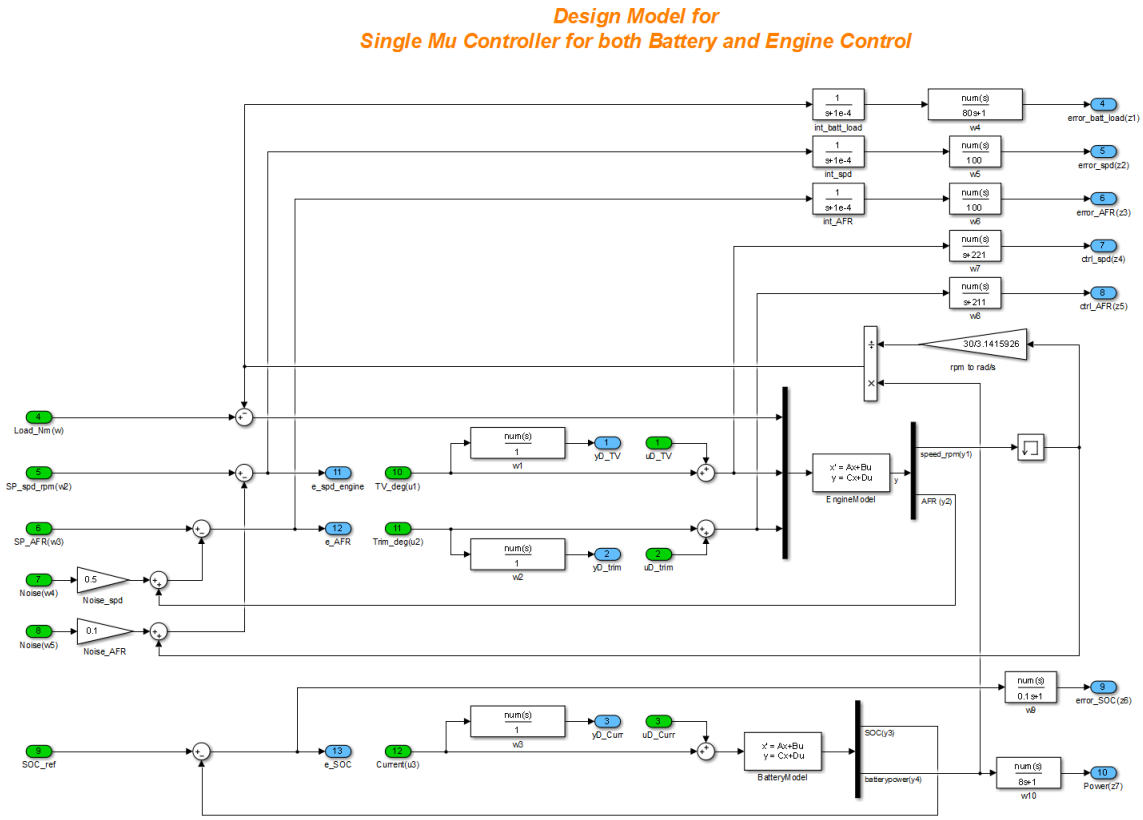

FIGURE 7.39. Simulink design model for microgrid with one MIMO robust controller.

7.6.2.2. *Weights Selections*

In this subsection, the weight functions for single MIMO controller configuration are presented first. Then how these weights are selected is discussed. Let us take a look at the weights on the error signals. In order to enhance system performance, the error signals should be minimized. As one can see, the weigh functions $W_{e_{speed}}$ and $W_{e_{AFR}}$ are the same

as the ones that used in section 7.4 as robust engine controller is designed. As we mentioned before, constant weights are selected first, then a modified integrator is combined to reduce the steady-state errors.

$$W_{e_{speed}} = \frac{17.33}{s + 10^{-4}} \tag{7.5}$$

and

$$W_{e_{AFR}} = \frac{7.11}{s + 10^{-4}} \tag{7.6}$$

The selected weight function for minimizing the SOC error signal is:

$$W_{e_{SOC}} = \frac{7 \cdot 10^{-5}}{0.1s + 1} \tag{7.7}$$

As shown in Fig.7.40, the Bode plots of the weight functions on engine error signals have low pass filter like characteristics and they roll off at $10^{-4} rad/s$. This is because of the modified integral action. For engine system, more punishment on error signal happens at low frequency. At high frequency, because of the slow engine dynamics, it cannot react fast enough. For high frequency load fluctuations, the storage system should take the responsibility and act on them. In our configuration, the storage system is used as power source. Hence, very small penalization has been applied on storage system SOC. The penalty functions on the inputs of engine system are also adapted from section 7.4. For more information about how these weights are selected, please refer to the corresponding section in this chapter.

There are two more weight functions, $W_{out_{battload}}$ and $W_{out_{batterypower}}$. This is their first appearance in this dissertation. These two weight functions are used to penalize the torque signal that will be subtracted from the total load and the storage system output power signal.

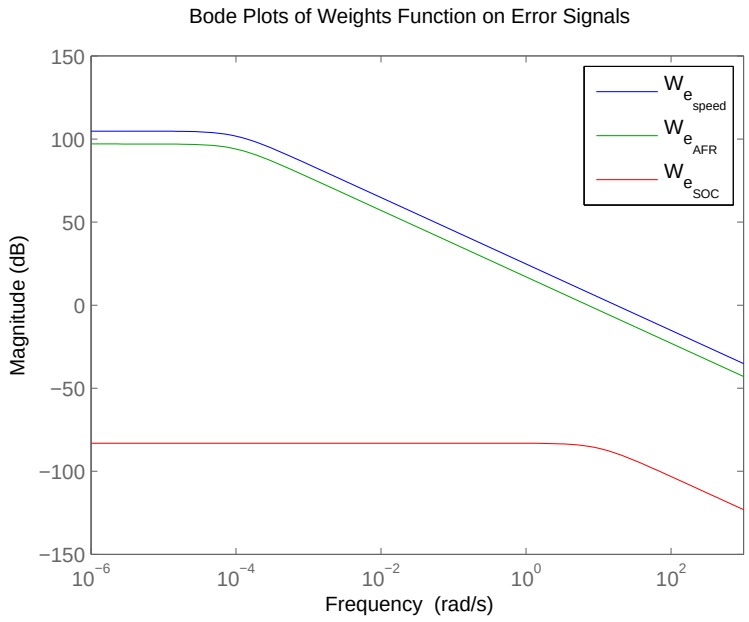

FIGURE 7.40. Bode plots of the weights on the error signals.

For the former, there is an integrator with modifications. This weight function ensures the torque provided by the storage system goes back to zero at steady-state conditions. By doing so, we ensure the storage system only acts as a power source. Most of the large slow load variations are taken care of by the engine system. In other words, the engine system output power follows the load trends.

$$W_{out_{battload}} = \frac{1}{s + 10^{-4}} \cdot \frac{3}{80s + 1} \tag{7.8}$$

and

$$W_{out_{batterypower}} = \frac{8 \cdot 10^{-4}s + 1}{8s + 1} \tag{7.9}$$

As shown in Fig.7.41, the penalties on the storage system at low frequency are very big. This implies the storage system should not act on low frequency load variations, because

such kind of load should be supplied by the engine system. The storage power is limited in the same manner. It only reacts to high frequency load variations and ignores large slow load fluctuations. Overall, engine system and storage system should work as a combined entity to improve the system performance.

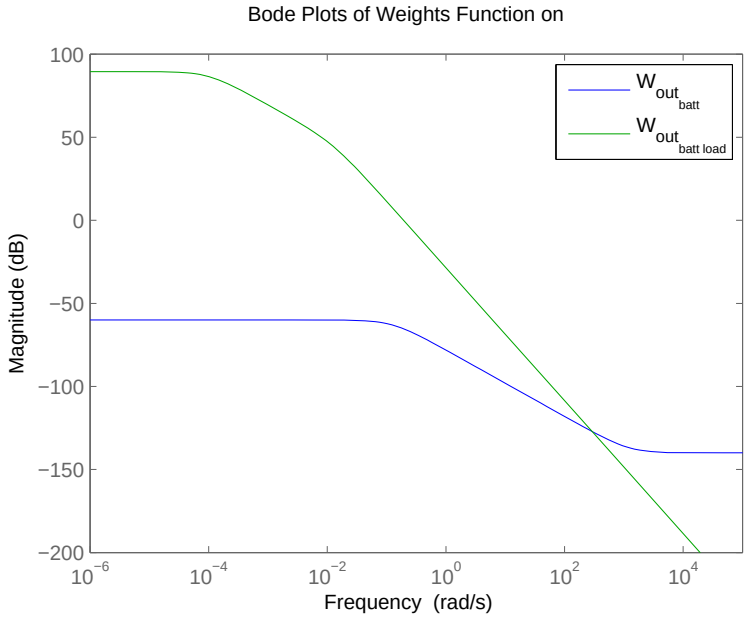

FIGURE 7.41. Bode plots of the weights applied on storage torque and power.

7.6.2.3. *Robust Simulation Model*

The simulation model of the system that is controlled alone by a single MIMO robust controller is presented in Fig.7.42. As one can see, there is only one controller, whose inputs are the engine speed error, engine AFR error and storage SOC error and its outputs are throttle angle, trim valve angle and storage system current. As usual, in the simulation model the full model of the engine system and storage system are used. In addition, noises and uncertainties are added as well. The torque signal going into the engine is the torque

difference between the 'net load' and the 'storage torque', which is obtained from storage power and engine speed.

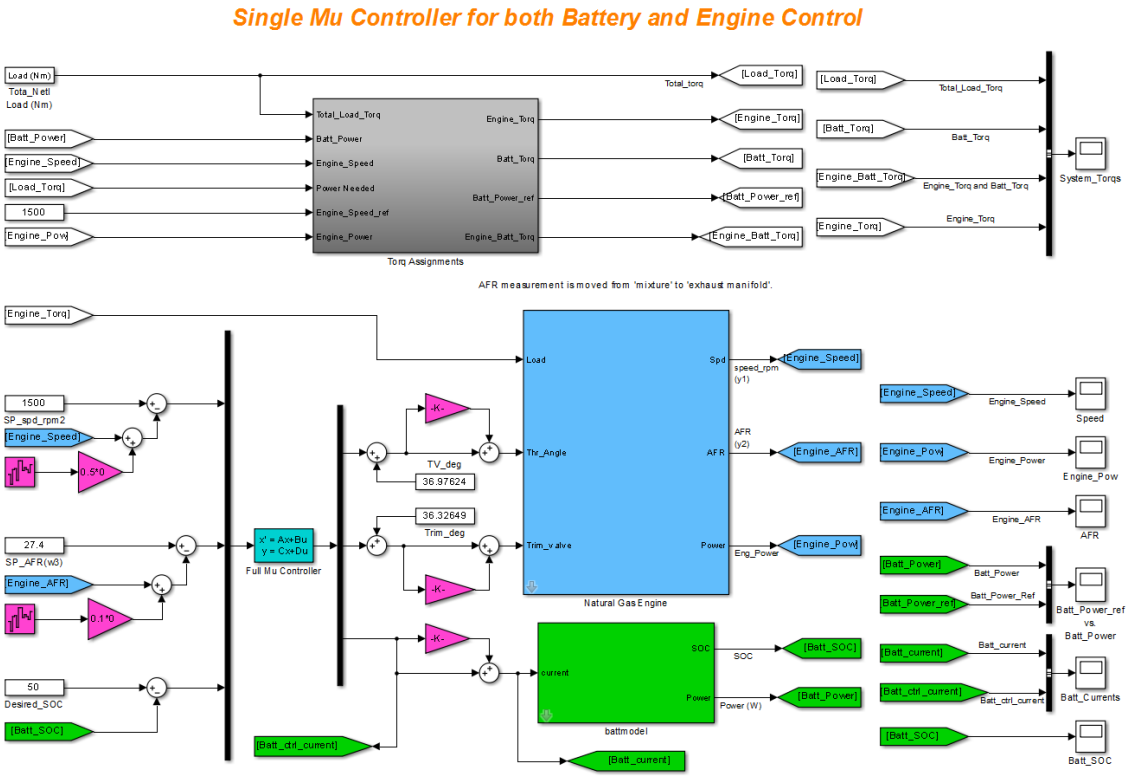

FIGURE 7.42. Simulink simulation model for microgrid with one MIMO robust controller.

7.6.2.4. *Simulation Results*

In this section, the simulation results of the single robust MIMO control system is presented with detailed analysis, discussion and studies. Several significant remarks are given. Overall, the single robust MIMO control achieves the best performances in terms of engine speed and AFR control. As shown in Fig.7.43, the maximum speed deviation is less than 3rpm when both noises and model uncertainties are applied. That is less than the injected speed measurement noise signal amplitude shown in Fig.7.5.

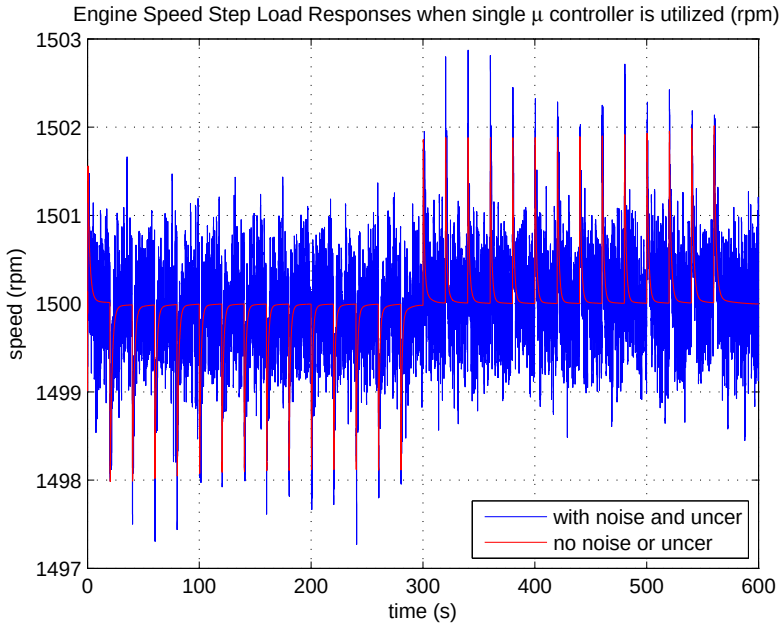

FIGURE 7.43. Engine speed step load responses with single μ controller.

The zoom in view of the step responses during step acceptance and step rejection around the engine rated load is shown in Fig.7.44. As one can see, the noises and model uncertainties do not affect the speed responses significantly during transients. Relatively they have more influences during the steady-state situations. Overall, the speed deviation is very small. The main point to be underlined here is that without any system hardware upgrade, expansion or reconfiguration, a mathematical control redesign based on modern MIMO control theory can improve the overall system performance significantly.

The AFR step load responses are shown in Fig.7.45. The maximum AFR deviation is less than 3%. In the two μ controller setup, robust controllers were used, but there is a lack of communication between those two controllers. The maximum AFR deviation is around 5% as shown in Fig.7.31. By using a single MIMO controller, the AFR deviations are reduced compared to the setup that has two μ controllers are deployed in Fig.7.31. Further

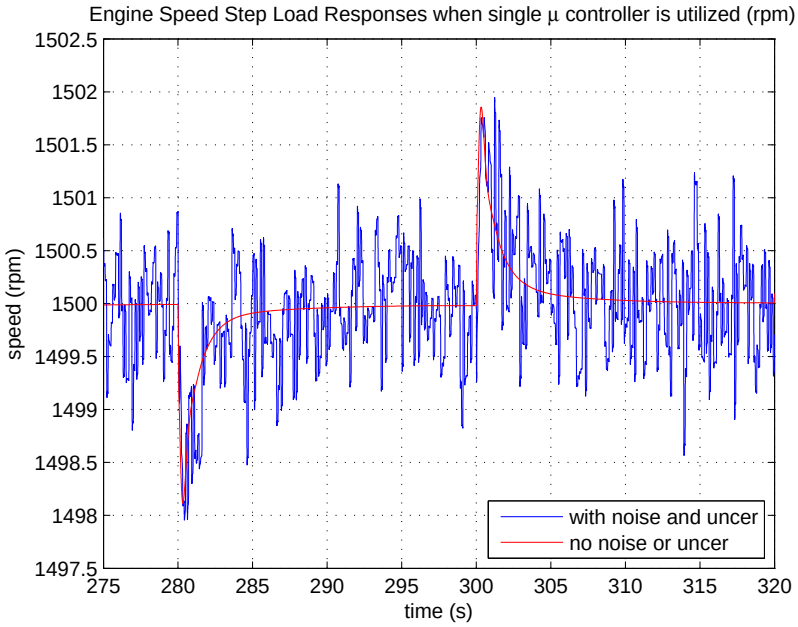

FIGURE 7.44. Engine speed step load responses with single μ controller.

comparing to the system when PID controllers are implemented as shown in Fig. 7.22, the AFR deviation is reduced significantly. The systems used for obtaining these three figures all have the same storage system attached. Again, what has changed is just the design method of the controller. This modification can be done with just software alterations.

The biggest AFR deviations take place after the 540th second. A closer view of AFR step responses during this period is shown in Fig.7.46. It shows that the noises and model uncertainties do not affect the AFR control noticeably in a negative sense. In fact, the simulation results here show that the perturbed system has smaller overshoots. In addition, the perturbed system responses deviate around the unperturbed system. This implies the designed controller is robust to disturbances and system uncertainties.

Fig.7.47 shows how the battery system reacts to the step load. It can be seen the storage system delivers or absorbs maximum amount of power to the load at the very beginning of

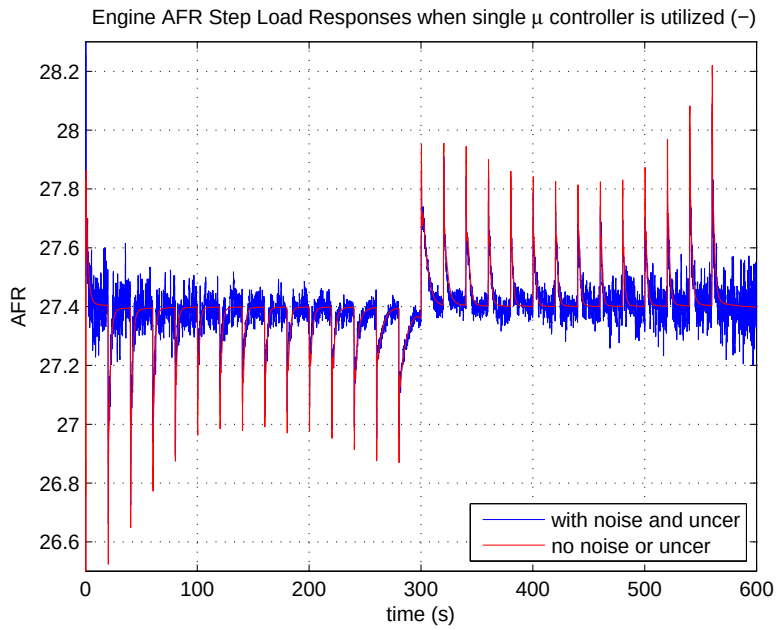

FIGURE 7.45. Engine AFR step load responses with single μ controller.

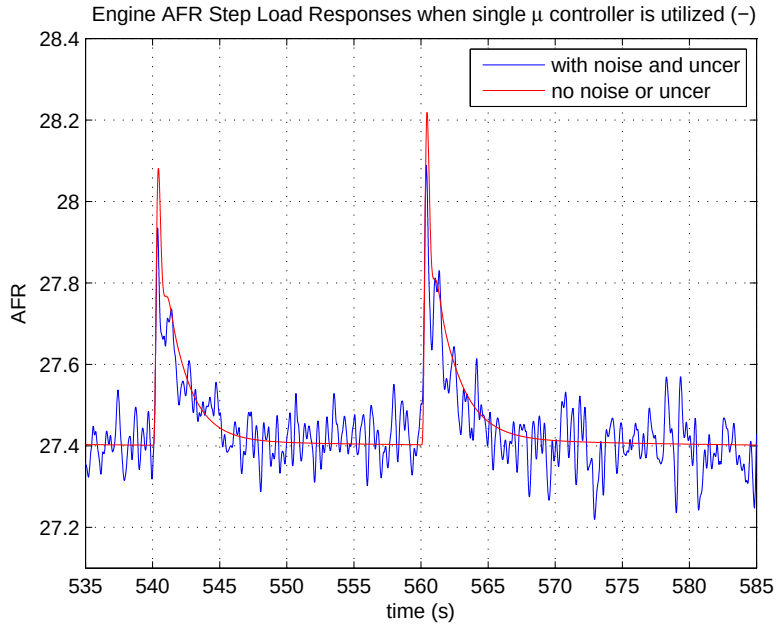

FIGURE 7.46. Engine AFR step load responses with single μ controller.

each step load. As mentioned in section 7.6.1, the storage system takes care of the entire load step up and step down at the very beginning. When the engine system catches up gradually, the storage system starts to pull out. This desirable behavior minimizes the storage capacity by minimizing the charge and discharge durations. At the same time the battery life is protected because of the small SOC variations.

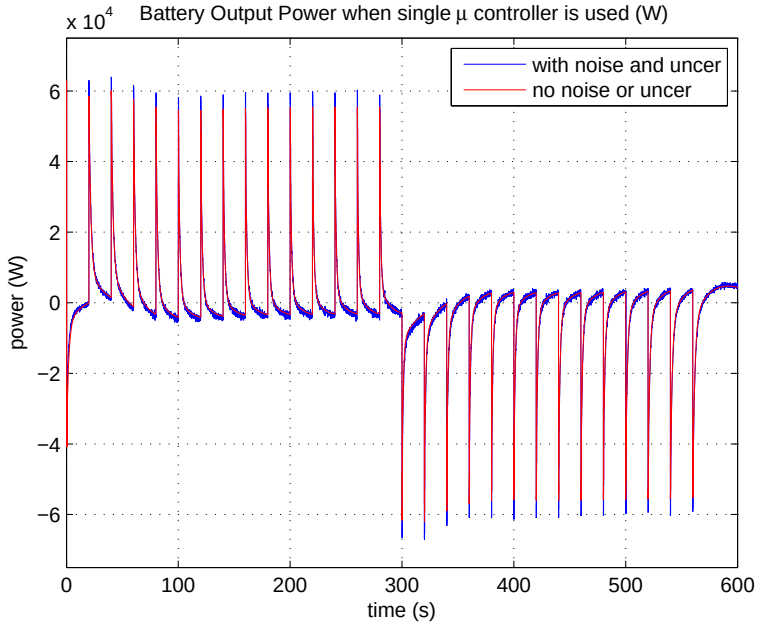

FIGURE 7.47. Storage power step load responses with single μ controller.

Let us take a close look at the battery power step response. As shown in Fig.7.48, storage output instantaneously discharges and reaches to about 60kW to cope with the 400Nm load increases at the 280th second. Soon after there is a 400Nm load rejection at the 300th second. The storage system acts on it instantly too. For both processes, the storage system power returns to absolute values of less than 10kW in about 2 seconds. The storage system output power does not return to 0W because only a very small penalty is applied to storage SOC error. In other words, we did not ask for very rapid SOC recovery. Hence, the storage

takes longer to recover its SOC. This is acceptable in this setup since the SOC deviation is minor even though there is not much energy usage constraints applied on storage.

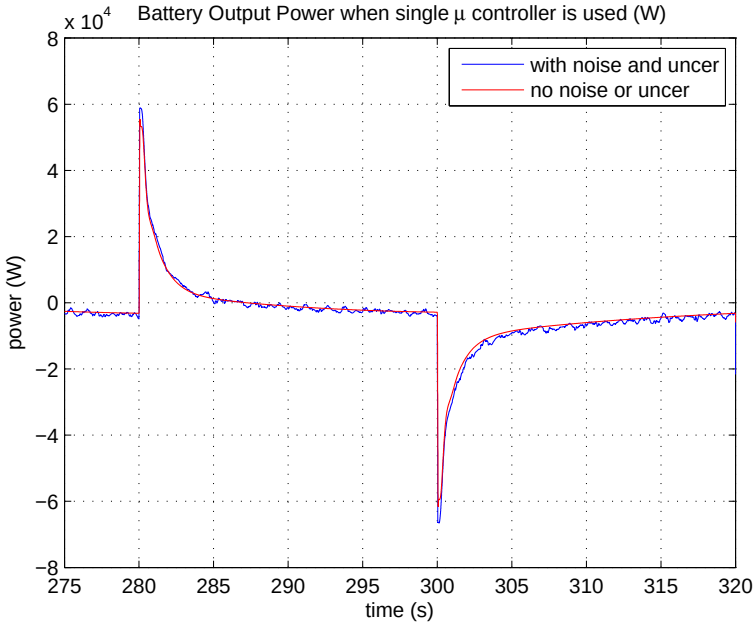

FIGURE 7.48. Storage power step load responses with single μ controller.

In Fig.7.48, the storage power returns to around 0W in about 4 seconds. The storage system backs off because the load is taken care of by engine system bit by bit. Two load transfer processes are shown in Fig.7.49. During the first transfer, engine takes the load from the battery step by step. Storage system reduces its output from positive to 0W. To recover the SOC, it further reduces its output to negative for charging. For the second transfer, storage system absorbs power from the engine system. Since the SOC is lower than 50% as shown in Fig.7.50, the storage system power is kept negative to continuously charge itself from the engine system. In such as case, the engine system produces more power than the power requirement of the engine. The excess power goes into the storage for SOC recovery.

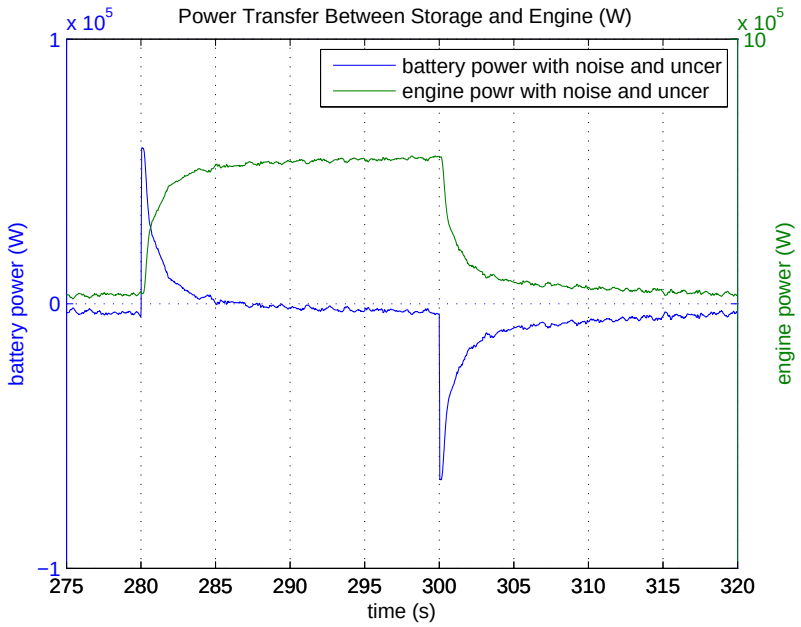

FIGURE 7.49. Step load power handover between storage system and engine system with single μ controllers.

The most interesting SOC variations take place after the 300th second. At the 300th second, the system changes from load acceptance mode to load rejection. The load that is taken off from the engine system is directly injected to the storage system. This explains why there is a big SOC recovery action. As one can easily notice, this particular SOC recovery is larger than the others. The reason is that the storage system just had series of discharge actions, and so there is the biggest SOC deviation at that time. When there is excess power within the microgrid, the controller of the storage system does not put limitations on the charging current. The possible limitation is the allowed hardware charging current. With more and more charging actions, its SOC recovers and the controller starts to limit the charging current to maintain its SOC again.

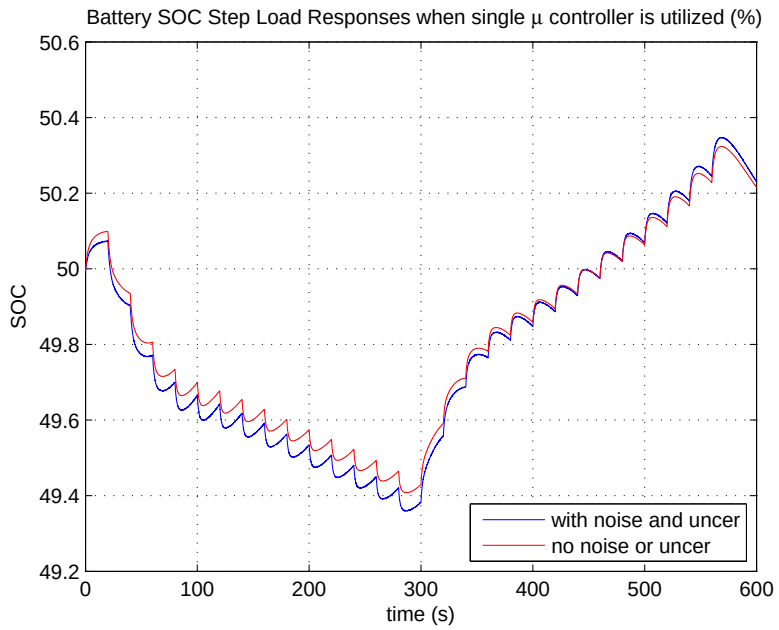

FIGURE 7.50. Storage system SOC step responses with single μ controller.

7.7. Case Study with Processed Real Microgrid Load Data

Till now, the proposed engine and storage combined system has been studied by using step load with various controllers. Let us test the system by using some real microgrid load data with the MIMO robust controller proposed in section 7.6.2. A processed microgrid load profile is shown in Fig.7.51. The resolution of the original data is 5 seconds and it spans for nearly a day. For our research, the data is down scaled 10 times in x-axis. Each load step is now 500 milliseconds. By doing so, we made the problem even harder. As one can see, there is a 800Nm load step up at around the 600th second. Consequently, that is the most difficult load step for the system to cope with. The most interesting transients happen around this region.

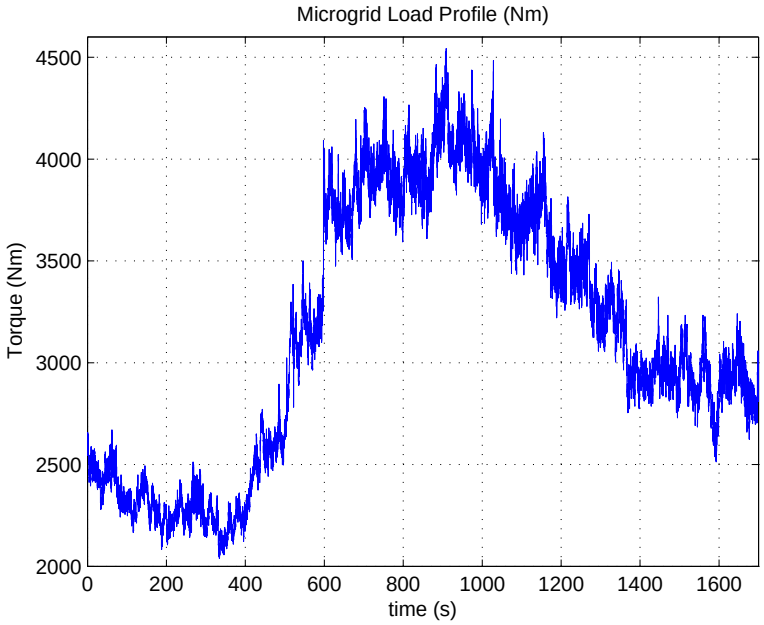

FIGURE 7.51. Processed real microgrid load profile.

It can be seen from Fig.7.52, the biggest engine speed deviation happens at this particular load transient. Thankfully with the help of the storage system and MIMO robust controller, the maximum engine speed deviation is limited within 3rpm.

Fig.7.53 shows the storage system power. At this large load transient, the storage power is about 110kW when there is no current limiter is activated. Most of time, the storage system power is kept within the band of plus minus 40kW. Since the natural gas engine is rated at 1MW, the maximum storage system instantaneous power usage is about 11% of the engine power and mostly they are limited within 4%. Let us use current limiter to mimic different size of storage systems that are utilized in the microgrid. Since the worst scenario happens at this particular period, let us take a more detailed study.

In Fig.7.54, the engine speed deviations between the 594th second and the 603 second is shown when 40kW, 60kW, 80kW and 100kW storage systems are attached. It is trivial to

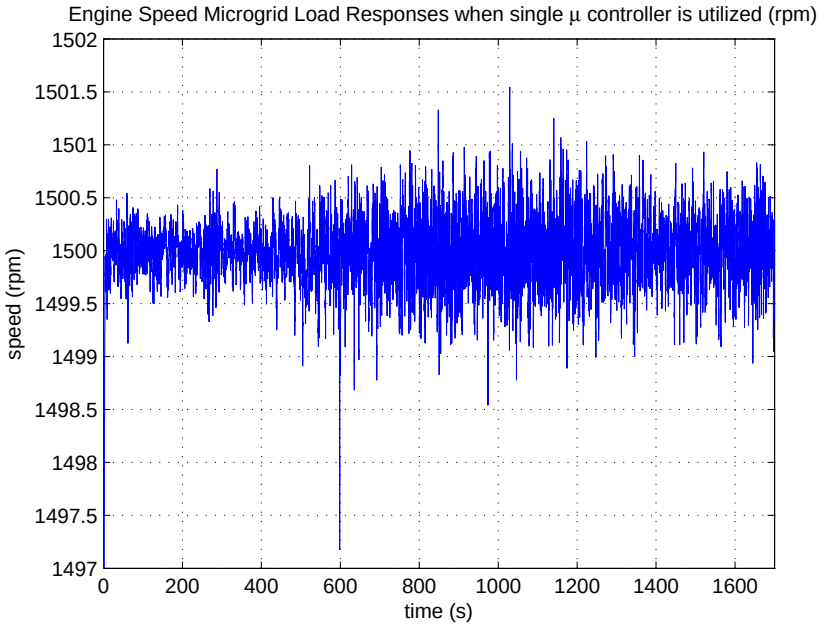

FIGURE 7.52. Engine speed responses with real microgrid load.

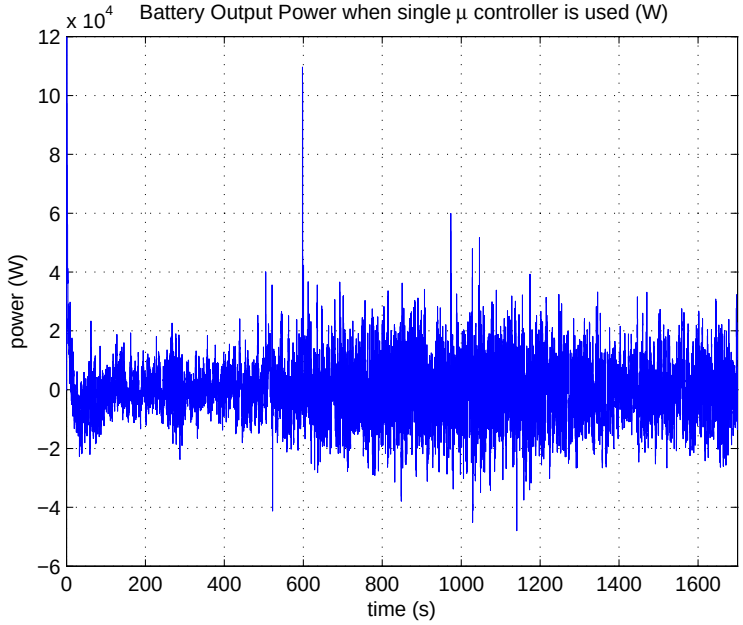

FIGURE 7.53. Storage system power with real microgrid load.

notice that with bigger size storage, the speed deviation is smaller. It is simple to explain, because the larger storage power implies a smaller load imbalance and results a small speed deviation. The extreme example is if the storage system has infinite energy capacity and infinite power density, there would not be any speed deviation. However, this assumption is not practical. As shown in the figure, when 80kW storage system is deployed, the engine speed deviation is less than 5rpm. As 5rpm speed deviation is the worst case over the entire test, the other deviations are all smaller than 5rpm. In addition, by increasing the storage system size, the speed deviation reduction at other loads are limited since they only require less than 50kW storage power.

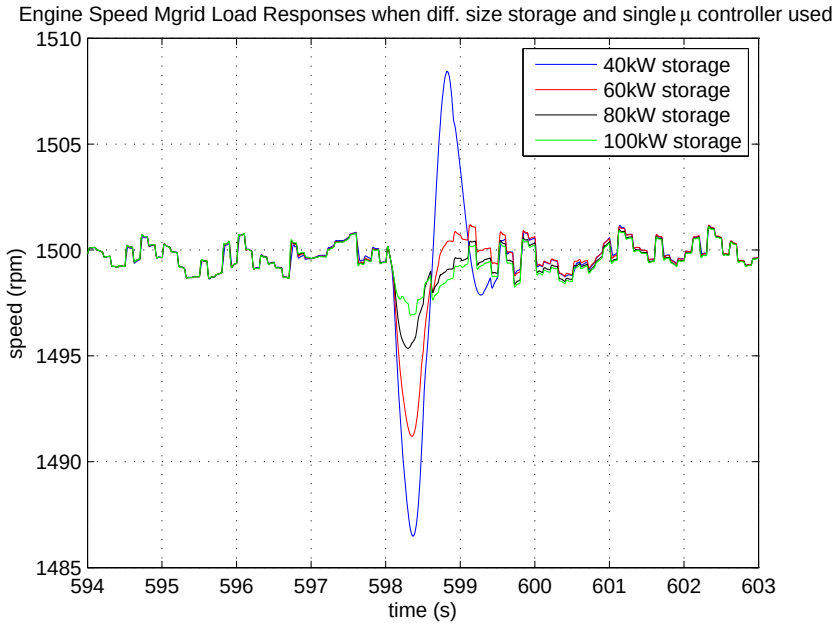

FIGURE 7.54. Engine speed responses with real microgrid load and different size storage attached.

As shown in Fig.7.55, the storage system output power only deviates around 0W, which is the desired behavior for a storage system. This implies the storage system capacity and cost are minimized. As one can notice even further, the storage charges and discharges very

quickly to cope with high frequency load variation. The slow load trends are taken care of by slow engine system as it follows the main load fluctuations. Fig.7.55 also shows the engine torque follows the total load trends and battery torque is combined onto it.

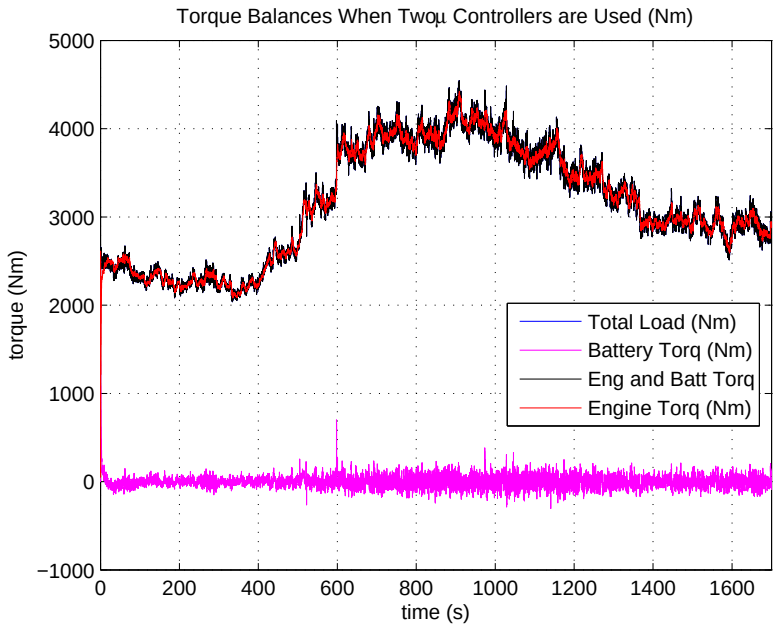

FIGURE 7.55. Torque balances with real microgrid load.

AFR deviation is shown in Fig.7.56 when there is no storage power limitation applied. In such a setup, the maximum AFR deviation is around 2%, which is very small. This implies even at very big and fast load transients, the system emission is controlled tightly.

AFR deviation comparison are shown in Fig.7.57 when 40kW, 60kW, 80kW and 100kW storage system are attached. The figure shows that with 80kW storage system deployed, there is a 3.6% of AFR deviation. However, if only 40kW storage is used, the AFR deviation can be as big as 9.1%. In this particular application, we would suggest a 80kW storage system for achieving good system performance.

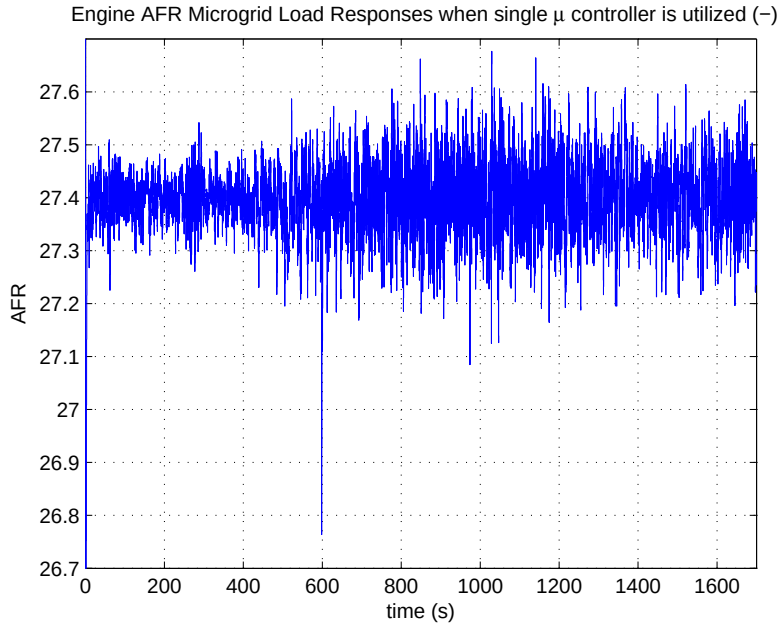

FIGURE 7.56. Engine AFR responses with real microgrid load.

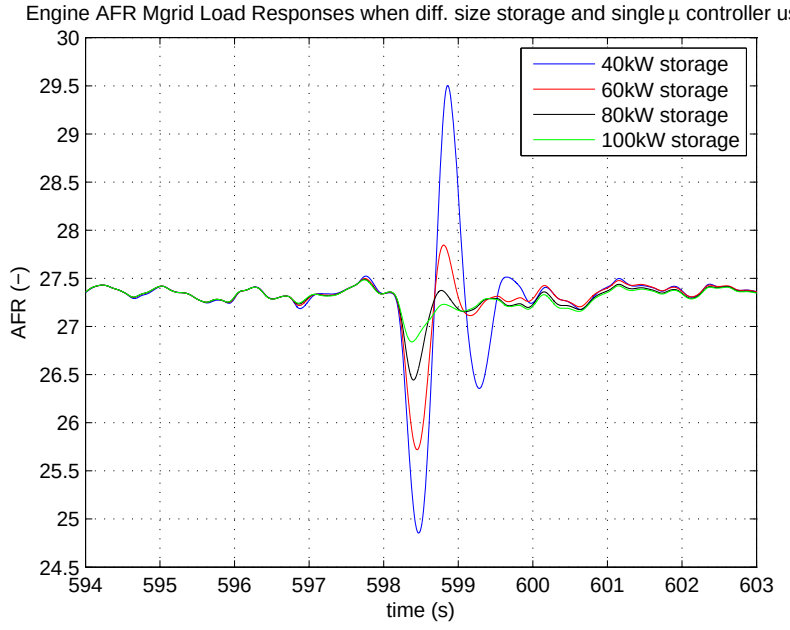

FIGURE 7.57. Engine AFR responses with real microgrid load and different size storage attached.

The SOC variation of the storage system is shown in Fig.7.58. This figure shows that with different size of storage system attached, the SOC variation is not significantly different from each other. This is because of the fast charging and discharging action the storage system can take. At the same time, the high frequency load fluctuations are rapidly jumping up and down, which gives the storage system opportunities to recover its SOC all the time. In addition, the SOC variation is more sensitive to large load variations. In other words, it is used as an energy source. However, the large and slow load variations that have deeper effects on storage system SOC are taken care of by the engine system in our setup.

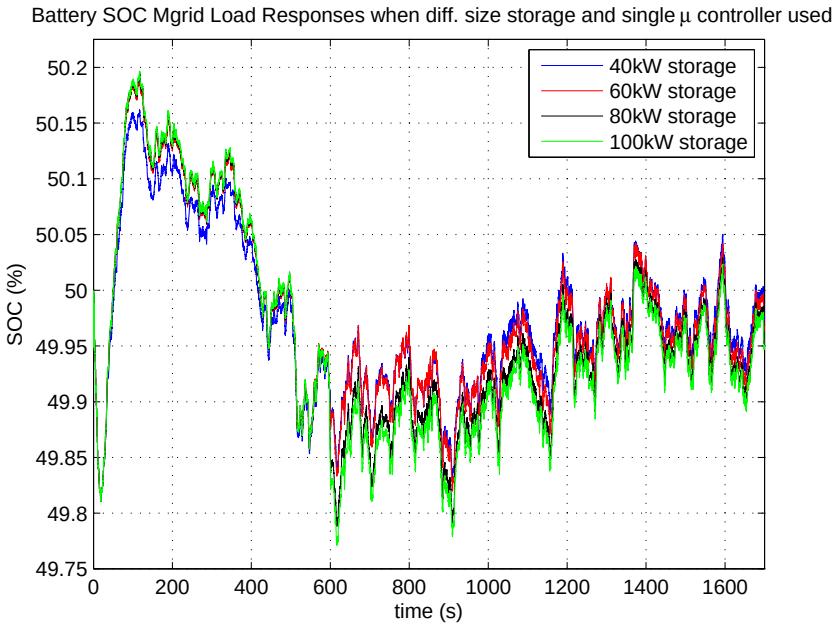

FIGURE 7.58. Storage system SOC with real microgrid load and different size storage attached.

7.8. Conclusion

In this chapter, multiple configurations for both natural gas engine control and microgrid control are presented. Overall the simulation results show that MIMO robust control has dramatically better performance than the classical control system.

In the engine control application, the MIMO robust control based system has much better performance than the multiple SISO PID controlled system. In industrial world, PID based control approaches are still heavily deployed. However, because of PID control inherent drawbacks, it can no longer provide the desired system performance with the growing system complexity and even higher performance criteria. More advanced control algorithms should be pushed into industrial applications. PID control is really an experience based tuned controller. There is a lack of the understanding of the physical system. In addition, multiple SISO controllers are not equivalent to a MIMO controller. There is the lack of knowing the interactions between each input and output. Furthermore, with state estimation and adaption, system performance can be further improved with modern controls.

In the microgird control application, the single MIMO control based system has better performance than the two MIMO robust controller based system. In this microgrid system, the engine system and the storage system have been well coordinated to work together. The task of the controller here is to control the system based on their characteristics in terms of their reaction time, energy density and power density. As our presented simulation results in this chapter have shown, a properly designed controller can dramatically improve the system performance without any system modification and expansion. In addition, with reasonable storage system attached, microgrid system performance is further improved noticeably. Many hardware related control issues with classical controls are thus resolved.

In particular, this research may enable the use of natural gas engines for many applications where before they were not practical because of the unsatisfactory transient performance. The major contribution toward engine performance improvement that have been achieved in this dissertation is summarized here. This summary is done separately for the cases that the storage system is attached or not attached.

(1) Engine system performance improvement by utilizing robust control (without storage system attached)

- Proposed MIMO robust control configuration for engine speed and AFR control.
- Significant engine speed deviation reduction compared to PID controllers based system setup.
- Transient AFR control for emission reduction is achieved without significant deviation.
- Engine speed settling time and raise time reduction.
- Disturbance rejection to noises and load fluctuations.
- Robustness to model uncertainties.

(2) Engine system performance improvement by utilizing robust control (with storage system attached)

- Transient performance improvement sufficient to potentially open up new applications for natural gas engine microgrids.
- Structurally modified engine control configuration - Added storage system for fast load transients support.

- Proposed MIMO robust control configuration for engine speed, engine AFR and storage current control.
- Further noticeable engine speed deviation reduction.
- Further noticeable engine AFR control improvement.
- Further noticeable engine speed settling time and raise time reduction.
- Storage system control for coping with high frequency load fluctuations.
- Storage system energy capacity minimization.

In order to benefit human beings by using the proposed engine control system, the proposed MIMO robust engine control concepts have to be accepted by industry first before they can be commercialized.

CHAPTER 8

Conclusion and Future Work

In this dissertation, we have conducted an overall study on microgrids in various aspects, including microgrid optimization, modelling and control. Microgrids are complicated systems. Their related studies are performed on the system level. This system consists of several key subsystems, such as renewable energy generators, engine systems, electrical generators, storage systems and loads. Each subsystem can be a very complex system in its own right. It is also a system that comprises electrical, mechanical, chemical, controls, economics and other aspects. The purpose of this research is to provide technical contributions towards microgrid development on system level, in order to make the microgrid power solution feasible. Thus microgrids can be readily developed, deployed and accepted by general public.

We would like to promote microgrid systems development and implementation in a larger scale. By promoting microgrids, more people, enterprises, governments and other organizations will have a better understanding regarding to microgrids, so they are willing to invest, conduct research activities, pass new legislations and contribute toward microgrids. The ultimate goal of this research is to maximize the benefits of microgrid by resolving its related (unsolved) technical challenges to further enable its capabilities. More importantly, by solving these technical problems, the impact is not limited to economic considerations. It also helps to reduce the human impact to this planet we all live on and secure our energy demands in the future.

In this chapter, we would like to conclude our contributions in senses of:

- resolving technical issues and
- providing system level study methodology

For the first part, our technical contributions are listed and discussed briefly. These resolved issues have significant impact toward the real microgrids investments, construction, operation and management. By studying such a complicated system, some system level methodology can be concluded for other studies that involve systems having distinct characteristics and properties. First of all, let us review the notable technical contributions this research has provided to microgrids.

8.1. Technical Contributions and Remarks

From technical point of view, through this research we delivered our contributions towards microgrid optimization, modelling and control. The technical contributions aim to tackle the technical challenges and difficulties that stop microgrids from being feasible for deployment and commercialization. In the following subsections, these contributions are listed and concluded.

8.1.1. *Microgrid Optimization*

The contributions toward microgrid optimization are two-fold. In the first part, the conducted research dispatches load optimally to minimize the overall microgrid fuel usage. The 'load' considered here is the net load that has to be provided by fossil fuel. It is the difference between microgrid total load and renewable power. In the second part, when a historic load profile is given, a set of generators are selected optimally for fuel usage minimization. Within this topic, a Matlab^{TM} based simulation tool is developed. This tool is developed for solving microgrid cost related problems, mainly for fuel usage but not

limited to it. The microgrid optimization work can be found in chapter 4, 3 and some of our publications including [98], [115], [23] and [99].

8.1.1.1. *Load Dispatch for Fuel Usage Minimization*

If the fuel consumption curves of each generator within a microgrid is known, the developed optimization tool can optimally dispatch the load to each engine for fuel usage minimization. The re-dispatching time interval can be freely defined to minimize the fuel usage. The global minimum solution is obtained. In addition, to incorporate real world scenarios, some real world constraints are put into consideration. The discussion of this topic is performed by considering idle mode and shutoff mode, because of the differences of the cost functions in these two cases. Regardless of the difference of the cost functions, the KKT-conditions based methods deliver the minimized fuel consumption for load optimal dispatch compared to the existing load dispatch methods, such all uniformly dispatch (AUD), descend uniformly dispatch (DUD) and maximum load uniformly dispatch (MLUD).

8.1.1.2. *Generator Selection for Microgrid formation*

If a historic load profile and a set of fuel characteristic curves of several generators are known, the developed optimization tool is used for generator optimal selection for forming a minimum fuel usage microgrid. In this case, all the possible combinations that meet the load requirement are studied by using the developed tool, which computes the total fuel consumption for each combination. Again, the re-dispatching time interval can be freely defined to make the optimal dispatch more flexible. The particular combination(s) that consume(s) the least amount of fuel is chosen for guiding the selection of generators when a microgrid is formed. Multiple combinations can have the same minimum fuel usage. In such case, an economic life cycle analysis is utilized for determining which combination makes the

most economic sense. This economic life cycle analysis ensures our microgrid formation is not only technically feasible, but it is also reasonable from economic judgments.

8.1.2. *Microgrid Modelling*

Two major contributions are provided in this topic. The modelling work can be found in chapter 5 and 6 for a natural gas engine and a storage system, respectively. The developed models can be used not only for power system studies, but also for control system studies, natural gas engine control concepts validation, microgrid concepts demonstration and many other hybrid systems studies. It provides a set of tools that helps the microgrid studies go deeply into subsystem components level, such as how the turbocharger dynamics affect microgrid frequency recovery, how does the actuator dynamics influence the microgrid transient performance, etc. By gathering more information at these deeper levels, better system integration and control can be achieved. It has particular significance when model based advanced control is desired and implemented.

8.1.2.1. *Engine System Model Development*

A control orientated natural gas engine mean value model is developed. Compared to a diesel engine model, a natural gas engine model is much more complicated. The complexities arise from the engine configuration and the fuel type. For a natural gas engine, AFR is controlled for meeting emission requirements. Hence, mixture properties in each volume element of the engine model are tracked at run time. For a diesel engine, there is no AFR control. Also, there is noticeable fuel transport delay between the point of fuel injection, fuel combustion and torque generation. Contrast that with a diesel engine, which has the fuel directly injected into the combustion chamber, and so much less time delay between fuel injection and torque production. The change of the fuel dynamics has significant effects on

engine power control especially during transients. In addition, turbocharger dynamics are also modeled in this developed model. The developed natural gas engine model is suitable for conducting engine related and microgrid related research. The developed model balances the model running time and model accuracy, so it is suitable for control related tasks.

8.1.2.2. *Storage System Model Development*

A modified analytical battery model is developed for better representing its voltage dynamics with SOC and current variations. The proposed battery model is validated against real battery discharge curves at different 'C-rates'. Compared to the existing battery models, the proposed battery model is more sensitive to battery current and its SOC level. Therefore, it is a better model for capturing battery voltage dynamics that correlate with battery current and SOC. Based on the developed battery model, a storage system model is developed. The storage model is appropriate for conducting research work in the fields of microgrids, hybrid vehicles and other storage system related research subjects. Note again this model yields better accuracy, over wider range, compared to models of similar complexity.

8.1.3. *Microgrid Control*

In modern society, control plays a very important role. It manipulates the system, so it can accomplish the tasks as desired. In addition, it is really the modern industry glue and lubricant that integrates various systems together and make them functioning together to achieve a desired goal for maximizing humans' interests. For any system, the control system is indispensable. With increasing system complexity and higher system order, more sophisticated control algorithms are desirable.

Within a microgrid, different control approaches and configurations have been studied in this dissertation. The configuration with a single MIMO robust controller controlling the

entire system accomplished the best overall performance. The simulation results shows the system performance is amazing. Especially the engine speed and engine AFR deviations are very well reduced compared to traditional PID controlled systems. As a MIMO control setup, the controller has access to all the actuators as well as system inputs and outputs. In a multi-subsystem system, a MIMO controller has better understanding over all the subsystems and it can have each subsystem work cooperatively and make mutual compromises to achieve the goals. The setup with two individual robust controllers has the second best performance. Extensive studies have been performed in chapter 7. A complete microgrid system, engine system and storage system robust controller design and simulation tool package is developed in the Matlab™ and Simulink™ environment. This part of our work is presented in chapter 7.

8.1.3.1. *Microgrid Performance Control*

Various microgrid control structures are realized in simulation within this dissertation. Overall, the single MIMO robust control configuration delivers the best system performance. Within microgrids, the controllers are responsible for engine speed, engine AFR, storage power and storage SOC control. Regardless of load variation, renewable generation fluctuation and model uncertainties, the designed controller has presented robustness and good responses to meet desired control specifications. In addition, the settling time and raise time is reduced significantly in contrast to classical control system.

The performance is really excellent. It delivers very strong disturbance rejection (with minimal transient errors during load changes), and delivers it across the whole operating range without oscillatory response.

The structural change of engine control has a significant impact. Many hardware associated problems for controlling power generation engines are resolved when an appropriately controlled storage system is attached. Noticeably, turbocharger effects on engine dynamics are damped out after the storage system is utilized. With the help of a storage system, there are limited sudden load transients applied to the engine system. This means the engine system has enough time to have smooth ramp up and down during transients. There are several benefits when an engine does not have to cope with fast transients, such as avoiding undesired combustion, extending engine and actuators' life time and reducing fuel consumption to power ratio.

8.1.3.2. *Engine Speed and AFR Control*

Engine system is one of the key components within a microgrid system. Here an engine control is a byproduct of the developed microgrid control system. However, engine control has significant meaning in various industrial applications, such as: natural gas compressor stations, backup power generations, locomotive and marine applications. Our research shows that by developing a design approach utilizing a robust controller, the engine performance has improved dramatically compare to classical control when the same fluctuation load, uncertainties and noises are applied.

For power generation applications, the microgrid frequency is controlled via the engine crankshaft speed control. With a very solid engine speed control, the microgrid frequency is well maintained. It means the microgrid can provide high quality power in islanded mode. This further implies that when utility power is not available, or a microgrid is preferred for other reasons, and this approach improves power quality versus microgrid using traditional control. With the improved natural gas engine AFR control, engine emission is reduced and

it has significant meaning for the transportation applications, especially for many heavily polluted East Asian cities.

With the significant engine performance improvements we have achieved, this research may also extend the natural gas engine applications that were not feasible before because of the unacceptable transient performance.

8.1.3.3. *Storage System Control*

For a storage system, its output power and SOC are monitored and controlled. The storage system delivers the desired amount of power to the load to stabilize the grid frequency while the engine system catches up. By deploying the designed robust controller, the storage SOC does not drift significantly from its reference. This means there is no deep discharge requirement (little energy storage needed) which is a significant feature because it allows for cheap battery/storage options. In addition, this suggests that advanced control can reduce required storage capacity for certain hybrid system applications. The developed storage system controller can also be used for other storage applications, such as hybrid vehicle, pure electrical vehicle and diesel-electric submarine battery systems control and management.

8.1.3.4. *Determination of Storage Size*

By using a given historic microgrid load profile and desired microgrid performance specifications, the appropriate storage system size is determined based on simulation results. By choosing storage size properly, the microgrid performance is guaranteed and the cost of the storage system is minimized at the same time. There is always the a trade off between system performance and the storage system size. This study provides an analytical solution tool to deal with such kind of problems. The determined results are also used for guiding microgrid formation.

8.1.3.5. *Microgrid Configuration Examination*

If the storage system size is predetermined, the simulation tool can predict the system performance. By applying different step loads, one can find what size step load can push the system to the boundary of the acceptable performance. In this way, the maximum allowed load transients are found. By analysing the load historical profiles, renewable generation, engine size, storage energy capacity and power density, can all be analyzed and verified for the microgrid configuration.

8.2. System Studies Contributions and Remarks

By studying such a complicated large scale system, there are some contributions and remarks we would like to make toward the methodology of systems studies. In this section, our system study remarks are illustrated by using microgrid as an example.

8.2.1. *Subsystem Selection*

A system consisting of various subsystems is used to achieve certain goals, accomplish some tasks and fulfill various requests. However, to achieve such goals, tasks and requests, different subsystem combinations might be feasible. Which combination should be chosen? To make a wise decision, we essentially go down to the following fundamental elements, such as location, revenues, running cost, maintenance feasibility, capital costs, environmental impact, legislations, life time, overall performance and so on.

In a microgrid system, what kind of renewable generation should be selected? What kind of fossil fuel generation should be selected? What kind of storage system should be selected? What kind of control architecture should be selected? Based on the mentioned fundamental elements, the following choices are made. In Colorado, plenty of solar and

wind power are available for renewable generations. However, it is not feasible to acquire tidal energy here. In the U.S., the availability, lower cost and lower emission of natural gas supplies is sound. It is also sufficient for many decades to come. Hence, it makes more sense to deploy natural gas fossil engines when a microgrid is formed. In order to run such a complicated system smoothly with good robustness to disturbances, model uncertainties and internal dynamics, classical controls can no longer provide desired performance. Here we have successfully applied robust control techniques for microgrid control and amazing results have been achieved.

8.2.2. *Dominant Subsystem*

In a complex system, the subsystems are interconnected to work together and achieve various goals. Among these subsystems, there is a dominant subsystem(s), which has bigger impact toward the whole system or it is the essential element of the system. Without it, the entire system could not operate successfully. Such kind of subsystems should be studied more extensively.

In our microgrid studies, we focus on natural gas engine and storage system control. Each system has its own notable significance. Just by improving engine system performance, it is beneficial for many applications, such as power generation and transportation. On top of that we also extend the possible applications of natural gas engines. By studying storage system extensively, we would like to minimize its required energy capacity and extend its life time for our applications. The storage size minimization has significant impact when the whole system is deployed. Other subsystems within a microgrid are simply not within our scope of study.

8.2.3. *Maximize Capabilities of Each Subsystem*

Each subsystem within a system has its own unique skills. In order to have a complex system functioning as well as it potentially can, one of the key factors is to maximize the unique skills of each subsystem. In order to stimulate the maximum potential, it is necessary to know each subsystem property very well. As long as there are differences between subsystems, it is beneficial for the entire system. In some cases, if the subsystems are complementary in terms of their characteristics, it may even further enhance the overall system performance.

In a microgrid system, the storage system and engine system have their own unique accomplishments and characteristics. A storage system has much faster response, but it is expensive to ask for huge capacity. An engine system can provide huge power capacity. However, its transient responses are sluggish and unsatisfactory. In order to cope with fluctuating loads and renewable generations, the best strategy is to let the storage system catch the high frequency load variations and use the engine system to fulfill the slow and big load trends. By deploying such kind of strategies, we have achieved some amazing results in the simulation studies.

8.3. Future Work

The ultimate goal is to deliver a technically sound microgrid power solution. Because of the complexity of the research, in this dissertation, the further work is divided into three phases for achieving this ultimate goal. Each phase has its own tasks to be accomplished. The next phase can be started only when the previous phase is fully completed.

There is a powerhouse campus at Colorado State University. On this campus, there is some essential equipment, such as natural gas engine, load bank, wind and solar generation

simulators. This equipment can be utilized together to mimic a microgrid system. We can take advantage of the available equipment to further pursue our research. There are several tasks that need to be completed first, including:

(1) Storage system design and realization.

(2) Microgrid subsystems integration.

(3) Microgrid PID control realization in hardware.

(4) System uncertainties identification.

(5) Experimental data collection for models validation.

(6) Model validation with publications.

This phase one work focuses on having a running microgrid and validates the developed models based on simulation results and collected real data. A real microgrid control baseline is obtained as well. Once these tasks are accomplished, the second phase is triggered. In the second phase, we would like to complete the following tasks.

(1) Advanced MIMO controller realization in hardware.

- Ensure the control algorithm is implementable on give hardware. Laboratory type hardware setup is acceptable, such as National Instruments^{TM} and DSpace^{TM} products.

(2) Performance studies in terms of engine speed deviation, engine AFR deviation and storage SOC deviation.

- Deploy PID controlled microgrid control (Done in phase one.).
- Deploy two μ controller based microgrid control.
- Deploy single μ controller based microgrid control.
- Performance comparison, analysis and discussion.

(3) Efficiency study in terms of engine thermal efficiency and fuel consumption rate.

- Study based on PID controllers.
- Study based on two μ controllers.
- Study based on single μ controller.
- Efficiencies and costs comparison and conclusion.

(4) Stability study in terms of disturbance rejection (load acceptance, load rejection and measurement noises).

- When PID controllers are utilized.
- When two μ controllers are utilized.
- When single μ controller is utilized.
- Stability comparison, analysis and conclusion.

(5) Robustness study in terms of model uncertainties.

- Weights selection for performance orientated control setup.
- Weights selection for robustness orientated control setup.
- Weights selection for performance and robustness balanced. control setup.

At this point phase two is complete and a set of MIMO controls are realized in real-time. Through phase two, we have solid understanding of system performance, efficiency, stability and robustness. Also, the robust control theory is proven to work well in practice for a microgrid. In phase three, we have the following targets that need to be accomplished.

(1) Controller order reduction.

(2) Industry standard control unit deployment. (In many cases, the industrial hardware capacity is relatively limited for implementing sophisticated algorithms.)

(3) Extensive experimental test by using various load profiles, storage technologies, weather conditions and other real world considerations.

(4) Various levels of system protection for avoiding personal injury and hardware damage.

(5) Number of microgrid configurations for several typical applications are pre-determined, including hospital, industrial campuses, universities and so on.

(6) Conquered logistical issues, such as operation manual, safety guidance for operation, maintenance, troubleshooting and so on.

After phase three, the whole setup is technically verified, ready for commercialization and a complete customized microgrid solution can be provided.

Bibliography

[1] U.S. Department of Energy, "The smart grid: An introduction," Jan. 2011. [Online]. Available: http://www.doe.energy.gov/SmartGridIntroduction.htm

[2] C. Hernandez-Aramburo, T. Green, and N. Mugniot, "Fuel consumption minimization of a microgrid," *IEEE Transactions on Industry Applications*, vol. 41, no. 3, pp. 673–681, May, June 2005.

[3] A. M. Howlader, Y. Izumi, A. Uehara, N. Urasaki, T. Senjyu, A. Yona, and A. Y. Saber, "A minimal order observer based frequency control strategy for an integrated wind-battery-diesel power system," *Energy*, vol. 46, no. 1, pp. 168–178, 2012.

[4] GPI International Ltd., *GP Batteries Data Sheet (Model No.: GP18650CH)*, GP18650CH, GPI International Ltd.

[5] The Shift Project, "Breakdown of electricity generation by energy source," Website, Dec. 2012. [Online]. Available: http://www.tsp-data-portal.org/

[6] H. Pidd, "India blackouts leave 700 million without power," Dec. 2012. [Online]. Available: http://www.guardian.co.uk/world/2012/jul/31/india-blackout-electricity-power-cuts

[7] T. Del Carpio Huayllas, D. Ramos, and R. Vasquez-Arnez, "Microgrid systems: Current status and challenges," in *Transmission and Distribution Conf. and Expo.: Latin America (T&D-LA)*. IEEE/PES, Nov. 2010, pp. 7–12.

[8] N. Santhi and S. Kadloor, "Cascading failures on power grids." [Online]. Available: http://cnls.lanl.gov/~chertkov/SmarterGrids/Talks/Santhi.pdf

[9] P. Hines, K. Balasubramaniam, and E. Sanchez, "Cascading failures in power grids," *IEEE Potentials*, vol. 28, no. 5, pp. 24–30, Sep.,Oct. 2009.

[10] H. Sarma and R. Russell, "Second day of india's electricity outage hits 620 million," Dec. 2012. [Online]. Available: http://www.usatoday.com/news/world/story/2012-07-31/india-power-outage/56600520/1

[11] IEEE, "Institut of electrical and electronics engineers,." [Online]. Available: http://www.ieee.org

[12] IET, "Distributed generation," The Institution of engineering and Technology, Tech. Rep., Sep. 2006.

[13] SIEMENS, "Microgrids," white paper, 2011.

[14] C. Williams, "Distributed energy," *CHP systems*, pp. 57–59, Mar., Apr. 2004.

[15] R. H. Lasseter, "Microgrids and distributed generation," *Journal of Energy Engineering, American Society of Civil Engineers*, vol. 133, no. 3, pp. 144–149, Sep. 2007.

[16] T. Ehara and Mizuho information & research institute, Inc., Japan in co-opeartion with task 10 experts, "Overcoming PV grid issues in urban areas," International Energy Agency Photovoltaic power systems program, Tech. Rep. IEA-PVPS T10-06-2009, Oct. 2009.

[17] S. Bando, Y. Sasaki, H. Asano, and S. Tagami, "Balancing control method of a microgrid with intermittent renewable energy generators and small battery storage," in *Power and Energy Society General Meeting: Conversion and Delivery of Electrical Energy in the 21st Century*, July 2008, pp. 1–6.

[18] R. H. Lasseter and P. Piagi, "Control and design of microgrid components," *PSERC Publication 06*, vol. 3, 2006.

[19] R. Lasseter and P. Paigi, "Microgrid a conceptual solution," in *IEEE 35th Annu. Power Electronics Specialists Conf. (PESC)*, vol. 6, June 2004, pp. 4285–4290.

[20] M. Agrawal and A. Mittal, "Micro grid technological activities across the globe: A review," *International Journal of Research and Reviews in Applied Sciences*, vol. 7, no. 2, pp. 147–152, May 2011.

[21] R. L. Dohn, "The business case for microgrids," white paper, 2011.

[22] Y. Agarwal, T. Weng, and R. Gupta, "Understanding the role of buildings in a smart microgrid," in *Design, Automation Test in Europe Conf. Exhibition (DATE)*, Mar. 2011, pp. 1–6.

[23] Y. Han, P. Young, and D. Zimmerle, "Microgrid generation units optimum dispatch for fuel consumption minimization," pp. 1–17, 2012.

[24] Galvin Electricity Initiative, "Understanding microgrids," Galvin Electricity Initiative, Tech. Rep., 2009. [Online]. Available: http://www.galvinpower.org/sites/default/files/Hill_Briefing_FINAL.pdf

[25] B. Kroposki, R. Lasseter, T. Ise, S. Morozumi, S. Papatlianassiou, and N. Hatziargyriou, "Making microgrids work," *IEEE Power and Energy Magazine*, vol. 6, no. 3, pp. 40–53, May, June 2008.

[26] B. Perera, P. Ciufo, and S. Perera, "Point of common coupling (pcc) voltage control of a grid-connected solar photovoltaic system," in *The 39th Annu. Conf. of the IEEE on Industrial Electronics Society (IECON)*, Nov. 2013, pp. 7475–7480.

[27] J.D.Kueck, R.M.Staunton, and B.J.Kirby, "Microgrids and demand response," public utilities fortnightly, May 2003.

[28] M. Agrawal and A. Mittal, "Micro grid technological activities across the globe: A review." *International Journal of Research & Reviews in Applied Sciences*, vol. 7, no. 2, 2011.

[29] M. Barnes, J. Kondoh, H. Asano, J. Oyarzabal, G. Ventakaramanan, R. Lasseter, N. Hatziargyriou, and T. Green, "Real-world microgrids-an overview," in *IEEE Int. Conf. on System of Systems Engineering (SoSE)*, Apr. 2007, pp. 1–8.

[30] S. Bahramirad and E. Camm, "Practical modeling of smart grid sms^{TM}storage management system in a microgrid," in *Transmission and Distribution Conf. and Expo. (T&D)*. IEEE/PES, May 2012, pp. 1–7.

[31] H. Zhou, T. Bhattacharya, D. Tran, T. Siew, and A. Khambadkone, "Composite energy storage system involving battery and ultracapacitor with dynamic energy management in microgrid applications," *IEEE Transactions on Power Electronics*, vol. 26, no. 3, pp. 923–930, 2011.

[32] R. Arghandeh, M. Pipattanasomporn, and S. Rahman, "Flywheel energy storage systems for ride-through applications in a facility microgrid," *IEEE Transactions on Smart Grid*, vol. PP, no. 99, pp. 1–8, 2012.

[33] G. Morris, C. Abbey, S. Wong, and G. Joos, "Evaluation of the costs and benefits of microgrids with consideration of services beyond energy supply," in *Power and Energy Society General Meeting*. IEEE, July 2012, pp. 1–9.

[34] F. Katiraei, R. Iravani, N. Hatziargyriou, and A. Dimeas, "Microgrids management," *IEEE Power and Energy Magazine*, vol. 6, no. 3, pp. 54–65, 2008.

[35] N. Hatziargyriou, H. Asano, R. Iravani, and C. Marnay, "Microgrids," *IEEE Power and Energy Magazine*, vol. 5, no. 4, pp. 78–94, July, Aug. 2007.

[36] H. Jiayi, J. Chuanwen, and X. Rong, "A review on distributed energy resources and microgrid," *Renewable and Sustainable Energy Reviews*, vol. 12, no. 9, pp. 2472–2483, 2008.

[37] S. Morozumi, "Micro-grid demonstration projects in japan," in *Power Conversion Conf. (PCC)*, Apr. 2007, pp. 635–642.

[38] P. Basak, A. K. Saha, S. Chowdhury, and S. P. Chowdhury, "Microgrid: Control techniques and modeling," in *Proceedings of the 44th Int. Universities Power Engineering Conf. (UPEC)*, 2009, pp. 1–5.

[39] R. Zamora and A. K. Srivastava, "Controls for microgrids with storage: Review, challenges, and research needs," *Renewable and Sustainable Energy Reviews*, vol. 14, no. 7, pp. 2009–2018, 2010.

[40] Y. Han, A. Jain, P. Young, and D. Zimmerle, "Robust control of microgrid frequency with attached storage system," in *IEEE Conf. on Decision and Control (CDC)*, Dec. 2013, pp. 3043–3048.

[41] J. Pahasa and I. Ngamroo, "Coordinated control of wind turbine blade pitch angle and phevs using mpcs for load frequency control of microgrid," in *IEEE Systems Journal*, vol. 1, no. 99, Jan. 2014, pp. 1–9.

[42] Y. You, G. Wang, C. hua Zhang, and J. ru Lian, "An improved frequency control method for microgrid in islanded operation," in *2nd Int. Symposium on Instrumentation and Measurement, Sensor Network and Automation (IMSNA)*, Dec. 2013, pp. 296–299.

[43] G. Mallesham, S. Mishra, and A. Jha, "Ziegler-nichols based controller parameters tuning for load frequency control in a microgrid," in *Int. Conf. on Energy, Automation, and Signal (ICEAS)*, Dec. 2011, pp. 1–8.

[44] J. Mongkoltanatas, D. Riu, and X. LePivert, "H infinity controller design for primary frequency control of energy storage in islanding microgrid," in *European Conf. on*

Power Electronics and Applications (EPE), Sep. 2013, pp. 1–11.

[45] A. F. Mohd, "Development of modular grid architecture for decentralized generators in electrical power supply system with flexible power electronics," Ph.D. dissertation, The University of Applied Sciences, 2009.

[46] J. Guerrero, N. Berbel, J. Matas, J. Sosa, and L. de Vicuna, "Droop control method with virtual output impedance for parallel operation of uninterruptible power supply systems in a microgrid," in *22nd Annu. IEEE Applied Power Electronics Conf. (APEC)*, 2007, pp. 1126–1132.

[47] L. Wang, X. Q. Guo, H. R. Gu, W. Wu, and J. Guerrero, "Precise modeling based on dynamic phasors for droop-controlled parallel-connected inverters," in *IEEE Int. Symposium on Industrial Electronics (ISIE)*, 2012, pp. 475–480.

[48] C. Rowe, T. Summers, R. Betz, D. Cornforth, and T. Moore, "Arctan power 2013 frequency droop for improved microgrid stability," *IEEE Transactions on Power Electronics*, vol. 28, no. 8, pp. 3747–3759, 2013.

[49] C. Gao, R. Yang, J. Jiao, and Z. Dou, "Power control strategy design in an islanded microgrid based on virtual frequency," in *IET Renewable Power Generation Conf.*, Sep. 2013, pp. 1–4.

[50] M. Shao, R. Liu, and D. Lv, "Control strategy of voltage and frequency for islanded microgrid," in *Power Electronics and Motion Control Conf. (IPEMC)*, vol. 3, June 2012, pp. 2085–2089.

[51] E. Rokrok and M. E. H. Golshan, "Adaptive voltage droop scheme for voltage source converters in an islanded multibus microgrid," *Generation, Transmission Distribution, IET*, vol. 4, no. 5, pp. 562–578, 2010.

[52] Y. A. R. I. Mohamed and E. El-Saadany, "Adaptive decentralized droop controller to preserve power sharing stability of paralleled inverters in distributed generation microgrids," *IEEE Transactions on Power Electronics*, vol. 23, no. 6, pp. 2806–2816, 2008.

[53] L. Xu and D. Chen, "Control and operation of a dc microgrid with variable generation and energy storage," *IEEE Transactions on Power Delivery*, vol. 26, no. 4, pp. 2513–2522, Oct. 2011.

[54] Y. Zhangang, C. Yanbo, and W. Chengshan, "Construction, operation and control of a laboratory-scale microgrid," in *Int. Conf. on Sustainable Power Generation and Supply*, Apr. 2009, pp. 1–5.

[55] P. Degobert, S. Kreuawan, and X. Guillaud, "Micro-grid powered by photovoltaic and micro turbine," in *Int. Conf. on Renewable Energies in France*, 2006.

[56] M. Kao and J. Moskwa, "Turbocharged diesel engine modeling for nonlinar engine control and state estimation," *Journal of dynamic system, measurement and control*, vol. 117, pp. 20–30, 1995.

[57] M. Müller, E. Hendricks, and S. C. Sorenson, "Mean value modelling of turbocharged si engines," *Modelling of SI and Diesel Engines, SAE Special Publications*, pp. 125–145, 1998.

[58] L. Eriksson, L. Nielsen, J. Brugard, J. Bergstrom, F. Pettersson, and P. Andersson, "Modeling of a turbocharged si engine," *Annu. Reviews in Control*, vol. 26, no. 1, pp. 129–137, 2002.

[59] A. G. Stefanopoulou, I. Kolmanovsky, and J. S. Freudenberg, "Control of variable geometry turbocharged diesel engines for reduced emissions," *IEEE Transactions on*

Control Systems Technology, vol. 8, no. 4, pp. 733–745, 2000.

[60] A. Sivasubramanian and P. Meckl, "Numerical solution for multivariable idle speed control of a lean burn natural gas engine," in *Proceedings of American Control Conf.*, vol. 1, 2004, pp. 138–143.

[61] J. Wahlström and L. Eriksson, "Modelling diesel engines with a variable-geometry turbocharger and exhaust gas recirculation by optimization of model parameters for capturing non-linear system dynamics," *Proceedings of the Institution of Mechanical Engineers, Part D: Journal of Automobile Engineering*, vol. 225, no. 7, pp. 960–986, 2011.

[62] M. Kao and J. J. Moskwa, "Turbocharged diesel engine modeling for nonlinear engine control and state estimation," *Journal of Dynamic Systems, Measurement and Control*, vol. 117, no. 1, pp. 20–30, 1995.

[63] R. Omran, R. Younes, and J.-C. Champoussin, "Optimal control of a variable geometry turbocharged diesel engine using neural networks: Applications on the etc test cycle," *IEEE Transactions on Control Systems Technology*, vol. 17, no. 2, pp. 380–393, Mar. 2009.

[64] D. N. Malkhede, B. Seth, and H. C. Dhariwal, "Mean value model and control of a marine turbocharged diesel engine," *SAE technical paper series*, vol. 01, no. 3889, Oct. 2005.

[65] M. Jankovic and I. Kolmanovsky, "Constructive lyapunov control design for turbocharged diesel engines," *IEEE Transactions on Control Systems Technology*, vol. 8, no. 2, pp. 288–299, Mar. 2000.

[66] A. Stefanopoulou, I. Kolmanovsky, and J. Freudenberg, "Control of variable geometry turbocharged diesel engines for reduced emissions," in *American Control Conf.*, vol. 3, June 1998, pp. 1383–1388 vol.3.

[67] J. Wahlström and L. Eriksson, "Modelling diesel engines with a variable-geometry turbocharger and exhaust gas recirculation by optimization of model parameters for capturing nonlinear system dynamics," *Proceedings of Institution of Mechanical Engineers, Part D: Journal of Automobile Engineering*, vol. 225, May 2011.

[68] Y. Li-ping, M. Xiu-zhen, and S. En-zhe, "Influence of mixture quality on nonlinear combustion process of natural gas engine," in *Int. Conf. on Intelligent System Design and Engineering Application (ISDEA)*, vol. 1. IEEE, 2010, pp. 861–865.

[69] Y. Yildiz, A. Annaswamy, D. Yanakiev, and I. Kolmanovsky, "Spark-ignition-engine idle speed control: An adaptive control approach," *IEEE Transactions on Control Systems Technology*, vol. 19, no. 5, pp. 990–1002, 2011.

[70] Y. He and C.-C. Lin, "Development and validation of a mean value engine model for integrated engine and control system simulation," *SAE Paper*, pp. 1–1304, 2007.

[71] D. T. Hountalas and R. G. Papagiannakis, "development of a simulation model for direct injection dual fuel diesel natural gas engines," *SAE Paper*, 2000.

[72] D. McGowan, D. Morrow, and M. McArdle, "A digital pid speed controller for a diesel generating set," in *Power Engineering Society General Meeting*, vol. 3. IEEE, 2003.

[73] H. Nishizawa, M. Osawa, K. Ohtoshi, and T. Iwai, "Gain adjusting device for pid controller for controlling rotational speed of internal combustion engine," May 1993, uS Patent 5,213,077.

[74] M. Jankovic and I. Kolmanovsky, "Constructive lyapunov control design for turbocharged diesel engines," *IEEE Transactions on Control Systems Technology*, vol. 8, no. 2, pp. 288–299, 2000.

[75] R. B. Chedid, S. H. Karaki, and C. El-Chamali, "Adaptive fuzzy control for wind-diesel weak power systems," *IEEE Transactions on Energy Conversion*, vol. 15, no. 1, pp. 71–78, 2000.

[76] E.-S. Koo, H.-D. Lee, S.-K. Sul, and J.-S. Kim, "Torque control strategy for a parallel hybrid vehicle using fuzzy logic," in *IEEE Industry Applications Conf. (IAS Annu. Meeting)*, vol. 3. IEEE, 1998, pp. 1715–1720.

[77] J. Ruckert, F. Richert, A. Schlofier, D. Abel, O. Herrmann, S. Pischinger, and A. Pfeifer, "A model based predictive attempt to control boost pressure and egr-rate in a heavy duty diesel engine," *Modeling and control of economic systems 2001 (SME 2001)*, p. 111, 2003.

[78] E. Perez, X. Blasco, S. Garcia-Nieto, and J. Sanchis, "Diesel engine identification and predictive control using wiener and hammerstein models," in *IEEE Int. Conf. on Control Applications*. IEEE, 2006, pp. 2417–2423.

[79] R. Omran, R. Younes, and J.-C. Champoussin, "Optimal control of a variable geometry turbocharged diesel engine using neural networks: Applications on the etc test cycle," *IEEE Transactions on Control Systems Technology*, vol. 17, no. 2, pp. 380–393, 2009.

[80] C. Station, "Pi control," PPT, 2007.

[81] P. Dolovai, H. Joergl, and J. Hirzinger, "H_∞ controller design for speed control of a natural gas engine," in *27th Chinese Control Conf. (CCC)*, 2008, pp. 642–647.

[82] F. Zhang, K. Grigoriadis, M. Franchek, and I. Makki, "Linear parameter-varying lean burn air-fuel ratio control," in *IEEE Conf. on Decision and Control (CDC)*, 2005, pp. 2688–2693.

[83] G. J. Balas, "Linear, parameter-varying control and its application to aerospace systems," *Int. Council of Aeronautical Sciences*, 2002.

[84] Z. Weige, J. Jiuchun, X. Yuan, and Z. Xide, "Cng engine air-fuel ratio control using fuzzy neural networks," in *The 2nd Int. Workshop on Autonomous Decentralized System*, 2002, pp. 156–161.

[85] O. Tremblay, L.-A. Dessaint, and A.-I. Dekkiche, "A generic battery model for the dynamic simulation of hybrid electric vehicles," in *Vehicle Power and Propulsion Conf. (VPPC)*, Sep. 2007, pp. 284–289.

[86] L. Gao, S. Liu, and R. Dougal, "Dynamic lithium-ion battery model for system simulation," *IEEE Transactions on Components and Packaging Technologies*, vol. 25, no. 3, pp. 495–505, 2002.

[87] V. Agarwal, K. Uthaichana, R. DeCarlo, and L. Tsoukalas, "Development and validation of a battery model useful for discharging and charging power control and lifetime estimation," *IEEE Transactions on Energy Conversion*, vol. 25, no. 3, pp. 821–835, 2010.

[88] S. Ahmed, D. Boroyevich, F. Wang, and R. Burgos, "Development of a new voltage source inverter (vsi) average model including low frequency harmonics," in *Twenty-Fifth Annu. IEEE Applied Power Electronics Conf. and Expo. (APEC)*, 2010, pp. 881–886.

[89] A. Roshan, R. Burgos, A. Baisden, F. Wang, and D. Boroyevich, "A d-q frame controller for a full-bridge single phase inverter used in small distributed power generation systems," in *Applied Power Electronics Conf. (APEC)*, 2007, pp. 641–647.

[90] E. Wu and P. Lehn, "Digital current control of a voltage source converter with active damping of lcl resonance," in *Twentieth Annu. IEEE Applied Power Electronics Conf. and Expo. (APEC)*, vol. 3, 2005, pp. 1642–1649.

[91] R. Zhang, M. Cardinal, P. Szczesny, and M. Dame, "A grid simulator with control of single-phase power converters in dq rotating frame," in *Power Electronics Specialists Conf. (PESC)*, vol. 3. IEEE, 2002, pp. 1431–1436.

[92] U.S. Department of Energy, "Grid 2030: A national vision for electricity's second 100 years," *Transforming the Grid to Revolutionize Electric Power in North America*, July 2003.

[93] U.S. Energy Information Administration, *Energy Infobooks*, ser. Natural Gas. National Energy Education Development Porject (NEED), 2012.

[94] J. Pratte, "Fossil fuels: Natural gas," Environmental Science Activities for the 21st Century, July 2004.

[95] U.S. Energy Information Administration, "Annu. energy review 2011," U.S. Energy Information Administration, Tech. Rep., 2011.

[96] Q. Zhong, *Robust Control of Time-delay Systems*. Springer, 2006.

[97] P. A. Ioannou and J. Sun, *Robust adaptive control*. Courier Dover Publications, 2012.

[98] Y. Han, P. Young, and D. Zimmerle, "Optimum generation units dispatch for fuel consumption minimization," pp. 7206–7211, Dec. 2011.

[99] Y. Han, P. Young, and D.Zimmerle, "Optimal selection of generators in a microgrid for fuel usage minimization," in *IEEE Power and Energy Society General Meeting (PES)*, 2013, pp. 1–5.

[100] J. Doyle, B. Francis, and A. Tannenbaum, *Feedback control theory.* Macmillan Pub. Co., 1992.

[101] I. Sigurd Skogestad Postlethwaite, *Multivariable Feedback Control: Analysis and Design*, 2nd ed. John Wiley and sons Inc, 2005.

[102] H. Koc, D. Knittel, M. De Mathelin, and G. Abba, "Modeling and robust control of winding systems for elastic webs," *IEEE Transactions on Control Systems Technology*, vol. 10, no. 2, pp. 197–208, 2002.

[103] M. Anderson, M. Buehner, P. Young, D. Hittle, C. Anderson, J. Tu, and D. Hodgson, "Mimo robust control for hvac systems," *IEEE Transactions on Control Systems Technology*, vol. 16, no. 3, pp. 475–483, 2008.

[104] A.-H. Mohsenian-Rad, V. Wong, J. Jatskevich, and R. Schober, "Optimal and autonomous incentive-based energy consumption scheduling algorithm for smart grid," in *Innovative Smart Grid Technologies (ISGT)*, Jan. 2010, pp. 1–6.

[105] T. Liu, Y. Yang, X. Li, Z. Xing, F. Wang, P. Su, and H. Luo, "Energy saving generation dispatch for sustainable development of energy utilizing in china," in *Power and Energy Engineering Conf. (APPEEC) Asia-Pacific*, Mar. 2010, pp. 1–4.

[106] M. Yoshikawa, N. Toshida, H. Nakajima, Y. Harada, M. Tsurugai, and Y. Nakata, "On-line economic load dispatch based on fuel cost dynamics," *IEEE Transactions on Power Systems*, vol. 12, no. 1, pp. 315–320, Feb. 1997.

[107] S. Das, A. Konar, and U. K. Chakraborty, "Two improved differential evolution schemes for faster global search," in *Proceedings of the conf. on Genetic and evolutionary computation*. ACM, 2005, pp. 991–998.

[108] G. Liao, "Using chaotic quantum genetic algorithm solving environmental economic dispatch of smart microgrid containing distributed generation system problems," in *Int. Conf. on Power System Technology (POWERCON)*, Oct. 2010, pp. 1–7.

[109] M. Cordaro, "Understanding base load power. what it is and why it matters," *New York Affordable Reliable Electricity Alliance (New York AREA)*, Oct. 2008.

[110] M. A. Ortega-Vazquez and D. S. Kirschen, "Optimizing the spinning reserve requirements using a cost/benefit analysis," *IEEE Transaction on Power System*, vol. 22, no. 1, pp. 24–33, Feb. 2007.

[111] M. J. Thompson, "Fundamentals and advancements in generator synchronizing systems," *Proceedings of POWER-GEN Int., Orlando, FL*, Dec. 2010, Schweitzer Engineering Laboratories, Inc.

[112] D. Kirschen and G. Strbac, *Fundamentals of Power System Economics*, 1st ed. John Wiley & Sons., 2004.

[113] Z. Yuan, Z. Hou, and C. Jiang, "Economic dispatch and optimal power flow based on chaotic optimization," in *Int. Conf. on Power System Technology (PowerCon)*, vol. 4, 2002, pp. 2313–2317.

[114] E. K. P. Chong and S. H. Zak, *An Introduction to Optimization (Wiley-Interscience Series in Discrete Mathematics and Optimization)*, 3rd ed. Wiley-Interscience, Feb. 2008.

[115] Y. Han, P. Young, and D. Zimmerle, "Constrained optimum generator dispatch for fuel consumption minimization," IEEE, pp. 1–5, 2013.

[116] Y. Rebours and D. Kirschen, "What is spinning resrve?" The University of Manchester, Notes, 2005.

[117] J. Casazza and F. Delea, *Understanding Electric Power Systems: An Overview of the Tehcnology and the Marketplace*. Wiley inter-science, 2003.

[118] A. von Meier, *Electric Powr Sytems A Conceptual Introduction*. A John Wiley and Sons, INC.,, 2006.

[119] A. Eberhand, M. Lazarus, S. Bernow, C. Rajan, T. Lefevre, M. Cabrera, D. O'Leary, R. Peters, B. Svensson, and R. Wilkinson, "Electricity supply and demand side management options," *WCD Thematic Reviews Options Issues Series IV.1*, Mar. 2000, World Commission on Dams Secretariat.

[120] Caterpillar, "Electrical power ratings guide-generator sets," Caterpillar Power Generation Resource Center, Tech. Rep., Mar. 2011.

[121] Cashman Power Solutions, "Generator set ratings," Cashman Power Solutions, Tech. Rep., May 2010.

[122] Kohler Power Systems, "Generator set ratings guidelines," Kohler Power Systems, Tech. Rep. Technical Information Bulletin, Sep. 2000.

[123] B. S. Blanchard and W. J. Fabrycky, *Systems Engineering and Analysis*, 5th ed., ser. Prentice Hall International Series in Industrial and System Engineering. Prentice Hall, 2011.

[124] J. M. Fisher, T. I. Hyde, T. G. S. Landen, and D. Thompsett, "Three-way catalyst," Jan. 2004, uS Patent 6,680,036.

[125] E. Alfieri, A. Amstutz, and L. Guzzella, "Gain-scheduled model-based feedback control of the air/fuel ratio in diesel engines," *Control Engineering Practice*, vol. 17, no. 12, pp. 1417–1425, 2009.

[126] C. Alippi, C. de Russis, and V. Piuri, "A neural-network based control solution to air-fuel ratio control for automotive fuel-injection systems," *IEEE Transactions on Systems, Man, and Cybernetics, Part C: Applications and Reviews*, vol. 33, no. 2, pp. 259–268, May 2003.

[127] L. Guzzella and C. Onder, *Introduction to Modelling and Control of Internal Combustion Engine Systems*. Springer, 2004.

[128] L. Eriksson, L. Nielsen, J. Brugrd, J. Bergstrm, F. Pettersson, and P. Andersson, "Modeling of a turbocharged si engine," *Annual Reviews in Control*, vol. 26, no. 1, pp. 129–137, 2002.

[129] J. Heywood, *Internal combustion engine fundamentals*, ser. McGraw-Hill series in mechanical engineering. McGraw-Hill, 1988.

[130] L. Guzzella and C. Onder, *Introduction to Modelling and Control of Internal Combustion Engine Systems*. Springer, 2004.

[131] D. N. Malkhede, B. Seth, and H. Dhariwal, "Mean value model and control of a marine turbocharged diesel engine," *SAE Technical Paper*, 2005.

[132] M. Jankovic, M. Jankovic, and I. Kolmanovsky, "Constructive lyapunov control design for turbocharged diesel engines," *IEEE Transactions on Control Systems Technology*, vol. 8, no. 2, pp. 288–299, 2000.

[133] R. Hedinger and N. Zsiga, "Engine systems," Eidgenossische Technische Hochschule Zric, Institute for Dyanmic Systems and Control, Tech. Rep., Sep. 2013.

[134] E. Duve, J. Heilenbach, and J. Panos, "Turbocharger rotor with ball bearings," Oct. 2002, eP Patent App. EP20,020,004,193.

[135] M. Kao and J. J. Moskwa, "Turbocharged diesel engine modeling for nonlinear engine control and state estimation," *Journal of dynamic systems, measurement, and control*, vol. 117, no. 1, pp. 20–30, 1995.

[136] R. Omran, R. Younes, and J.-C. Champoussin, "Optimal control of a variable geometry turbocharged diesel engine using neural networks: Applications on the etc test cycle," *IEEE Transactions on Control Systems Technology*, vol. 17, no. 2, pp. 380–393, 2009.

[137] M. Boley and C. L. Hagen, "Simulation of turbocharged marine diesel engine for electrical power system trainer," in *ASME Internal Combustion Engine Division Spring Technical Conf.* American Society of Mechanical Engineers, 2012, pp. 691–702.

[138] K. Patton, R. Nitschke, J. Heywood, and S. of Automotive Engineers, *Development and Evaluation of a Friction Model for Spark-ignition Engines*. Society of Automotive Engineers, 1989.

[139] D. Sandoval and J. B. Heywood, "An improved friction model for spark-ignition engines," *SAE transactions*, vol. 112, no. 3, pp. 1041–1052, 2003.

[140] A. Ganguli and R. Rajamani, "Tractable model development and system identification for longitudinal vehicle dynamics," *Proceedings of the Institution of Mechanical Engineers, Part D: Journal of Automobile Engineering*, vol. 218, no. 10, pp. 1077–1084, 2004.

[141] I. Gyuk, P. Kulkarni, J. Sayer, J. Boyes, G. Corey, and G. Peek, "The united states of storage [electric energy storage]," *Power and Energy Magazine*, vol. 3, no. 2, pp. 31–39, 2005.

[142] D. Linden, "Handbook of batteries and fuel cells," *New York*, 1984.

[143] K. Divya and J. Ostergaard, "Battery energy storage technology for power systemsan overview," *Electric Power Systems Research*, vol. 79, no. 4, pp. 511–520, 2009.

[144] K. Yoshimoto, T. Nanahara, and G. Koshimizu, "New control method for regulating state-of-charge of a battery in hybrid wind power/battery energy storage system," in *Power Systems Conf. and Expo. (PSCE)*. IEEE, 2006, pp. 1244–1251.

[145] C. Shepherd, "Design of primary and secondary cells ii. an equation describing battery discharge," *Journal of the Electrochemical Society*, vol. 112, no. 7, pp. 657–664, 1965.

[146] O. Tremblay, L.-A. Dessaint, and A.-I. Dekkiche, "A generic battery model for the dynamic simulation of hybrid electric vehicles," in *Vehicle Power and Propulsion Conf. (VPPC)*, Sep. 2007, pp. 284–289.

[147] T. Olivier and D. Louis-A., "Experimental validation of a battery dynamic model for ev applications," *World Electric Vehicle Journal*, vol. 3, 2009.

[148] H. Wenzl, I. Baring-Gould, R. Kaiser, B. Y. Liaw, P. Lundsager, J. Manwell, A. Ruddell, and V. Svoboda, "Life prediction of batteries for selecting the technically most suitable and cost effective battery," *Journal of Power Sources*, vol. 144, no. 2, pp. 373–384, 2005.

[149] F. Milano, *Power system modelling and scripting*. Springer, 2010.

[150] A. Cherif, M. Jraidi, and A. Dhouib, "A battery ageing model used in stand alone PV systems," *Journal of Power Sources*, vol. 112, no. 1, pp. 49–53, 2002.

[151] G. Seeling-Hochmuth, *Optimisation of hybrid energy systems sizing and operation control*. Kassel University Press, 1998.

[152] J. Schiffer, D. U. Sauer, H. Bindner, T. Cronin, P. Lundsager, and R. Kaiser, "Model prediction for ranking lead-acid batteries according to expected lifetime in renewable energy systems and autonomous power-supply systems," *Journal of Power Sources*, vol. 168, no. 1, pp. 66–78, 2007.

[153] M. Zheng, B. Qi, and X. Du, "Dynamic model for characteristics of li-ion battery on electric vehicle," in *IEEE Conf. on Industrial Electronics and Applications (ICIEA)*, May 2009, pp. 2867–2871.

[154] P. M. Gomadam, J. W. Weidner, R. A. Dougal, and R. E. White, "Mathematical modeling of lithium-ion and nickel battery systems," *Journal of Power Sources*, vol. 110, no. 2, pp. 267–284, 2002.

[155] Battery University. (2014, Aug.) What is the c-rate? [Online]. Available: http://batteryuniversity.com/learn/article/what_is_the_c_rate